# Identifying the signature and mechanism of long-term permanent strain along the Cascadia coastline, southwestern Washington

Kelsay M. Stanton

A dissertation

submitted in partial fulfillment of the requirements for

the degree of

Doctor of Philosophy

University of Washington

2024

Reading Committee:

Juliet Crider, Chair

Harvey Kelsey

Alison Duvall

David Schmidt

Program Authorized to Offer Degree:

Earth and Space Science

University of Washington

## Abstract

Identifying the signature and mechanism of long-term permanent strain along the Cascadia coastline, southwestern Washington

Kelsay M. Stanton

Chair of the Supervisory Committee:

Dr. Juliet Crider

Department of Earth and Space Sciences

Long-term deformation at a subduction margin (i.e., over many earthquake cycles) implies permanent strain accumulation. This complicates regional strain budgets as well as expectations of earthquake cyclicity based on the elastic rebound model because not all interseismic strain is released during an earthquake. Characterizing the extent, timing, and rate of forearc deformation at a subduction zone is crucial to understanding the strain budget and subduction zone earthquake cycle. Characterizing coastal uplift is also necessary for assessing the possible mechanisms accommodating permanent deformation in the forearc, such as crustal folding or faulting on the overriding plate. Finally, constraining permanent strain accumulation informs tectonic models and provides key information for estimating seismic hazards.

Pleistocene coastal uplift is observed at the Cascadia subduction zone, although no prior studies constrained long-term uplift in coastal southwestern Washington. This dissertation presents new mapping and luminescence dating of Quaternary deposits near Grays Harbor and Willapa Bay to show that estuarine deposits record a late Pleistocene average uplift rate of 0.4 ± 0.1 mm/yr. Uplift rates of this magnitude are consistent with other Pleistocene uplift and incision rates in Cascadia, and when compared to observed interseismic vertical deformation, the rates suggest that about one-tenth of interseismic strain may become permanent. Other locations in Cascadia with similar uplift rates are characterized by crustal folds or faults, but no faults are evident in the onshore Quaternary deposits near Grays Harbor and Willapa Bay. Map-view interpretation and two-dimensional modeling with gravity and magnetic data indicate north- and northwest-trending faults underlie the Quaternary deposits. The modeling suggests two 20-25° east-dipping reverse faults. One fault aligns with the active Willapa Bay fault zone, identified previously from offshore seismic-reflection studies, and the other fault aligns with the Raymond fault, previously inferred from geophysical modeling. Uplift recorded in the estuarine deposits is likely accommodated by the Willapa Bay fault zone. The modeling also suggests that faults mapped in regional bedrock with small lateral offsets must also have a significant vertical component of slip. The geophysical modeling combined with previous geologic mapping thus suggests that regional faults may be oblique. Coastal southwestern Washington may be transitional between deformational domains, with faults accommodating both east-directed, subduction-related strain and north-directed strain related to tectonic block rotation. Active subsurface faults may leave a geomorphic signature of deformation. Where geophysical modeling locates the Raymond fault, geomorphic analyses indicate knickpoints in stream profiles that may reflect a relict fluvial system once graded to a base level 85-150m higher than current sea level. Because Quaternary

sea level fluctuations cannot account for 85-150 m of base level fall, the base level change likely reflects regional rock uplift, possibly accommodated by the Raymond fault. The Willapa Bay fault zone, however, does not produce surficial lineaments nor measurable differences in stream profile steepness where it projects ashore nor where geophysical maps indicate a change in strike. The geomorphic analyses of longitudinal stream profiles indicate a close relationship between steepened channels, bedrock faults, and lithologic contacts, an observation that supports structural and geophysical models for uplifted fault-bound blocks of basalt. Taken together, long-term permanent uplift in coastal southwestern Washington is at least partially accommodated by long-lived, active crustal faults.

# Table of Contents

# List of Tables

# List of Figures

# Acknowledgements

None of us completes our work without help. My advisory committee for my dissertation has been wonderful! Thank you to Juliet Crider, not only for her mentorship on this work, but for all the mentorship she has provided in the past and hopefully, in the future. Thank you to Harvey Kelsey for many years of intellectual stimulation and support. Thank you to Alison Duvall and David Schmidt for their time as committee members and their willingness to help however they could. Thank you to Megan Anderson for great conversations about geophysics and modeling, tectonics and Washington geology. Thank you to Lydia Staisch for help in the field and for thoughtful conversations about regional tectonics. Thank you to Jim Feathers for his patience as I learn about luminescence dating. Thank you to Brian Atwater for pushing ideas and papers my way. Thank you to Jody Bourgeois for feedback and goodwill.

I have many colleagues who have provided meaningful conversation about my work and about regional geology and tectonics. There are too many to list so I'll thank you next time we meet!

Most importantly, thank you to Ben Stanton.

This work was funded by grants provided by the U.S. Geological Survey National Earthquake Hazard Reduction Program, the Earth and Space Sciences Department at the University of Washington, the Geological Society of America, and the Northwest Scientific Association.

# Chapter 1. Introduction

The Cascadia subduction zone (CSZ or Cascadia), located off the west coast of Oregon, Washington, and northern California, USA, and of British Columbia, Canada, hosts active convergence between the Juan de Fuca oceanic plate and the North America plate. The Holocene geologic record from Washington and Oregon indicates coastal subsidence associated with Cascadia megathrust earthquakes (e.g., Atwater, 1987, 1992; Atwater and Yamaguchi, 1991; Witter et al., 2003); yet, long-term coastal uplift is observed in northern Washington, Oregon, and northern California in the form of uplifted marine sediments and coastal topography (e.g., Palmer, 1967; Kelsey, 1990; Kelsey et al., 1994; Kelsey et al., 1996, Thackray, 1996, 1998; Padgett et al, 2019). Although mapping in coastal southwestern Washington indicated marine deposits at elevations above sea level (e.g., Wagner 1967a, b; Walsh et al., 1987) many questions remained regarding the extent, rate, and mechanism of uplift.

This dissertation characterizes the long-term deformation observed in coastal southwestern Washington and investigates the mechanisms accommodating that strain. Deformation of the overriding plate at a subduction zone denotes interseismic strain accumulation. Subduction-related interseismic strain accumulation may result in coastal uplift on the overriding plate, probably as the result of locking of the subduction interface. A subsequent earthquake releases the strain, causing subsidence of the coastal region (e.g., Hyndman and Wang, 1995; Clague, 1997). Although most interseismic strain is thought to be released elastically (i.e., elastic rebound; Reid, 1910; Whipple, 1936), it is also well recognized that a portion of interseismic strain must be converted to permanent deformation as there are uplifted marine or coastal deposits at many

subduction zones (e.g., Saillard et al., 2009; Melnick et al., 2006; Matsu'ura et al., 2015, 2019; Kelsey, 1990; Kelsey et al., 1994, 1996; Stanton et al., 2023, Chapter 2).

Permanent strain accumulation complicates the expectation of regular earthquake cyclicity predicted by the elastic rebound model (Thatcher, 1984). In this simple model, if all interseismic strain is released elastically, and if stress rate and threshold stress are constant, then the time interval between events should be consistent (e.g., Reid, 1910; Bufe et al., 1977; Shimazaki and Nakata, 1980, Sykes and Quittmerye, 1981; Bakun and McEvilly, 1984). The estimation of recurrence interval is more complex, however, if not all interseismic strain is released elastically. An estimation of the amount of permanent strain accommodated in a fault system can serve as a first-order correction to earthquake recurrence models relying on estimates of interseismic strain from geodetic measurements (e.g., Fialko, 2006; Szeliga et al, 2012; Cheloni et al, 2014). Accordingly, evaluation of permanent deformation at a subduction zone is crucial to understanding the strain budget and earthquake cycle.

Permanent deformation of the forearc also signifies subduction-related processes that contribute to convergent margin evolution. For example, a variety of mechanisms have been proposed for accommodating permanent deformation at a subduction zone: sediment underplating of the overriding plate (Delph et al., 2021); subduction of bathymetric asperities (e.g., Freisleben et al., 2021); mantle wedge buoyancy (Bodmer et al., 2020); or post-seismic slip (e.g., Sawai et al., 2004; Kelsey et al., 2006). Crustal folding or faulting on the overriding plate may also accommodate permanent subduction-related strain (e.g., Thatcher, 1984; McCrory, 1997; Kelsey et al., 1996; Delano et al., 2017). Characterizing the extent, timing, and rate of forearc deformation may

establish constraints for competing tectonic models at a subduction zone, not to mention provide key information for estimating seismic hazards from both the megathrust and forearc faults.

An overarching question guides my research: what is the extent, rate, and mechanism(s) of long-term deformation recorded by Pleistocene sedimentary deposits in southwestern Washington? This broad inquiry is best approached through a series of more specific questions, each one addressed as a chapter in this dissertation.

1) What are the lithologies, ages, and uplift rates of Quaternary deposits near Grays Harbor and Willapa?
2) Can I estimate the existence and rates of active structures under Willapa Bay and the coastal Quaternary deposits using geophysical data and related modeling?
3) Do fluvial systems in coastal southwestern Washington record geomorphic evidence of regional deformation?

Chapter 2 (Stanton et al., 2023) describes my work mapping the Quaternary deposits south of Grays Harbor and near Willapa Bay in coastal southwestern Washington. These deposits were previously mapped as a single unit, Quaternary terraces (Qt) that were inferred to be Pleistocene marine deposits (Wagner, 1967a, b; Kvenvolden et al., 1979; Clifton, 1983; Walsh et al., 1987). Through mapping at approximately 1:24,000 scale, I identified nine new units, including estuarine and fluvial deposits. I used luminescence dating, along with an evaluation of previous ages from fossil shells and an assessment of relative age based on soil maturity and terrace elevation, to establish the probable ages of three estuarine units. These estuarine units were deposited at sea-level high stands during marine isotope stages 5a, 5c, and 5e. The terraced estuarine units record an average uplift rate of $0.4 \pm 0.1$ mm/yr, consistent with other Pleistocene

uplift and incision rates in Cascadia (e.g., Palmer, 1967; Kelsey, 1990; Kelsey et al., 1994; Kelsey et al., 1996, Thackray, 1996, 1998; Padgett et al, 2019). When compared to observed interseismic vertical deformation, these rates suggest that about one-tenth of interseismic strain may become permanent (Stanton et al., 2023). A version of this chapter was published as an article within the journal Quaternary Research (Stanton et al., 2023). Co-authors Juliet Crider and Harvey Kelsey provided guidance on the premise of the work and edited the manuscript. Co-author James Feathers conducted the luminescence dating and provided guidance on the methodology portion of the manuscript. All co-authors provided some assistance in the field.

Although the uplifted estuarine deposits record uplift at rates that, at other locations in Cascadia, are accommodated by crustal folds or faults, no faults are evident in the onshore Quaternary deposits in coastal southwestern Washington. Thus, in Chapter 3, I explore the possibility of subsurface faults near Willapa Bay using gravity and aeromagnetic data for map interpretation and two-dimensional geophysical modeling. I identify north and northwest trending faults underlying Quaternary deposits and Willapa Bay from gravity and magnetic maps. The two-dimensional modeling suggests two 20-25° east-dipping reverse faults. One of the faults aligns with the active Willapa Bay fault zone identified previously from offshore seismic-reflection studies (McCrory et al., 2002). The uplift recorded in the estuarine deposits is likely accommodated by the Willapa Bay fault zone. The other fault aligns with the Raymond fault. The Raymond fault, previously inferred from other geophysical studies, uplifts Crescent Formation basalts exposed east and northeast of the fault in the Raymond Hills. Based on the geophysical models along, I estimate that the Willapa Bay fault and the Raymond fault have a long-term average slip rate of ~0.05 mm/yr since the late Eocene, assuming pure dip-slip motion. Additionally, the models indicate that faults previously mapped with small lateral offsets in

Eocene-Miocene rocks east of Willapa Bay may have a significant vertical component. Taken together, the modeling and the previous mapping suggest oblique regional faults. Coastal southwestern Washington might be a transition between deformational domains, with faults accommodating both east-directed, subduction-related strain and north-directed strain related to forearc tectonic block rotation (Stanton et al., *in preparation*). This chapter is being prepared for submission to the journal Tectonics. Co-authors Juliet Crider, Harvey Kelsey, and Lydia Staisch provided guidance on the premise of the manuscript and contributed editorial suggestions. Lydia Staisch assisted with collection of gravity data during summer 2019. Megan Anderson and Todd Lau provided mentorship in geophysical modeling, with Megan Anderson also providing guidance on manuscript structure and editing.

In Chapter 4, I assess whether the subsurface faults inferred from geophysical maps and models are causing surface deformation reflected in patterns of rivers that flow across the surface of this region. In particular, I analyze the longitudinal profiles of a selection of streams to assess variability of channel steepness and concavity, shown to reflect deformation in other settings (Kirby and Whipple, 2012). I also search for evidence of deformation manifesting as surficial lineaments in the topography located above modeled subsurface faults. I find slope-break knickpoints in stream profiles near the Raymond fault. Relict sections of flatter channel profiles upstream of these knickpoints are graded to a base level 85-150 m higher than current sea level. Because Quaternary sea-level fluctuation cannot accommodate 85-150 m of base level fall, the base level change likely reflects regional rock uplift, possibly accommodated by the Raymond fault. Additionally, regional analyses of channel steepness indicate a close relationship between steepened channels, bedrock faults, and lithologic contacts, an observation that supports structural models for regional fault-bound blocks of basalt. The Willapa Bay fault zone, which is

active (McCrory et al., 2002) and likely responsible for the uplifted estuarine deposits (Stanton et a., 2023; Stanton et al., *in preparation*), does not produce surficial lineaments nor measurable differences in stream profile steepness and concavity where it projects ashore nor where geophysical maps indicate a change in strike.

In addition to these chapters, I have placed my geologic maps, associated topographic sections, and all field notes and photos on the University of Washington Research Archive (https://digital.lib.washington.edu/researchworks/handle/1773/46938). All gravity data, including the gravity data collected during this research, can be access on the Washington State Department of Natural Resources Geologic Information Portal (https://www.dnr.wa.gov/geologyportal). The aeromagnetic data (Blakely and Sherrod, 2020) used for magnetic maps and modeling in this study are available at the U.S. Geological Survey ScienceBase-Catalog ( https://doi.org/10.5066/P9T4UC6W). A ~1:24,000 Quaternary geologic map and accompanying pamphlet and plates may be found in Appendix 1 of this dissertation. Supplemental materials for Chapter 2 may be found in Appendix 2 of this dissertation. Supplemental materials for Chapter 3 may be found in Appendix 3 of this dissertation. Supplemental materials for Chapter 4 may be found in Appendix 4 of this dissertation.

# Chapter 2. The signature of accumulated permanent uplift, northern Cascadia subduction zone.



Stanton, Kelsay M., Crider, Juliet G., Kelsey, Harvey M., and Feathers, James K., 2023, The signature of accumulated permanent uplift, northern Cascadia subduction zone, Quaternary Research, 1-21, https://doi.org/10.1017/qua.2023.59.

## Abstract

Uplift of the overriding plate at a subduction zone denotes interseismic strain accumulation, which is subsequently released during a megathrust earthquake. Although most interseismic strain is thought to be released elastically, observations of uplifted coastal regions at subduction zones world-wide indicate that some strain may result in permanent uplift. The Grays Harbor and Willapa Bay (Washington, USA) coastal region of the Cascadia subduction zone hosts flights of marine terraces testifying to late Pleistocene rock uplift. Our new detailed mapping of the marine terraces recognizes nine new units, including estuarine and fluvial sediments. Luminescence dating, relative age based on soil maturity and terrace elevation, and an evaluation of previous ages from fossil shells collectively constrain the probable ages of three estuarine units to sea-level high stands during marine isotope stages 5a, 5c, and 5e. We estimate an average uplift rate of 0.4 ± 0.1 mm/yr for the terraced estuarine units, consistent with other Pleistocene uplift and incision rates in Cascadia. When compared to observed interseismic vertical deformation, these

rates suggest that about one-tenth of interseismic strain may become permanent. The values are permissible within the uncertainties of uplift based on regional estimates of interseismic vertical strain rates and of coseismic subsidence.

## Introduction

At subduction zones around the world we see apparent mismatch between subsidence related to megathrust earthquakes and Pleistocene uplift. In a common conceptual model, interseismic strain accumulation resulting from plate locking at the subduction interface uplifts the overriding plate; a subsequent earthquake releases the strain, causing subsidence (e.g., Hyndman and Wang, 1995; Clague, 1997). Although most interseismic strain is thought to be released elastically (i.e., elastic rebound; Reid, 1910; Whipple, 1936), observations indicate some strain may result in permanent deformation. For example, more than a meter of co-seismic and pre-seismic subsidence accompanied the 2011 Tohoku-Oki megathrust earthquake (Nishimura, 2014), but terraces preserved above sea level in northeast Japan record late Pleistocene uplift at rates between 0.2 and 0.46 mm/yr (Matsu'ura et al., 2015; 2019). In Chiloe, south-central Chile, buried soil sequences indicate co-seismic subsidence (Atwater et al., 1992; Garrett et al., 2015), but coastal marine terraces record Pleistocene uplift rates between 0.1 and 2 mm/yr (Melnick et al., 2006; Saillard et al., 2009). For uplift to occur, some portion of the interseismic strain must be converted to permanent deformation. Permanent deformation may be accommodated by crustal folding or faulting, or by processes related to subduction, such as sediment underplating of the overriding plate (Delph et al., 2021), subduction of bathymetric anomalies (e.g., Freisleben et al., 2021), mantle buoyancy (Bodmer et al., 2020), or post-seismic slip (e.g., Sawai et al., 2004, Kelsey et al., 2006). Measurements of uplift along subduction zones on the timescale of

tens-to-hundreds-of-thousands years are crucial to understanding how and why this longer-term strain accommodation departs from the elastic rebound model.

The Cascadia subduction zone (CSZ or Cascadia), located off the coast of Oregon, Washington, and northern California USA, and British Columbia, Canada, hosts convergence between the Juan de Fuca and the North America plates (Fig. 2-1a). The Holocene geologic record from Washington and Oregon indicates coastal subsidence associated with Cascadia megathrust earthquakes (e.g., Atwater, 1987, 1992; Atwater and Yamaguchi, 1991; Witter et al., 2003); yet, long-term coastal uplift is observed at many locations along Cascadia in the form of uplifted marine sediments and coastal topography (e.g., Palmer, 1967; Kelsey, 1990; Kelsey et al., 1994; Kelsey et al., 1996, Thackray, 1996, 1998; Padgett et al, 2019). Constraining the Pleistocene uplift and uplift rates along Cascadia is a first step for evaluating permanent deformation in the framework of the elastic rebound model. While other studies have documented Pleistocene coastal uplift rates in northern Washington, Oregon and northern California, lack of detailed Quaternary mapping in southwestern Washington left a gap in our understanding.

Uplifted coastal marine terraces have yielded information on deformation rates and fault activity in active tectonic settings around the world, including New Zealand (e.g., Berryman, 1993; Clark et al., 2010), California (e.g., Merritts and Bull, 1989; Lajoie et al., 1991; Hanson et al., 1994), and Alaska (e.g., Plafker and Rubin, 1978). A marine terrace typically forms during a sea-level high stand, with the inner edge (also called shoreline angle) of the terrace representing the former shoreline (Bradley and Griggs, 1976). The inner edge serves as a horizontal datum for recording the magnitude and rate of coastal uplift (Bradley and Griggs, 1976; Lajoie, 1986). Shallow crustal deformation can be measured and constrained in time if uplifted inner edges are mapped

and assigned an age (e.g., Kelsey, 1990; Berryman, 1993). Southwestern Washington is one of the few areas in Cascadia where estuarine deposits are preserved as marine terraces and therefore offers an ideal location for examining long-term sediment accumulation along an active margin for evidence of permanent deformation. The sedimentary deposits south of Grays Harbor and east of Willapa Bay (Fig. 2-1b) were previously mapped as a single unit (Quaternary terrace deposits, Qt) and were inferred to be Pleistocene estuarine sediments resting on marine terraces, in some locations over 160 m above sea level (a.s.l.) (Wagner, 1967a, b; Kvenvolden et al., 1979; Wells, 1981; Clifton, 1983). This elevation for Pleistocene coastal deposits implies potentially rapid uplift rates, possibly related to regional faults (McCrory, 1997; McCrory et al, 2002; McCrory and Wilson, 2019; Steely et al., 2021). The terraces offer a record of sedimentation and possible deformation that extends into the Pleistocene, but dense vegetation and limited access prevented previous workers from documenting uplift magnitude and rates.

Here, we present detailed mapping and luminescence ages to evaluate the extent and rate of Pleistocene uplift of estuarine deposits south of Grays Harbor and along Willapa Bay (Fig. 2-1b). Our analysis incorporates other recent luminescence dating (Steely et al., 2021) and previous fossil shell dating (Kennedy, 1978; Kvenvolden et al., 1979; Kennedy et al., 1982). The resulting uplift rate is consistent with long-term uplift rates from other studies along Cascadia. In contrast to the elastic model of earthquake cycles, we find that a small fraction of permanent uplift is permitted in the total budget for vertical land-level change, given published estimates of interseismic uplift and coseismic subsidence during subduction zone earthquakes, and this is sufficient to resolve the apparent discrepancy in short- and long-term records.

## Regional Geology and Tectonics

Washington State is situated above the Cascadia subduction zone, with the subducting margin ~100km west of the coast (Fig. 2-1a; Atwater, 1970; Clague, 1997). Northern Washington coastal topography is dominated by the Olympic Mountain range, an accretionary complex comprised of Eocene–Pliocene rocks that began exhumation around 16 Ma with continued active deformation to the present, shown by long-term exhumation rates for the Olympic Peninsula of ~0.3 mm/yr (Brandon and Vance, 1992; Brandon et al., 1998; Pazzaglia and Brandon, 2001). Along the Olympic coastline in northwestern Washington, Miocene–Pliocene near-shore and shallow marine sedimentary units are overlain by late Pleistocene alpine glacial till and outwash. The Miocene-Pliocene near-shore and shallow marine sedimentary units are several hundred meters above sea level (Campbell and Nesbitt, 2000), implying uplift rates since the late Neogene of ~0.1 mm/yr or less (Pazzaglia and Brandon, 2001). The Quaternary sediments are broadly folded and uplifted, with uplift rates between -0.03 and 0.5 mm/yr (Thackray, 1998).

Southwestern Washington and the Willapa Hills were not glaciated in the Pleistocene although the Olympic Mountains, north of the field area, hosted alpine glaciations throughout the Pleistocene and were a topographic high confining multiple advances of the Puget Lobe of the Cordilleran Ice Sheet to the Puget Lowlands (Booth, 1987). During the last glacial maximum, the Vashon advance, and likely during the Double Bluff advance of marine isotope stage (MIS) 6, the Puget Lobe terminated south of Olympia, Washington, but did not extend west around the southern side of the Olympic Mountains (Fig. 2-1a; Booth, 1987; Booth et al., 2003). Coastal southwestern Washington remained free of both continental and alpine ice throughout the Pleistocene.

Coastal topography south of the Quinault River is less pronounced than in the Olympic Mountains. Modern estuarine systems are found in Grays Harbor and Willapa Bay (Fig. 2-1), with highlands south of Grays Harbor and east of Willapa Bay. Regional bedrock includes basalts of the Eocene Crescent Formation (Armentrout, 1987), part of the Siletzia igneous province and associated sedimentary units that accreted to North America approximately 51 Ma (Snavely and MacLeod, 1974; Wells et al., 2014). The Crescent Formation has been folded and faulted, with folded and faulted Oligocene–Miocene sedimentary rocks in both conformable and unconformable contact with the basalts (Snavely and Wagner, 1982; Armentrout, 1987). Miocene basalts of the Columbia River Basalt Group are also found regionally (Armentrout, 1987).

Quaternary sediment deposits at elevations up to 160 m a.s.l. are mapped onshore, proximal to the Grays Harbor and Willapa Bay estuaries. As early as 1854, Gibbs described the near-shore sediments as recording "recent" elevation change due to the presence of shell layers within the sea-cliffs (Gibbs, 1854). Wagner (1967a, b) identified the sediments as undifferentiated terrace deposits (Qt) consisting of "relatively unconsolidated" clay to gravel, and with "ancient bay-fill deposits" at elevations over 100 m. Although later mapping differentiated some deposits in the southern part of Willapa Bay (Wells, 1979; Wells, 1981), maps continued to show the region directly south of Grays Harbor and around Willapa Bay as a single unit (Walsh et al., 1987). The 1:250,000 scale map describes the unit as "silt, sand, and gravel of diverse composition and origins, such as … uplifted marine and estuarine deposits" (Walsh et al., 1987).

Clifton (1983) identified and described subtidal and intertidal sediment at Willapa Bay and documented that the late Pleistocene sediment exposed in sea cliffs consists of subtidal and

intertidal sediment similar to what is being deposited in Willapa Bay today. These deposits were dated to the late Pleistocene based on amino acid racemization ages from bivalve shells (Kvenvolden et al.,1979). Clifton (1983) describes the exposed sediments as estuarine deposits of past sea-level high stands that have been uplifted since deposition. He notes that higher-elevation deposits are likely older terraces. Due to poor access, Clifton did not describe these deposits.

As part of a geotechnical study to address erosion of State Route 105, the Washington State Department of Transportation (WSDOT) used drilling and geophysical surveys to characterize shallow subsurface geology at the northwestern part of Willapa Bay, near the main tidal channel. Their work indicates dense to very dense silts and sands at depths around 20 m below sea level, underlying looser sand and Holocene sediments near sea level. WSDOT (1997) also describes a laterally extensive offshore bench (terrace) of dense sands and silts at around 9 m below sea level. They interpret these dense sediments to be the same Pleistocene terrace deposits that form cliffs along northern Willapa Bay (WSDOT, 1997), what Clifton (1983) called “older terraces”.

Although regional bedrock is folded and faulted (Pease and Hoover, 1957; Wagner 1967a.b; Wells, 1979, 1981; Walsh et al., 1987; Moothart, 1992), previous mapping did not indicate deformation of Quaternary deposits near Willapa Bay. Offshore studies by McCrory et al. (2002) show faults in Willapa Bay offsetting late Pleistocene sediments, while recent mapping east of Willapa Bay shows faults that may project into the coastal Quaternary deposits (Steely et al., 2021).

## Methodology

### Geologic mapping

We revisited regions previously mapped at 1:62,000 scale as a single Quaternary terrace unit (Qt), with our mapping at approximately 1:24,000 scale (Fig. 2-2). Our complete geologic map, geomorphic maps, topographic profiles, stratigraphic sections, and accompanying pamphlet can be found at the University of Washington ResearchWorks archive (Stanton, 2021). Geomorphic analyses of slope angle and topographic smoothness on 1 m and 10 m resolution digital elevation models (DEM) aided field identification of terraces (Washington Department of Natural Resources Lidar Portal, 2019; U.S. Geological Survey National Map Viewer, 2019). We also used DEMs to identify terrace back edge traces. Terrace mapping was supported by observations at outcrops and hand-dug pits (Fig. 2-3). These included hand sample and stratigraphic descriptions, gravel point counts, and where possible, depth measurements to the oxidated C-horizon (Cox horizon) in soil profiles. The Cox horizon is the location in a soil column where oxidized parent materials are encountered and represents the depth where soil forming processes are minimal (Birkeland, 1984). In the case where other soil forming factors (relief, climate, vegetation and parent material) are constant, time for soil development is a useful variable to discern the relative age of soils. Specifically, in the case of marine terraces on the Pacific coast, Bockheim et al. (1992; 1996) show that depth to the Cox horizon is a useful criterion to distinguish soils of different ages. We use depth to the Cox horizon as a proxy for soil maturity and thus, for relative age between units with similar lithologies. Twenty-three (23) field locations provided suitable outcrop to measure the depth to the Cox horizon, with fourteen (14) of those sites within estuarine units (Qt1, Qt2, Qss in Appendix 2 Table S1).

**Luminescence dating**

Luminescence dating using feldspar grains is commonly used for deposits up-to-and-older-than 200 ka because feldspars do not become saturated with absorbed energy at low doses, unlike quartz (Preusser et al., 2008). Kvenvolden et al. (1979) suggest the sediments near Willapa Bay could be 120 ka or older, so we use feldspars for our luminescence dating. In our experience, quartz also tends to have low luminescence sensitivity in western Washington.

Feldspars are dated using infrared stimulated luminescence (IRSL). Although feldspar grains become saturated at much higher radioactive energy doses than quartz grains, feldspars are subject to athermal loss of the accumulated energy. This is called anomalous fading and has been explained as the leak of electrons from the traps through quantum tunneling, even when the grain has not been exposed to light. Some traps are more likely to fade than others and the fading results in an underestimation of age. Measuring fading from laboratory-induced irradiation and extrapolating to long time periods can be used to correct for natural fading, but this works best for samples younger than 50 ka (Huntley and Lamothe, 2001).

A technique called post-infrared infrared stimulated luminescence (pIRIR; e.g. Buylaert et al., 2012; Li et al., 2014) attempts to reduce the effect of fading by first applying a high preheat and a low-temperature IR stimulation to empty the traps more prone to fading, followed by a higher-temperature IR stimulation to tap the traps with lower fading rates (Thomsen et al., 2008; Jain and Ankaergaard, 2011). However, these traps are also less likely to be bleached (zeroed) in nature so pIRIR measurements can overestimate the age due to pre-burial partial bleaching. A new method, called post-isothermal infrared luminescence (pIt-IR; Lamothe et al., 2020) seeks to circumvent anomalous fading without depending on hard-to-bleach traps. The technique

measures low- and high-temperature IRSL after isothermal treatments that mimic natural fading until an isothermal treatment is found where the low- and high-temperature IRSL produce the same amount of absorbed radiation, called the equivalent dose. The procedure does not eliminate fading, but rather, ensures that the density of electrons in traps is the same for both naturally irradiated and artificially irradiated feldspars, so that the true equivalent dose can be obtained (Lamothe et al., 2020). Since the pIt-IR method avoids relying on hard-to-bleach traps, it provides a test of overestimation of age by pIRIR. If the sample is not partially bleached or contains grains of mixed ages, then the pIt-IR age should be the same as the pIRIR age. We compare dates from low temperature IRSL with fading correction, pIRIR, and pIt-IR to see if fading can be circumvented, as well as to detect any overestimation of age due to an unbleached residual signal from partial bleaching.

We dated eight samples to obtain sediment ages at deposits well representative of Quaternary geologic units determined from mapping (Fig. 2-4). Samples were collected by driving light-tight cylinders into exposed profiles. Samples collected at the mouth of the Johns River (21GW0819.5 and 20GW0713.5) were from sands within units Qt1 and Qt2, respectively (Stanton, 2021). Although representative of these units at these locations, their proximity to the river means these sediments may have been reworked since deposition. Samples collected near Bay Center (19GW826.1, 21GW0819.9, and 21GW0819.10) were from very fine sands within unit Qt1 (Stanton, 2021). In addition to dates on estuarine sediments, we also report feldspar luminescence ages from sediments collected in fluvial sands and gravels (sample 19GW827.1 in unit Qgs; Stanton, 2021), for sands related to the Nemah River (sample 19GW826.2 in unit Qrt; Stanton, 2021) and for sands and gravels near Elma, WA mapped as undifferentiated, pre-Fraser-

glaciation continental glacial drift (Qgp) from the 1:250,000 regional geologic map (sample 21GW0819.4; Walsh et al., 1987).

To determine the natural radiation dose rate, sample radioactivity was measured on bulk samples by alpha counting and flame photometry, as well as by beta counting. Radioactivity concentrations were translated into dose rates following Guérin et al. (2011). Cosmic radiation was determined after Prescott and Hutton (1988). Measured moisture contents ranged from 8 to 27 %, but samples were collected in the summer (dry season), so the smaller values may underestimate typical moisture content. We used 20 ± 5 % moisture content for all samples in the age calculation. Luminescence was measured on potassium feldspars so some of the natural dose rate will arise from $^{40}K$ internal to the grains. This was not measured but was estimated to be 10 ± 3%, which was recommended by Smedley et al. (2012), although we used a slightly larger error term.

The target particles for dating were fine sand-sized single-grain (180-212 μm) potassium feldspars because this grain size best fits the single-grain disks used for measurement. pIT-IR requires lengthy machine time so most of those measurements were made on multi-grain aliquots, although a limited number of single-grain measurements were also made. Single-grain analysis allows an age to be computed for each grain to produce a distribution of ages for a sediment sample. An over-dispersion value, a measure of spread beyond what can be accounted for by differences in precision, can be determined from this distribution of ages. The over-dispersion can be accounted for by many things, such as intrinsic differences in luminescence properties among grains, differences in dose rates to individual grains, or differential fading in grains. Once these differences are accounted for, a significant spread in ages indicates mixture of

ages, either because of partial bleaching of grains or post-depositional movement of grains, such as by sediment reworking by streams or tides.

We made initial low temperature IRSL measurements at 50°C following a preheat of 250°C for 60s. For pIRIR, we set the low temperature stimulation at 50°C and the high temperature stimulation at 290°C with a preheat of 320°C for 60s. This combination has been shown to reduce fading considerably (Buylaert et al., 2012). For pIT-IR measurements we used 50°C and 225°C stimulations, a 250°C 60s preheat, and isothermal measurements at 270°C. Single-grain measurements were made using a Risø TL/OSL DA-20 reader, with an IR single-grain attachment. Stimulation used a 150 mW 830 nm IR laser, set at 30% power and passed through an RG 780 filter. Emission was collected by the photomultiplier through a blue-filter pack, allowing transmission in the 350-450nm range. Multi-grain single aliquots were measured on a TL.OSL DA-15 reader, using 830nm IR diodes for stimulation. For single grains, equivalent dose (De) was determined using the single-aliquot regenerative dose (SAR) protocol (Murray and Wintle, 2000), as applied to feldspars by Auclair et al. (2003). The SAR method measures the natural signal and the signal from a series of regeneration doses on a single aliquot, and uses a test dose to correct for sensitivity changes that occur during this procedure.

An advantage of single-grain dating is the opportunity to remove from analysis grains with unsuitable characteristics by establishing a set of criteria grains must meet. Grains are eliminated from analysis if they (1) had poor signals (as judged from errors on the test dose greater than 30 percent or from net natural signals not at least three times above the background standard deviation), (2) did not produce, within 20 percent, the same signal ratio (often called recycle ratio) from identical regeneration doses given at the beginning and end of the SAR sequence,

suggesting inaccurate sensitivity correction, (3) yielded natural signals that did not intersect saturating growth curves, or (4) had a signal larger than 10 percent of the natural signal after a zero dose and showed a visible decay.

A dose recovery test was performed on some single grains. The luminescence was first removed by exposure to 100 s of 875nm diodes (122 mW/cm2) and to 1 s of the laser, both at 50°C. A dose of known magnitude was then administered. The SAR procedure was then applied to see if the known dose could be obtained. Successful recovery, shown by ratios near 1 of average derived dose to given dose, is an indication that the procedures are appropriate. The dose recovery test also provides an over-dispersion value that represents the expected over-dispersion from intrinsic differences of grains in a single-age sample.

Anomalous fading (g-value) was measured using the procedures of Auclair et al. (2003) on single grains. Ages were determined based on Aitken (1985) and were corrected following Huntley and Lamothe (2001). For pIRIR, both an uncorrected and a fading-corrected age was obtained for each suitable grain. Even if all grains are the same true age, an identical age value is not obtained for each grain because of varying precision and other factors, including fading. Instead, as noted, a distribution is produced. The central age model (CAM) of Galbraith (Galbraith and Roberts, 2012) is a statistical tool used to determine the central tendency from the single-grain dates assuming a natural distribution of estimated age values. It also computes an over-dispersion parameter which can be compared to the over-dispersion value of the dose recovery test. An over-dispersion value that is higher than the dose recovery test over-dispersion value may indicate partial bleaching or post-depositional mixing of grains. Similar over-

dispersion values from uncorrected and fading-corrected ages indicate differential fading is not causing high over-dispersion.

For single-grain distributions with high over-dispersion values, we employed a finite mixture model (FMM) to study the structure of the distribution. This model (Galbraith and Roberts, 2012) uses maximum likelihood to separate the grains into single-aged components based on the input of an over-dispersion value thought to be typical of a single-aged sample and the assumption of a log normal distribution for each component. We use the over-dispersion values from the dose-recovery tests, which by definition are single-aged samples, to guide the selection of an appropriate over-dispersion value for the FMM input. Differential within-grain K content can also increase over-dispersion, but we tried to take that into account by using a higher error term on internal K than what was recommended by Smedley et al. (2012). The FMM estimates the number of components, the weighted average of each component, and the proportion of grains assigned to each component. The FMM is most useful for samples that have discrete, rather than continuous, age populations due to mixing, although the most abundant component does not necessarily represent the most likely depositional age. Further, we assume that any mixing has occurred vertically within a stratigraphic column with similar radioactivity or between grains with a similar source. FMM can be misleading if grains from sources with a very different radioactivity are mixed. In any case, the FMM provides a structure to the age distribution, which is useful for evaluating the depositional age in a geologic context. The FMM is most usefully employed with radial graphs that visually graph the distribution of components, which we have included in the supplementary material (Appendix 2 Fig. S1).

## Results

### Geology of marine deposits

Our new mapping identifies nine units within what was previously mapped only as Qt (Fig. 2-2; Stanton, 2021). Units range from shallow marine or estuarine sands and silts, to tidal channel sands and gravels, to cross-bedded fluvial gravels and sands with occasional silt interbeds. The marine/estuarine units (units Qt1, Qt2, Qss and TQss; Fig. 2-2) are found along the southern margin of Grays Harbor and along Willapa Bay (Fig. 2-1).

Unit TQss (late Pliocene to mid-Pleistocene shallow marine to near-shore deposits) consists of laterally extensive, indurated, stiff, thinly bedded silts and fine sands (Fig. 2-3a), and massive-to-cross bedded, fine-to-medium sands cut by oxidized, cross-bedded medium-to-fine sand to cobbles with silt rip-up clasts (Stanton, 2021). This unit forms cliffs along northern Willapa Bay. Near Bruceport, where TQss forms the sea cliffs, less indurated marine terrace sediments of unit Qt2 sit stratigraphically on top of TQss and fill embayments and channels cut into TQss. Based on geotechnical borings and seismic surveys by WSDOT (1997), we infer that a bathymetric bench at approximately 9 m below sea level at northwestern Willapa Bay to be cut into unit TQss, which underlies the marine terrace deposits of unit Qt1. A wave/tide-cut bench cut into unit TQss is thus the eroded surface that younger estuarine sediments (units Qt2 and Qt1) were deposited atop.

Unit Qt2 (marine terrace deposits, MIS5c) consists of thinly bedded, blue-grey-to-brown silts and fine sands, and massive-to-cross bedded, fine-to-medium sands (Fig. 2-3b) that form a geomorphically smooth surface between 35 and 48 m a.s.l. at numerous locations around the

field area. Soils forming in unit Qt2 are orange-to-brown, with a depth to the Cox horizon between 1 and 2 m (Stanton, 2021).

We map sediments on a lower geomorphically smooth surface at between 13 and 22 m a.s.l. as unit Qt1 (marine terrace deposits, MIS5a). Unit Qt1 consists of thinly bedded silts and fine sands with minor clay, and massive-to-cross bedded, fine-to-medium sands with silt rip-up clasts. Channel deposits, several meters to tens of meters wide, cut the finer sediments and consist of cross-bedded, medium-to-coarse sand to cobbles with rip-up clasts of silt and clay. The depth to the Cox horizon in soils forming in unit Qt1 is between 0.5 and 0.75 m, shallower than in unit Qt2. Based on soil maturity and elevation, unit Qt1 is presumably younger than unit Qt2. Unit Qt1 is found throughout the field area and is fossil bearing, with shell layers visible along eastern Willapa Bay within the low sea cliff (Fig. 2-3c; Kennedy, 1978; Kvenvolden et al., 1979; Stanton, 2021). The basal contact is not exposed but exposures at Bay Center are up to 13 m high.

Unit Qss (silt and sand near South Bend, MIS5e) is found only in northeastern Willapa Bay (Fig. 2-2) at elevations approximately 35–140 m a.s.l.. Although its total thickness cannot be estimated because basal contacts are not exposed, it is found along roadcuts and within a small quarry at exposures between 6 and 8m high. It does not form a geomorphically smooth surface, and the relationship of unit Qss to units Qt1, Qt2 and TQss is not obvious in the field. Unit Qss consists of thinly bedded, blue-grey-to-tan silts and clays, to bedded-to-massive, slightly oxidized, fine sands with silt lag deposits (Fig. 2-3d). The silt lag deposits, or drapes, suggests a tidal environment, where tidal slack water deposits fine grain sediments between sand ripples (e.g., Dalrymple and Choi, 2007). Depth to the Cox horizon in soils on Qss is between 1 and

1.5m (Stanton, 2021). The soil maturity of Qss suggests it is older than unit Qt1, although its relative age compared to unit Qt2 cannot be determined based solely on soil maturity.

**Luminescence ages**

Table 2-1 shows concentrations of relevant radioactive elements used to calculate the total natural dose rate. Three methods for determining equivalent dose were used in this study: fading corrected IRSL, pIRIR, and pIt-IT.

*Fading corrected IRSL at 50°C*

This procedure was only done on 19GW826.1, 19GW826.2, 19GW827.1, and 20GW0713.5. Table 2-2 shows the number of grains measured, the number of accepted grains, the average equivalent dose and the average g-value (fading rate). Average fading rates range from 4 to 7 %/decade. Table 2-3 shows the age using the central age model (CAM) as well as the over-dispersion value. The ratio of average derived dose to given dose in the dose recovery test was 1.02 ± 0.3, indicating the procedure was appropriate. The over-dispersion of the dose recovery test was 13.2 ± 2.9 %. The over-dispersion of the samples is between 28 and 79%, much higher than the over-dispersion of the dose recovery, which by design is a single-aged sample. This suggests the samples could be of mixed age.

*Post-IRIR at 290°C*

Table 2-2 shows the grains measured and accepted, as well as the average equivalent dose and the average fading rate. Average fading rates range between 0.6 and 6%/decade. No fading test was conducted on 20GW0713.5. Only two samples, 19GW826.1 and 21GW0819.5, show fading

rates significantly above 1.5 %/decade, but weighted averages for those two samples are not significantly above that value. Buylaert et al. (2012) consider fading rates that low to be artifacts of measurement. Table 2-3 gives the age using the CAM as well as the over-dispersion value for the pIRIR at 290°C signal, using both fading corrected and uncorrected data. The over-dispersion values for corrected data and uncorrected data are similar, suggesting that the fading correction did not reduce the age scatter. Similarity in ages between corrected and uncorrected data also show that fading in the pIRIR signal is likely not significant, and only the uncorrected ages are considered further. Radial graphs (Appendix 2 Fig. S1), explained in the caption, show the distribution of single-age grains for the uncorrected ages from pIRIR at 290°C measurements. A dose recovery test was performed on 100 grains from 19GW826.1. The ratio of average derived dose to administered dose was 1.10 ± 0.05, which is satisfactory at 2-sigma, but not as good as the dose recovery in the IRSL dose recovery test. The over-estimation for the pIRIR at 290°C dose recovery test may reflect the greater difficulty in bleaching for that signal, which may not have been completely zeroed before the administered dose was given. Over-dispersion for the pIRIR at 290°C dose recovery test was 14.4 ± 4.3%, nearly the same as for the IRSL dose recovery test. As with the IRSL, the high over-dispersion values of the samples (Table 2-3) compared to the dose recovery test over-dispersion value suggests the samples could be of mixed ages, so, the age distributions for the pIRIR at 290°C were evaluated using a finite mixture model (FMM). The FMM divides the distribution into single-aged components assuming a normal distribution and inputting over-dispersion values thought to be typical of a single-aged sample. The over-dispersion used was 15%, just slightly higher than what was obtained from the dose recovery test. Table 2-4 shows the results from the FMM. Sample 19GW826.1 resolved in a single component for the corrected data and 76% of the grains were consistent with one

component in the uncorrected data. About 70-75% of the grains were consistent with one component for both corrected and uncorrected data for 19GW826.2. All other samples resolved into multiple component mixtures.

*pIt-IR*

The pIt-IR procedure was run on multi-grain aliquots for samples 19GW826.1, 20GW0713.5, 21GW0819.4, 21GW0819.5, and 21GW0819.9. The procedure was done on 2-3 aliquots for each sample. A limited amount of single-grain pIT-IR measurements were made on 19GW826.2 and 19GW827.1 but the analysis showed that only a handful of grains from each sample were acceptable. This was not enough to do a distributional analysis of their ages, so the single-grain pIT-IR analysis was abandoned. No pIT-IR measurements were done on 21GW0819.10 because of limited material.

The pIT-IR ages are given in Table 2-5 along with the uncorrected pIRIR at 225°C ages, which were done in conjunction with pIT-IR. In samples 21GW0819.4 and 21GW0819.9 the pIT-IR age is much older than the pIRIR at 225°C age. This may be an indication that the samples were not well-bleached prior to burial. It is believed that pIT-IR will badly overestimate the age if the sample is poorly bleached (Lamothe et al., 2020), although the exact effect of poor bleaching is still under study. For samples 19GW826.1, 20GW0713.5 and 21GW0819.5 there is agreement between the pIT-IR age and the pIRIR at 225°C age. This indicates that these samples are well-bleached.

# Discussion

## Age

In the Willapa Bay and Grays Harbor region, estuarine units (Qt1 and Qt2) are deposited on benches cut into the older unit TQss. Wave-cut or tide-cut benches, and the associated back edges are assumed to form during sea-level high stands (Bradley and Griggs, 1976; Lajoie, 1986), which during the Quaternary correlate to odd numbered marine isotope stages (MIS) determined from benthic $\delta^{18}O$ records (Lisiecki and Raymo, 2015). Even-numbered MIS are sea-level low stands associated with continental ice-sheet advances. We discuss relative soil maturity, luminescence ages, and previous dating based on fossil shells to determine the most likely MIS (and thus depositional age) for each estuarine unit (Qt1, Qt2, and Qss).

### *Soil development with elevation*

Silts and sands make up the estuarine units (Qt1, Qt2, and Qss). Numerous studies use the depth to the Cox horizon as proxy for soil maturity and thus, to assess the relative age between similar sediments experiencing the same climatic conditions (e.g., Birkeland, 1984; Kelsey, 1990; Padgett et al., 2019). For this study, the depth to the Cox horizon in unit Qt1 (n=3), the lowest elevation deposit, ranges between 0.5 and 0.75 m, with the depth to the Cox horizon in unit Qt2 (n=6), the next highest elevation deposit, ranging between 1 and 2 m, and in unit Qss, the highest elevation deposit, between 1 and 1.5m (n=5). The relative age of units Qt2 and Qss cannot be determined from soil development alone, but both are likely older than unit Qt1.

*Luminescence*

In our single-grain analyses for both fading corrected IRSL and for pIRIR, most of the samples show a large over-dispersion of ages when compared to a dose recovery test, suggesting that mixing may have occurred, either by partial bleaching of grains prior to deposition or by post-depositional movement of grains. We evaluate the ages of the samples using the results of the CAM and FMM for pIRIR and using the ages from the IRSL and pIT-IR techniques. The fading rates (g-values) are relatively small and we do not have fading corrected data for all samples. We use the ages from uncorrected data in our discussion. Table 2-6 presents the most likely ages for pIRIR at 290°C for all samples. We focus on the estuarine samples (19GW826.1, 20GW0713.5, 21GW0819.5, 21GW0819.9, 21GW0819.10) here. The non-estuarine samples are from fluvial and glacial units and not pertinent to the Pleistocene uplift in the field area, although dating the samples contributed to the new Quaternary map (Stanton, 2021). For a discussion of the ages of the non-estuarine samples (19GW827.1, 19GW826.2, 21GW0819.4) please see the Supplementary Text. In Table 2-6 we also include dates from OSL (using quartz) samples (CB-OSL-561, CB-OSL-101) collected by WGS and dated at Utah State University (Steely et al., 2021) from sites that we have correlated to our newly mapped estuarine units.

Samples 19GW826.1 and 21GW0819.10 are from the same stratigraphic section just above the beach at Bay Center in unit Qt1 marine terrace sediments. 19GW826.1 is above and 21GW0819.10 is below a layer of shells. The FMM (Table 2-4) suggests that 19GW826.1 conforms to a single-aged sample with no evidence of partial bleaching or post-depositional movement. The agreement in age between pIRIR and pIT-IR supports this. The CAM (Table 2-3) should therefore give a good estimate of the age. The uncorrected value is 74.8 ± 3.21 ka, in

good agreement with the pIT-IR age (Table 2-5). This agreement also suggests that the pIRIR signal is well bleached. The fading corrected age of the 50°C IRSL measurement is substantially lower than all other ages suggesting that the Huntley-Lamothe fading correction is not effective for this aged sample. We do not consider the fading corrected IRSL measurements for further samples. The CAM date for 19GW826.1 anchors our interpretation of FMM results for other samples.

Sample 21GW0819.10 suffers from small sample size because of limited material available. It also seemed to have been contaminated with younger grains. The FMM (Table 2-4) suggests a large portion of grains, about a third, is in the 14-18 ka range. This does not agree with the data from sample 19GW826.1 and could represent contamination, possibly during sampling. The 2nd FMM component in the uncorrected data suggests that the age could be 70.2 ± 7.35 ka if the sample was poorly bleached prior to burial so that the 2nd component represents the true youngest grains. This age is within error range of sample 19GW826.1 and would represent rapid deposition. Given the high over-dispersion values, partial bleaching is probably the best interpretation, making the ~70 ka age the best estimate and explaining the presence of older grains (3rd FMM component).

Sample 21GW0819.9 is from the east side of Willapa Bay, also from a section mapped as unit Qt1 marine terrace sediments. The pIT-IR analysis (Table 2-5) suggests partial bleaching, giving a likely over-estimated age of 188± 23 ka compared to the pIRIR analyses (at 225°C and 290°C). The youngest component of the FMM (Table 2-4) suggests a small portion of very young grains, probably contamination. The second component gives an age of 74.5 ± 7.61 ka. This is

consistent with the ages from samples 19GW826.1 and 21GW0819.10. There are older grains within the sample which supports the partial bleaching interpretation.

We correlated our luminescence ages to marine isotope stages (MIS; Lisiecki and Raymo, 2015) for the mapped estuarine units near Willapa Bay (Table 2-7). Within error, each luminescence sample date could correspond to one of several different MIS. For example, samples 19GW826.1, 21GW0819.10, and 21GW0819.9 could have formed during MIS 4 or MIS 5a. MIS 4 was a sea-level low stand and estuarine sediments were unlikely to have been deposited in Willapa Bay at that time, leaving the MIS 5a age as the most likely.

The ages are not as straight forward for sample 20GW0713.5 in unit Qt2 and sample 21GW0819.5 in unit Qt1, both obtained from the mouth of the Johns River where it empties into Grays Harbor. The very large over-dispersion values suggest mixing. The youngest FMM component (Table 2-4) of sample 21GW0819.5 (component 1 of uncorrected data) represents a small percentage of grains at a very young age and likely represents contamination. Disregarding this contaminated age, the ages from the youngest FMM components in uncorrected data are 49.1 ± 10.8 ka for 20GW0713.5 and 20.8 ± 1.63 ka for 21GW0819.5. The oldest FMM components in uncorrected data give ages of 162.4 ± 13.4 ka for 20GW0713.5 and 129 ± 11.4 ka for 21GW0819.5. These mixtures could result from older sediments being partially reset sometime after deposition to give some younger aged grains. In this case, the deposit sampled would be the older age, with later, partial reworking or bleaching of sediments. Alternatively, the samples could be from sediment deposited more recently, but with most grains retaining a residual charge resulting from incomplete bleaching prior to burial. The pIT-IR age (Table 2-5) for 20GW0713.5 is 162 ± 13.4 ka and for sample 21GW0819.5 is 124± 15.6 ka, in agreement

with the oldest FMM components in the pIRIR uncorrected data. The agreement between pIT-IR and pIRIR ages might suggest the samples were not partially bleached at all, but if that is the case, then the origin of the younger component needs explaining. It is also possible that the river has continually reworked the sediments. In that case, perhaps none of the luminescence ages for these samples represents the depositional age of the sediments forming unit Qt2 and unit Qt1 at this location. Additional dating of the terraces at the Johns River would be required to say something more concrete about the depositional ages and processes at work.

We use the ages of the OSL samples collected by WGS (Steely et al., 2021) in our age interpretation of Quaternary units (Table 2-6). Based on the sample location, sample CB-OSL-561 (95.42 ± 15.02 ka) is from silts and fine sands within an embayment near Bruceport (Fig. 2-4). We interpret the sediments to be part of unit Qt2, deposited within a drainage or embayment cut into unit TQss. The WGS location for sample CB-OSL-101 (119.64 ± 23.91 ka) places it within sands in a small sand quarry near South Bend (Fig. 2-4) that we correlate to unit Qss. The OSL dates provide a depositional age of MIS 5a, 5c or 5d for unit Qt2 and a depositional age of MIS 5c, 5e or MIS 6 for unit Qss (Table 2-7). Despite the larger error compared to our IRSL dates, the OSL dates suggest that units Qt2 and Qss at eastern Willapa Bay are likely older than the MIS 5a unit Qt1.

Taken together, luminescence ages from all samples suggest an increasing age for sediments found at increasing elevations. With the exception of dates for the samples near the Johns River that may indicate reworking, the ages of progressively higher estuarine deposits are also sequential, as would be expected from estuarine sediments deposited during different sea-level high stands that have been uplifted through time.

*Fossil shells*

Kvenvolden et al. (1979) used amino acid racemization to date fossil shell fragments from low cliffs near Bay Center in eastern Willapa Bay (unit Qt1). They obtained a mean D/L leucine ratio of 0.31 (n=48) and a calculated date of 120 ka ±40 ka. They admit that their date is highly dependent both on the actual temperature of Willapa Bay through time, and the actual age of the calibration location in California.

Kennedy (1978) and Kennedy et al. (1982), using a combination of dating methods, provided probable ages for Pleistocene fauna along the west coast from Washington to central California. They note that southern extralimital species (i.e., warm water) are found on independently dated MIS5e terraces while northern extralimital species (i.e., cool water) are found on independently dated MIS5c and 5a terraces. They then correlate species type and amino acid racemization D/L leucine ratios from poorly dated locations to those from independently dated terraces. Amino acid racemization D/L leucine ratios on two whole bivalve shells from the low cliffs at Bay Center (unit Qt1) are 0.29 and 0.317, which they correlated to MIS5a (or about 84 ka).

The age obtained by Kvenvolden et al. (1979) corresponds to MIS5e but overlaps within error to a MIS5a age. Kennedy (1978) and Kennedy et al. (1982) reject a MIS5e age for these shells because the D/L leucine ratios from both their study as well as from Kvenvolden et al. (1979) are much lower than at other coastal locations that are independently dated to MIS 5e. The presence of a supposed cool-water species in the lower terrace deposits at Willapa Bay supports assignment of this deposit to MIS5a (Kennedy et al., 1982), although Kennedy (1978) admits that more southerly conditions (i.e., warm-water) is a possibility.

In addition to dating shells in the low cliffs near Bay Center, Kennedy (1978) also used amino acid racemization dating on shells collected at cliff exposures along northern Willapa Bay (our unit TQss). Addicott (1974) provides a late Pliocene to early Pleistocene age for these deposits based on the correlation of a fossil shallow marine or estuarine mollusk (*Mytilus condoni* Dall) to dated deposits in northern California. More recent work on the northern California deposits suggests they may be as young as mid-Pleistocene (Meyer et al., 1991). Kennedy (1978) obtains D/L leucine ratios of 0.81, corresponding to an age of around 1.3–1.5 Ma based on age correlations elsewhere along the coast. Kennedy (1978) does note that this age is far from exact, but it supports an early Pleistocene age for unit TQss.

*Age summary*

Based on soil maturity, units Qt2 and Qss are both older than unit Qt1. Based solely on elevation, Qss is likely also older than unit Qt2 because it is found at a consistently higher elevation than Qt2, thus implying that the sediments have been uplifted for a longer period of time. Fossil shells found in unit Qt1 provide an age either of MIS 5a (Kennedy, 1978) or MIS 5e (Kvenvolden et al., 1979). Assuming these preserved marine terrace sediments were deposited during sea-level high stands only, IRSL dating provides an age of 5a for Qt1. OSL dating provides an age of either MIS 5a or 5c for Qt2, and of either MIS 5c or 5e for Qss. Both the luminescence ages and the soil maturity suggest an age progression of youngest sediments at low elevation to oldest sediments at high elevation.

The date for fossil shells in unit Qt1 provided by Kvenvolden et al. (1979) has a large error of 40 ka. Within error, their date could be as old as 160 ka (MIS 6) or as young as 80 ka (MIS 5a). If their date of 120 ka (MIS 5e) is correct, then all luminescence ages for all samples are incorrect

because all sediments at higher elevations, with increased soil maturity, must be older than MIS 5e. If, however, their younger date within error is correct (MIS 5a), it correlates to the age determined for unit Qt1 from fossil shells by Kennedy (1978) as well with our IRSL dates.

In summary, our age assignments for the late Pleistocene estuarine units are MIS 5a for unit Qt1, MIS 5c for unit Qt2, and MIS5e for unit Qss. Based on cross cutting relationships and superposition, unit TQss is older, and thus likely Pliocene to mid-Pleistocene, as suggested by fossil shells.

**Uplift and uplift rates**

The sediments (units Qt1 and Qt2) underlying the geomorphically smooth surfaces we have called terraces are estuarine in nature and are therefore deposited in proximity to sea level. Uplift of estuarine or marine deposits is the difference between the modern elevation and the sea-level elevation (compared to modern) at the time of sediment deposition. Uplift calculations for marine terraces typically use the elevation of the inner edge of the terrace because a terrace inner edge represents the location of the former sea cliff and therefore can be used as a datum approximating mean high water (Fig. 2-5; Bradley and Griggs, 1976; Lajoie, 1986; Keller and Pinter, 2002). We estimate the inner edge elevation by subtracting the range of minimum cover-sediment thickness from the terrace back edge elevation.

We identify the back edge as the position of greatest change in surface slope in the region between two terraces (Fig. 2-5). In the study area, the terraces have a range of elevations (13–22 m for the lower terrace and 35–48 m for the upper terrace) and are eroded and dissected by streams. Distinct back edges are generally obscured except as fragments, which we traced on

lidar and the 10 m DEM for both lower and upper terraces. We used standard GIS tools to determine the elevation and elevation standard deviation of these traces. This provides a mean back edge elevation for the lower terrace (overlain by unit Qt1) of 21 m ±3 m and of 42 m ±8 m for the back edge of the upper terrace (overlain by unit Qt2).

The estuarine sediment units Qt1 and Qt2 overlie wave-cut or tide-cut strath surfaces eroded into older sediments. Unit Qt2 (marine terrace deposits, MIS5c) consists of sediments that sit on top of the early Pleistocene TQss unit. Qt2 also fills embayments and drainages cut into TQss. This implies that the younger Qt2 was deposited on an eroded surface of TQss. Where visible in the modern sea-cliff, Qt2 is approximately 2–4 m thick above TQss, but exposures of this contact are limited to the northern part of Willapa Bay, and it is possible that these exposures of the contact between TQss and Qt2 are not representative of the region. For comparison, the exposures of unit Qt1 (marine terrace deposits, MIS5a) near Bay Center are 8–13 m thick, with no exposures of the wavecut TQss underlying Qt1. Work by WSDOT identifies the older terrace unit (TQss) as forming a bench at ~ 9 m below sea level at northwestern Willapa Bay with up to 9 m of dense sand and silt (perhaps Qt1) and several meters of Holocene beach sand above it (WSDOT, 1997). Additionally, exposures of Qt2 near the Johns River in southern Grays Harbor show 6–9 m of sands and silts without exposing a contact with TQss. These exposures may include material deposited from the Johns River, however. We estimate that eroded surfaces in TQss are 9 m ±5 m below the upper surfaces of the terraces, at a minimum. This thickness of sediments for units Qt1 and Qt2 is consistent with sediment thicknesses overlying marine terraces at other places in Cascadia (e.g., Kelsey, 1990; McInelly and Kelsey, 1990; Polenz and Kelsey, 1999; Kelsey and Bockheim, 1994; Padgett et al., 2019) although those locations are more exposed to wave processes than the estuarine environment of northern Willapa Bay.

The inner edge (also called the ‘shoreline angle’) represents sea level as eroded by breaking waves (Bradley and Griggs, 1976; Lajoie, 1986; Keller and Pinter, 2002). In an estuary, erosion may occur from both waves and tidal current. Willapa Bay, a macrotidal estuary, has a tidal range between 1.25 and 3m (Emmett et al., 2000; Banas and Hickey, 2005) and we use the modern mean tidal range for Willapa Bay of ±2 m (6.8 ft; Michalsen et al., 2010) as a minimum error for inner edge elevation based on tidal fluctuation. Therefore, the uncertainty in the assigned elevation of the inner edge (e. g., shoreline angle) is ±2 m.

Paleo-sea-level high stand elevations have typically been reported as global mean, or eustatic, sea levels estimated from dated sea-level markers in regions of limited tectonic activity. These can vary widely. For example, studies from Bermuda and the Bahamas estimate MIS 5a eustatic sea level at approximately the same as modern sea level (Vacher and Hearty, 1989; Hearty and Kindler, 1995), while other estimates place MIS 5a eustatic sea level at ~ -19 m ±5 m (Chappell and Shackleton, 1986). More recently, recognition of the importance of glacial isostatic adjustment (GIA) has led to the development of geodynamic models whereby relative sea level locally can vary from global mean sea level as a response to expansion and contraction of ice sheets (Simms et al., 2015; Creveling et al., 2015, 2017). Along the west coast of North America, relative sea level may have varied regionally up to 30 m during MIS 5c and up to 35 m during MIS 5a (Creveling et al., 2017). Additionally, relative sea level at a single site may vary over the interval of a particular MIS. Although estimates of a MIS sea level high stand based on site-specific GIA would provide the most accurate estimate of total uplift, detailed modeling for most of Cascadia is currently unavailable. Similar to other recent uplift studies in Cascadia (e.g., Padgett et al., 2019) we use the range of mean sea level for MIS 5a and 5c based on geodynamic

modeling at a location close to the field area, in this case, from Coquille, OR (Creveling et al., 2017); thus, mean paleo-sea level is -19 m ±7 m for MIS 5a and -10 m ±7 m for MIS 5c.

Given these inputs, we estimate the total uplift for the inner edge of the terraces as:

$$uplift = (back\ edge\ elevation - cover\ sediment\ thickness) + MSL - PSL$$

where *PSL* is the paleo-sea level and *MSL* is mean sea level, taken here to be the mean tidal range. To obtain an uncertainty in uplift, we propagate the uncertainty for the variables using addition in quadrature (also called the square root of the sum of the squares; Taylor, 1997). Given these inputs and assigning MIS 5a age to Qt1, and MIS 5c age to Qt2, the total uplift for the Qt1 terrace is 31 m ±9 m and the total uplift for the Qt2 terrace is 43 m ±12 m (Table 2-8).

Unit Qss consists of estuarine sands and silt but does not form a geomorphically smooth surface with a distinct back edge. We do not have evidence of a wave/tide-cut surface that Qss sediments sit on, nor do we have an estimate of the sediment thickness. We thus cannot assess the total uplift of unit Qss.

We calculate the late Pleistocene uplift rates for units Qt1 and Qt2 terraces as

$$uplift\ rate = uplift/age$$

where *age* is the time since deposition (Table 2-8). Again, we propagate the uncertainty of these values to obtain uncertainty to the uplift rate (see Appendix 2 Table S2 for ranges of uplift rates). We are using uplift of the inner edge of the terraces for units Qt1 and Qt2, which presumably formed during peak sea-level high stands, so we use the peak ages for the sea-level high stands based on recent studies of global benthic $\delta^{18}O$ records, which have an uncertainty of ±4 k.y.

(Lisiecki and Raymo, 2005). The preferred age for unit Qt1 terrace is 82 k.y. ±4 k.y. (MIS 5a) and is 96 k.y. ±4 k.y. for Qt2 terrace (MIS 5c). Given these ages, the maximum uplift rates are 0.4 ± 0.12 mm/yr for Qt1 and 0.4 ± 0.13 mm/yr for Qt2 (Table 2-8).

There is significant uncertainty in paleo-sea-level elevation, as noted previously, with eustatic estimates and geodynamic models providing different values. For terraces underlying units Qt1 and Qt2, uplift rates are calculated using GIA-adjusted paleo sea-level high stand elevations from Coquille, OR. For comparison, we calculate uplift rates for the terraces using estimates of global eustatic paleo-sea-level elevation (Appendix 2 Table S3) as well as estimates of GIA-adjusted paleo-sea-level elevation near to the field area from Simms et al. (2015; Appendix 2 Table S4). The uplift rates using global eustatic sea level are 0.1–0.5 mm/yr for unit Qt1 terrace and 0.3–0.5 mm/yr for unit Qt2 terrace, while the uplift rates using sea level from Simms et al. (2015) are 0.2–0.6 mm/yr for unit Qt1 terrace and 0.4–0.7 mm/yr for unit Qt2 terrace. The uplift rates using paleo-sea-level elevations for Coquille, OR (Creveling et al., 2017) are within the range of uplift rate estimates that do not employ GIA-adjusted, paleo-sea-level high-stand estimates.

**Comparison to other Cascadia Pleistocene uplift rates**

Pleistocene uplift rates in Cascadia based on uplifted marine terraces, as well as long-term stream incision rates averaged over >10k.y., range between -0.03 and 1.8 mm/yr, comparable to rates for coastal southwestern Washington from this study (Fig. 2-6). Deformation of a folded wave-cut surface and glacial outwash sediments at Kalaloch, WA, just north of Grays Harbor, includes uplift rates between -0.03 and 0.5 mm/yr, depending on the age of the wave-cut surface (site 1, Fig. 2-6; Thackray, 1998). If formed during MIS7, the vertical deformation consists of uplift only. If formed during MIS5e, vertical deformation may include minor subsidence

(Thackray, 1998). The Clearwater River in the western Olympic Mountains shows long-term incision rates between 0.1 and 0.9 mm/yr, although the uplift inferred from the incision rates is interpreted as related to growth of the Olympics only, with Pazzaglia and Brandon (2001) noting that Pliocene marine sediments on the coast have elevations near to their formation elevation based on foraminifera distribution (site 2, Fig. 2-6; Pazzaglia and Brandon, 2001; Pazzaglia et al., 2003). Stream incision on the Wynoochee River (north and east of our study area) shows incision rates as high as 1.8 mm/yr associated with a local fault (site 3, Fig. 2-6; Delano et al., 2017). Incision of coastal Oregon streams shows rates up to 1.3 mm/yr (sites 5-13, Fig. 2-6; Personius, 1995). Late Pleistocene marine terraces in Oregon show uplift rates between 0 and 1.4 mm/yr, with higher rates associated with folding or faulting (sites 14-20, Fig. 2-6; Kelsey, 1990; Muhs et al., 1990, 1992; McInelly and Kelsey, 1990; Ticknor, 1993; Kelsey et al., 1994; Kelsey and Bockheim, 1994; Kelsey et al., 1996). Marine terraces in northern California show uplift rates between 0 and 1.05 mm/yr, associated with regional folding (sites 21, 22, Fig. 2-6; Polenz and Kelsey, 1999; Padgett et al., 2019). In all studies, uplift rates of ~0.5 mm/yr and greater are associated with local folds or faults (see Appendix 2 Tables S5-S7 for additional details on rates and studies).

**Vertical uplift budget**

Interseismic uplift of the overriding plate at a subduction zone denotes strain accumulation, probably as the result of locking of the subduction interface (Hyndman and Wang, 1995). A subsequent earthquake releases the strain, causing co-seismic subsidence of the overriding plate, which is recorded by buried coastal wetland soils or tsunami deposits (e.g., Atwater and Hemphill-Haley, 1997; Kelsey et al., 2002; Witter et al., 2003). Although most interseismic

strain is thought to be released elastically as co-seismic subsidence (i.e., elastic rebound; Reid, 1910; Whipple, 1936), some strain may result in permanent deformation (Thatcher, 1984) manifest as long-term uplift (e.g., Saillard et al., 2011, 2017). Accumulation of long-term uplift (i.e., over the Pleistocene) results when not all interseismic uplift is released co-seismically. We use the subduction zone earthquake vertical deformation cycle as the premise for a vertical strain budget to assess if long-term uplift of the marine terrace deposits in SW Washington is allowable within the framework of an interseismic uplift estimated using modern geodetic measurements of uplift rate and the observed Holocene co-seismic subsidence associated with the 1700 CE Cascadia subduction zone earthquake.

Modern Cascadia uplift rates from geodetic measurements (GPS, continuous global navigation satellite systems, tide data, leveling) are typically assumed to represent interseismic strain related to plate locking on the subduction zone (e.g., Hyndman and Wang, 1993, 1995; Wang et al., 2003; Li et al., 2018). Southwestern Washington has up to ~2.5 ± 1.5 mm/yr modern uplift rate, with a north-south vertical velocity gradient ranging between 0.6 mm/yr at 49°N and -0.7 mm/yr at 45.5°N that likely represents glacial isostatic adjustment (GIA; Newton et al., 2021). Compared to the measured vertical velocity, the GIA signal is relatively small, less than the error range; therefore we do not consider GIA in this calculation.

The amount of co-seismic subsidence varies between earthquake cycles depending on the time between earthquakes. Recent quantitative estimates of co-seismic subsidence based on fossil foraminiferal and diatom assemblages use transfer functions to reduce uncertainty (Hawkes et al., 2011; Wang et al., 2013; Kemp et al, 2018; Hong et al., 2021). In southwestern Washington, deposits at both the Niawiakum River and the Willapa River record evidence of subsidence from

a series of great earthquakes (Atwater and Hemphill-Haley, 1997), with estimates of subsidence between 1.41±0.78 m and 2.12±0.83 m for six events over the past 3,500 yr (Hong et al., 2021).

A simple vertical strain budget sums the interseismic uplift and the coseismic subsidence. During an interseismic period of 400–680 yr (Nelson et al., 2021) leading up to the 1700 C.E. Cascadia earthquake, southwestern Washington may have experienced 1.4 m ±0.9 m uplift related to interseismic strain at the modern uplift rate of ~2.5 ± ~1.5 mm/yr (Newton et al., 2021), assuming interseismic uplift rates are constant over that interval. Hong et al. (2021) estimate 1.41 m ± 0.78 m of subsidence related to the 1700 C.E. earthquake at the Niawiakum River in the field area. Although these estimates permit the possibility that the interseismic uplift was fully recovered in that earthquake, uncertainties in these estimates also allow of up to 1.6 m of permanent vertical land motion. Assuming that permanent uplift accumulates at constate rate, our long-term uplift rates of 0.4 ± 0.1 mm/yr for southwestern Washington suggest 0.2 m ±0.1 m of permanent uplift over the interseismic interval prior to the 1700 C.E. earthquake, well within the permissible range of permanent uplift. Assuming the observed interseismic rate is representative of the past hundred-thousand years, and comparing our long-term uplift rate, we estimate that about one-tenth of the interseismic strain is preserved as permanent deformation.

Within error using the above rates, only a minor portion of the interseismic strain results in permanent uplift thatis not easily resolved in the Holocene geologic record. For southwestern Washington, we estimate that the permanent uplift component ranges between ~0.1 and 0.3 m per earthquake cycle depending on the cycle duration (200-800 yrs) and the consistency of the uplift rate (~0.4 mm/yr). Tidal or estuarine processes and active sedimentation may obscure much of the uplift, particularly if it is gradual. A global sea-level elevation fall, such as those

related to glacial cycles, is necessary to preserve not only the wave/tide-cut surface formed during sea-level high stands (Fig. 2-7a), but also to preserve the evidence of permanent uplift over thousands of years. The preserved terrace surface will still fluctuate in elevation according to the earthquake cycle (i.e., interseismic uplift/co-seismic subsidence) but, once the terrace is above sea level the depositional environment (marsh to subtidal) no longer changes with each earthquake cycle (Fig. 2-7b, c). The permanent component of interseismic uplift accumulates through thousands of years so that later sea-level rise does not erode the terrace, resulting in a series or flight of terraces associated with previous late-Pleistocene sea-level high stands (Fig. 2-7d, e). Gradual permanent uplift might be accommodated by one or a combination of several processes related to subduction such as sediment underplating of the overriding plate (Delph et al., 2021), subduction of bathymetric anomalies (e.g., Freisleben et al., 2021), mantle buoyancy (Bodmer et al., 2020), or post-seismic slip (e.g., Sawai et al., 2004, Kelsey et al., 2006).

Alternatively, permanent uplift could be punctuated, occurring only with certain earthquakes, or could be accommodated by folding or faulting in the upper plate. Based on long-term uplift rates elsewhere in Cascadia, the southwestern Washington uplift rates are high enough that they may include some contribution from local folding or faulting. Our Quaternary mapping did not identify faults or folds, although Pliocene–Eocene bedrock shows multiple stages of folding and faulting (e.g., Pease and Hoover, 1957; Wagner 1967a.b; Wells, 1981; Walsh et al., 1987; Moothart, 1992; Campbell and Nesbitt, 2000). Dense vegetation and limited access originally hindered detailed mapping in the region, and although access and recent lidar facilitated our new mapping, it is possible that deformation, particularly faulting, was missed even at the 1:24,000 scale. Additionally, faulting could be restricted to blind structures not observable at the surface.

Further work is necessary to identify regional faults or folds, especially in the subsurface, and to evaluate regional deformation indicative of uplift, such as knickpoints in stream channel profiles.

Our mapping does reveal a puzzling feature. Unit TQss is a late Pliocene-to-mid-Pleistocene, shallow marine-to-near-shore-fluvial deposit. Our work suggests modest late Pleistocene uplift rates (~0.4 mm/yr.), yet the older unit TQss remains at elevations relatively close to sea level, with maximum elevations of TQss exposures near 60 m. This elevation for unit TQss implies very low uplift rates (<0.1 mm/yr), regardless of the exact age of the unit (late Pliocene or mid-Pleistocene).

It is possible that the exposures of unit TQss in the field area do not represent the entire original sedimentary package. The Pliocene Quinault Formation on coastal Washington north of the study area is similar to unit TQss, although slightly older, and shows over 700 m of estuarine and near-shore fluvial sediment, thought to have been deposited over the course of 1.5–2 Ma (Campbell and Nesbitt, 2000). While we did not observe the upper or lower contacts of TQss, the current thickness of TQss is likely much less than the similar Quinault Formation. One possible explanation is that TQss was originally a thicker deposit. The upper, younger portions eroded, possibly by an ancient Willapa River graded to a lower sea level. Later sea-level rise drowned the terraces created by the river, allowing estuarine sediments such as units Qt2 and Qt1 to be deposited.

## Conclusions

Previous work in southwestern Washington has focused on the spectacular Late Holocene record of paleo-subduction zone earthquakes that occasioned abrupt subsidence events in Cascadia (e.g.,

Atwater, 1987, 1992; Atwater and Yamaguchi, 1991; Witter et al., 2003; Hong et al., 2021). From a perspective of the last 100,000 years, however, the landscape shows evidence of long-term permanent rock uplift. Our new mapping subdivides a previously mapped single unit, recognizing nine new units including estuarine and fluvial sediments. Luminescence dating, relative age based on soil maturity and unit elevation, and evaluation of ages from previous fossil shell dates constrain the probable ages of the late Pleistocene estuarine units to sea-level high stands during MIS 5a, 5c, and 5e, respectively. Given these ages and current elevations of the 5a and 5c marine terrace deposit units, we estimate an average uplift rate of 0.4 ± 0.1 mm/yr over the last ca. 100 ky. These rates are the first rates from southwestern Washington and are consistent with estimates from elsewhere in Cascadia. In southwestern Washington (and Cascadia regionally) the long-term uplift rates are small enough that net uplift over a single seismic cycle may be hidden in the measurement uncertainties of interseismic strain and coseismic subsidence. Therefore, both the observed Holocene coseismic subsidence and uplift over the late Pleistocene can be accommodated within the expected interseismic vertical strain budget.

## Acknowledgements

Thank you to Lydia Staisch, Ginevra Moore, and Ben Stanton for assistance in the field. We are grateful to Michel Lamothe for thoughtful comments on this work. Reviews by Rob Witter, Gino de Gelder, Barbara Mauz and Lewis Owen substantially improved the manuscript. This material is based upon work supported by the U.S. Geological Survey under Grant No. G20AP00065, by the Earth and Space Sciences Department at University of Washington, by the Geological Society of America, and by the Northwest Scientific Association. The views and conclusions

contained in this document are those of the authors and should not be interpreted as representing the opinions or policies of the U.S. Geological Survey. Mention of trade names or commercial products does not constitute their endorsement by the U.S. Geological Survey.

## Tables

**Table 2-1. Concentrations of elements in ppm or % used to calculate natural dose and dose rate (Gy/ka).**

| Sample | $^{238}$U (ppm) | $^{233}$Th (ppm) | K (%) | Dose rate (Gy/ka) | | | | |
|---|---|---|---|---|---|---|---|---|
| | | | | alpha | beta | gamma | cosmic | total |
| **19GW826.1** | 1.83±0.16 | 7.79±1.13 | 1.91±0.20 | 0.09±0.05 | 1.89±0.24 | 0.80±0.07 | 0.10±0.02 | 2.88±0.25 |
| **19GW826.2** | 1.35±0.11 | 3.97±0.73 | 1.86±0.08 | 0.06±0.04 | 1.49±0.19 | 0.54±0.04 | 0.17±0.03 | 2.25±0.20 |
| **19GW827.1** | 0.87±0.10 | 5.52±0.85 | 0.52±0.06 | 0.06±0.04 | 1.01±0.18 | 0.40±0.04 | 0.13±0.03 | 1.60±0.19 |
| **20GW0713.5** | 0.80±0.06 | 0.94±0.34 | 0.81±0.04 | 0.02±0.02 | 1.10±0.17 | 0.27±0.02 | 0.14±0.03 | 1.54±0.17 |
| **21GW0819.4** | 0.72±0.09 | 3.88±0.76 | 0.76±0.04 | 0.05±0.03 | 1.11±0.17 | 0.37±0.04 | 0.17±0.03 | 1.69±0.18 |
| **21GW0819.5** | 0.65±0.12 | 9.79±1.24 | 0.81±0.02 | 0.09±0.05 | 1.24±0.17 | 0.61±0.06 | 0.14±0.03 | 2.07±0.19 |
| **21GW0819.9** | 0.95±0.11 | 5.77±0.93 | 1.31±0.16 | 0.06±0.04 | 1.50±0.23 | 0.58±0.06 | 0.15±0.03 | 2.30±0.24 |
| **21GW0819.10** | 1.95±0.16 | 7.49±1.11 | 1.29±0.04 | 0.09±0.05 | 1.54±0.18 | 0.68±0.05 | 0.09±0.02 | 2.41±0.19 |

**Table 2-2. Grains measured, the number accepted for dating, the average equivalent dose (Gy) from the central age model (CAM) and the average g-value (fading rate).**

| Sample | IRSL at 50°C | | | | pIRIR at 290°C | | | |
|---|---|---|---|---|---|---|---|---|
| | Number of grains measured | Accepted | Equivalent dose (Gy) | Average g-value (%/decade)** | Number of grains measured | Accepted | Equivalent dose (Gy) | Average g-value (%/decade)** |
| **19GW826.1** | 393 | 103 | 103.7 ± 5.81 | 5.9 ± 1.2 | 593 | 97 | 215.5 ± 9.25 | 4.2 ± 1.1^ |
| **19GW826.2** | 197 | 34 | 141.9 ± 14.3 | 7.2 ± 5.0 | 1771 | 69 | 298.2 ± 21.9 | 1.7 ± 1.0 |
| **19GW827.1** | 393 | 29 | 200.6 ± 29.9 | 4.0 ± 2.9 | 589 | 44 | 171.9 ± 24.9 | 3.3 ± 2.4 |
| **20GW0713.5*** | 590 | 64 | 105.5 ± 10.2 | 4.4 ± 1.6 | 395 | 24 | 198.5 ± 25.1 | -- |
| **21GW0819.4*** | -- | -- | -- | -- | 1078 | 122 | 262.0 ± 20.9 | 3.4 ± 1.6 |
| **21GW0819.5*** | -- | -- | -- | -- | 2257 | 53 | 92.2 ± 12.5 | 5.9 ± 3.9^^ |
| **21GW0819.9*** | -- | -- | -- | -- | 787 | 150 | 256.6 ± 10.2 | 0.7 ± 0.6 |
| **21GW0819.10*** | -- | -- | -- | -- | 491 | 67 | 119.3 ± 16.4 | 0.6 ± 1.3 |

*** Symbol "- -" indicates no data was collected. **A decade is a power of 10. By convention, the g-value is standardized to a time constant of 2 days, so that successive decades are 2, 20, 200, 2000 days, etc. ^ A weighted average for this value is 2.3 ± 1.1 %. ^^ A weighted average for this value is 0.02±3.9%.**

**Table 2-3. Ages and over-dispersion values for IRSL at 50°C and for pIRIR at 290°C using the central age model (CAM). Ages are either corrected for anomalous faded or uncorrected, and are quoted with 1-sigma errors, using 2021 as the reference for before present designations.**

| Sample | IRSL at 50°C | | | pIRIR at 290°C | | | | | |
|---|---|---|---|---|---|---|---|---|---|
| | Number of grains | Corrected Age (ka) CAM | Over-dispersion (%) | Number of grains | Corrected Age (ka) CAM | Over-dispersion (%) | Number of grains | Uncorrected Age (ka) CAM | Over-dispersion (%) |
| **19GW826.1** | 82 | 48.7 ± 3.22 | 28.8 ± 6.6 | 83 | 91.6 ± 4.92 | 31.3 ± 5.0 | 97 | 74.8 ± 3.21 | 35.5 ± 3.5 |
| **19GW826.2** | 28 | 71.5 ± 10.0 | 44.9 ± 12.3 | 61 | 155.9 ± 16.5 | 53.3 ± 9.3 | 69 | 132.6 ± 9.74 | 51.9 ± 5.9 |
| **19GW827.1** | 19 | 186 ± 28.6 | 40.0 ± 13.7 | 45 | 101.2 ± 19.4 | 95.6 ± 15.6 | 54 | 107.0 ± 15.5 | 97.0 ± 11.1 |
| **20GW0713.5*** | 44 | 86.1 ± 14.5 | 79.7 ± 13.7 | -- | -- | -- | 24 | 124.6 ± 15.8 | 51.4 ± 10.3 |
| **21GW0819.4*** | -- | -- | -- | 61 | 161.1 ± 23.3 | 102.6 ± 11.3 | 122 | 154.6 ± 12.3 | 81.2 ± 6.0 |
| **21GW0819.5*** | -- | -- | -- | 31 | 42.7 ± 9.3 | 99.6 ± 16.9 | 53 | 44.6 ± 6.0 | 88.7 ± 10.4 |
| **21GW0819.9*** | -- | -- | -- | 120 | 128.5 ± 6.3 | 37.1 ± 4.2 | 150 | 111.7 ± 4.4 | 43.0 ± 3.1 |
| **21GW0819.10*** | -- | -- | -- | 47 | 50.8 ± 10.9 | 115.7 ± 16.8 | 67 | 49.4 ± 6.8 | 106 ± 10.2 |

*** Symbol "- -" indicates no data was collected.**

**Table 2-4. Finite mixture model ages for pIRIR at 290°C. Ages are either corrected or uncorrected for anomalous fading, and are quoted with 1-sigma errors, using 2021 as the reference for before present designations.**

| Sample | Corrected for fading | | | Uncorrected for fading | | |
|---|---|---|---|---|---|---|
| | Component | Age (ka) | Proportion of grains (%) | Component | Age (ka) | Proportion of grains (%) |
| **19GW826.1** | 1 | 91.6 ± 4.92 | 100 | 1 | 19.0 ± 3.17 | 5.3 |
| | | | | 2 | 54.1 ± 8.50 | 18.2 |
| | | | | 3 | 87.2 ± 3.93 | 76.5 |
| **19GW826.2** | 1 | 75.8 ± 10.9 | 24.6 | 1 | 24.1 ± 5.91 | 2.6 |
| | 2 | 201 ± 22.8 | 75.4 | 2 | 76.7 ± 6.11 | 29.4 |
| | | | | 3 | 180 ± 9.13 | 68.0 |
| **19GW827.1** | 1 | 42.4 ± 5.78 | 43.8 | 1 | 21.5 ± 3.07 | 17.8 |
| | 2 | 280 ± 33.1 | 56.2 | 2 | 46.1 ± 5.73 | 19.9 |
| | | | | 3 | 195 ± 17.5 | 49.5 |
| | | | | 4 | 396 ± 63.8 | 12.9 |
| **20GW0713.5** | 1 | 71.1 ± 13.5 | 23.1 | 1 | 49.1 ± 10.8 | 28.0 |
| | 2 | 157 ± 28.2 | 19.3 | 2 | 162.4 ± 13.4 | 72.0 |
| | 3 | 295 ± 25.0 | 57.6 | | | |
| **21GW0819.4** | 1 | 14.1 ± 2.04 | 8.5 | 1 | 14.1 ± 1.52 | 6.6 |
| | 2 | 106 ± 17.9 | 24.5 | 2 | 65.1 ± 10.1 | 7.1 |
| | 3 | 275 ± 23.0 | 66.9 | 3 | 161 ± 10.9 | 55.5 |
| | | | | 4 | 301 ± 29.6 | 30.8 |
| **21GW0819.5** | 1 | 21.9 ± 1.80 | 52.1 | 1 | 5.48 ± 1.04 | 4.7 |
| | 2 | 123 ± 18.8 | 47.9 | 2 | 20.8 ± 1.63 | 40.1 |
| | | | | 3 | 54.8 ± 8.13 | 22.7 |
| | | | | 4 | 129 ± 11.4 | 32.5 |
| **21GW0819.9** | 1 | 96.6 ± 6.98 | 49.2 | 1 | 24.4 ± 3.40 | 4.8 |
| | 2 | 172 ± 13.3 | 50.8 | 2 | 74.5 ± 7.61 | 22.8 |
| | | | | 3 | 127 ± 6.21 | 62.2 |
| | | | | 4 | 225 ± 24.9 | 10.2 |
| **21GW0819.10** | 1 | 18.2 ± 3.06 | 38.1 | 1 | 14.4 ± 1.09 | 35.4 |
| | 2 | 117 ± 9.86 | 61.9 | 2 | 70.2 ± 7.35 | 24.5 |
| | | | | 3 | 124 ± 8.65 | 40.1 |

**Table 2-5. Ages averaged from two or three multi-grain aliquots for pIt-IR and for pIRIR at 225°C collected in conjunction with pIT-IR. pIRIR at 225°C ages are not corrected for anomalous fading. Ages are quoted with 1-sigma errors, using 2021 as the reference for before present designations.**

| Sample | pIT-IR | pIRIR at 225°C * |
|---|---|---|
| **19GW826.1** | 68.8 ± 4.0 | 70.7 ± 7.4 |
| **20GW0713.5** | 162 ± 13.4 | 162 ± 26.1 |
| **21GW0819.4** | 329 ± 40.7 | 275.8 ± 46.0 |
| **21GW0819.5** | 124 ± 15.6 | 99.3 ± 10.1 |
| **21GW0819.9** | 188 ± 23 | 150.0 ± 18.6 |

**Table 2-6. Summary of luminescence ages. pIRIR ages quoted with 1-sigma errors, using 2021 as the reference for before present designations.**

| Sample | Latitude (°N) /Longitude (°W) | Elevation above sea-level (m) | Unit | OSL (ka) | Age pIRIR at 290°C (ka) |
|---|---|---|---|---|---|
| **19GW826.1*** | 46.62977, -123.9578 | 3 | Qt1 | -- | 74.8 ± 3.21 (CAM) |
| **19GW827.1*** | 46.81367, -123.8709 | 154 | Qgs | -- | 195 ± 17.5 (FMM 3rd) |
| **19GW826.2*** | 46.51767, -123.9037 | 9 | Qrt | -- | 76.7 ± 6.11 (FMM 2nd)<br>180 ± 9.13 (FMM 3rd) |
| **20GW0713.5*** | 46.89594, -123.9785 | 14 | Qt2 | -- | 49.1 ± 10.8 (FMM 1st)<br>162 ± 13.4 (FMM 2nd) |
| **21GW0819.4*** | 46.96388, -123.5002 | 75 | Qgp** | -- | 200 ± 9.19 (FMM 3rd/4th) |
| **21GW0819.5*** | 46.90696, -123.9949 | 5 | Qt1 | -- | 20.8 ± 1.63 (FMM 2nd)<br>129 ± 11.4 (FMM 4th) |
| **21GW0819.9*** | 46.57772, -123.9150 | 11 | Qt1 | -- | 74.5 ± 7.61 (FMM 2nd) |
| **21GW0819.10*** | 46.62977, -123.9578 | 2 | Qt1 | -- | 70.2 ± 7.35 (FMM 2nd) |
| **CB-OSL-561^** | 46.67848, -123.9032 | 9.5 | Qt2 | 95.42 ± 15.02 | -- |
| **CB-OSL-010^** | 46.66050, -123.8383 | 60 | Qss | 119.64 ± 23.91 | -- |

***All samples with labels starting with 19GW, 20GW and 21GW were dated using pIRIR at 290°. Single-grain ages evaluated using a finite mixture model (Galbraith and Roberts, 2012). Mixture model component ages (e.g., FMM 2nd) provide constraint on the most likely depositional ages as assessed by the likelihood of partial bleaching and sediment reworking, listing two where there were bimodal age distributions. Ages are uncorrected for fading. CAM, central age model. FFM, finite mixture model, symbol "- -" indicates no data was collected.**

****Sample collected outside field area from sand and gravels near Elma, WA, mapped as Qgp, undifferentiated pre-Fraser-glaciation continental glacial drift from 1:250,000 regional geological map (Walsh et al., 1987),**

**^ Washington Geological Surveys samples (samples CB-OSL-561 and CB-OSL-010) were dated using OSL at Utah State University. See Steely et al. (2021) for details.**

**Table 2-7. Age determinations for uplifted estuarine units correlated to marine isotope stages (MIS), with ages quoted with 1-sigma errors, using 2021 as the reference for before present designations.**

| Sample | Unit | OSL (ka) | pIRIR-290°C (ka) | MIS^ |
|---|---|---|---|---|
| **19GW826.1** | Qt1 | -- | 74.8 ± 3.21 (CAM) | 5a |
| **21GW0819.9** | Qt1 | -- | 74.5 ± 7.61 (FMM 2nd) | 4, 5a |
| **21GW0819.10** | Qt1 | -- | 70.2 ± 7.35 (FMM 2nd) | 4, 5a |
| **CB-OSL-561*** | Qt2 | 95.42 ± 15.02 | -- | 5a, 5c, 5d |
| **CB-OSL-010*** | Qss | 119.64 ± 23.91 | -- | 5c, 5e, 6 |

**^ Within error, some samples correlate to several MIS.**
*** See Reedy et al. (2019) and Van Dassow et al. (2019) for details.**

**Table 2-8. Uplift rates for terraced estuarine sediments near South Bend, WA.**

| Unit | Back edge elevation (m) [1] | Cover sediment thickness (m) [2] | Sea-level fluctuation (m) [3] | Paleo sea-level compared to modern (m) [4] | Uplift (m) [5] | Age (ka) [6] | Uplift rate (mm/y) [7] |
|---|---|---|---|---|---|---|---|
| **Qt1** | 21 ± 3 | 9 ± 5 | ± 2 | -19 ± 7 | 31 ± 9 | Peak MIS 5a: 82 ± 4 | 0.4 ± 0.12 |
| **Qt2** | 42 ± 8 | 9 ± 5 | ± 2 | -10 ± 7 | 43 ± 12 | Peak MIS 5c: 96 ± 4 | 0.4 ± 0.13 |

**[1] Terrace back edge elevation estimated from eroded traces on DEM.**
**[2] Minimum sediment thickness from Qt2 exposures at modern sea-cliffs near Bay Center. Qt1 sediment thickness is at least 14 m, greater than the lowest terrace surface elevation of ~13 m. Sediment thickness thus 9 ±5 m.**
**[3] Wave cut benches mark mean sea-level, which varies with tides and storms. We use the tidal fluctuation for Willapa Bay of ±2 m (Michalsen et al., 2010).**
**[4] Paleo-sea-level elevation has not been modeled for the field area so we used the range of elevations at Coquille, OR from geodynamic models (Creveling et al., 2017).**
**[5] Uplift is the difference between the paleo sea-level elevation and the current elevation of the inner edge (back edge minus sediment thickness) plus/minus the sea-level fluctuation.**
**[6] MIS peak age, with an uncertainty of ± 4 ka (Lisiecki and Raymo, 2005).**
**[7] Uplift rate is the total uplift divided by the age of the terrace surface. Uncertainty calculated using standard error propagation methods.**

## Figures

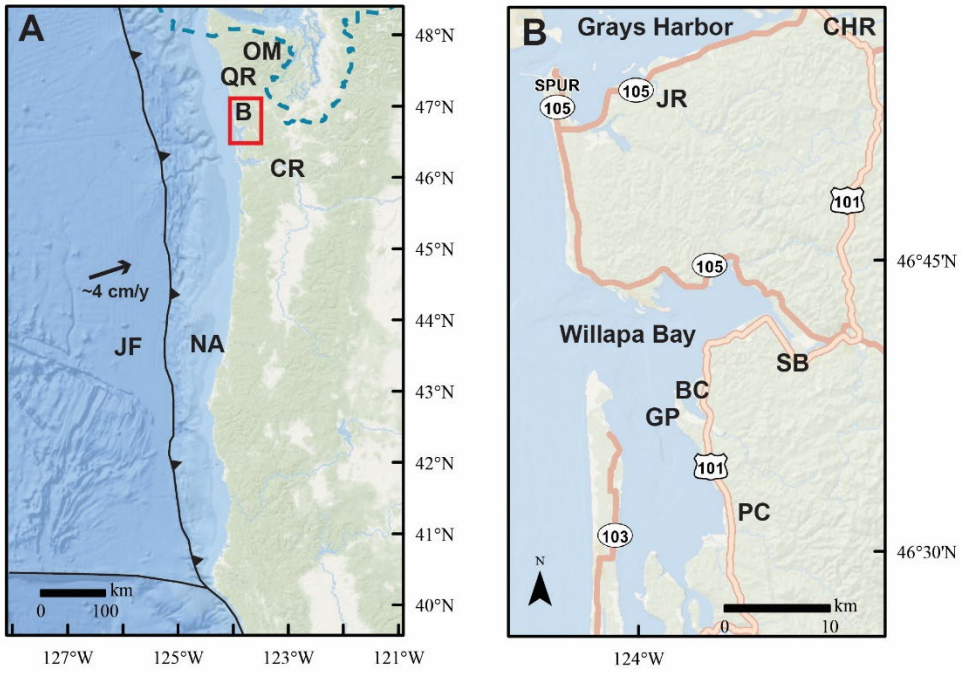


Figure 2-1. Location of field area with respect to the Cascadia subduction zone (CSZ) margin. A. The Juan de Fuca plate subducts beneath North America at about 4 cm/yr toward the northeast (Heaton and Hartzell, 1987). Blue dashed line shows extent of the Cordilleran ice sheet during the last glacial maximum. Red box indicates location of panel B. JF – Juan de Fuca plate, NA – North America plate, OM – Olympic Mountains, QR – Quinault River, CR – Columbia River. B. The field area is south of Grays Harbor and along Willapa Bay. Circled numbers are state highways. CHR – Chehalis River, JR – Johns River, SB – South Bend, BC – Bay Center, GP – Goose Point, PC – Pickernell Creek. Map base layer credits: Esri, Garmin, GEBCO, NOAA, NGDC and others.

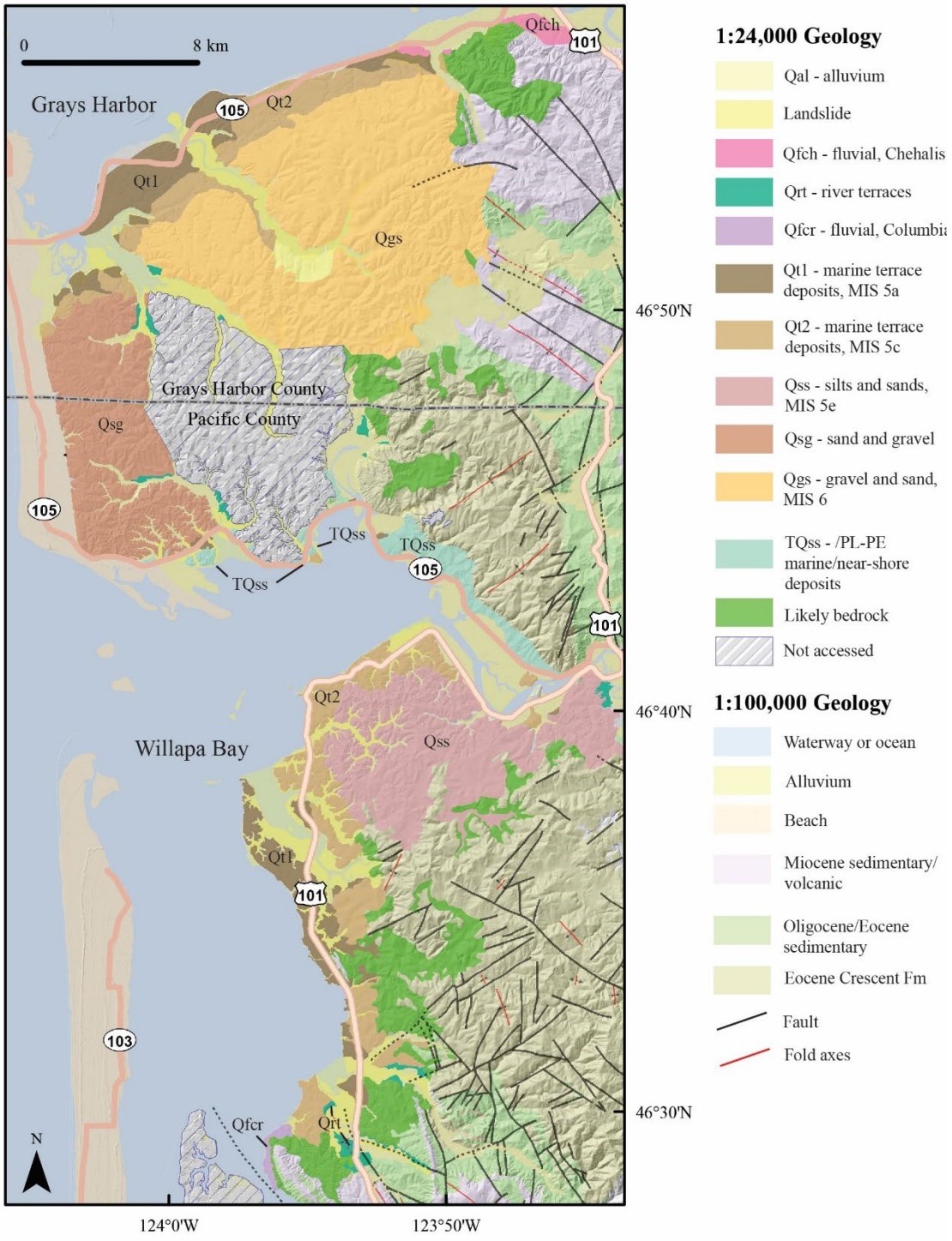


Figure 2-2. Geological map of region previously mapped as Quaternary terraces. The newest mapping, done at a 1:25,000 scale, overlies geologic mapping at 1:100,000 scale (Washington Division of Geology and Earth Resources, 2016), shown here in lighter colors. Base map is 10 m

DEM hillshade. See Stanton (2021) for additional maps and unit descriptions. “Likely bedrock” indicates locations previously mapped as Quaternary terrace deposits that are probably bedrock. “Not accessed” indicates locations not mapped because landowners did not grant permission or because of limited road access.

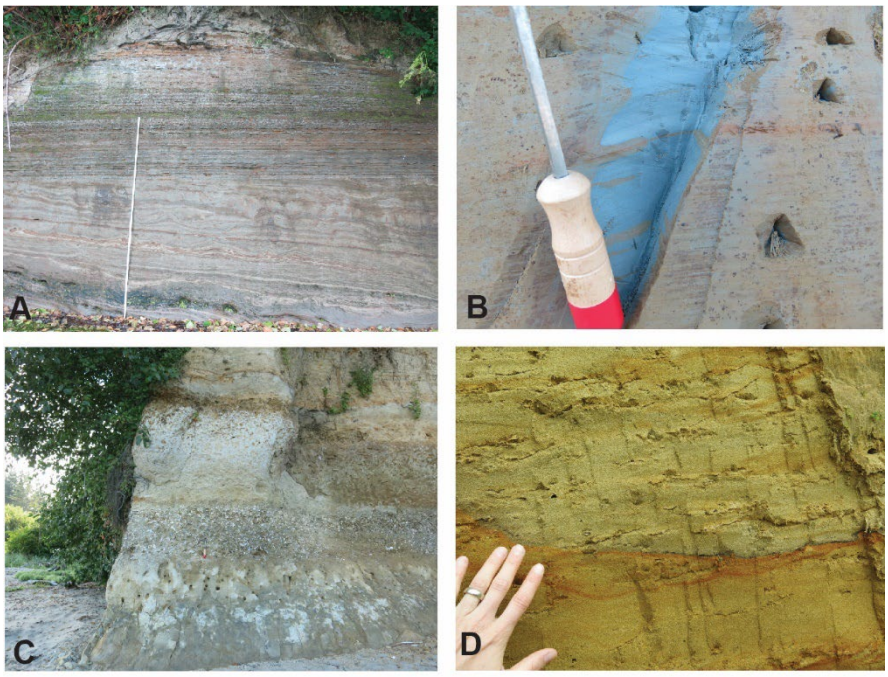


Figure 2-3. Quaternary sediments mapped near Willapa Bay and Grays Harbor. A. Dense, compacted silts, clays and fine sands in unit TQss near Bruceport County Park, meter stick for scale. B. Blue-grey silts within unit Qt2 near Bruceport County Park. Tool handle is approximately 12.5 cm long. C. Layer of broken shells within unit Qt1 near Bay Center. Silts and fine sand layers above and below the shells. Red-handled tool from B is visible at the base of the shell layer. D. Fine sands with silt lag deposits in unit Qss near South Bend. Secondary oxidation likely from groundwater or soil processes. All photos by Kelsay Stanton.

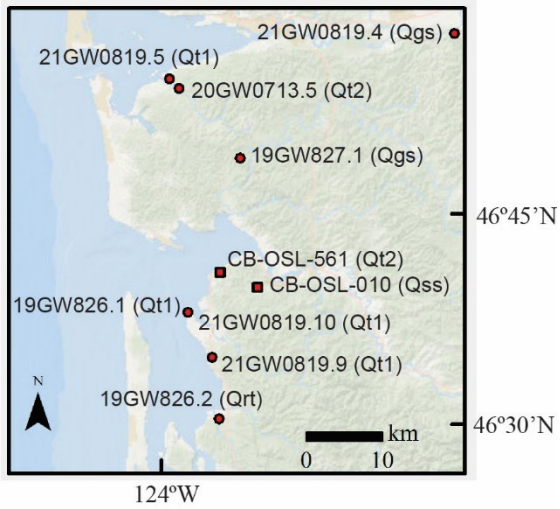


Figure 2-4. Map of luminescence sample location with lithologic unit code from Fig. 2-2 listed. Samples from this study have labels starting with 19GW, 20GW, and 21GW. Samples collected by Washington Geological Survey (Steely et al., 2021) are CB-OSL-561 and CB-OSL-010. Map base layer credits: Esri, Garmin, GEBCO, NOAA, NGDC and others.

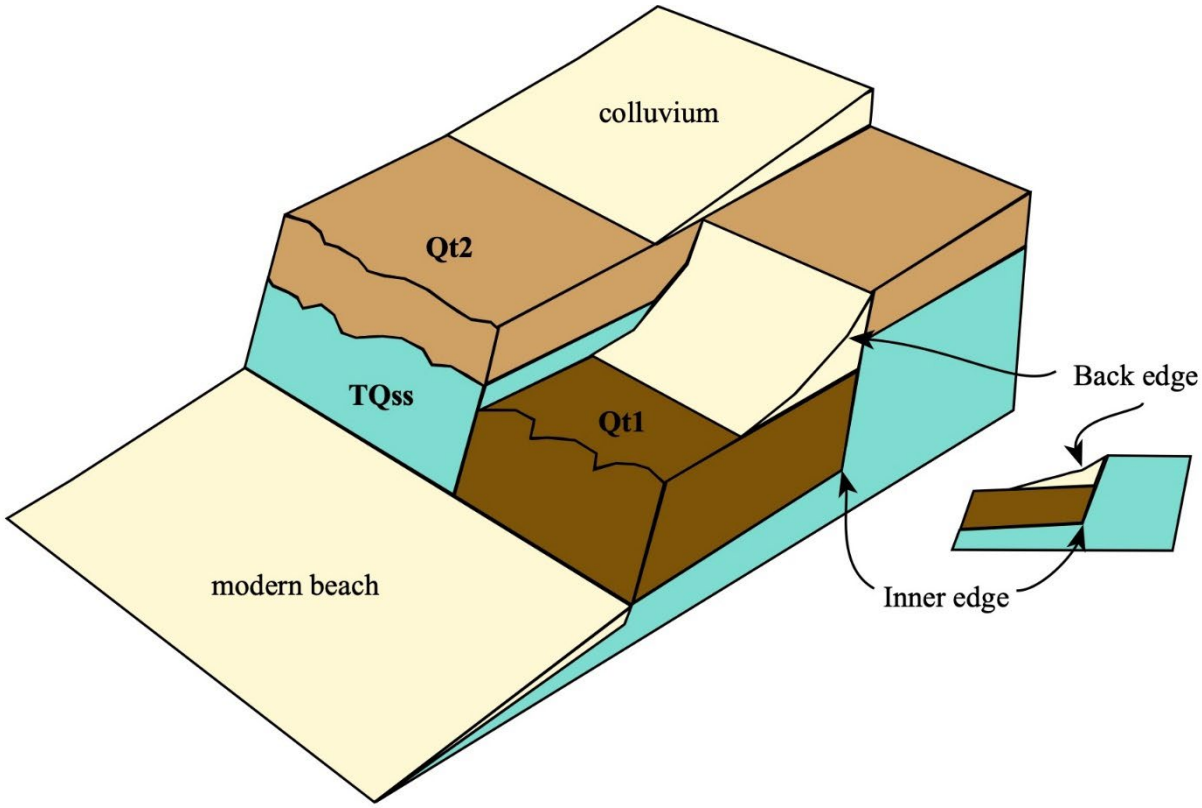


Figure 2-5. Block diagram illustrating the relationship of estuarine units Qt1 and Qt2 to unit TQss. Unit Qss is also estuarine but the relationship to other estuarine units could not be determined in the field and it is not included in this diagram. Also shown are the location of the back edge and the inner edge of the terrace. The back edge elevation is determined by the average elevation of remnant back edge fragments from 1m DEMs. The inner edge elevation is estimated by subtracting the estimated sediment thickness from the back edge elevation.

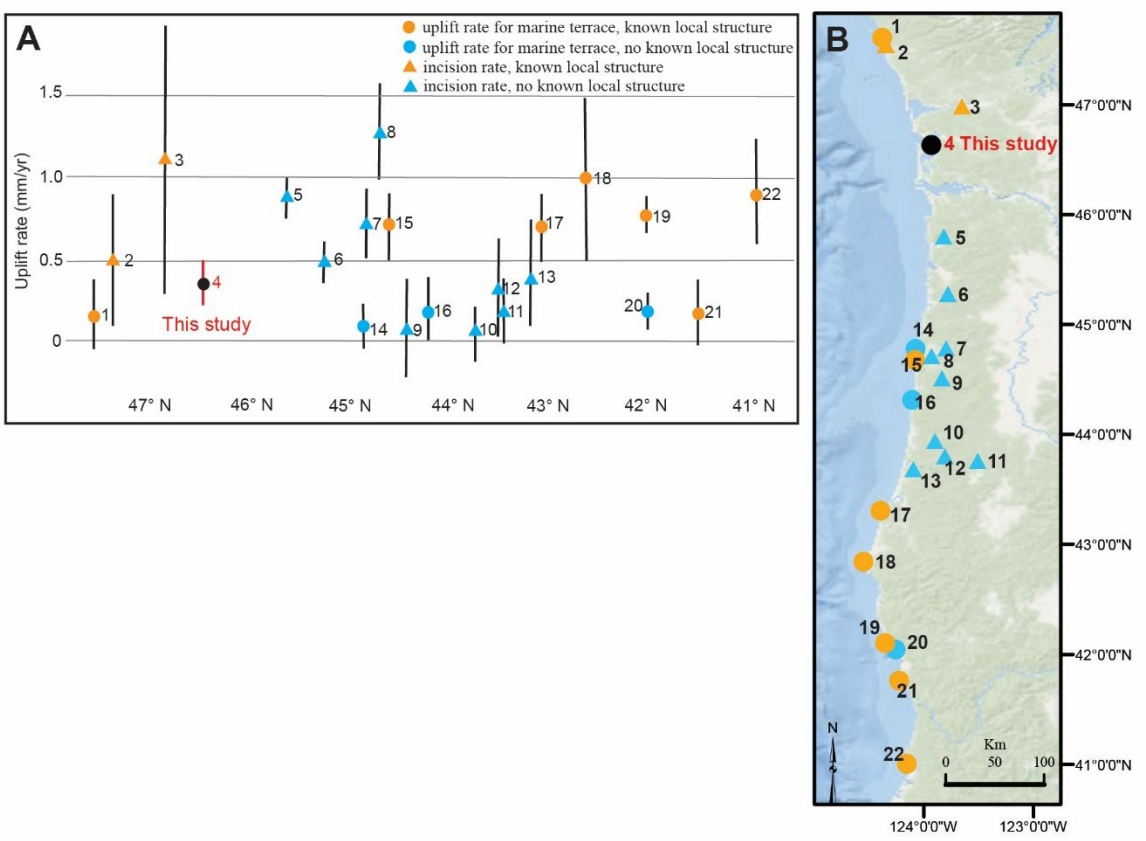


Figure 2-6. A. Uplift and incision rates along the Cascadia margin. B. Uplift and incision study sites. Circles are uplifted marine terraces. Triangles are incision rates. Orange indicates known local structures may affect uplift rate. Blue indicates local structures have not been identified. Rates discussed in more detail in the text. Appendix 2 Tables S5-S7 provide additional details on studies and uplift rates. Sources: 1. Thackray, 1996, 1998. 2. Pazzaglia and Brandon, 2001. 3. Delano et al., 2017. 5-13. Personius, 1995. 14-16. Kelsey et al., 1996; Ticknor, 1993. 17. McInelly and Kelsey, 1990; Muhs et al., 1990, 1992; Kelsey et al., 1994. 18. Kelsey, 1990; Muhs et al., 1990, 1992; Kelsey et al., 1994. 19. Kelsey and Bockheim, 1994; Kelsey et al., 1994. 20. Kelsey and Bockheim, 1994. 21. Polenz and Kelsey, 1999. 22. Padgett et al., 2019. Map base layer credits: Esri, Garmin, GEBCO, NOAA, NGDC and others.

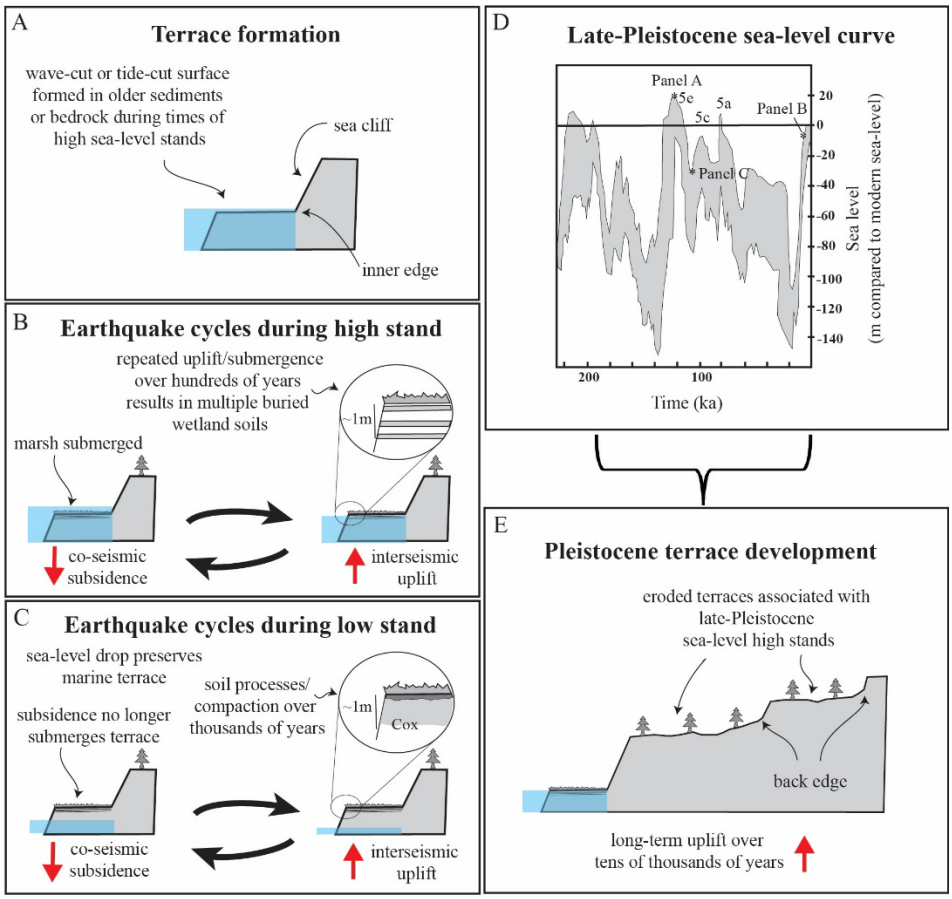


Figure 2-7. Terrace processes at earthquake cycle time scale (i.e., Holocene) and over many earthquake cycles (i.e., Pleistocene). A. Terraces form during times of high sea-level stands, such as MIS 5a, 5c, and 5e. B. During sea-level high stands, and in the context of long-term, gradual relative sea level rise, earthquake cycles of interseismic uplift and co-seismic subsidence result in multiple buried soils as uplifted marshes are submerged during an earthquake, and subsequently slowly buried by tidal mud during interseismic gradual sea level rise. C. Sea level falls during the progression to low stands (MIS 2, 4, 5b, 5d, 6) and preserves the high-stand terrace; the emergent terrace no longer hosts relative sea level changes related to the earthquake deformation cycle. Soil forming processes on the emergent terrace obscure evidence of high-stand buried soils in those locales where tidal marshes are preserved. D. Sea-level curve over the late Pleistocene

showing the range in mean global sea level in grey after Rabineau et al. (2006) with MIS 5e, 5c, and 5a high stands noted. E. Long-term uplift over tens of thousands of years results in development of a series or flight of terraces associated with previous sea-level high stands. This model assumes gradual accumulation of permanent uplift.

# Chapter 3. Gravity and magnetic evidence for potentially active crustal faulting, northern Cascadia forearc.

Contents of this chapter are part of a manuscript in preparation with planned submission to Tectonics, in collaboration with Juliet Crider, Megan Anderson, Todd Lau, Lydia Staisch, and Harvey Kelsey.

## Abstract

Late Pleistocene estuarine deposits record long-term coastal uplift in southwestern Washington, with uplift rates similar to other coastal sites in Cascadia where local folds or faults contribute to the vertical motion. Here we investigate whether there are identifiable forearc structures near the uplifted late Pleistocene deposits at Willapa Bay and Grays Harbor. We use map-view interpretation and two-dimensional modeling with observations from gravity and aeromagnetic data to identify N- and NW-trending faults. Modeling suggests two 20-25° east-dipping reverse faults. One modeled fault aligns with the active Willapa Bay fault zone identified previously from offshore seismic-reflection studies. The uplift recorded in the estuarine deposits is likely accommodated by the Willapa Bay fault. The other modeled fault aligns with the Raymond fault, inferred from previous geophysical studies. The Raymond fault uplifts Crescent Formation basalts exposed east and northeast of the fault in the Raymond Hills. Longitudinal profiles of streams near the Raymond fault show knickpoints, with stream segments upstream of the knickpoints reflecting relict streams graded to a base level ~85-150 m higher than current sea level. Because Quaternary sea-level fluctuation cannot accommodate this amount of base level fall, the base level change likely reflects regional rock uplift, possibly accommodated by the

Raymond fault. The geophysical models also suggest that faults previously mapped with small lateral offsets in Eocene-Miocene rocks east of Willapa Bay may have a vertical component. The geophysical modeling combined with previous geologic mapping suggests that many N-and NW-trending regional faults are transpressional. Coastal southwestern Washington may be a transition between deformational domains, with faults accommodating both east-directed, subduction-related strain and north-directed strain related to intraplate tectonic block rotation.

## Plain Language Summary

Although subduction zones are often associated with very large earthquakes occurring where the two plates meet, geologic uplift along coastal regions at subduction zones may mean there are faults onshore or nearshore that could present additional seismic hazard. In southwestern Washington near Willapa Bay uplift of marine deposits suggests there may be faults in the subsurface. We use information about the relative density and magnetic properties of the rocks to inform about possible faults below the surface. Our models suggest that the marine deposits have been uplifted by a fault under Willapa Bay. The nearby Raymond fault may also be recently active. Additionally, nearby faults that were mapped with lateral motion probably also have vertical motion. Faults in coastal southwestern Washington may be accommodating both the motion related to subduction and the motion related to rotating onshore blocks.

## Introduction

Interseismic strain, the strain accumulating between earthquakes at a locked fault, is commonly considered to be released elastically during the next earthquake (Reid, 1910; Whipple, 1936). At subduction zones, coastal co-seismic subsidence has been interpreted to be the result of elastic

rebound, as the nearshore land level drops vertically after being uplifted during plate locking (e.g., Atwater, 1987, Hyndman and Wang, 1995; Clague, 1997). Yet it is also well recognized that a portion of interseismic strain must be converted to permanent deformation because uplifted marine/coastal deposits are observed at many subduction zones at elevations greater than can be produced by a single earthquake cycle (e.g., Kelsey, 1990; Kelsey et al., 1994, 1996; Melnick et al., 2006; Saillard et al., 2009; Matsu'ura et al., 2015, 2019; Stanton et al., 2023). A variety of mechanisms have been proposed for accommodating permanent uplift at a subduction zone: sediment underplating of the overriding plate (Delph et al., 2021); subduction of bathymetric topography or asperities (e.g., Freisleben et al., 2021); mantle wedge buoyancy (Bodmer et al., 2020); or post-seismic slip (e.g., Sawai et al., 2004; Kelsey et al., 2006). Crustal folding or faulting on the overriding plate may also accommodate permanent subduction-related strain. Along the Cascadia subduction zone (herein termed Cascadia; Fig. 3-1a), numerous studies have documented late Pleistocene marine deposits that indicate uplift rates between 0.1-1.4 mm/yr (Kelsey, 1990; Muhs et al., 1990; McInelly and Kelsey, 1990; Ticknor, 1993; Kelsey et al., 1994; Kelsey and Bockheim, 1994; Kelsey et al., 1996; Polenz and Kelsey, 1999; Padgett et al., 2019). In these studies, uplift rates of ~0.5 mm/yr and greater are associated with local folds or faults.

In coastal southwestern Washington (Fig. 3-1b), terraced estuarine deposits date to marine isotope stage 5 (Kvenvolden et al., 1979; Kennedy, 1978; Kennedy et al., 1982; Stanton et al., 2023). Stanton et al. (2023) use luminescence dating along with relative age dating based on soil maturity and fossil shells ages from previous studies to obtain an average uplift rate for multiple terraces of 0.4 ±0.1 mm/yr (Qt1 and Qt2 in Fig. 3-2). For the remainder of this study we refer to the uplift rate as ~0.4 mm/yr. Stanton et al. (2023) also suggest that the observed uplift in Willapa Bay may be accommodated, partially or fully, by a local fault(s) because the uplift rate

is similar to that at other Cascadia sites where faults or folds may accommodate long-term coastal uplift (Kelsey, 1990; Muhs et al., 1990; McInelly and Kelsey, 1990; Ticknor, 1993; Kelsey et al., 1994; Kelsey and Bockheim, 1994; Kelsey et al., 1996; Polenz and Kelsey, 1999; Padgett et al., 2019). In the study area, previous mapping indicates numerous faults in Eocene–Miocene bedrock (Fig. 3-2; e.g., Wagner, 1962 a, b; Snavely and Wagner, 1982; Wells, 1981, 1989a; Moothart, 1992), with some studies suggesting the predominant fault motion is reverse/thrust (Snavely and Wagner, 1982) and other studies focusing on mapped lateral offset to support a regional strain model of primarily north-verging strike-slip faults (e.g., Wells, 1981,1989a, b; Wells and Coe, 1985). McCrory et al. (2002) used seismic-reflection to map an offshore, NNW-trending, 3-km-wide, 30-km-long fault zone through Willapa Bay that may extend onshore (Fig. 3-2), but no additional faults or folds have been mapped in Quaternary deposits. Yet, aeromagnetic surveys show magnetic lineaments that underlie the southwestern Washington coast (Blakely et al., 2016; Blakely and Sherrod, 2020), suggesting the presence of faults or folds in the subsurface that may not be expressed at the surface or that may be concealed by heavy vegetation or unknown due to poor access for field study. Linear aeromagnetic anomalies at other locations in the Pacific Northwest have been used to map the extent of active deformation zones as well as provide information about the fault geometry at depth (e.g., Blakely et al., 2002, 2009, 2011; Staisch et al., 2017; Steely et al., 2021). In lieu of geologic evidence of folding or faulting in the Quaternary deposits, we use aeromagnetic and gravity data to investigate the possibility of active faulting in coastal southwestern Washington, as well as to differentiate between proposed regional fault motions.

Gravity and magnetics data help constrain subsurface faults and folds (Blakely, 1996; Saltus and Blakely, 2011). Lateral variations in rock density and magnetic properties result in gravity and

magnetic anomalies, respectively. Using gravity and magnetic map and profile data in conjunction with geologic mapping provides independent constraint on position and geometry of subsurface structures, and results in a narrower range of possible hypotheses to explain those structures than any dataset alone. Here, we report on map-view interpretation and two-dimensional forward modeling of gravity and aeromagnetic data to show that there are likely active subsurface faults in coastal southwestern Washington that contribute to the observed late Pleistocene uplift. Additionally, the modeling suggests many regional faults have vertical offset, some of which were previously mapped with lateral motion. Thus, the fault motion is likely oblique, accommodating strain resulting both from oblique subduction of the Juan de Fuca Plate and from regional crustal block rotation in the overriding North America Plate.

## Background

### Tectonic setting

Washington State is situated above the Cascadia subduction zone, where the Juan de Fuca oceanic plate subducts obliquely under North America toward the northeast (Fig. 3-1a, e.g., Atwater, 1970; Clague, 1997). The oblique nature of subduction has led to speculation that significant lateral slip has occurred on forearc faults at Cascadia since at least the Miocene (e.g., Beck, 1980; Wells and Coe, 1985; Brocher et al., 2017). Dextral strike-slip or transpression along western North America is also hypothesized by kinematic models of relative plate motion between the Pacific Ocean plates (e.g., Kula, Farallon, and Pacific plates) and North America plate (Doubrovine and Tarduno, 2008; Wilson and McCrory, 2022) although no lengthy, distinct, margin-parallel and continuous strike-slip faults have been mapped in Oregon or Washington (McCaffery et al., 2007; Wilson and McCrory, 2022). Instead, offshore faults along the

subduction margin document east-directed subduction-related compressional and lateral strain (e.g., Goldfinger et al., 1992; Goldfinger et al., 1997; Fleuh et al., 1998) while the origin and motion of nearshore and onshore faults is more complicated.

Geodetic and paleomagnetic measurements suggest that the upper crust of North America in the PNW moves as tectonic blocks (e.g., Wells et al., 1998; McCaffery et al., 2007, 2013; Wilson and McCrory, 2022). After accounting for interseismic strain related to a locked subducting plate, the geodetic signal in southwestern Washington indicates north-directed movement, interpreted as the northwestern edge of the Oregon Coast Range/Siletzia block moving northward relative to the Olympic Mountain block (Fig 3-1a.; McCaffery et al., 2013; Wilson and McCrory, 2022). Bedrock faults in the study area have been interpreted by some studies to primarily accommodate the strain resulting from this tectonic block interaction (e.g., Wells and Coe, 1985; McCrory et al., 2002; Brocher et al., 2017) although other studies suggest the bedrock faults accommodate primarily subduction-related strain (e.g., Snavely and Wagner, 1982).

**Geology**

Southwestern Washington geology consists of Paleocene–Eocene basalts underlying Eocene–Miocene fluvial to marine sedimentary rocks and flood basalts, as well as Quaternary fluvial, estuarine, and near shore marine deposits (Fig. 3-2). We review geologic mapping for the study area to inform our geophysical modeling and map interpretation, but also to provide a framework for evaluating subsurface structures revealed from geophysical observations in terms of regional structural models.

*Paleocene–Quaternary rocks*

The oldest exposed rocks in southwestern Washington comprise the Crescent Formation (Formation). The Crescent Formation consists primarily of Paleocene–Eocene tholeittic to alkalkic basalts and associated intrusives. These basalts erupted both subaerially and submarine and are interbedded with marine sedimentary rocks and volcanic breccias (Snavely et al., 1958; Armentrout, 1987). The Crescent Formation and associated igneous rocks have emplacement or eruption ages between 53.18 ±0.17 Ma and 48.364 ±0.036 Ma (Globerman et al., 1982; Polenz et al., 2016; Eddy et al, 2017). The Crescent Formation is part of a larger igneous terrane called Siletzia. Siletzia underlies much of the Cascadia forearc from Vancouver to southern Oregon (OCR/Siletzia in Fig. 3-1a), is between 10-32 km thick, and accreted to North America between 50.5–45 Ma (Wells et al, 2014 and citations therein). On the Olympic Peninsula, the Crescent Formation is steeply folded around and thrust over younger sediments of the accretionary complex that make up the bulk of Olympic Mountains (OM in Fig. 3-1a; Tabor and Cady, 1978; Eddy et al., 2017). South of the Olympic Mountains, near Willapa Bay, the Crescent Formation exhibits a ridge-and-basin structure, with faults or shear zones bounding uplifted basaltic basement (Gower and Pease, 1965; Wagner 1967a, b; Wolfe and McKee, 1968, 1972; Wells, 1981, 1989a).

Starting in the middle Eocene, marine and near-shore sedimentary rocks and interbedded volcanics of the McIntosh Formation were deposited overlying and interfingering with the Crescent Formation (Snavely et al., 1951; Wolfe and McKee, 1968, 1972; Wells, 1981; Wells, 1989a; Walsh et al., 1987; Moothart, 1992; Polenz et al., 2017; Sadowski et al., 2019). Near the Naselle River in southern Willapa Bay, Eocene gabbros and basalts intrude both the McIntosh

and the Crescent Formations (Wells, 1989a). The late Eocene–early Miocene shallow marine sandstones and siltstones of the Lincoln Creek Formation unconformably overlie the McIntosh Formation and onlap onto folded Crescent Formation (Pease and Hoover, 1957; Snavely et al., 1958; Walsh, 1987; Sadowski et al., 2018; Polenz et al., 2019; Steely et al., 2021). Detrital zircons indicate the Lincoln Creek Formation was deposited between 36-20 Ma (Sadowski et al., 2018, 2019; Polenz et al., 2019).

The Lincoln Creek Formation is overlain by the early-to-middle Miocene Astoria Formation, the middle Miocene Columbia River Basalt Group, and the late Miocene Montesano Formation. The Astoria Formation consists of shallow marine sandstones and siltstones deposited between 22–11.6 Ma (Snavely et al., 1958; Wagner 1967a, b; Armentrout, 1987; Wells, 1989a; Sadowski et al., 2018). These unconformably overlie and possibly grade into the Lincoln Creek Formation. Basalts of the Columbia River Basalt Group (CRBG) are found throughout southwestern Washington (Snavely et al., 1958, 1973; Wells, 1981, 1989a; Armentrout, 1987). The normally magnetized Sentinel Bluffs Member of the Grand Ronde Basalt is common within the field area, mostly toward the base of the Astoria Formation near the study area, where it is conformable between the sedimentary beds and has an $Ar^{40}/Ar^{39}$ age of 16.42 ±0.85 Ma (Steely et al., 2021).The reversely magnetized Pomona Member of the Saddle Mountain Basalt interfingers with the Astoria Formation and has a $Ar^{40}/Ar^{39}$ age of 11.6 ±0.03 Ma (Steely et al., 2021). The middle-to-late Miocene Montesano Formation consists of shallow marine to fluvial sedimentary rocks that unconformably overlie both the Astoria Formation, and at structural highs, the Lincoln Creek Formation (Gower and Pease, 1965; Bigelow, 1987; Armentrout, 1987). The Montesano Formation grades into and in some places, is indistinguishable from, the Astoria Formation

(Steely et al., 2021). Two detrital zircons provide a maximum depositional age of ≤~12 Ma (Steely et al., 2021).

Quaternary deposits south of Grays Harbor and along Willapa Bay consist of sedimentary deposits ranging from fluvial to marine (Wagner, 1967a, b; Walsh et al., 1987; Stanton, 2021; Stanton et al., 2023), including uplifted late Pleistocene estuarine terraces (Kvenvolden et al., 1979; Clifton, 1983; Stanton et al., 2023).

*Deformation and faulting*

Coastal southwestern Washington south of Grays Harbor exhibits two major sets of bedrock faults in Eocene–Miocene rocks (Fig. 3-2; Pease and Hoover, 1957; Gower and Pease, 1965; Wagner, 1967a, b; Wolfe and McKee, 1968; Wells, 1981, 1989a; Moothart, 1992; Steely et al., 2021): 1) East dipping, NW-trending faults, often bounding the western side of crustal blocks with Crescent Formation at the surface; 2) WNW- and NE-trending faults. Some mappers have identified slickenlines that indicate a component of dextral motion on the NW-trending faults (Wells, 1989a, b; Moothart, 1992). Some studies present a regional structural model of predominantly strike-slip motion on longer, NW-trending faults, with shorter, conjugate faults acting as Reidel shear faults, and displaying lateral, thrust, and normal motion (Wells and Coe, 1985; Wells, 1989b; Moothart, 1992). This model is supported by paleomagnetic data that indicates differential rotation between Crescent Formation blocks south and east of Willapa Bay (Beck, 1980; Wells and Coe, 1985). Brocher and others (2017) show focal mechanisms in southwestern Washington that indicate primarily dextral strike-slip faulting with some thrust faults.

In another interpretation, faults in both NW- and NE-trending orientations are interpreted to be structures that splay off a major east-dipping thrust fault west of the coastline that places Crescent Formation basalts over younger oceanic crust and subduction-related mélange (Snavely and Wagner, 1982). The presence of this fault is supported by seismic velocity studies that indicate a sharp velocity change west of Willapa Bay that Parsons et al. (1999) interpret as a steeply dipping fault between Crescent Formation and the accretionary complex. The presence of the fault is also supported by a regional geophysical model (Finn, 1990). McCrory et al. (2002) suggest this fault is the margin between the OCR/Siletzia and Olympic Mountain/accretionary complex tectonic blocks (Fig. 3-1a).

While structural evidence indicates extensive upper crustal deformation in Miocene and older rocks, evidence of Quaternary deformation near Willapa Bay is more limited. McCrory (1996, 1997) documented faulting and folding of Quaternary deposits north of Grays Harbor. Within Willapa Bay, McCrory et al. (2002) describe an offshore, ~30-km long, NNW trending fault zone in Willapa Bay that offsets a widespread unconformity inferred to be Quaternary. In some locations, the unconformity is offset by as much as 10-12 m. McCrory et al. (2002) conjecture that this fault zone represents backthrusts to a deeper, east-dipping fault that places Paleogene-Miocene bedrock over Miocene and younger subduction complex mélange (e.g., Snavely and Wagner, 1982; Finn, 1990; Parsons et al., 1999). Alternatively, McCrory et al. (2002) suggest the offset could result from relative motion between parallel strike-slip faults within the upper crust that creates graben or sags between the strands. Either way, there are multiple, probably active faults strands within the bay that generally align with onshore faults mapped in Eocene–Miocene rocks south of Willapa Bay (Fig. 3-2; Wells, 1989a).

Other evidence of Quaternary deformation includes late Pleistocene estuarine deposits near Willapa Bay that record vertical uplift of ~0.4 mm/yr (Stanton et al., 2023). When compared to other Cascadia studies of uplifted marine deposits where uplift rates greater than ~0.5 mm/yr are associated with crustal faults or folds (e.g., Kelsey, 1990; Muhs et al., 1990; McInelly and Kelsey, 1990; Ticknor, 1993; Kelsey et al., 1994; Kelsey and Bockheim, 1994; Kelsey et al., 1996; Polenz and Kelsey, 1999; Padgett et al., 2019), this rate is consistent with fault(s) or fold(s) partially or fully accommodating the Quaternary uplift observed in coastal southwestern Washington.

**Previous gravity and magnetic studies**

We use previous regional geophysical studies to inform our interpretation of geophysical anomalies in coastal southwestern Washington. Finn (1990) used the limited gravity and magnetic data available at the time to produce geophysical maps and cross-sections of western Washington. In conjunction with data from previous seismic and geologic studies, Finn (1990) models basalts of the Crescent Formation at the coast as underthrust by a subduction complex. The model requires that the subduction complex be denser than sediments within the trench, and Finn (1990) interprets this to mean the subduction complex is a combination of sediments and offscraped basaltic oceanic crust. Although too coarse to differentiate gravity and magnetic anomalies in the upper several kilometers of the crust, Finn's (1990) model provides a broad framework for location and geometries of mid-lower crustal and deeper geologic components in southwestern Washington.

As part of the Chehalis Basin Project, Steely et al. (2021) collected gravity data in southwestern Washington and produced geophysical maps and cross-sections, some of which include the

region south of Grays Harbor and around Willapa Bay. Their models do not extend further west than eastern Willapa Bay nor south of northern Willapa Bay. They infer a fault zone west of the Raymond Hills they call the North River fault zone (NRFZ in Fig. 3-2) as well as an east-dipping reverse fault bounding the western side of the Raymond Hills that they call the Raymond fault (RF in Fig. 3-2). They model the Willapa River fault zone (WRFZ in Fig. 3-2) on the eastern side of the Raymond Hills with steep, low-offset faults. Additionally, Steely et al. (2021) infer a previously unknown, dense and highly magnetic feature under much of southwestern Washington that they call the South Puget magnetic crustal block (SPMCB). This feature is not found at the surface but is required for geophysical models to match observed gravity and magnetic data. Steely et al. (2021) note that the geometry of the SPMCB is unknown, leading to some uncertainty to the short-wavelength gravity and magnetic anomalies that may represent the SPMCB contact with the Crescent Formation.

## Methods

### Data

Aero- and ground magnetic surveys map the local magnetic anomalies within Earth's magnetic field produced by lateral changes in the magnetic properties of geologic units. These magnetic anomalies may be used for mapping the extent of geologic units and structures. In conjunction with gravity measurements, surface geologic mapping, and measurement of rock properties, the magnetic anomalies may also be used for modeling subsurface distribution of geologic units. We use aeromagnetic data collected in a regional study (Blakely and Sherrod, 2020) and processed by Washington Geological Survey (WGS) following procedures in Steely et al. (2021). During processing, a filter was applied to enhance the anomalies resulting from shallower sources, called

the residual. Additionally, a reduction to pole filter was applied, which shifts the anomaly to be located over its source. The reduced-to-pole anomalies also reflect the symmetry (or lack thereof) of the source.

Lateral variations in rock density produce a local gravity anomaly that reflects the geometry and spatial relationship of geologic units. Similar to magnetic anomalies, gravity anomalies can be used to map geologic structures and model the subsurface. We used a Lacoste and Romberg gravimeter (serial #G-908) to collect data from 229 new stations in 2019 (Appendix 3 Fig. A3-1). Because the closest established base station was prohibitively far from the field sites for daily measurement, we established a new base station in Aberdeen, WA to tie our data to the U.S. gravity network. We located new stations along transects at approximately 500 m spacing, with the transects selected to measure gravity across and perpendicular to abrupt magnetic gradients. Station sites were selected to avoid topography and to thus minimize field terrain corrections. We used a Javad Triumph-2 GPS incorporating a differential correction with local base stations in postprocessing for horizontal and vertical position measurements. These data were incorporated into the WGS Chehalis Basin Project, with all data reduction and processing as described in Steely et al. (2021). For geophysical map interpretation and forward-models, we used a compilation of gravity data from this study as well as from Finn et al. (1991), from the Pan-American Center for Earth and Environmental Studies (PACES) repository, and from additional gravity surveys conducted by WGS for the Chehalis Basin Project (Steely et al., 2021). All data collected by WGS and in this study, as well as the new base station information, may be obtained through the Washington Geologic Information Portal (Washington State Department of Natural Resources, 2023). The data processing included applying standard methods for Bouguer, Earth curvature, and terrain corrections to create a Bouguer anomaly, and

further reducing the complete Bouguer anomaly to an isostatic anomaly. The isostatic corrections adjust for long-wavelength anomalies caused by deeper sources, with the resulting isostatic anomaly useful for interpreting mid-to-shallow crustal sources. Steely et al. (2021) suggest that the uncertainties in the gravity data are mostly due to uncertainty in vertical position during data collection and in the terrain corrections. We assume the same for our interpretations, and interpret gravity anomalies greater than 1mGal as interpretable density variations in the upper crust.

Rock density and magnetic characteristics are necessary inputs for modeling geophysical profiles from geologic cross sections. For mapped units we used ranges of density and magnetic susceptibility values (Table 3-1) based on a database of values measured by WGS on regional samples. The full dataset is available through Steely et al. (2021). In the study area, the Crescent Formation has been mapped as both normally and reversely magnetized. Additionally, the Crescent Formation has interbeds of volcanic breccias and sedimentary rocks, and particularly near the Willapa Hills near the Nemah River, is intruded by Eocene mafic rocks of nearly the same age as the Crescent Formation (Wells, 1989a). The heterogeneity of the Crescent Formation is reflected in the range of possible densities and magnetic properties we use in modeling. For undifferentiated Eocene sedimentary and volcanic rocks, we use general values of density and magnetic properties similar to other Eocene units found in western Washington (e.g., McIntosh Formation, Carbonado Formation, Northcraft Formation) and measured by Steely et al. (2021). The slight magnetic susceptibility assigned to the Eocene sedimentary units reflects that many Eocene sediments are interbedded with volcanic rocks. The Oligocene and younger sedimentary rocks are much less dense with very low to no magnetic susceptibility. Both the normally magnetized Sentinel Bluff member and the reversely magnetized Pomona member of

the Columbia River Basalts are denser and more magnetically susceptible than the sedimentary rocks. Similar to Steely et al. (2021), we use the South Puget magnetic crustal block in our models, with the same density and magnetic properties they employ. We model trench sediments and subduction complex units within the deeper portions of the cross-sections and we use density and magnetic properties for these units from Finn (1990).

**Geophysical maps**

We use the software package Geosoft Oasis montaj (Geosoft, 2021) to interpolate (minimum curvature) both magnetic and gravity data in southwestern Washington, resulting in gridded map datasets of the study area that we export for use into ArcGIS software (Fig. 3-3, Appendix 3 Figs. A3-1 and A3-2). Steep gradients between high and low anomalies may indicate a juxtaposition of sources with differing properties, such as what occurs when a fault juxtaposes rocks of differing properties. We use the gravity and magnetic maps to interpret possible faults traces based on those gradients and identified by data contours (Fig. 3-4).

**Two-dimensional forward modeling of potential field anomalies**

We use the Oasis montaj software extension GM-SYS to produce 2-D forward models of cross-sections (Figs. 3-5 and 3-6, Appendix 3 Figs. A3-3 – A3-11) at two locations in southwestern Washington. The northern Willapa Bay cross-section (A-A' Fig. 3-2, Fig. 3-5, Appendix 3 Figs. A3-3 – A3-7) spans from the Pacific Ocean in the west to Blue Mountain in the east, crossing just north of Willapa Bay near North Cove (NC on figures) and intersecting the Raymond Hills (RH on figures). The southern Willapa Bay cross-section (B-B' Fig. 3-2, Fig. 3-6, Appendix 3 Figs. A3-8 – A3-11) spans from the Pacific Ocean in the west to the southwestern Willapa Hills

(WH on figures) in the east, crossing Willapa Bay at Long Island (LI on figures) and including Sunshine Point (SP on figures) on the eastern side of the bay. Our model locations correspond to the location of our detailed gravity surveys and include the data collected at those stations as well as sample from the regional isostatic gravity and aeromagnetic grids described above.

We use the GM-SYS software to calculate the gravity and magnetic anomaly produced by blocks within a cross-section. We define density and magnetic properties (Table 3-1) for the units in the cross-section and inform and constrain our cross-sections with surface 1:100k geologic mapping compiled from various sources (Washington State Department of Natural Resources, 2023; Walsh, 1987; Walsh et al., 1987; Wells, 1981, 1989a). The software allows us to compare the modeled anomalies to the observed geophysical data at that location as we manipulate the unit geometries in the cross-section. For both models, this process involved multiple iterations where we started with simple geometric configurations for geologic units to obtain a general fit to the observed gravity and magnetic data (e.g., Appendix 3 Figs. A3-3 and A3-8). Later iterations focused on fitting details within the observed anomalies by making changes to fault and fold location and varying the dip of units and faults (e.g., Appendix 3 Figs A3-4 -A3-6, A3-9 – A3-10). We assess “fit” of anomalies by the degree of error compared to observations, with less error as a better fit. We follow the potential-fields modeling philosophy of Blakely (1996) and use all available independent information in the interpretation process. In addition to geologic maps, we use drill logs obtained from the Washington State Department of Natural Resources Geologic Information Portal to constrain regional depth to geologic contacts as well as previous geophysical models (Finn, 1990; Steely et al, 2021) to inform locations and geometries of geologic units.

## Gravity and aeromagnetic map and model interpretation

### Gravity and aeromagnetic maps

High gravity anomalies correspond to high-density rocks near to the surface, while high magnetic anomalies correspond to rocks with high magnetic susceptibility or strong normally magnetized remanence (or both). Low gravity anomalies occur in areas with low-density rocks in the subsurface and magnetic lows correspond to locations with rocks with low or no magnetic susceptibility or strong reversely magnetized remanence. The wavelength and form of the anomalies also change with the depth and shape of the rock body. For example, long-wavelength anomalies result from deep, regionally extensive rock bodies while shallow crustal features produce short-wavelength anomalies or small steps and inflections points on the long-wavelength forms. Steep or narrow gradients between gravity and magnetic anomalies tend to indicate the contact between rocks with differing density and magnetic properties, respectively, and in some instances, these may be faults. We use the term “facing” to describe the relative position of the highs and lows, with a west-facing gradient having a high anomaly to the east and a low anomaly to the west.

The map of the horizontal gradient of the magnetic anomaly and of the gravity anomaly (Fig. 3-3; Appendix 3 Figs. A3-1 and A3-2) show a general gradient from higher gravity anomalies in the east to lower anomalies in the west, implying that an underlying dense rock is at greater depth in the west. This change marks the geophysical signature of the Crescent Formation basalts, which are exposed at the surface in the Raymond Hills, Willapa Hills, and east (e.g., Wells, 1981, 1989a; Steeley et al., 2021), but are at greater depths under the coastline and offshore (Snavely and Wagner, 1982). There is a NW-trending, west-facing magnetic gradient in

Willapa Bay, coming onshore near North Cove (NC in Fig. 3-3). The gravity contours align with the magnetic gradient and indicate a west-facing gravity gradient at North Cove as well. The steepness of the gradients suggests a steeply-dipping contact that we interpret as a fault corresponding to the Willapa Bay fault zone (WBFZ on Fig. 3-4), mapped offshore by McCrory et al (2002). Although Crescent Formation is not exposed at the surface near North Cove, the basalt is likely producing the high magnetic anomaly observed there and within Willapa Bay, where the basalt is faulted against sedimentary units with no or low magnetic susceptibility. Gravity data are insufficient in Willapa Bay to complete the grid there, leaving a gap in the gravity contours on the map. At North Cove the NW trending magnetic high does not continue far onshore but there is a fainter, collinear magnetic high that trends north toward Grays Harbor with a west-facing gradient. This corresponds to a linear, north trending, west-facing gravity gradient that indicates a denser rock, such as the Crescent Formation, near to the surface compared to further west. Thus, the fault either changes strike near North Cove from NW-trending to N-trending, or the N-trending gradients mark a different structure, such as a conjugate fault or the unfaulted contact between rock with differing magnetic and density characteristic. There is another NW-trending magnetic anomaly with a west-facing gradient along the northern part of Long Shore (LS in Fig. 3-3) and a NW-trending, east-facing magnetic gradient through central Long Shore. The gravity data at Long Shore are sparser. We interpret the magnetic gradients tentatively as faults (Fig. 3-4).

The Raymond Hills (RH in Fig. 3-3) and Willapa Hills (WH in Fig. 3-3) both show strong magnetic and gravity highs that correspond to Crescent Formation basalts mapped at the surface, with steep gradients on both east and west side suggesting faults. We interpret the Raymond Hills to be bound on the east by the Willapa River fault zone (WRFZ on Fig. 3-4) and on the

west by the North River fault zone (NRFZ on Fig. 3-4), following interpretations by Steely et al. (2021). We infer the Willapa Hills also to be bound on the east by the Willapa River fault zone, following regional mapping (Wagner, 1967a, b; Wells, 1981, 1989a; Wells and Coe, 1985; Moothart, 1992). There is a steep, west-facing gravity gradient along the southwestern side of the Raymond Hills near the shoreline of Willapa Bay that corresponds to the location of the Raymond fault (Fig. 3-2; Steely et al., 2021) and we map it as such (RF on Fig. 3-4). There are gravity and magnetic low anomalies east of the Raymond Hills and the Willapa Hills, suggesting a region with low density rocks that have low or no magnetic susceptibility. Sedimentary rocks of the Lincoln Creek and Astoria Formations are mapped there (Wagner, 1967b; Wells, 1981; Moothart, 1990) and presumably produce the anomalies. A strong magnetic low anomaly at Sunshine Point (SP on Fig. 3-3) is more linear and corresponds on the geologic map with the reversely magnetized Pomona member of the Columbia River Basalts (Wells, 1989a). Likewise, a curving magnetic high south of Sunshine Point corresponds to normally magnetized basalt flows mapped at the surface (Wells, 1989a).

**Two-dimensional cross-sections**

We interpret the subsurface geologic structure along two transects (A-A' and B-B' on Fig. 3-2), constrained by our new terrestrial gravity survey, existing geologic mapping, and existing aeromagnetic and gravity data.

*Northern Willapa Bay model*

The geophysical model A-A' trends west to east from north of Willapa Bay, across Raymond Hills, to Blue Mountain (Fig. 3-5, Appendix 3 Figs. A3-3 – A3-7). We use high-resolution

gravity data collected at approximately 500-m intervals from North Cove in the west to just east of Raymond Hills (Fig. 3-5b). The remainder of the model east to Blue Mountain and west into the Pacific Ocean uses lower resolution grid data (sampled at 1 km spacing). West of Raymond Hills the surface geology consists of Quaternary deposits with no mapped faults or folds. Possible structures and underlying bedrock are not well constrained. From Raymond Hills eastward, mapping constrains geologic structures and bedrock geology at the surface, providing information about faulting, folding, and dip of bedding (Washington State Department of Natural Resources, 2023; Walsh, 1987; Walsh et al., 1987; Wells, 1989a). The models directly honor all mapped faults, folds, or geologic units that cross the line of section.

The modelled cross-sections are the result of an iterative forward modeling process. In early iterations, we attempted to fit the general form of the observed gravity and magnetic anomalies using simple geometries for the geologic units (Appendix 3 Fig. A3-3). The long-wavelength form of the observed gravity and magnetic anomalies results from the regional geologic geometries below and beyond the extent of the model shown in Fig. 3-5 (see Appendix 3 Fig. A3-7 for wide-scale view of model shown in Fig. 3-5). Short-wavelength forms, including small steps or inflection points in the observed anomalies, indicate changes in geologic geometries closer to the surface. These influence the interpretation of shallow crustal structures, smaller displacement faults, and thinner, near-surface geologic units shown in Fig. 3-5.

From the west the transect crosses a steep gradient to a NW trending, west-facing magnetic and gravity high in Willapa Bay near North Cove (NC in Fig. 3-5) that we interpret from geophysical and geologic maps as being a fault within the Willapa Bay fault zone (Fig. 3-4). We model it as an ~25° east-dipping reverse fault (location i on Fig. 3-5c) uplifting the Crescent Formation, with

approximately 1km dip-slip motion since the deposition of the Lincoln Creek Formation. Changing the dip angle results in mismatch between calculated and observed geophysical anomalies (e.g., Appendix 3 Fig. A3-6). McCrory et al. (2002) suggest the fault zone intersects a deeper, east-dipping fault that they infer to be the major contact between Crescent Formation and younger subduction complex rocks proposed by Snavely and Wagner (1982). Our model requires the east-dipping fault between Crescent Formation and subduction complex to be ~15 km west of Willapa Bay in the Pacific Ocean (Appendix 3 Fig. A3-7), a location supported by other geophysical studies (Finn, 1990; Parsons et al., 1999). According to our analysis, the fault zone mapped by McCrory et al. (2002) would intersect the east-dipping reverse fault under Willapa Bay (i) and would offset sedimentary and Quaternary units with similar densities and no-to-low magnetism, resulting in no geophysical anomaly.

The west side of Raymond Hills (RH in Fig. 3-5) shows a steep NNW-trending, west-facing magnetic and gravity gradient that we interpret as the Raymond fault (Fig. 3-4). We model this as an east-dipping reverse fault with ~20° dip (location ii in Fig. 3-5c) that places Crescent Formation over Eocene sedimentary rocks, with a short, steeper east-dipping reverse fault ~1.5 km east of the main fault. As with the dip of the fault underlying Willapa Bay, changing the dip angle of the Raymond fault results in mismatch between calculated and observed geophysical anomalies (e.g., Appendix 3 Fig. A3-5). The fault shows approximately 1.8km of dip-slip motion since the deposition of the Lincoln Creek Formation. The Raymond fault uplifts Crescent Formation basalt, exposing it at the surface in the Raymond Hills where it produces a high magnetic and gravity anomaly.

Because the western part of the model is under Quaternary cover and there are therefore fewer constraints on bedrock structure, we attempt to model the structure under Willapa Bay and the west side of the Raymond Hills without faulting (Appendix 3 Fig. S4). Even with a very steep contact under Raymond Hills, the no-fault model shows less fit to the observed magnetic and gravity anomalies than the fault model. In both the gravity and the magnetic anomaly, the best no-fault interpretation results in misfit along the western portion of the anomaly (marked by red arrows on Appendix 3 Fig. S4). Because of this misfit, our preferred model requires a reverse fault thrusting Crescent Formation over sedimentary units at Raymond Hills. The westernmost structure under Willapa Bay can be fit without a fault, although there is less fit to the magnetic data on the western side. A fault here is our preferred model especially because McCrory et al. (2002) map a fault zone within Willapa Bay that co-locates with the modeled fault.

East of Raymond Hills geologic mapping shows the sedimentary rocks of the Lincoln Creek Formation and Astoria Formation dipping to the east and northeast near the contact with Crescent Formation basalt, as we show in Fig. 3-5c. The mapping also shows many faults with small offset (Fig. 3-2) and multiple studies describe strike-slip indicators for these short regional faults (e.g., Wells, 1981, 1989a; Moothart, 1992). We interpret the fault directly east of Raymond Hills (location iii in Fig. 3-5c) to be primarily strike-slip. Significant vertical offset is not possible to fit the geophysical data and the geologic units at the surface (Astoria Formation and Lincoln Creek Formation) have abrupt, fault-bound contacts with lateral offset. The gravity and magnetic anomalies require vertical components to the faults further east; there, we model an imbricate thrust array to fit small steps in the observed gravity and magnetic anomalies (location iv in Fig. 3-5c). The relationship of the westernmost fault of the imbricate thrusts to the strike-slip fault is not constrained. Taken together, the imbricate thrusts (iv.) and the strike-slip fault

(iii.) co-locate with the steep geophysical gradient we interpret as the northern portion of the Willapa River fault zone (Figs. 3-2 and 3-4). We model a steep NW-trending, west-facing magnetic and gravity gradient west of Blue Mountain as an east-dipping reverse fault that places Crescent Formation over steeply dipping Lincoln Creek Formation. The geological map indicates steeply dipping Sentinel Bluffs Member of the Columbia River Basalts in the footwall, also shown in our model.

We fit the majority of the observed anomalies with Crescent Formation having uniform density and magnetic characteristics ($\rho$ =2800 kg/m$^3$, $\chi$ = 60x 10$^{-3}$ SI, $M_r$ = 0.5 A/m), however, several small wavelength anomalies require variability of properties within the Crescent Formation. Other studies indicate that the Crescent Formation comprises a variety of basalt, basaltic sedimentary interbeds, and gabbro (e.g., Snavely et al., 1958; Wells, 1981, 1989a; Wells and Coe 1985; Armentrout, 1987; Steely et al., 2021). The variety of rock within the Crescent Formation supports the use of differing rock properties in the models. For simplicity's sake, we place Crescent Formation lenses with differing properties near the upper part of the larger Crescent Formation body. These lenses help to fit shorter wavelength variations in the observed anomalies but the exact location and geometry is not constrained. Specifically, our model requires a low density, lower magnetic susceptibility lens at ~23 km on the model ($\rho$ = 2600 kg/m$^3$; $\chi$ = 10 x 10$^{-3}$ SI; $M_r$ =0.3 A/m) and a slightly lower density, higher magnetic remanence lens between 40-50km on the model ($\rho$ = 2750 kg/m$^3$; $\chi$ = 60 x 10$^{-3}$ SI; $M_r$ =1 A/m). Additionally, a magnetic and gravity high at ~25 km on the model requires a body of igneous rock with density of 2950 kg/m$^3$. Numerous mappers have identified dikes and plugs of basalt and gabbro intruding the upper portions of the Crescent Formation and the lower McIntosh Formation in southwestern Washington (Wagner, 1967a, b; Wolfe and McKee, 1972; Wells, 1981). Additionally, rock

density measurements by Steely et al. (2021) indicate several samples associated in the field with Crescent Formation that had anomalously high densities and magnetic susceptibility (e.g., 3000 $kg/m^3$, $\chi$ =70 x $10^{-3}$ SI). These observations support the use of denser Crescent Formation lenses in the model. Additionally, in the models we assume most of the Crescent Formation is normally magnetized, but Wells and Coe (1985) note that both normally and reversely magnetized basalts are found throughout the Crescent Formation. We add reversely magnetized Crescent Formation ($\rho$ = 2870 $kg/m^3$; $\chi$ = 50 x $10^{-3}$ SI; $M_r$ = 2 A/m) to some portions of the model, such as under Willapa Bay and east of Raymond Hills. Finally, Wells (1981, 1989a) maps faults within the Crescent Formation in many locations in southwestern Washington, and it is possible some of the complexity of the observed magnetic anomalies within the Crescent Formation (such as between 17-26 km in the model) results from faulting or folding of heterogeneous basalts and volcanic breccias or thin sedimentary interbeds, not resolved in this study.

Crescent Formation of varying rock properties cannot explain all model misfits. For example, west of Blue Mountain between 35-49 km in the model is a plateau in the magnetic data that does not have a corresponding gravity high. Increasing the thickness of the Columbia River Basalt unit increases the gravity signal by a greater amount than the magnetic signal and furthermore, would require a thickness for the Columbia River Basalts not supported by mapping to reproduce the magnetic signal. Rather, the observed magnetic plateau may indicate a highly magnetic, low-density unit at depth, such as a volcanic unit. Various regionally mapped volcanic units could account for this anomaly, including the Eocene Northcraft Formation stratigraphically between the McIntosh Formation and the Lincoln Creek Formation. Whereas the Northcraft Formation does not outcrop along the model, its presence in the subsurface is a reasonable assumption since it outcrops elsewhere in southwestern Washington (Wagner, 1967a,

b). We do not add a lens of the Northcraft Formation to the models, thus leaving a misfit of the modeled magnetic signal to the observed magnetic anomaly between ~41-48km.

*Southern Willapa Bay model*

The geophysical model B-B' (Fig. 3-6, Appendix 3 Figs. S8-S11) trends west to east along southern Willapa Bay into the southwestern Willapa Hills (see Fig. 3-2 for location). We use our high-resolution gravity data collected at approximately 500-m intervals for the portion of the model from Sunshine Point (SP in Fig. 3-6) east into Nemah River valley. The remainder of the model east to Willapa Hills (WH in Fig. 3-6) and west into the Pacific Ocean uses lower resolution data sampled from the grid (1 km spacing; see Appendix 3 Fig. S11 for preferred model at wide view).

Early iterations (e.g., Appendix 3 Fig. S8) for this model use the model from farther north (A-A') as a framework for broad geologic geometries in the subsurface, including subduction complex rocks thrust under Crescent Formation. As with the northern model, the general form of both the gravity and magnetic anomalies requires a deeper, dense and magnetic body in the east, the South Puget magnetic crustal block (Steely et al., 2021). At Long Island (LI on Fig. 3-6) a broad gravity and magnetic high requires Crescent Formation within several hundred meters of the surface (i on Fig. 3-6c). This shallow depth is supported by a well log indicating a volcanic unit at ~700m depth in southern Willapa Bay (No. 1 Weyerhaeuser 7-11 oil well, Tideland Oil & Gas Corporation, 1959). The well log description also notes that the unit is interbedded with silts and sands, consistent with observations of volcanic breccias and interbedded sedimentary rocks in some portions of the Crescent Formation (e.g., Wells, 1981, 1989a; Wells and Coe, 1981).

Near Sunshine Point (SP on Fig. 3-6) is a NW-trending, west-facing gravity gradient that is aligned with the gradient farther north near North Cove. In model A-A', we model this gradient as a fault. Additionally, Wells (1989a) maps a tentative fault along the western side of Sunshine Point. Finally, the un-faulted alternative (Appendix 3 Fig. S9) has a misfit to the gravity anomaly (red arrow in Appendix 3 Fig. S9). Thus, our preferred model has a fault under Sunshine Point (ii. in Fig. 3-6c) that dips to the east at ~60°. The geologic mapping shows the Pomona Member, Columbia River Basalt Group exposed along the ridge line at Sunshine Point and we place it in the model. The Pomona Member is reversely magnetized (Wells, 1989a), which we interpret as causing the low magnetic anomaly at ~9 km in the model.

Modeled east-dipping reverse faults (~60° dip) to the east of Sunshine Point (iii. in Fig. 3-6c) agree with geologic mapping (Wells, 1989a). Mapped regional outcrops of the Pomona Member, Columbia River Basalt Group are shown in the model as interbedded within the Lincoln Creek Formation between 16-22 km. Near Nemah River valley at 22 km in the model, geologic mapping by Wells (1989a) places Lincoln Creek Formation and an older Eocene sedimentary unit correlative to McIntosh Formation in sharp contact with a Tertiary volcanic unit described as submarine basalt lapilli tuff, basalt breccia, and basaltic sandstone and conglomerate. Wells (1989a) interprets these as correlative to volcanic sedimentary layers at the top of the Crescent Formation elsewhere in the region. In the model we use a lower density and lower magnetism volcanic unit to represent the Eocene volcanics (Evt in Fig. 3-6c; $\rho = 2500$ kg/m$^3$; $\chi = 0.02 \times 10^{-3}$ SI; $M_r = 0.5$ A/m). The mapped geological contact between the Lincoln Creek Formation and the Eocene volcanic unit is sharp enough to support our interpretation of a fault, as shown in the model (iv. in Fig. 3-6c). Tests varying the fault dip result in less fit to the observed data (e.g., Appendix 3 Fig.S10).

The Willapa Hills, on the easternmost side of the model, are characterized by high gravity and magnetic anomalies resulting from the Crescent Formation exposed at the surface. However, the observed gravity also requires a higher-density body ($\rho$ = 3200 kg/m$^3$; $\chi$ = 60 x 10$^{-3}$ SI; $M_r$ = 0.5 A/m) that we model as the Eocene mafic intrusions from geologic mapping by Wells (1989a). We show these as denser Crescent Formation between 15-19 km in the model since the age of the intrusions is very similar to the Crescent Formation and because mapping indicates a complex intrusion pattern (Wells, 1989a) that is not resolvable with our data. As in the more northerly model, this model requires reversely magnetized Crescent Formation in some locations, consistent with regional studies (Wells and Coe, 1985). The model does not fit the observed magnetic anomaly as well as it fits the observed gravity anomaly. This is likely the result of complexities within the Crescent Formation from reversely magnetized lenses or interbeds of low magnetism volcanic sediments that are not resolvable with our data.

## 5 Discussion

### 5.1 Fault position and activity

The fault near North Cove in model A-A' (i in Fig. 3-5c) co-locates with faults mapped in Willapa Bay (McCrory et al., 2002) and we propose this modeled fault is part of the Willapa Bay fault zone (WBFZ, Fig. 3-4). The fault under Sunshine Point in model B-B' (ii in Fig. 3-6c) may indicate the fault zone extends to the south. McCrory et al. (2002) map multiple fault strands, with both west-side up and east-side up relative motion. They suggest that the faults could either be backthrusts to an east-dipping fault or parallel transpressional faults that intersect a deeper fault. Our models do not resolve faults only in sedimentary deposits, but based on location, the strands mapped by McCrory et al. (2002) could intersect our modeled fault. Offset late-

Pleistocene erosional surfaces imaged from high-resolution seismic-reflection profiles and sidescan-sonar suggest that the Willapa Bay fault zone is active, with slip rates potentially up to 0.5 mm/yr (McCrory et al., 2002).

Additionally, terraced, late Pleistocene estuarine deposits in the field area record ~0.4 mm/yr of uplift (Stanton et al., 2023), with the uplifted terraces east of the Willapa Bay fault zone (units Qt1 and Qt2 in Fig. 3-2). Stanton et al. (2023) conclude, based on a review of marine terrace uplift rates at other sites along Cascadia, that coastal uplift rates of ~0.5 mm/yr or greater are associated with local folds or faults, although some studies indicate uplift rates as low as 0.03-.3 associated with local structures (Thackray, 1996; Polenz and Kelsey, 1999). From such observations along the length of Cascadia, we conclude that vertical motion on the Willapa Bay fault zone is probably accommodating the uplift recorded in the terraced, late Pleistocene estuarine deposits near Willapa Bay. The geophysical models suggest an east-dipping reverse fault that would result in east-side up motion, consistent with the terrace uplift. This does not preclude a lateral component to the motion, but geophysical models cannot easily distinguish lateral motion unless it results in juxtaposition of rocks of differing densities and magnetic properties.

In addition to being active, the models indicate that the fault under Willapa Bay has up to 1km of dip-slip offset on the Crescent Formation since the deposition of the late Eocene-early Miocene Lincoln Creek Formation. Detrital zircons place Lincoln Creek Formation deposition between 36-20 Ma (Sadowski et al., 2018, 2019; Polenz et al., 2019). This gives a long-term average slip rate between 0.03-0.05 mm/yr since the Lincoln Creek Formation deposition, assuming pure dip slip. The current uplift rate of ~0.4-0.5 mm/yr (McCrory et al., 2002; Stanton et al., 2023)

suggests that the Willapa Bay fault zone has not been continuously active since the early Miocene or that it has increased slip rate during the Pleistocene.

At the Raymond fault (Figs. 3-2, 3-4 and ii. in Fig. 3-5c), modeled dip-slip offset on the Crescent Formation is approximately 1.8 km, with a long-term average slip rate between 0.05-0.09 mm/yr since the deposition of the Lincoln Creek Formation, assuming the Crescent Formation mapped at the surface corresponds to the top of the Crescent Formation at depth. The Raymond Hills produce a pronounced topographic high east of the trace of the Raymond fault, suggesting at least some uplift occurred recently enough to maintain relief across the fault. Where faults are not easily mapped at the surface (due to access limitations or vegetative cover, for example) or where subsurface faults control the tectonic activity, geomorphic analyses of digital elevation models (DEMs) can aid studies of surface deformation (e.g., Wobus et al., 2006). For example, changes to stream channel steepness as marked by slope-break knickpoints may indicate past changes to base level, possibly caused by changes in rock uplift rate (e.g., Ouchi, 1985; Merritts and Vincent, 1989; Kirby and Whipple, 2001). Where climate, lithology or tectonic forcing are not constant, a stream will adjust to compensate, resulting in measurable changes in steepness and (or) concavity along the longitudinal profile (e.g., Hack, 1973; Ouchi, 1985; Merritts and Vincent, 1989; Merritts et al., 1994; Holbrook and Schumm, 1999; Keller and Pinter, 2002). Thus, profile view observations of steepness and concavity along streams can be used to identify possible tectonic boundaries (e.g., Ouchi, 1985; Whipple and Tucker, 1999; Wobus et al., 2006) and may be used as a “reconnaissance” tool for estimating relative amounts of rock uplift (Whipple et al., 2013). To determine if streams flowing across the trace of the Raymond fault are responding to regional rock uplift (Fig. 3-7c), we used the graphical user interface (GUI) of the Topographic Analysis Kit (TAK) (Forte and Whipple, 2019) for TopoToolbox (Schwanghart and

Scherler, 2014) to produce longitudinal profiles of streams on the southwestern side of the Raymond Hills (Fig. 3-7a; see Appendix 3 and Chapter 4 text for GUI inputs). The stream profiles show slope-break knickpoints at approximately similar elevations (Fig. 3-7b). Stream segments upstream of the knickpoints may reflect a relict fluvial system once graded to a base level different than current sea-level. We project the segments along the longitudinal profiles as a way to estimate the previous base level (Fig. 3-7b). The projected profiles suggest the relict fluvial systems were graded to a baselevel ~85-150m higher than current sea level. Because late Pleistocene sea-level highstands were within 20-30 m of modern sea-level (e.g. Chappell and Shackleton, 1986; Simms et al., 2015; Creveling et al., 2015, 2017), the base level change likely reflects regional rock uplift, possibly accommodated by the Raymond fault. The geomorphic signature of uplift reflected in the streams does not constrain timing of uplift, beyond a very generalized interpretation that knickpoints on stream profiles are likely reflecting a base level drop more recent than the Eocene. Further mapping along the streams could facilitate a better understanding of timing as strath terraces may be present to offer an avenue for dating of terrace formation, and thus, of stream segment age.

Determining the activity of modeled and mapped faults further to the east is not as straight-forward. Faults east of Raymond Hills (iii. and iv. in Fig. 3-5c) are mapped with small lateral offsets between late Eocene-Miocene sedimentary rocks (Wagner, 1967a, b; Wells, 1981, 1989a; Walsh et al., 1987; Moothart, 1992) but there are few mapped Quaternary deposits there and thus far, no offset Quaternary deposits have been mapped. Both Wells and Coe (1981) and Moothart (1992) suggest these faults are mostly short strike-slip faults with some vertical motion. However, the geophysical models suggest that at least some of the faults must have a significant component of vertical motion, with approximately 0.8 km of cumulative offset on the Crescent

Formation. The imbricate nature of these faults implies they may connect to a deeper thrust, but faults solely within the Crescent Formation cannot be easily identified by the geophysical methods used here.

**Dominant fault style**

The geophysical data help characterize fault motion in coastal southwestern Washington. Previous models for dominant fault style suggest that NW-trending faults are either dextral strike-slip, accommodating north-directed strain related to tectonic block rotation (e.g., Wells and Coe, 1985; McCrory et al., 2002; Brocher et al., 2017), or thrust/reverse faults accommodating east-directed strain related to subduction (Snavely and Wagner, 1982). The geophysical models from this study suggest significant vertical motion on NW-trending faults, such as on the Willapa Bay fault zone (i in Fig. 3-5c and ii in Fig. 3-6c) and the Raymond fault (ii in Fig. 3-5c) as well as vertical motion on shorter, NE- and E-trending faults (iv in Fig. 3-5c and iii, iv in Fig. 3-6c). One modeled fault, mapped as a short, NNE-trending fault east of the Raymond Hills (ii in Fig. 3-5c), does not require vertical motion. The amount of possible strike-slip motion on all the modeled faults cannot be determined from our geophysical modeling but as noted, the geologic mapping suggests many of the faults have lateral offset (Wagner, 1967a, b; Wells, 1981, 1989a; Walsh et al., 1987; Moothart, 1992). The geologic mapping combined with the geophysical models implies that many faults in southwestern Washington are oblique, accommodating both strike-slip and thrust/reverse motion.

Southwestern Washington is positioned near the western edge of Siletzia, at the boundary between the OCR/Siletzia and the OM/accretionary complex tectonic blocks (dashed bold black line in Figs. 3-1 and 3-8; McCrory et al., 2002; Wells et al., 1999). Faults offshore to the west

accommodate predominantly east-directed shortening (e.g., Goldfinger et al., 1992) while faults to the east in western Washington accommodate north-directed shortening resulting from tectonic block rotation (Fig. 3-8; e.g., Steely et al., 2021; Barnett et al., 2010; Wells et al., 1999). Oblique faults near Willapa Bay may mark the edge of a deformational domain (Fig. 3-8) accommodating strain resulting both from subduction (ENE directed shortening, NW directed lateral motion) and from tectonic block rotation (N directed shortening, NNW directed lateral motion).

Although distinct strain partitioning occurs at some other subduction zones with oblique subduction, with margin parallel strike-slip fault systems accommodating lateral movement (e.g., Cashman et al., 1992; Tsuji et al, 2014), coastal southwestern Washington appears to behave differently, likely in part, because of Siletzia. Studies suggest that the strength and/or structural architecture of existing rocks, both in the upper plate and the subducting plate, may play a role in faulting style (e.g., Yonkee and Weil, 2015) or exert control on subduction margin conditions (e.g., Arnulf et al, 2022; Bloch et al., 2023). Siletzia is a thick, relatively coherent block (McCaffery et al.,2007, 2013; Wells et al., 2014) that is spatially correlated with margin-parallel phenomena at Cascadia, such as morphotectonic variability in the outer wedge (Watt and Brothers, 2020), zones of fault creep (Schmalzle et al., 2014), and changes in subducting slab dip and morphology (Bloch et al., 2013). McCrory et al. (2002) propose that Sileztia (OCR block) acts as a rigid indenter against which the weaker accretionary rocks are deformed. Siletzia may thus represent a rheologically strong block that breaks as diffuse zones of oblique faults, particularly at the margin, such as in the study area. Alternatively, pre-existing fault networks within Siletzia may preferentially accommodate strain related to both subduction and tectonic

blocks. Further work to model the expected behavior of Siletzia in existing strain conditions is necessary to distinguish the role of Siletzia in Cascadia margin structural regimes.

## Conclusions

Map-view interpretation and two-dimensional forward modeling of gravity and aeromagnetic data indicate two faults underlying Quaternary deposits near Willapa Bay, Washington. A NW-trending, linear magnetic gradient in the bay aligns with an active offshore fault system previously identified with seismic-reflection studies (McCrory et al., 2002) called the Willapa Bay fault zone. 2-D forward-modeling using the magnetic and gravity data suggests the Willapa Bay fault zone consists of backthrusts rooting into to a deeper, 25° east-dipping thrust fault. Marine terraces along Willapa Bay recording ~0.4 mm/yr of late Pleistocene uplift (Stanton et al., 2023) are located on the hanging wall block and their uplift is likely accommodated by the Willapa Bay fault. A continuation of the magnetic anomaly to the north may result from an extension of the fault zone. Our modeling also suggests the existence of a 20° east-dipping thrust fault, the Raymond fault (Steely et al., 2021), on the northeast side of Willapa Bay near the contact between Quaternary deposits and bedrock on the west side of Raymond Hills. Longitudinal stream profiles at the projected trace of the nearby Raymond fault show knickpoints and may reflect a relict fluvial system once graded to a base level 85-150 m higher than current sea level. The base level change likely reflects regional rock uplift accommodated by the Raymond fault. Bedrock faults east of Raymond Hills, previously-mapped with lateral offset (Wagner, 1962a, b; Wells, 1989a; Walsh et al., 1997; Moothart, 1992), also require a component of vertical motion in the 2-D models in order to fit the data.

Although some regional faults may display distinct strain partitioning to accommodate both compressional and lateral motion, as suggested by other studies (e.g., Wells and Coe, 1985; McCrory et al., 2002), our new geophysical modeling combined with previous geologic mapping reveals many faults are truly oblique, accommodating both subduction-related strain and strain related to tectonic block rotation. This oblique fault style may signify a change in deformational domains, with predominantly east-directed shortening offshore and predominantly north-directed shortening east of the study area.

## Acknowledgments

This work is based upon work supported by the U.S. Geological Survey under Grant No. G20AP00065, by the Earth and Space Sciences Department at University of Washington, by the Geological Society of America, and by the Northwest Scientific Association. The views and conclusions contained in this document are those of the authors and should not be interpreted as representing the opinions or policies of the U.S. Geological Survey. Mention of trade names or commercial products does not constitute their endorsement by the U.S. Geological Survey.

## Tables

Table 3-1. Rock density and magnetic properties used for geophysical forward modeling, from Steely et al., (2021) and Finn (1990).

| Unit | Density (kg/m3) | Magnetic susceptibility (SI) | Magnetic remanence (A/m) |
|---|---|---|---|
| **Quaternary sediments** | 2010 | | |
| **Astoria Formation** | 2200 | | |
| **CRB – Pomona (reverse)** | 2400 | 0.090 | 1.5 |
| **CRB – Sentinel Bluffs** | 2700 | 0.060 | 1.5 |
| **Lincoln Creek Formation** | 2200 | 0.001 | |
| **Eocene sedimentary** | 2300-2400 | 0.001-0.003 | |
| **Eocene volcanic** | 2500 | 0.020 | 0.5 |
| **Crescent Formation** | 2600 -3200 | 0.010-0.060 | 0.3 – 1.0 |
| **Crescent Formation (reverse)** | 2870 | 0.050 | 1.0-2.0 |
| **South Puget magnetic crustal block (SPMCB)** | 2900 | 0.150 | |
| **Trench sediments** | 2500 | | |
| **Subduction complex** | 2800 | | |
| **Oceanic crust** | 2700 | | |
| **Siletzia crust** | 2600 | | |
| **Continental crust** | 2400 | | |

## Figures

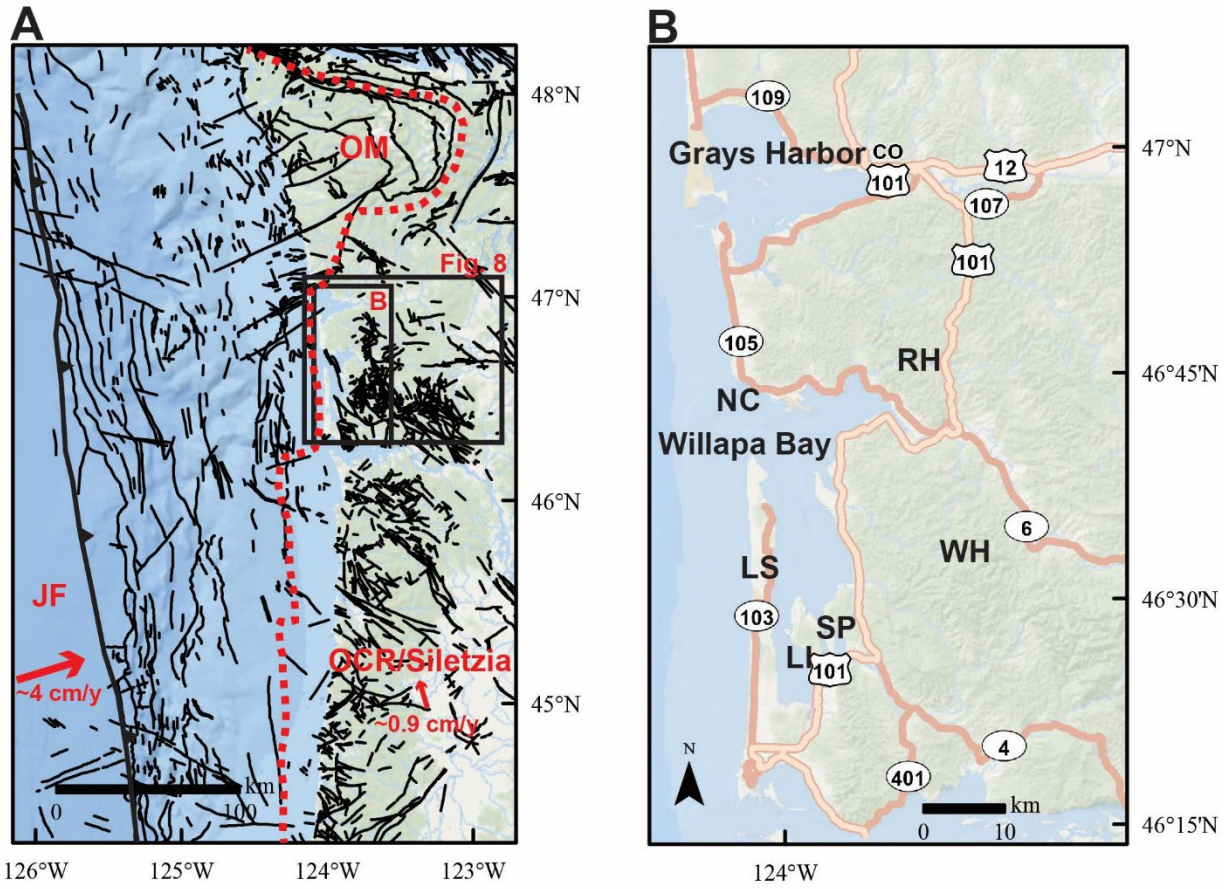


Figure 3-1. A. Study area location map. The study area is south of Grays Harbor and along Willapa Bay near to the Cascadia Subduction Zone margin. The Juan de Fuca (JF) plate subducts beneath North America at about 4 cm/yr toward the northeast (Heaton and Hartzell, 1987). Toothed thick black line is approximate subduction margin. Thin black lines are faults from 1:100k mapping in Washington state (Washington State Dept. of Natural Resources, 2023), from the 1:500k mapping in Oregon state (Walter and MacLeod, 1991) and from the U.S. Geological Survey Quaternary fault database (U.S. Geological Survey, 2023). Red dashed line is approximate contact between the Oregon Coast Range (OCR)/Siletzia and Olympic Mountain (OM)/accretionary complex tectonic blocks (from McCrory et al., 2002). Thick red arrows show approximate direction of movement of the JF plate and the OCR/Siletzia block relative to North

America (e.g., McCaffrey et al., 2013; McCrory et al, 2002; Wells et al, 1998). Boxes indicate locations of panel B and Fig. 8. B. Circled numbers are Washington state highways. RH – Raymond Hills, NC – North Cove, LS – Long Shore, LI – Long Island, SP – Sunshine Point.

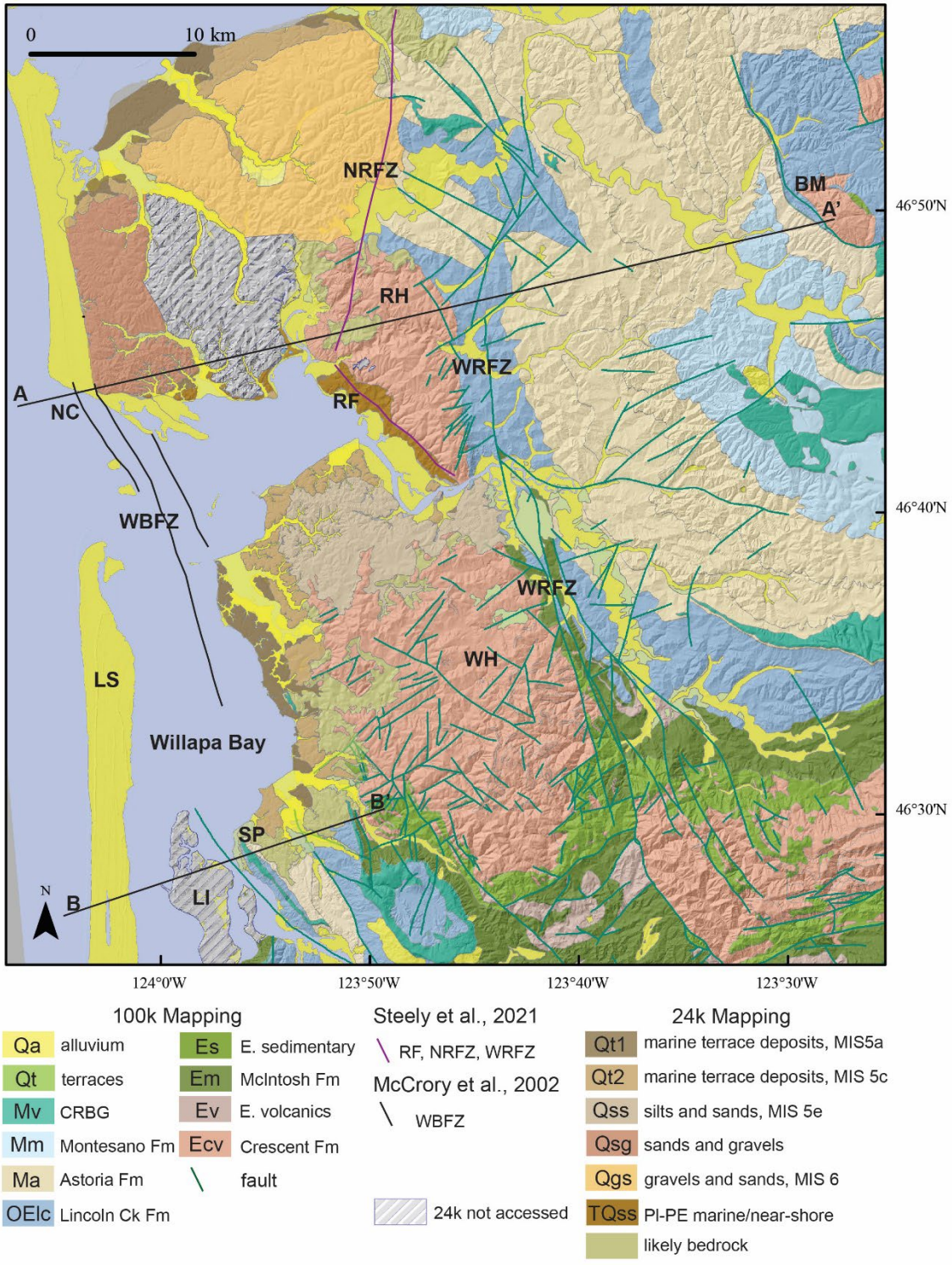
0
10 km
NRFZ
BM
A'
46°50'N
RH
WRFZ
A
NC
RF
WBFZ
46°40'N
WRFZ
WH
LS
Willapa Bay
B'
46°30'N
SP
N
B
LI
124°0'W
123°50'W
123°40'W
123°30'W
100k Mapping
Qa alluvium
Qt terraces
Mv CRBG
Mm Montesano Fm
Ma Astoria Fm
OElc Lincoln Ck Fm
Es E. sedimentary
Em McIntosh Fm
Ev E. volcanics
Ecv Crescent Fm
fault
Steely et al., 2021
RF, NRFZ, WRFZ
McCrory et al., 2002
WBFZ
24k not accessed
24k Mapping
Qt1 marine terrace deposits, MIS5a
Qt2 marine terrace deposits, MIS 5c
Qss silts and sands, MIS 5e
Qsg sands and gravels
Qgs gravels and sands, MIS 6
TQss PI-PE marine/near-shore
likely bedrock

Figure 3-2 (previous page). Geologic map of the study area compiled from 1:100,000 scale mapping of bedrock and faults (in green; Washington State Dept. of Natural Resources, 2023) as well as from 1:25,000 scale mapping of Quaternary coastal deposits (Stanton, 2021; Stanton et al., 2023). Trace of the Raymond fault (RF) and the North River fault zone (NRFZ) in purple from Steely et al. (2021). Trace of Willapa Bay fault zone (in black; WBFZ) from McCrory et al. (2002). Base map is 10m DEM hillshade. “Likely bedrock” indicates locations previously mapped as Quaternary terrace deposits that are probably bedrock as determined by 1:24k mapping (Stanton, 2021; Stanton et al., 2023). “Not accessed” indicates locations not mapped in 1:24k mapping because landowners did not grant permission or because of limited road access (Stanton, 2021; Stanton et al., 2023). BM = Blue Mountain. Other abbreviations per Fig. 3-1. A-A’ and B-B’ indicate locations of cross section for geophysical forward models.

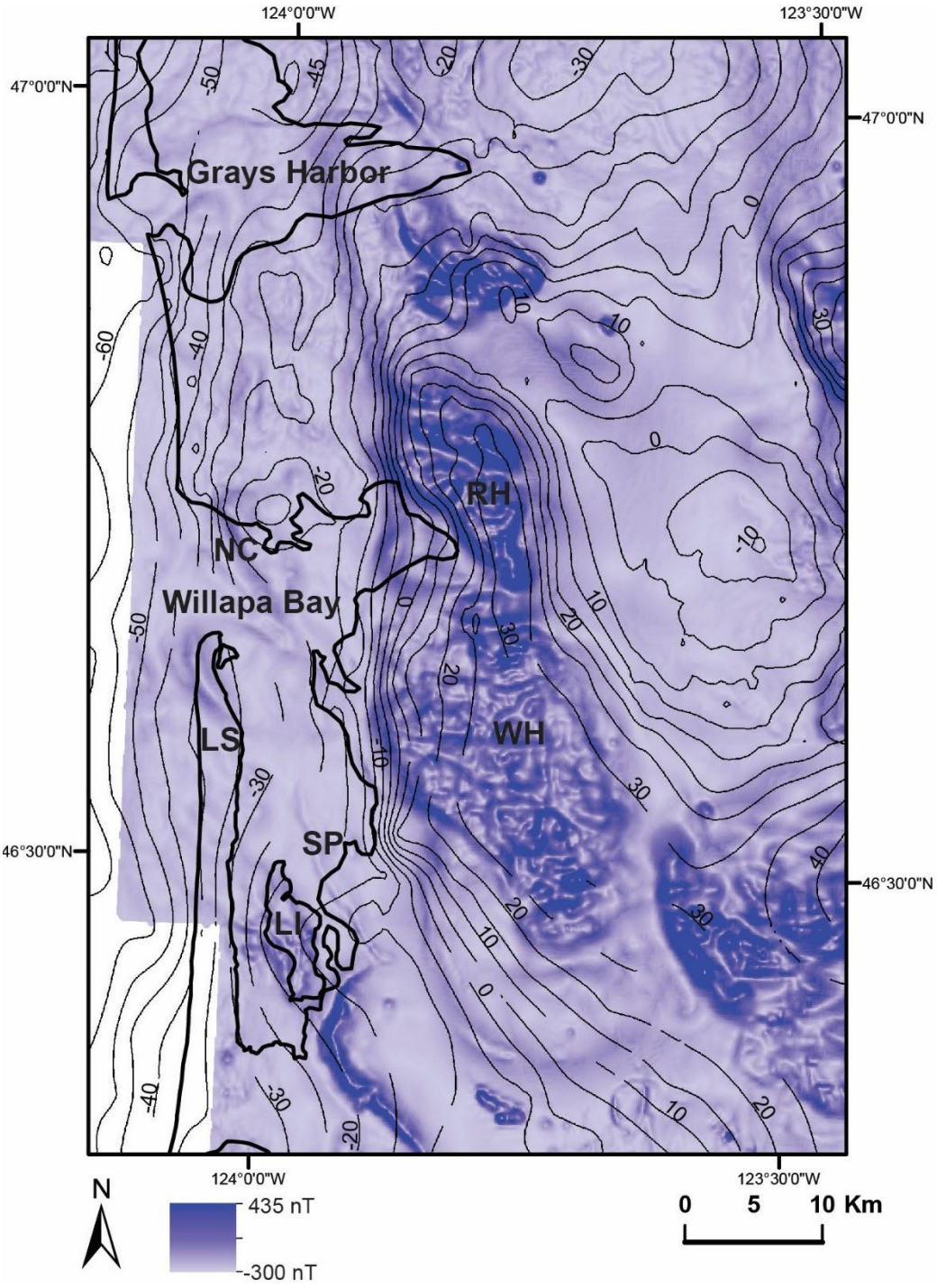


Figure 3-3. Map showing the horizontal gradient of the aeromagnetic grid for the study area overlain with contours from gravity grid in milligals (mGal). We use the horizontal gradient to accentuate details not easily visible in maps of the aeromagnetic grid alone. Darker purple

indicates steeper gradients. Contour spacing is 5 mGal. The gravity grid is not complete, reflected by gaps in contours. All notations as in Fig. 3-1. See Appendix 3 Fig. S1 for gravity grid with location of gravity stations from this study and Appendix 3 Fig. S2 for aeromagnetic grid in nanotesla (nT).

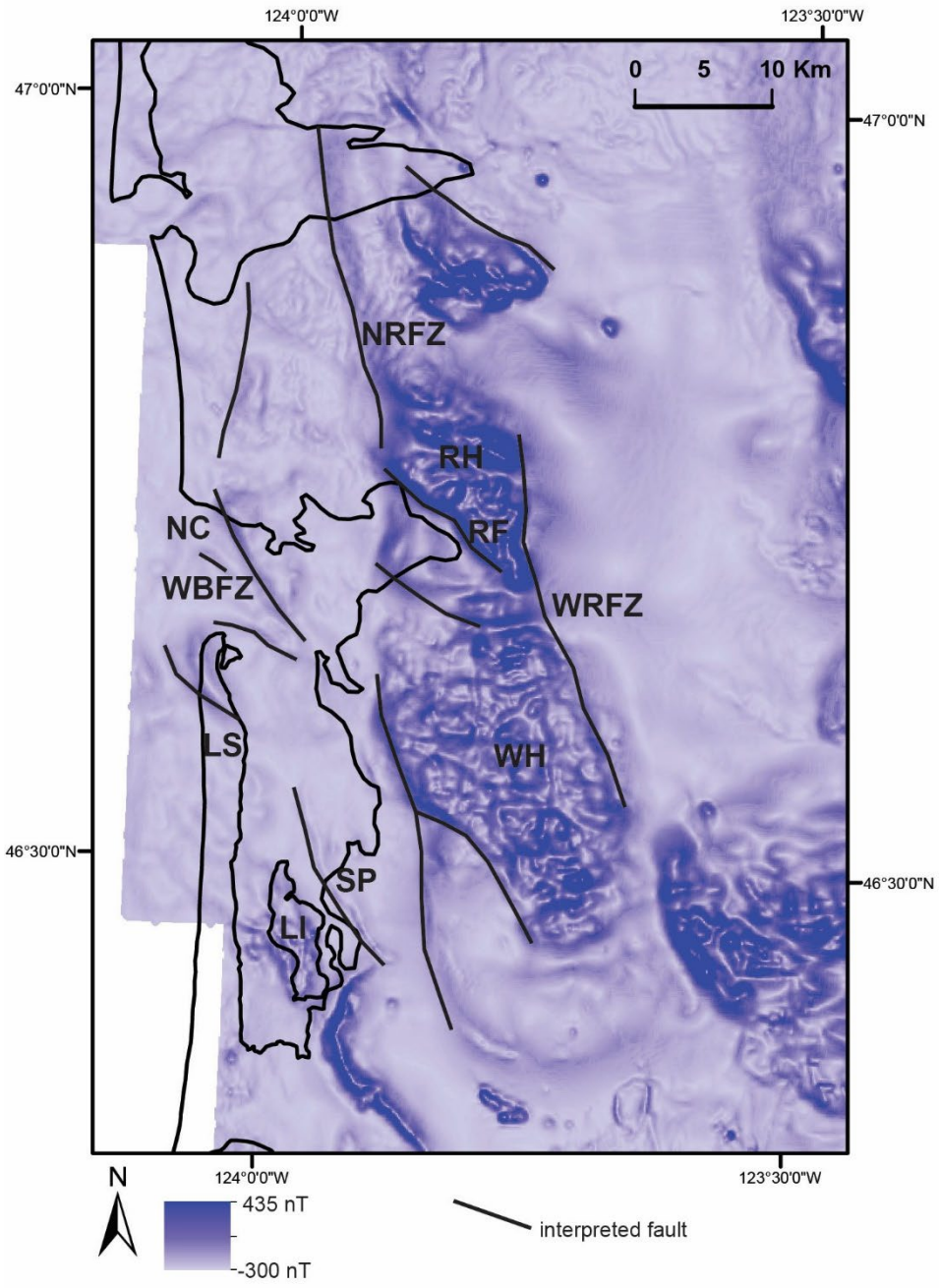


Figure 3-4. Map showing interpretation of fault trace location from aeromagnetic and gravity maps. Base map is horizontal gradient of the aeromagnetic grid with fault interpretations based on both aeromagnetic and gravity data (see Fig. 3-3, Appendix 3 Figs. S1-S2). Lines indicate faults interpreted from the gravity and magnetic maps in this study. Notations as in Figs. 3-1 and 3-2.

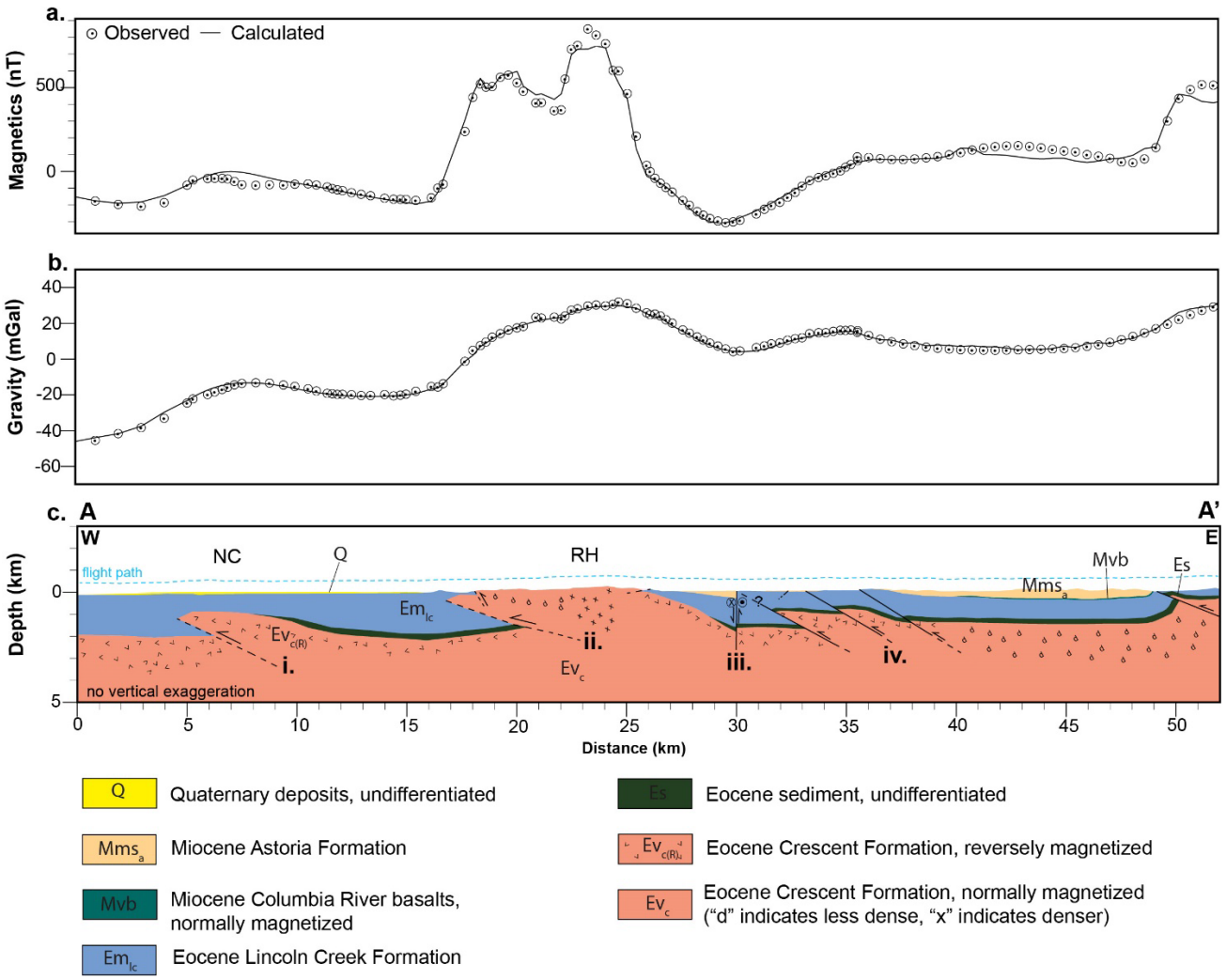


Figure 3-5. A. Observed aeromagnetic data (dots) and corresponding modeled magnetic anomaly (line). Error circles on magnetics have radius of approximately 25 nT. B. Observed gravity data (dots) and corresponding modeled gravity anomalies (line). Error circles on gravity have radius of approximately 2 mGal. For both aeromagnetic and gravity data, error circle values are visually estimated. C. Preferred cross-section forward model of A-A' produced using Oasis montaj software with GM-SYS extension. Location of cross section A-A' is shown on Figure 3-2. Geologic units are populated with densities and magnetic properties as listed in Table 3-1. The

software calculates expected geophysical anomalies based on the cross-section geometries and unit properties. NC – North Cove, RH – Raymond Hills. Lowercase roman numerals indicate features described in text.

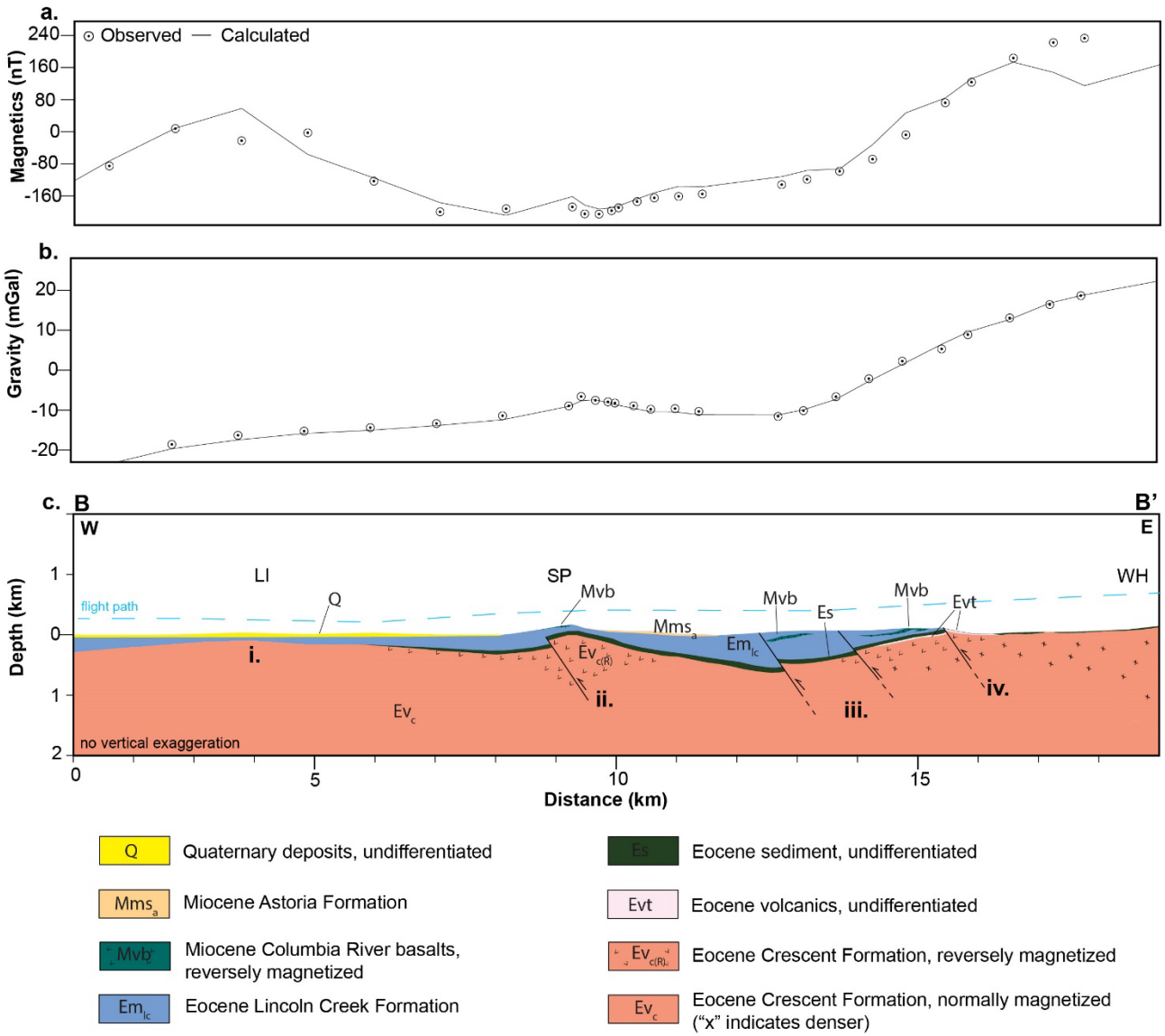


Figure 3-6. A. Observed aeromagnetic data (dots) and corresponding modeled magnetic anomaly (line). Error circles on magnetics have radius of approximately 20 nT. B. Observed gravity data (dots) and corresponding modeled gravity anomalies (line). Error circles on gravity have radius of approximately 1 mGal. For both aeromagnetic and gravity data, error values are visually estimated. C. Preferred cross-section forward model of B-B' produced using Oasis montaj

software with GM-SYS extension. The location of cross section B-B' is shown on Figure 3-2. Geologic units are populated with densities and magnetic properties as listed in Table 3-1. The software calculates expected geophysical anomalies based on the cross-section geometries. LI – Long Island, SP – Sunshine Point. Lowercase roman numerals indicate features described in text.

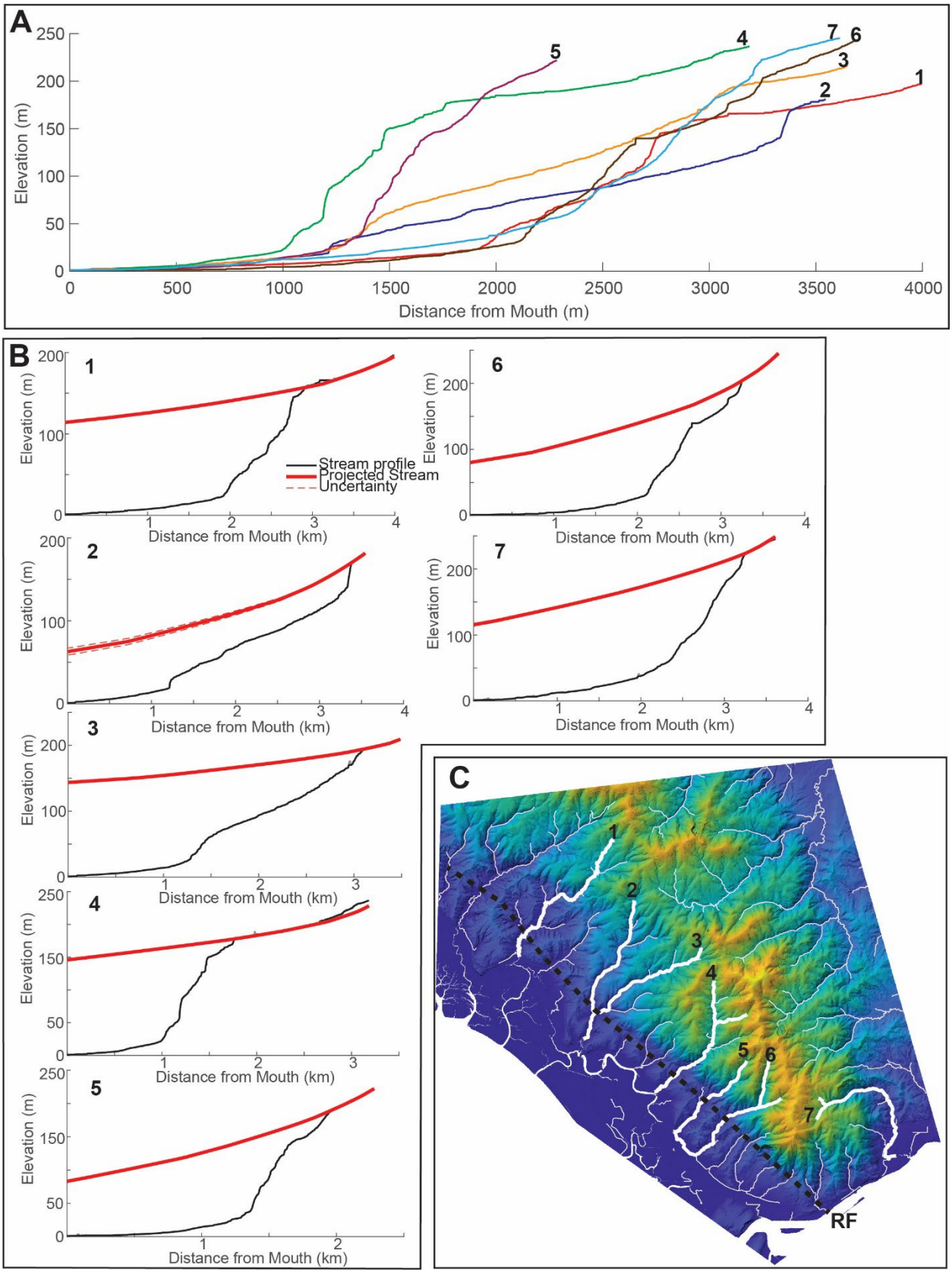
A
Elevation (m)
Distance from Mouth (m)
1
2
3
4
5
6
7
B
Stream profile
Projected Stream
Uncertainty
Elevation (m)
Distance from Mouth (km)
C
RF

Figure 3-7 (previous page). A. Longitudinal profiles of streams crossing the projected trace of the Raymond fault on the southwestern side of Raymond Hills. Numbers correspond to numbered streams in C. B. Shown in red are projected stream profiles from relict segments upstream of stream profile knickpoints. Shown in black are stream profiles as in A. C. Map showing streams on southwestern side of the Raymond Hills. RF – Raymond fault trace.

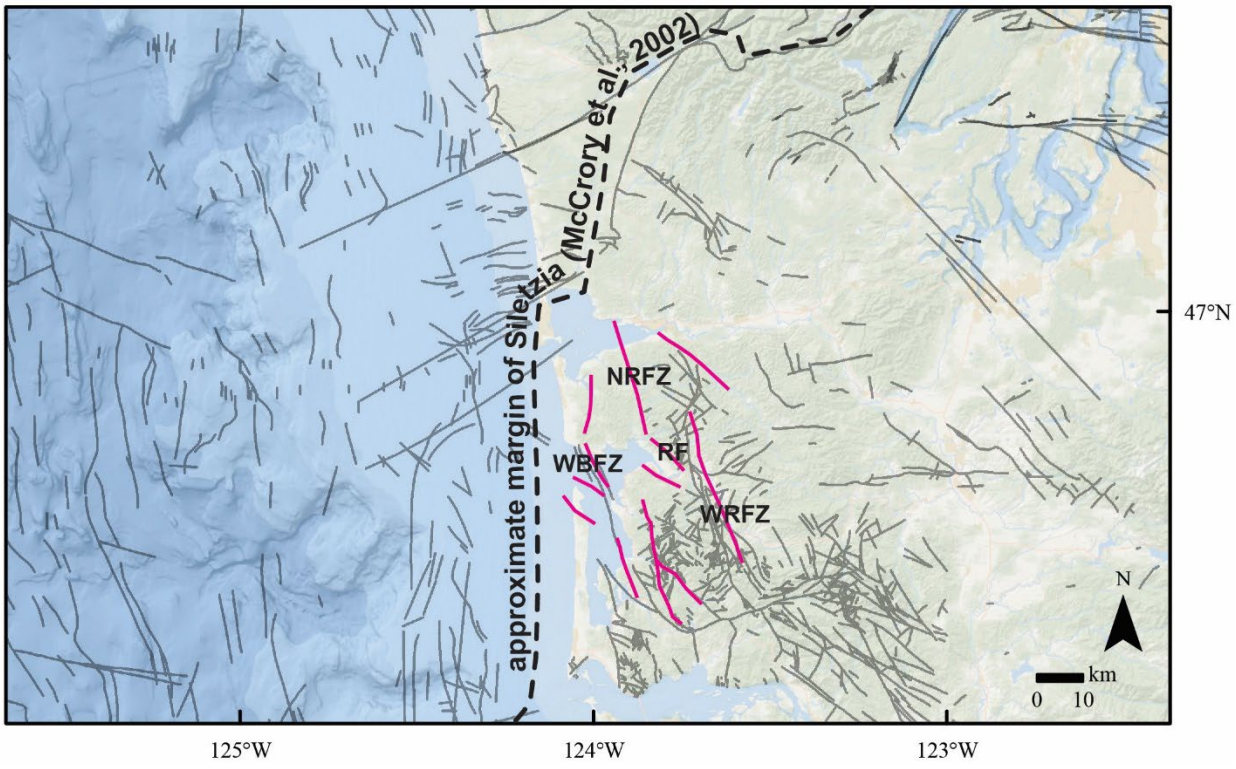


Figure 3-8. Map showing faults in field area and region. Pink lines are faults identified from geophysical modeling and maps in this study. Faint black lines are faults from 1:100k mapping or from the Quaternary fault database, as in Fig. 3-1. Thick black dashed line is approximate boundary between OCR/Siletzia and OM/accretionary complex tectonic blocks, as in Fig. 3-1, after McCrory et al. (2002). NRFZ – North River fault zone, RF – Raymond fault, WBFZ – Willapa Bay fault zone, WRFZ – Willapa River fault zone.

# Chapter 4. Tectonic geomorphic analyses of Quaternary deposits and regional bedrock, southwestern Washington

## Abstract

Permanent strain accumulation in the forearc of a subduction zone may be accommodated by crustal folds or faults. In coastal southwestern Washington, estuarine deposits record late Pleistocene uplift although no onshore faults that offset Quaternary sediments have been mapped. In this study I assess whether subsurface faults inferred from geophysical maps and models are causing surface deformation reflected in river profiles or as topographic lineaments. On the southwestern side of the Raymond Hills, where geophysical modeling indicates the east-dipping Raymond fault in the subsurface, geomorphic analyses indicate slope-break knickpoints in stream profiles as well as a topographic lineament. The stream profile knickpoints, which are at approximately similar elevations, appear to reflect a relict fluvial system once graded to a base level 85-150 m higher than current sea level. Because Quaternary sea-level highstands were not that high, the base level change likely reflects regional rock uplift, possibly accommodated by the Raymond fault. Regional analyses of channel steepness indicate a close relationship between steepened channels, bedrock faults, and lithologic contacts, an observation that supports structural and geophysical models for uplifted, fault-bounded blocks of basalt. Additionally, some stream channels that cross these structural blocks are deeply incised compared to regional topography and other channels. Together, the stream profiles, topographic lineament, and incised channels suggest uplift on the northeastern side of the Raymond fault. The likely-active Willapa Bay fault zone does not produce surficial lineaments nor measurable differences in stream profile steepness where it projects ashore nor where geophysical maps indicate a change in strike.

## Introduction

Uplifted estuarine deposits along the southwestern Washington coast near Willapa Bay and Grays Harbor (Fig. 4-1) date to marine isotope stage 5 (Kvenvolden et al., 1979, Kennedy, 1978, Kennedy et al., 1982; Stanton et al., 2023). Stanton et al. (2023) obtain an average uplift rate of ~0.4 mm/yr and suggest that uplift may be accommodated, partially or fully, by a local fault, because at other locations along the Cascadia subduction zone, coastal uplift rates greater than 0.4 mm/yr are generally associated with crustal faults or folds (e.g., Kelsey, 1990; Muhs et al., 1990; Kelsey et al., 1994, 1996; Padget et al., 2019). Stanton et al. (in preparation; Chapter 3) assess gravity and aeromagnetic data to identify linear anomalies they interpret as faults. Geophysical models of the subsurface from that study indicate two east-dipping thrust faults underlying Quaternary deposits. One of these faults aligns with the strands of the Willapa Bay fault zone (WBFZ on Fig. 4-2), mapped by offshore seismic studies, which offsets late Pleistocene and Holocene sediments in the bay (McCrory et al., 2002) and is likely responsible for the observed late Pleistocene uplift of estuarine sediments east of it (Stanton et al., in preparation; Chapter 3). Geophysical modeling indicates that the other fault, the Raymond fault (RF on Fig. 4-2), uplifts basalts in the Raymond Hills to the northeast of the fault (Stanton et al., in preparation; Chapter 3). Yet, Quaternary mapping did not identify faults (Stanton, 2021; Stanton et al., 2023; Chapter 2).

Where faults are not easily mapped at the surface (due to access limitations or vegetative cover, for example) or where subsurface faults control the tectonic activity, geomorphic analyses of digital elevation models (DEMs) can aid studies of surface deformation (e.g., Wobus et al., 2006; Jobe et al., 2024). For example, changes to stream channel steepness may indicate past changes

to base level, possibly caused by changes in rock uplift rate (e.g., Ouchi, 1985; Merritts and Vincent, 1989; Kirby and Whipple, 2001, 2012; Seybold et al., 2021). Additionally, topographic lineaments may denote a fault (e.g., Ahmadi and Pekkan, 2021; Solomon and Ghebreab, 2006; Marple and Hurd, 2020). Here, I assess the profile form of streams that traverse the Raymond fault to map knickpoints and evaluate variations in channel steepness. I also look for spatial patterns in stream channel steepness correlative with the positions of the northern trace of the Willapa Bay fault zone and near bedrock faults bounding the Raymond Hills and the Willapa Hills to evaluate deformation. In addition, I examine whether topographic lineaments co-locate with the faults.

## Geologic setting

Coastal southwestern Washington overlies the Cascadia subduction zone, where the Juan de Fuca oceanic plate subducts under the North America plate at ~4 cm/yr toward the northeast (Fig. 4-1; Heaton and Hartzell, 1987). Regional bedrock geology consists of Paleocene–Eocene basalts underlying Eocene–Miocene fluvial to marine sedimentary rocks and flood basalts (Fig. 4-2). The study area, near Willapa Bay and Grays Harbor (Fig. 1), is marked by topographic highlands consisting of blocks of Paleocene–Eocene Crescent Formation basalts (Wagner 1967a, b; Gower and Pease, 1965; Wolfe and McKee, 1968; Wells, 1981, 1989a). Younger sedimentary rocks overlie the Crescent Formation but also onlap basalt in some locations. Bedrock faults show evidence of both strike-slip and dip-slip sense of motion (Wagner 1967a, b; Wells, 1989a; Moothart, 1992), and some previous studies suggest the basalt blocks are structural highs that are bounded by long-lived faults accommodating regional transpressional strain (e.g., Wells and Coe, 1985; Stanton et al., in preparation; Chapter 3). Quaternary deposits in the study area

include late Pleistocene estuarine deposits recording ~0.4 mm/yr uplift, as well as fluvial and near shore marine deposits (Fig. 4-2; Stanton, 2021; Stanton et al., 2023; Chapter 2).

Geophysical maps and 2D geophysical models identify two, east-dipping thrust faults in the subsurface underlying the Quaternary deposits. The western-most fault co-locates with the likely-active Willapa Bay fault zone (WBFZ in Fig. 4-2; Stanton et al., in preparation; Chapter 3, McCrory et al., 2002). Although McCrory et al. (2002) presume the fault zone to project northward onshore near North Cove, Stanton et al. (in preparation) suggest the structure may change strike to the northeast near North Cove based on gravity and aeromagnetic maps. Geophysical models indicate up to 1.8 km of dip-slip offset since the Oligocene on the eastern-most fault, known as the Raymond fault (RF in Fig. 4-2), uplifting Cresent Formation basalts to the northeast of the fault (Stanton et al., in preparation; Chapter 3). There is no fault mapped at the surface. Geophysical maps and models, as well as regional geologic mapping, identify northwest- and north-striking faults bounding the eastern side of the Raymond Hills (RH in Fig. 4-2) and further to the south, the Willapa Hills (WH in Fig. 4-2; Stanton et al., in preparation; Wagner 1967a, b; Wells, 1989a; Moothart, 1992). Several studies suggest northwest trending faults in the study area have primarily strike-slip motion (e.g. Wells and Coe, 1985; Moothart, 1992) but geophysical models show that at least some of the faults have significant vertical motion (Stanton et al., in preparation; Chapter 3). There are currently no studies constraining Quaternary offset on the mapped bedrock faults and neither folds nor faults have been mapped in the Quaternary deposits near Willapa Bay.

## Methods

### Stream analyses

Fluvial systems, particularly alluvial rivers, respond to changes in factors such as base level, sediment load, and discharge (e.g., Mackin, 1948; Leopold and Maddock, 1953; Ouchi, 1985; Holbrook and Schumm, 1999; Whipple and Tucker, 2002). Topographic data from many natural fluvial systems shows a scaling relationship where channel slope is a power-law function of stream drainage area (e.g., Flint, 1974; Kirby and Whipple, 2001; Wobus et al., 2006; Harel et al., 2016):

$$S = k_s A^{-\theta} \qquad \text{Eq. 1}$$

where S is the channel slope, A is the upstream drainage area, $k_s$ is the steepness index and $\theta$ is the concavity index. Although there are many complexities to this simple model, it generally predicts that where climate, underlying lithology, and tectonic forcing are constant (i.e., steady-state conditions), the slope of a section of channel depends on the drainage area upstream. However, where climate, lithology or tectonic forcing are not constant, a stream will adjust to compensate, resulting in measurable differences to the longitudinal profile of a stream (e.g., Hack, 1973; Ouchi, 1985; Merritts and Vincent, 1989; Merritts et al., 1994; Holbrook and Schumm, 1999; Keller and Pinter, 2002). Where tectonic forcing causes a relative change in the base level of a stream, the stream will reflect the change by differences in the steepness and concavity in stream segments. These changes in channel steepness are reflected as “knickpoints” or abrupt breaks in slope of the longitudinal profile. Thus, map-view observations of steepness index coupled with longitudinal channel profiles can be used to identify possible tectonic

boundaries (e.g., Ouchi, 1985; Kirby and Whipple, 2001, 2012; Wobus et al., 2006) and may be used as a reconnaissance tool for estimating relative amounts or rates of rock uplift (Whipple et al., 2013).

Channel steepness is generally corrected for the dependence of local slope on the drainage area to give the normalized channel steepness ($k_{sn}$; e.g., Wobus et al., 2006).

$$k_{sn} = k_s A_{cent}^{(\theta_{ref} - \theta)} \quad \text{Eq. 2}$$

where $\theta_{ref}$ is a reference concavity and $A_{cent}$ is the midpoint value of drainage area for the analyzed stream segment. How $k_{sn}$ varies along a river profile may indicate changes in lithology or rock uplift rate when changes to climate are negligible (e.g., DiBiase et al., 2010; Duvall et al., 2004; Kirby and Whipple, 2001; Kirby et al., 2003; Wobus et al., 2006; Kirby and Whipple, 2012). I evaluate $k_{sn}$ on streams near Willapa Bay to determine if there is a systematic change to steepness that may be associated with known or inferred faults. I use the graphical user interface (GUI) of the open-access Topographic Analysis Kit (TAK) for TopoToolbox (Forte and Whipple, 2019) to analyze $k_{sn}$ from 10 m DEMs (U.S. Geological Survey National Map Viewer, 2019; see Appendix 4 for GUI inputs).

In tectonically active regions, knickpoints may mark the boundary between upstream "relict" stream segments adjusted to a previous base level and downstream stream segments adjusting to the current base level (e.g., Whipple et al., 2013). I used the TAK to select individual streams from 1m DEMs (Washington State Department of Natural Resources Lidar Portal, 2019) near the Raymond fault for longitudinal profile analysis. I project the stream segment upstream of prominent knickpoints along the entire length of the stream to approximate the steady-state

longitudinal stream profile recorded by the "relict" upstream segment. Differences in projected base elevation between stream segments adjusted to former base levels are a first order estimate of the base level change. The base level change may be considered loosely equivalent to uplift if climate and lithology have remained approximately constant (e.g., Clark et al., 2006; Wobus et al., 2006; Whipple et al., 2013; Racano et al., 2021).

Additionally, fluvial systems that have incised into a low-relief landscape may reflect a response to regional uplift, with the incision depth potentially reflecting the amount of long-term vertical deformation (Clark et al., 2006). Several streams in the northern Raymond Hills appear deeply incised where they flow through the Crescent Formation. basalts. I used standard topographic profile tools in ArcGIS 10.5.1 on the 1 m DEM to assess elevation changes perpendicular to the stream channels compared to surrounding topography, which has relatively low relief.

**Lineaments**

Identification of surficial or topographic lineaments may be used to delineate tectonic and geologic features (e.g., Ahmadi and Pekkan, 2021; Solomon and Ghebreab, 2006; Marple and Hurd, 2020). Lineaments are mappable linear features on Earth's surface that have a form different than adjacent features and that presumably reflect a subsurface phenomenon (O'Leary et al., 1976). A lineament that is not anthropogenic may reflect a difference in adjacent lithology or deformation related to faulting, folding, fracturing, or jointing.

I identified geomorphic lineaments visually, using 1 m DEMs as well as with red-scale and grey-scale hillshades produced from those DEMs using standard tools on ArcMap 10.5.1. Additionally, I used standard edge detection 3X3-cell filters, changing aspect views in 45-degree

increments on the 1 m DEM from which I visually identify lineaments (labeled as north, east, south, and west filters). I searched for lineaments at locations near the Raymond fault (RF in Fig. 4-2) and north of Willapa Bay at North Cove (NC in Fig. 4-2).

## Results

### Stream channel steepness

The map of $k_{sn}$ on streams from the 10 m DEM (Fig. 4-3) shows a distinct pattern of steeper channels corresponding to outcrops of the Crescent Formation basalts (Fig. 4-2). In particular, both the western and eastern sides of the Raymond Hills (RH in Figs. 4-2 & 4-3) and the eastern side of the Willapa Hills (WH in Figs. 4-2 & 4-3) have steeper channels relative to the stream channel segments within the sedimentary rocks or Quaternary deposits.

Longitudinal stream profiles (Fig. 4-4a) on the western side of the Raymond Hills near the Raymond fault (Fig. 4-4c) indicate less steep stream segments in the higher elevations and within the flat topography at the base of the slopes, but with steeper central stream segments. Profiles show distinct breaks in slope or knickpoints, where upstream channel concavity is distinctly different from downstream channel concavity and/or where there is a step in the elevation in the channel profile. While some of the profiles have multiple knickpoints, all streams have an upper knickpoint at elevations between ~150-200 m above sea level (a.s.l.). Stream segments upstream of the upper knickpoint project to a base level ~85-150 m higher than the current base level (Fig. 4-4b).

Streams on the eastern side of the Raymond Hills (Fig 4-5b) do not show as sharp along-profile contrast in channel steepness (Fig 4-5a.) although two (Fig. 4-5ai. and 4-5aii.) show a knickpoint

or knickzone at around 175-200m a.s.l. The third channel (Fig. 4-5aiii.) shows a profile convexity, possibly a broad knickzone. Knickzones, locally high-gradient reaches, may also indicate perturbations affecting the channel (e.g., Foster and Kelsey, 2012; Raming and Whipple, 2022). The profiles are for streams that are tributaries to other, larger streams and the profiles do not show the full distance to where they enter Willapa Bay. I do not project the segments upstream of the knickpoints because the profiles do not show the full distance to the current base level (i.e., Willapa Bay).

Although the $k_{sn}$ map from the 10 m DEM (Fig. 4-3) suggests abrupt changes in channel steepness for streams on the eastern side of the Willapa Hills (Fig. 4-6b), the longitudinal profiles do not show distinct knickpoints (Fig. 4-6a). The upstream portions are generally steeper than downstream, typical for streams near steady-state conditions.

Geophysical models and offshore mapping suggest the Willapa Bay fault zone may extend onshore near North Cove in northern Willapa Bay (McCrory et al., 2002; Stanton et al., in preparation; Chapter 3). The $k_{sn}$ map from the 10 m DEM (Fig. 4-3) does not indicate abrupt changes in steepness on streams near North Cove (NC on Fig. 4-3). The more detailed $k_{sn}$ map from the 1 m DEM indicates streams with steeper upstream segments relative to downstream segments (Fig. 4-7; color bar not directly comparable with Fig. 4-3). The map shows an east-west trending drainage divide through the central part of the map. Additionally, near North Cove, many of the streams flow east from a north-south trending drainage divide that runs approximately parallel to a former sea-cliff from North Cove to Grays Harbor (marked by white arrows).

In the northern Raymond Hills are several incised streams (Fig. 4-8). Topographic profiles perpendicular to these indicate the stream channel is between ~140-180 m below the surrounding topography. The northern stream channel (Fig. 4-8a-c) is at or near sea level for up to 20 km from the mouth, while the tributary to this main channel (Fig. 4-8d) has a channel base at only 20 m a.s.l., even up to 10 km upstream of the confluence. The elevation of the southern stream channel (Fig. 4-8e-g) changes only ~20 m between the upper reaches and lower reaches. Upstream of profiles Fig. 4-8d and Fig 4-8e, the relief between the stream channels and the surrounding topography decreases.

### Lineaments

Visible topographic lineaments from all directional filters trend mostly to the northwest, with some lineaments trending to the northeast that are most visible from east (pink lines in Fig. 4-9a) and west (orange lines in Fig. 4-9a) directional filters. The most prominent lineament from all directional filters is along the southwestern side of the Raymond Hills (Fig. 4-9). Topographically, this lineament features a break in slope and cuts across topographic contours (Fig. 4-9b). There are numerous smaller lineaments east of the Raymond Hills (Fig. 4-9a). These do not align with mapped faults and are located primarily within sedimentary bedrock. At North Cove, there is a prominent, linear cliff striking northward but no additional lineaments.

## Discussion

Stream response to tectonic forcing is reflected in map view changes in channel steepness and longitudinal profile view changes of channel steepness and concavity. Topographic lineaments may also indicate subsurface or near surface faults. Profiles from streams that cross the Raymond

fault show distinct knickpoints between ~150-200 m a.s.l. The stream segments upstream of this knickpoint may be “relict” and when projected along the stream profile, have a base ~85-150 m higher than current base level (i.e. sea-level; Fig 4-4b). This suggests that since these stream segments were in steady-state, the base level has dropped ~85-150 m. At no time during the past several million years has sea-level been more than ~30 meters higher than modern (Miller et al., 2005), so the stream segments were not adjusted to a higher sea-level. Potentially, the change in base level could result from ~85-150 m of rock uplift. Likewise, several streams in the northern Raymond Hills incise the Crescent Formation basalts to relief of~140-180 m (Fig. 4-8). This incision might represent a transient landscape response to uplift (e.g., Clark et al, 2006). The Raymond fault on the southwestern side of the Raymond Hills could be driving the uplift reflected both in the stream profiles and in the incised streams.

In addition to the geomorphic response of streams near the Raymond fault, a prominent topographic lineament occurs along the southwestern side of the Raymond Hills (Fig. 4-9) near the projected trace of the subsurface Raymond fault. The lineament along the southwestern side changes elevation between ~6-36 m a.s.l. along the topographic front (Fig. 4-9) and thus, is not the back edge of a wave cut surface, which would have a consistent elevation representing the former sea-level (e.g., Lajoie, 1986). This lineament and the projected trace of the fault are near the contact between Eocene Crescent Formation basalts and early-to-mid Quaternary marine/near-shore deposits (Fig. 4-2; Stanton et al., 2023; Chapter 2; Appendix 2). It is possible this contact is a fault, although limited access has prevented detailed mapping along the contact.

At a reconnaissance level, the geomorphic character of streams along the western Raymond Hills suggests a landscape response to regional rock uplift, and a lineament on the southwestern

Raymond Hills co-locates with the Raymond fault. Geologic and structural models for the region suggest that topographically high blocks of Crescent Formation basalt, such as the Raymond Hills and the Willapa Hills, are fault-bounded and have been uplifted and rotated (Wells and Coe, 1985). Additionally, geologic relationships between the basalt and nearby sedimentary rocks indicate the late Eocene to Miocene sedimentary rocks were not deposited over the basalt blocks but onlap onto the blocks or are tilted at the contacts (e.g., Wagner, 1967a, b; Wells 1981, 1989a; Moothart, 1992). Therefore, the blocks of Crescent Formation are tectonic features, including the Ramond Hills. Geophysical modeling near the Raymond Hills suggesting the Raymond fault has uplifted the Crescent Formation approximately 1.8 km since the late Eocene (Steely et al., 2021; Stanton et al., in preparation; Chapter 3). The stream profiles, incised streams, and lineament appear to reflect uplift on the northeast side of the Raymond fault, supporting findings from geophysical models and the structural model. The geomorphic signature of uplift reflected in the streams and lineament do not more tightly constrain timing of uplift, beyond a very generalized interpretation that knickpoints on stream profiles are likely reflecting a base level change more recent than the Eocene. Further mapping of the contact between the Crescent Formation basalt and the Quaternary deposits would facilitate a better understanding of timing, as larger streams may have strath terraces that could offer an avenue for dating.

Other locations near Willapa Bay do not have prominent geomorphic signatures of subsurface faults. At North Cove and north toward Grays Harbor, streams mostly flow eastward, away from the prominent, north-trending cliff. This cliff is near the projected trace of the Willapa Bay fault zone from McCrory et al. (2002) but the channel segments do not change steepness in a regular pattern (Fig. 4-7). It is possible the drainage divide (marked by white arrows) is controlled by

uplift that also creates the cliff, but the cliff could also be a former sea cliff carved by waves or tide and unrelated to faulting. Recent mapping suggests the sediments in the cliff to be sands and gravels, with large amplitude cross-bedding (up to 1 m; Stanton, 2021; Stanton et al., 2023; Chapter 2; Appendices 1 and 2) and therefore possibly related to tidal currents. Thus, while the Willapa Bay fault zone offsets offshore sediments (McCrory et al., 2002) and likely uplifts estuarine sediments in northern Willapa Bay (Stanton et al., in preparation; Chapter 3), the pattern of streams along the projected trace of the fault zone near North Cove do not definitively indicate divide migration or changes in channel steepness related to uplift. Neither are there topographic lineaments along these traces.

Likewise, geologic mapping shows faults on the eastern side of the Raymond Hills and the Willapa Hills, but these locations do not have geomorphic characteristics that definitively support vertical motion. On the eastern side of the Raymond Hills (Fig. 4-5), some stream profiles show a faint break in slope at around 175-200 m a.s.l. The location and elevations of the slope breaks do not correspond to lithologic contacts from geologic mapping. The channels are not smooth, are concave up and show a range of knickpoints and knickzones. These channels indicate fluvial disruption of some form and could relate to adjacent fault activity, small scale lithologic variability or landslides. It is also possible the breaks in slope reflect the regional uplift recorded by streams from the western side of the Raymond Hills and inferred from structural and geophysical models. The lineaments east of the Raymond Hills are located in sedimentary bedrock and are not lengthy or thorough going. These short lineaments are likely bedding planes and generally align with measurements of bedding strike from regional mapping (e.g., Washington State Dept. of Natural Resources Geologic Information Portal, 2023; Wagner, 1967 a, b). Stream channels in the Willapa Hills (Fig. 4-6) do not show distinct knickpoints in profile,

but at the scale of a 10 m DEM (Fig. 4-3) the change in channel steepness roughly aligns with the lithologic contact between Cresent Formation basalts and sedimentary rocks. It is possible the faults mapped in these locations are primarily strike-slip structures, as suggested by some studies (e.g., Wells and Coe, 1985; Moothart, 1992). Geophysical models on the eastern side of the Raymond Hills suggest the mapped, block-bounding fault there does not have vertical offset although faults further east accommodate up to 0.8 km of dip-slip offset on the Crescent Formation at depth (Stanton et al., in preparation; Chapter 3).

## Conclusion

Previous studies indicate subsurface faults near Willapa Bay that may be responsible for uplift recorded in late Pleistocene estuarine deposits (McCrory et al., 2002; Stanton et al., 2023; Stanton et al., in preparation; Chapters 2 and 3). Geophysical models suggest dip-slip offset of up to 1.8 km since the Oligocene on the Raymond fault, on the southwestern Raymond Hills (Steely et al., 2021; Stanton et al., in preparation; Chapter 3). This study shows that the geomorphic character of streams near the Raymond fault suggests a landscape response to regional rock uplift. Longitudinal profiles of streams that cross the projected trace of the Raymond fault show knickpoints. The knickpoints are at approximately similar elevations and may reflect a relict fluvial system once graded to a base level 85-150 m higher than current sea level. Since Quaternary sea-level high stands were not that high, the base level change likely reflects regional rock uplift accommodated by the Raymond fault. Streams in the northern Raymond Hills show incision of ~140-180 m and a lineament on the southwestern Raymond Hills co-locates with the projected trace of the Raymond fault. The stream profiles, incised streams, and lineament appear to reflect uplift on the northeast side of the Raymond fault, supporting findings from geophysical

models and the regional structural model of uplifted basalt blocks. Although geomorphic indicators are present for the Raymond fault, the Willapa Bay fault zone, which is likely active (McCrory et al., 2002) and responsible for uplifted estuarine deposits (Stanton et a., 2023; Stanton et al., in preparation; Chapters 2 and 3), does not produce surficial lineaments nor measurable differences in stream profile steepness where it projects ashore nor where geophysical maps indicate a possible change in strike.

**Figures**

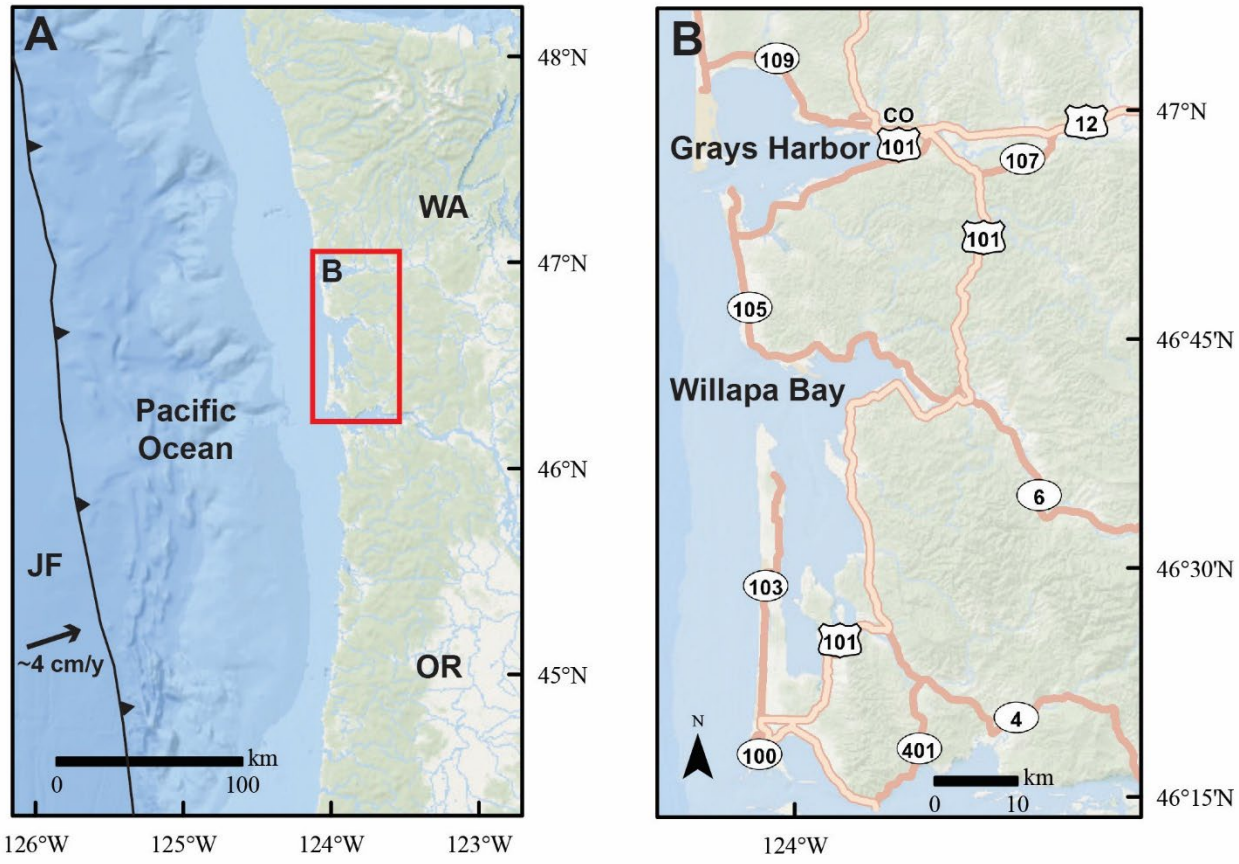


Figure 4-1. Map showing the location of field area with respect to the Cascadia subduction zone. A. The Juan de Fuca plate subducts under North America at ~4cm/yr toward the northeast (Heaton and Hartzell, 1987). B. The study area is south of Grays Harbor and around Willapa Bay. Circled numbers are state highways. JF – Juan de Fuca plate, NA – North America plate, OR- Oregon, WA-Washington. Service layer credits: Esri, Garmin, GEBCO, NOAA, NGDC, and other contributors.

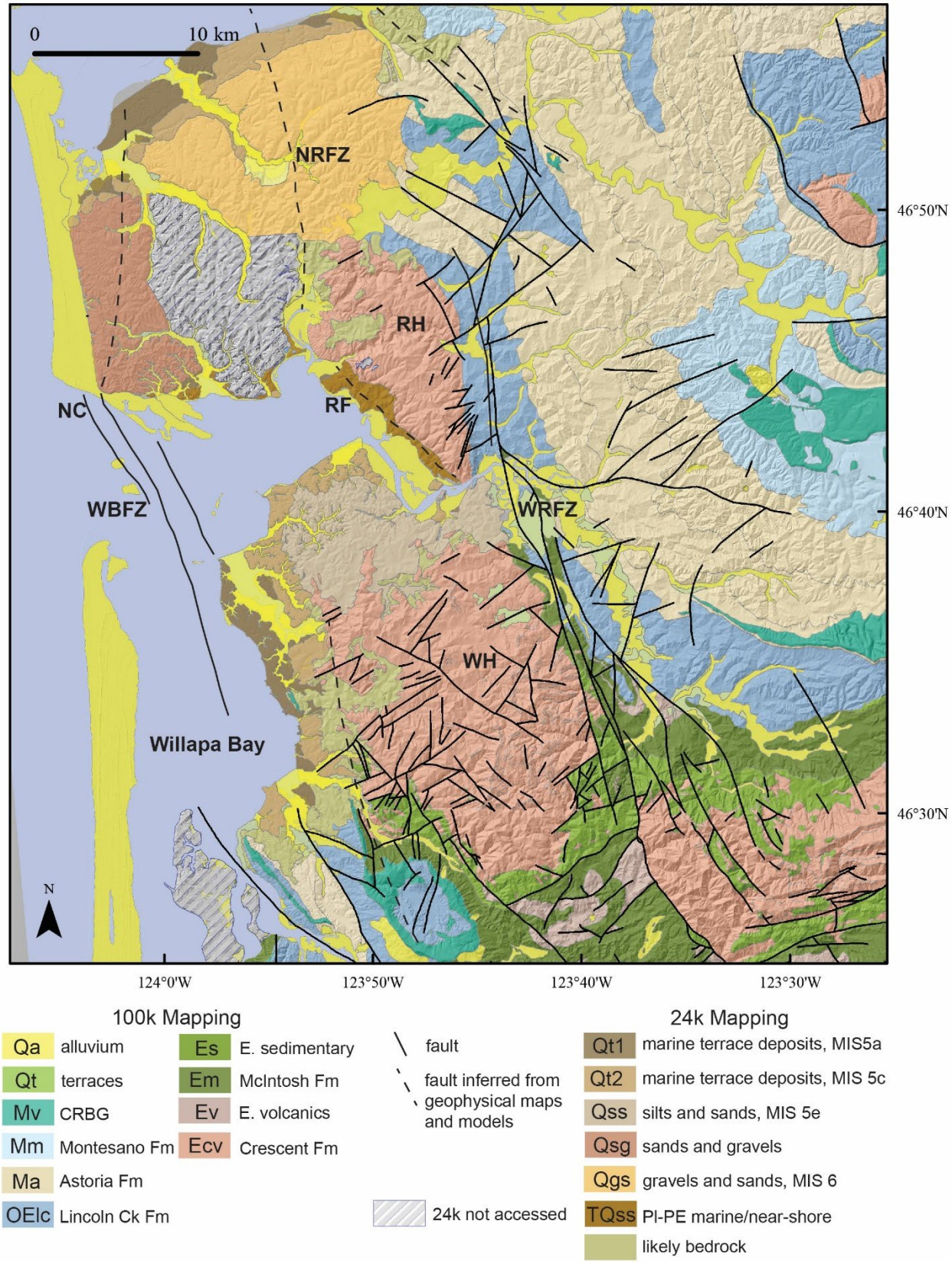
0
10 km
NRFZ
RH
RF
NC
WBFZ
WRFZ
WH
Willapa Bay
N
46°50'N
46°40'N
46°30'N
124°0'W
123°50'W
123°40'W
123°30'W
100k Mapping
Qa alluvium
Qt terraces
Mv CRBG
Mm Montesano Fm
Ma Astoria Fm
OElc Lincoln Ck Fm
Es E. sedimentary
Em McIntosh Fm
Ev E. volcanics
Ecv Crescent Fm
fault
fault inferred from geophysical maps and models
24k not accessed
24k Mapping
Qt1 marine terrace deposits, MIS5a
Qt2 marine terrace deposits, MIS 5c
Qss silts and sands, MIS 5e
Qsg sands and gravels
Qgs gravels and sands, MIS 6
TQss Pl-PE marine/near-shore
likely bedrock

Figure 4-2 (previous page). Geologic map of the study region with mapping from 1:100,000 scale mapping (Washington State Dept. of Natural Resources Geologic Information Portal, 2023) and from 1:24,000 scale mapping (Stanton, 2021; Stanton et al., 2023; Chapter 2). North River fault zone (NRFZ), Raymond fault (RF) locations from Steely et al. (2021) and Stanton et al (in preparation; Chapter 3). Willapa Bay fault zone (WBFZ) location from McCrory et al. (2002) and Stanton et al. (in preparation). Dashed lines are faults inferred from geophysical maps and models (Stanton et al., in preparation; Chapter 3). Other abbreviations are as follows: NC – North Cove, NRFZ – North River fault zone, RF – Raymond fault, RH – Raymond Hills, WH – Willapa Hills, WRFZ – Willapa River fault zone.

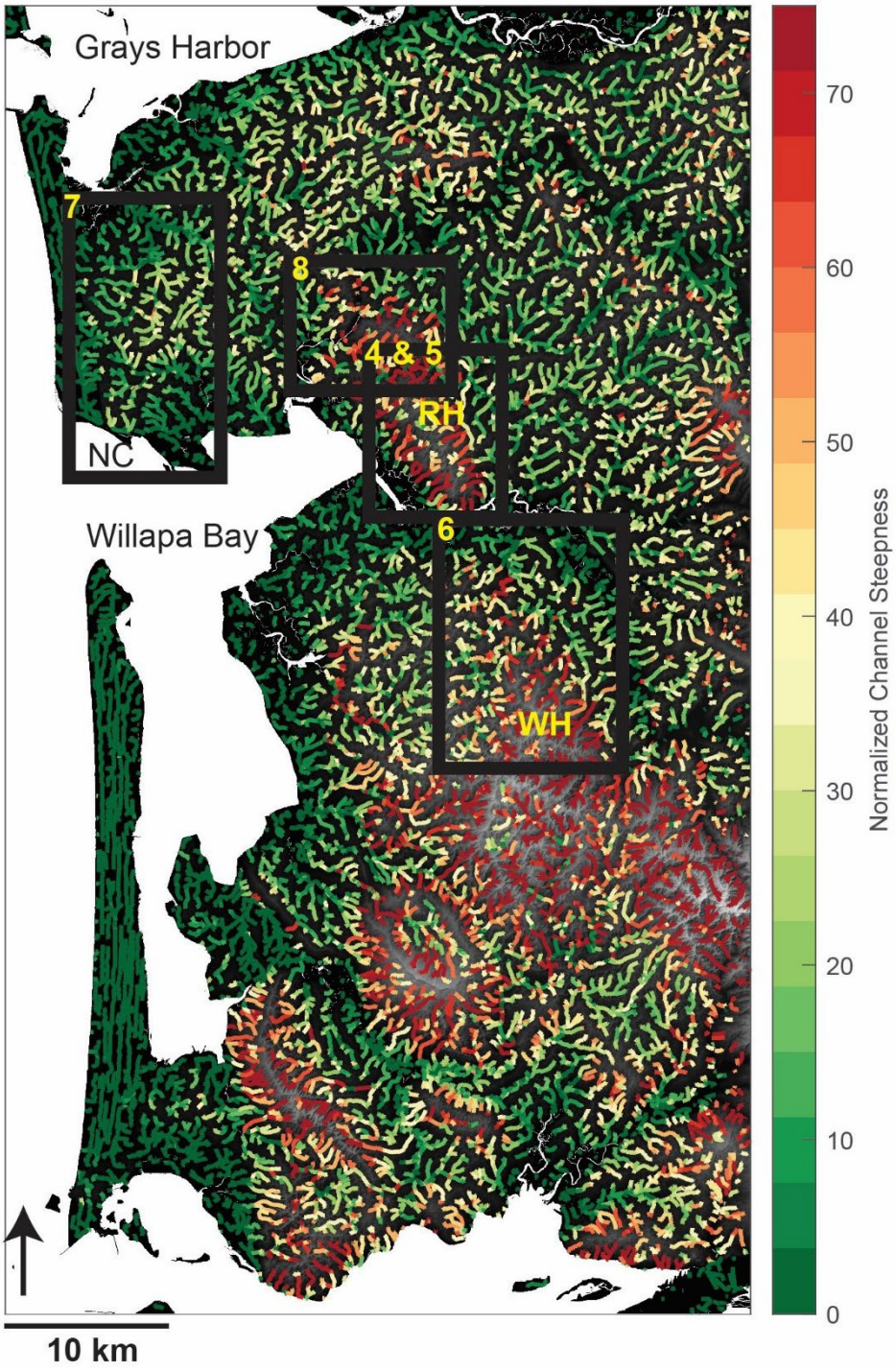


Figure 4-3. Map showing normalized channel steepness, $k_{sn}$, on the 10m DEM for the study region. Warmer colors indicate steeper stream segments. Color bar is not directly comparable

with other figures. Black boxes show locations of more detailed analyses of normalized channel steepness using the 1 DEM. Abbreviations as in Figure 2.

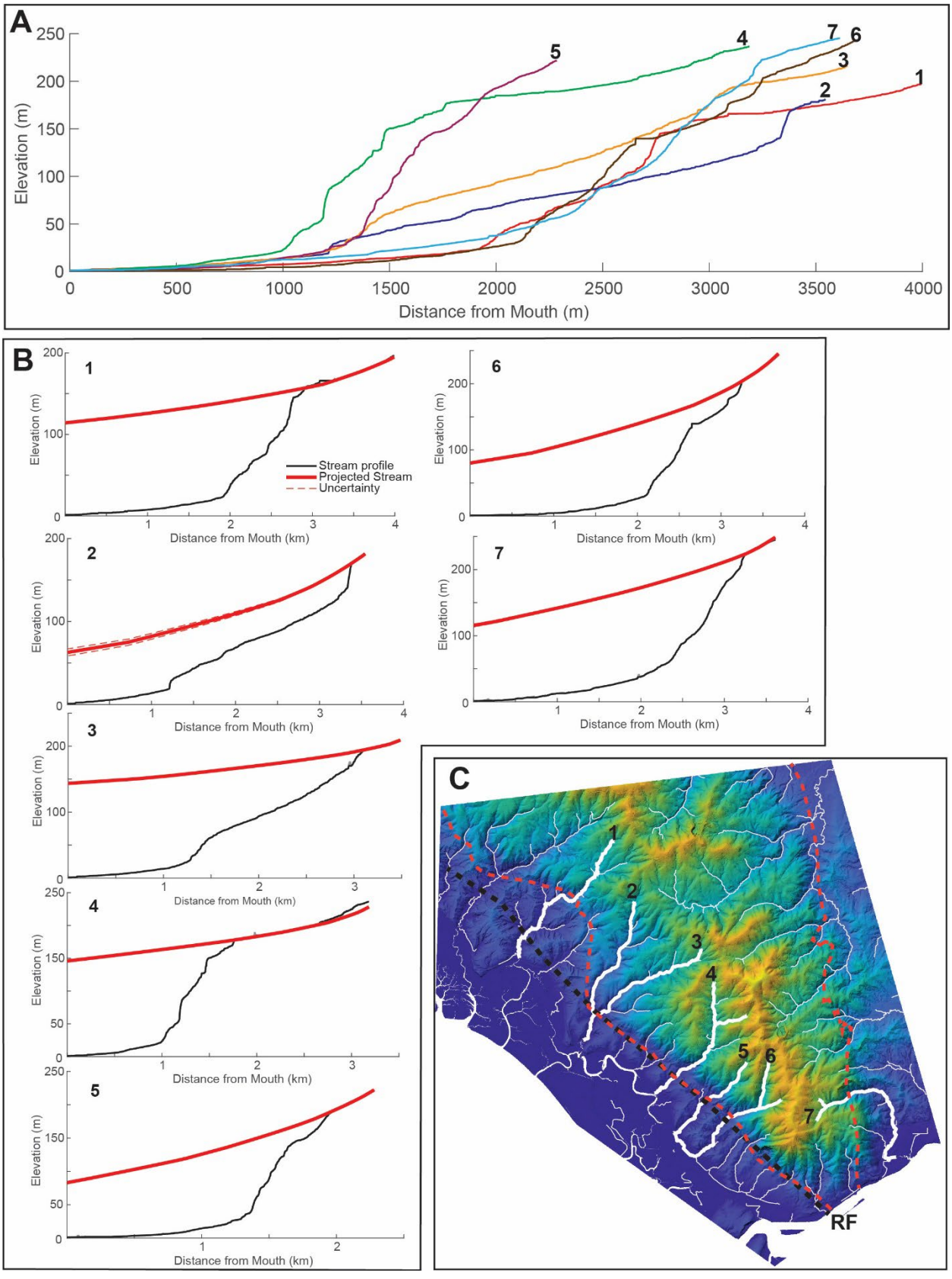
A
Elevation (m)
Distance from Mouth (m)
1
2
3
4
5
6
7
B
Stream profile
Projected Stream
Uncertainty
Elevation (m)
Distance from Mouth (km)
C
RF

Figure 4-4 (previous page). A. Longitudinal profiles for streams on the southwestern side of the Raymond Hills that cross the projected trace of the Raymond fault. Numbers correspond to profiles in panel B and streams in panel C. B. Longitudinal profiles for streams in A with segments upstream of the highest elevation knickpoint projected along the entire profile. C. Location of streams on 1m DEM. Black dashed line is projected trace of the Raymond fault (RF). Red dashed lines are the contacts for Crescent Formation basalts from Fig. 2.

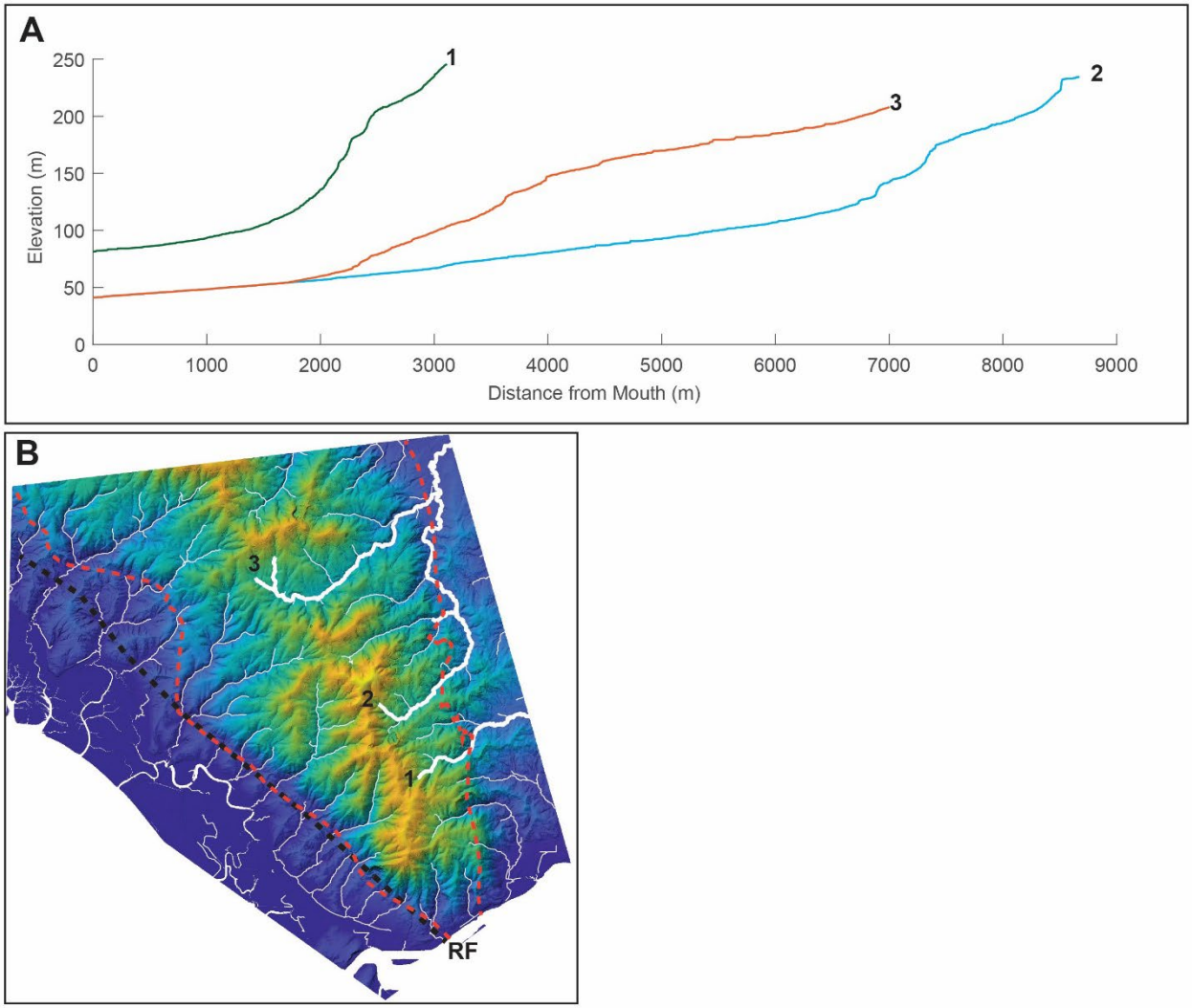


Figure 4-5. Longitudinal profiles for streams on the northeastern side of the Raymond Hills. Numbers correspond to streams in panel B. B. Location of streams on 1m DEM. Black dashed line is projected trace of the Raymond fault (RF). Red dashed lines are the approximate contacts for Crescent Formation basalts from Fig. 4-2.

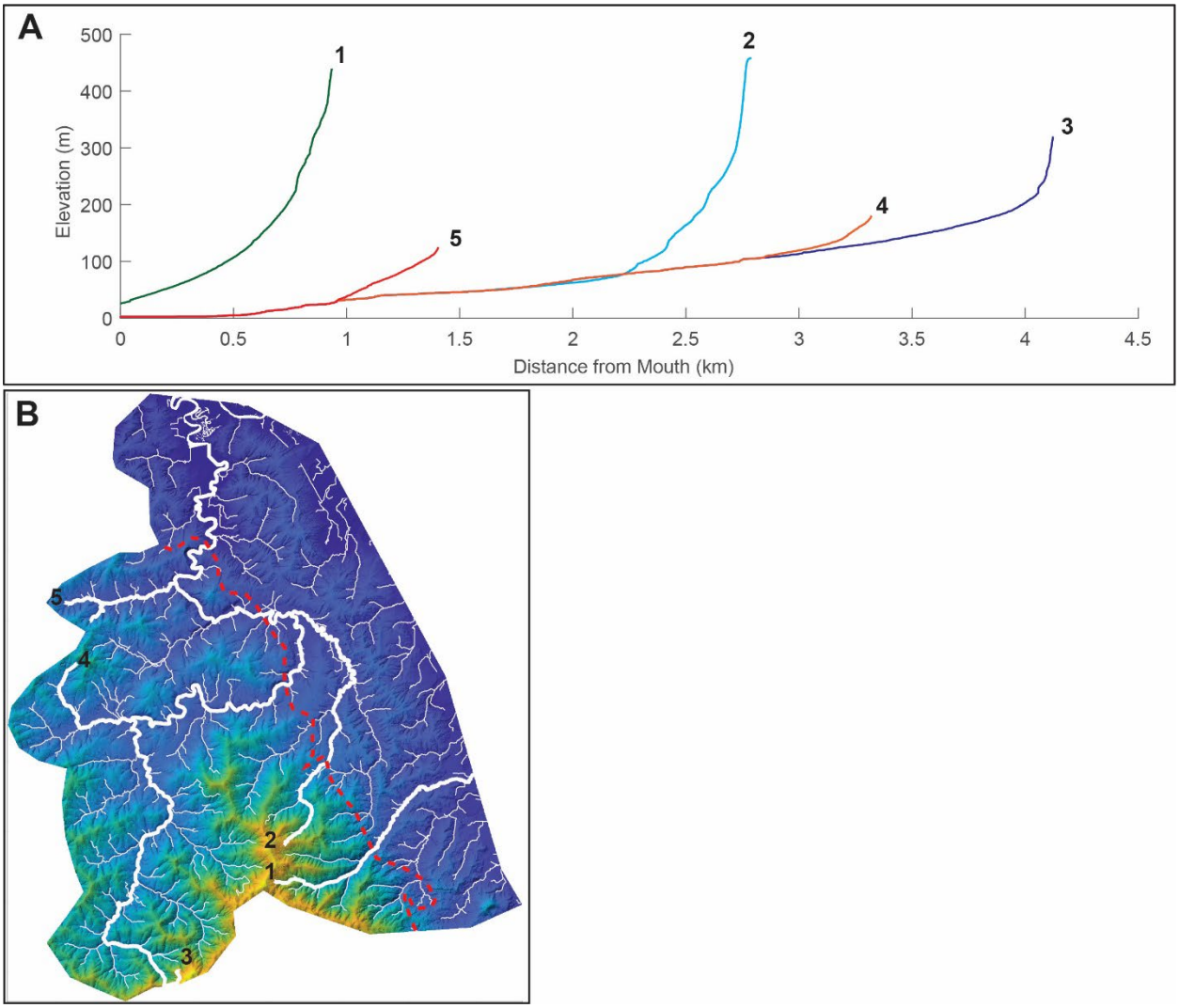


Figure 4-6. A. Longitudinal profiles for streams on the eastern side of the Willapa Hills. Numbers correspond to streams in panel B. B. Location of streams on 1m DEM. Red dashed line is the approximate contact for Crescent Formation basalts from Fig. 4-2.

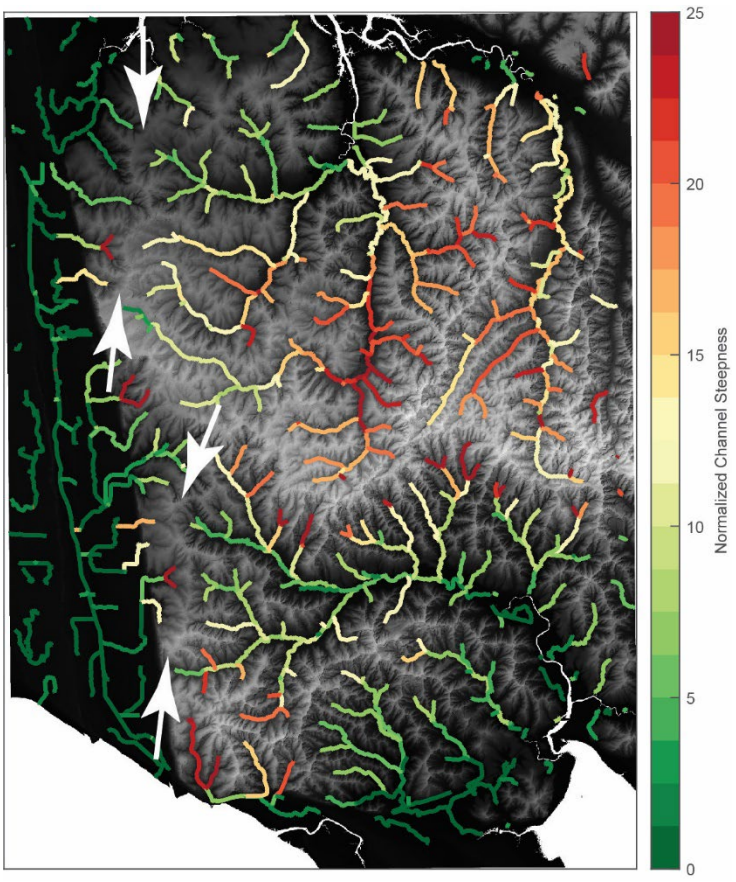


Figure 4-7. Map showing normalized channel steepness, ksn, on the 1 m DEM for North Cove. Warmer colors indicated steeper stream segments. Color bar is not directly comparable to Fig. 4-3. White arrows indicate divide discussed in text.

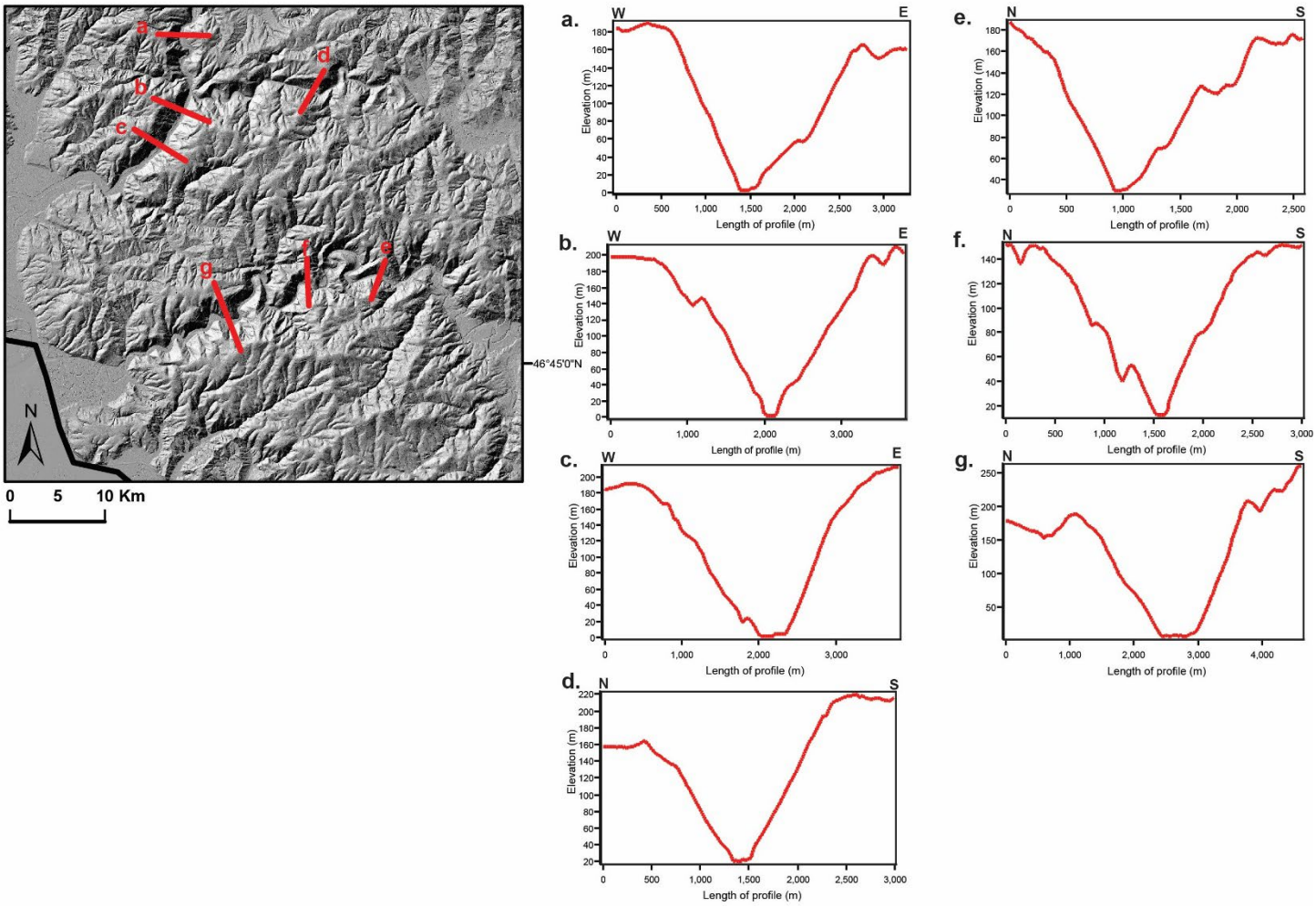


Figure 4-8. Map of hillshade from 1m DEM of two incised streams north of the Raymond Hills along with topographic profiles perpendicular to the channel to show relief between channel and surrounding highlands. Letters correspond to the topographic profiles. Dark black line is approximate shoreline of Willapa Bay.

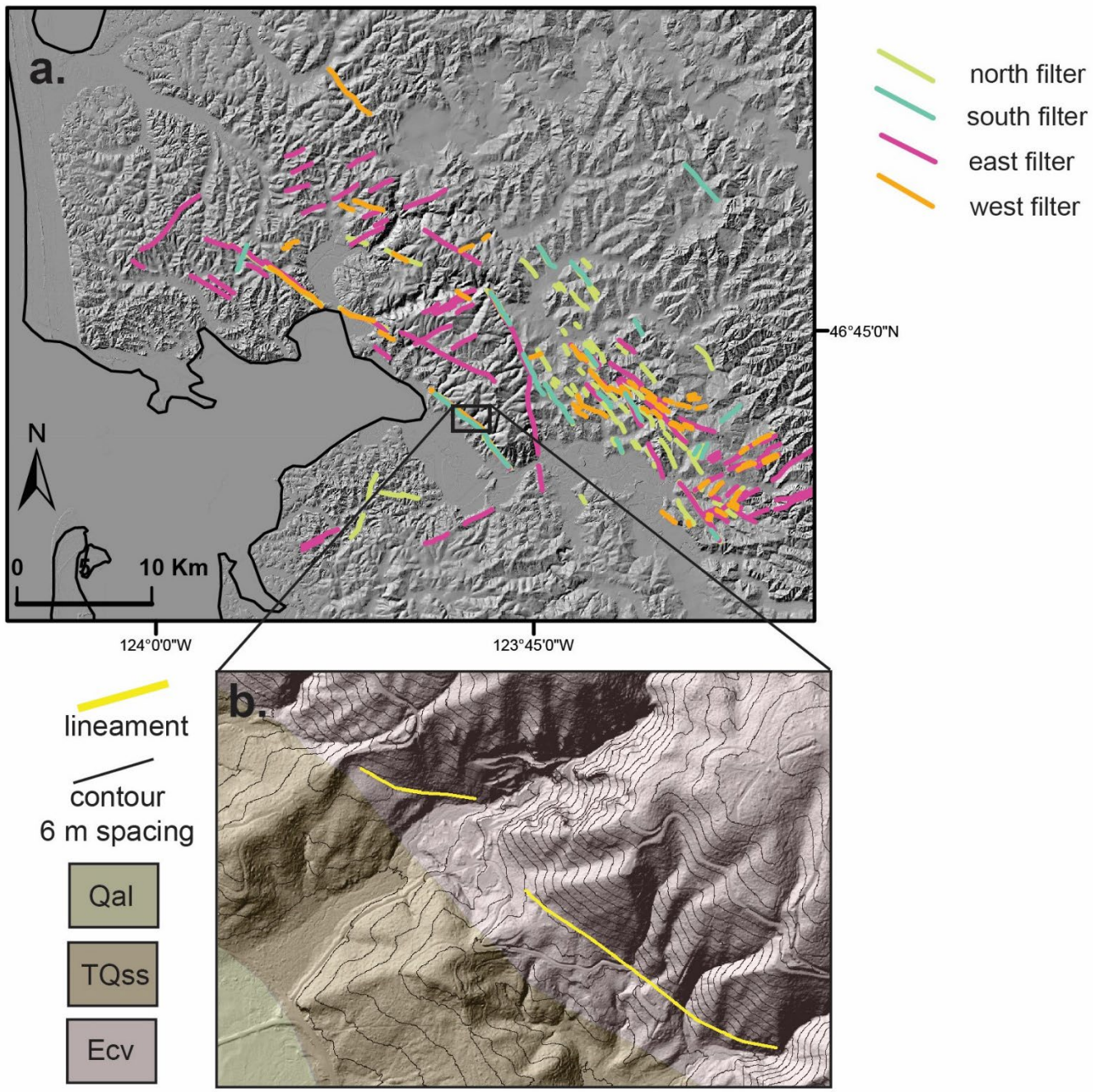


Figure 4-9. A. Map of hillshade from 1m DEM showing the region around northern Willapa Bay. Colored lines are lineaments mapped visually on hillshades produced with standard edge detection 3X3-cell filters with aspect views in 45-degree increments (labeled as north, east, south, and west filters). B. Geologic units overlying a hillshade of the 1m DEM with 6m

contours in green and mapped lineament (yellow) along the western side of the Raymond Hills. The lineament is not at a common elevation but crosses contour lines.

# Chapter 5. Summary

The Holocene geologic record from Washington and Oregon indicates coastal subsidence associated with Cascadia megathrust earthquakes (e.g., Atwater, 1987, 1992; Atwater and Yamaguchi, 1991; Witter et al., 2003); yet, long-term coastal uplift is observed in northern Washington, Oregon, and northern California in the form of uplifted marine sediments and coastal topography (e.g., Palmer, 1967; Kelsey, 1990; Kelsey et al., 1994; Kelsey et al., 1996, Thackray, 1996, 1998; Padgett et al, 2019). Questions regarding the extent, rate, and mechanism of uplift recorded by Pleistocene sedimentary deposits in coastal southwestern Washington guided my research. I approached this inquiry through more specific questions, each one addressed as a chapter in this dissertation.

1) What are the lithologies, ages, and uplift rates of Quaternary deposits near Grays Harbor and Willapa?
2) Can I estimate the existence and rates of active structures under Willapa Bay and the coastal Quaternary deposits using geophysical data and related modeling?
3) Do fluvial systems in coastal southwestern Washington record geomorphic evidence of regional deformation?

The work presented here addresses long-term uplift along the southwestern Washington coast and situates the observed uplift in the context of regional structural models and fault styles. It includes geologic and geochronological constraints on the amount and timing of uplift at Willapa Bay, as well as uses gravity and magnetic data to model subsurface faults, and geomorphic analyses of regional streams and topography to assess potential deformation.

New geologic mapping at ~1:24,000 scale identifies nine new Quaternary units (Stanton, 2021; Stanton et al., 2023; Chapter 2; Appendix 1) in what was previously mapped as a single marine terrace unit (e.g. Wagner 1967 a, b). These deposits range from fluvial sands and gravels, to tidal deposits, and include three estuarine units at up to 140 m a.s.l. The two lower estuarine units are terraced. New luminescence dating, relative age based on soil maturity and terrace elevation, and an evaluation of previous ages from fossil shells collectively constrain the probable ages of three estuarine units to sea-level high stands during marine isotope stages 5a, 5c, and 5e. The terraced estuarine units record an average uplift rate of ~0.4 mm/yr (Stanton et al., 2023; Chapter 2), consistent with other Pleistocene uplift and incision rates in Cascadia (Thackray, 1998; Pazzaglia and Brandon, 2001; Pazzaglia et al., 2003; Delano et al., 2017; Personius, 1995; Kelsey, 1990; Muhs et al., 1990, 1992; McInelly and Kelsey, 1990; Ticknor, 1993; Kelsey et al., 1994; Kelsey and Bockheim, 1994; Kelsey et al., 1996; Polenz and Kelsey, 1999; Padgett et al., 2019). When compared to observed interseismic vertical deformation, the coastal southwestern Washington rates suggest that about one-tenth of interseismic strain may become permanent. The values are permissible within the uncertainties of uplift based on regional estimates of interseismic vertical strain rates and of coseismic subsidence (Stanton et al., 2023; Chapter 2).

At other coastal sites in Cascadia with uplift rates of ~0.5 mm/yr and more, local folds or faults contribute to the vertical motion (e.g. Kelsey, 1990; Muhs et al., 1990, 1992; McInelly and Kelsey, 1990; Ticknor, 1993; Kelsey et al., 1994; Kelsey and Bockheim, 1994; Kelsey et al., 1996; Polenz and Kelsey, 1999; Padgett et al., 2019). The uplift rates recorded in the estuarine terraced units in coastal southwestern Washington near that rate, prompting an investigation for identifiable forearc structures at Willapa Bay and Grays Harbor. Map-view interpretation of gravity and aeromagnetic data indicate N- and NW-trending faults (Stanton et al., in preparation;

Chapter 3). Two-dimensional forward modeling using gravity and aeromagnetic observations suggests two 20-25° east-dipping reverse faults near Willapa Bay. One modeled fault aligns with the active Willapa Bay fault zone identified previously from offshore seismic-reflection studies (McCrory et al., 2002). The uplift recorded in the estuarine deposits is likely accommodated by the Willapa Bay fault (Stanton et al., in preparation; Chapter 3). The other modeled fault aligns with the Raymond fault, inferred from previous geophysical studies (Steely et al., 2021). The Raymond fault uplifts Crescent Formation basalts exposed east and northeast of the fault in the Raymond Hills. Longitudinal profiles of streams near the Raymond fault show knickpoints, with stream segments upstream of the knickpoints reflecting relict streams graded to a base level ~85-150 m higher than current sea level. Because Quaternary sea-level fluctuation cannot accommodate this amount of base level fall, the base level change likely reflects regional rock uplift, possibly accommodated by the Raymond fault (Stanton et al., in preparation; Chapters 3 and 4).

The geophysical models also suggest that faults previously mapped with small lateral offsets in Eocene-Miocene rocks east of Willapa Bay may have a vertical component (Stanton et al., in preparation; Chapter 3). Within the framework of previous structural models that propose thrust faulting (e.g. Snavely and Wagner, 1982) or strike-slip faulting (e.g. Wells and Coe, 1985; Brocher et al., 2017) as the primary fault style, the faults in and near Willapa Bay appear to be oblique (Stanton et al., in preparation; Chapter 3). They may represent a change in deformational domain, between primarily east-directed strain offshore (e.g., Goldfinger et al., 1992) and primarily north-directed strain in western Washington (e.g., Steeley et al., 2021), thus accommodating both subduction-related strain and strain related to moving tectonic blocks that comprise western North America (Stanton et al., in preparation; Chapter 3). Further work to

constrain faulting kinematics and timing in coastal southwestern Washington will elucidate our understanding of this structural system, as well as provide key constraints for hazard and risk assessment. Likewise, continued work to determine the causes of long-term permanent strain at other locations along Cascadia is poised to advance our ability to evaluate the strain budget and assess coastal earthquake hazard.

# Works Cited

Addicott, W.O., 1966, Marine paleoecology and zoogeography in central California, U.S. Geological Survey, Professional Paper 523-C, pp. 21, 4 plates.

Addicott, W.O., 1974, Recognition and distribution of *Mytilus condoni* Dall, a unique Pliocene and Pleistocene bivalve from the Pacific Coast, The Veliger, v. 16, p.354-358.

Ahmadi, H. and Pekkan, E., 2021, Fault-based geological lineaments extraction using remote sensing and GIS – A review, Geosciences, v. 11., pp. 31.

Aitken, M.J., 1985, Thermoluminescence Dating, Academic Press, London, 351 pp.

Armentrout, J.M., 1987, Cenozoic stratigraphy, unconformity-bound sequences, and tectonic history of southwestern Washington, Washington Division of Geology and Earth Resources Bulletin, no. 77, p. 291-320.

Arnulf, A.F., Basset, D., Harding, A.J., Kodaira, S., Nakanishi, A., & Moore, G., 2022, Upper-plate controls on subduction zone geometry, hydration and earthquake behavior, Nature Geoscience, v. 15, p. 143-148.

Atwater, B., 1987, Evidence for great Holocene earthquakes along the outer coast of Washington State, Science, v. 236, p.942-944.

Atwater, B., 1992, Geologic evidence for earthquakes during the past 2000 years along the Copalis River, southern coastal Washington: Journal of Geophysical Research, Solid Earth, v.97, p. 1901-1919.

Atwater, B., and Yamaguchi, D., 1991, Sudden, probably coseismic submergence of Holocene trees and grass in coastal Washington State, Geology, v. 19, n.7, p.706-709.

Atwater, B.F., Nuñez, H.J., and Vita-Finzi, C, 1992, Net late Holocene emergence despite earthquake-induced submergence, south-Central Chile, Quaternary International, v. 15.16, p. 77-85.

Atwater, B. F., and Hemphill-Haley, E., 1997, Recurrence intervals for great earthquakes of the past 3,500 years at northeastern Willapa Bay, Washington, U.S. Geological Survey professional paper 1576, pp. 108.

Atwater, T., 1970, Implications of plate tectonics for the Cenozoic tectonic evolution of western North America, Geological Society of America Bulletin, v. 81, p. 3513-3536.

Auclair, M., Lamothe, M., and Huot S., 2003, Measurement of anomalous fading for feldspar IRSL using SAR, Radiation Measurements, v. 37, p. 487-492.

Bakun, W.H., and McEvilly, T.V., 1984, Recurrence models and Parkfield, California earthquakes, Journal of Geophysical Research, v.,89, n. B5, p. 3051-3058.

Banas, N.S., and Hickey, B.M., 2005, Mapping exchange and residence time in a model of Willapa Bay, Washington, a branching, macrotidal estuary, Journal of Geophysical Research, v. 110, doi:10.1029/2005JC002950, pp.20.

Barnett., E.A., Haugerud, R.A., Sherrod, B.L., Weaver, C.S., Pratt, T.L., and Blakely, R.J., compilers, 2010, Preliminary atlas of active shallow tectonic deformation in the Puget Lowlands, Washington: U.S. Geological Survey Open-File Report 2010-1149, 32 p., 14 maps.

Beck, M. E Jr., 1980, Paleomagnetic record of plate-margin tectonic processes along the western edge of North America, Journal of Geophysical Research, v. 85, p. 7115-7131.

Berryman, K.R., 1993, Distribution, age, and deformation of late Pleistocene marine terraces at Mahia Peninsula, Hikurangi subduction margin, New Zealand, Tectonics, v. 12, n. 6, p. 1365-1379.

Bigelow, P.K., 1987, The petrology, stratigraphy, and basin history of the Montesano Formation, southwestern Washington and southern Olympic Peninsula, Western Washington University thesis, 263 p.

Birkeland, P.W., 1984, Soils and geomorphology: New York, Oxford University Press, 372 p.

Blakely, R.J., 1996, Potential theory in gravity and magnetic applications, Cambridge University Press, pp. 441.

Blakely, R.J., Wells, R.E., Weaver, C.S., & Johnson, S.J., 2002, Location, structure, and seismicity of the Seattle fault zone, Washington: Evidence from aeromagnetic anomalies, geologic mapping, and seismic-reflection data, GSA Bulletin, v. 114, p. 169-177.

Blakely, R.J., Sherrod, B.L., Hughes, J.F., Anderson, M.L., Wells, R.E., & Weaver, C.S., 2009, Saddle Mountain fault deformation zone, Olympic Peninsula, Washington: western boundary of the Seattle uplift, Geosphere, v. 5, p. 105-125.

Blakely, R.J., Sherrod, B.L., Weaver, C.S., Wells, R.E., Rohay, A.C., Barnett, E.A., & Knepprath, N.E., 2011, Connecting the Yakima fold and thrust belt to active faults in the Puget Lowland, Washington, Journal of Geophysical Research, v. 116, 33 p.

Blakely, R.J., Wells, R.E., Sherrod, B.L., & Brocher, T.M., 2016, Segmentation of the Cascadia forearc in southwestern Washington; evidence from new potential-field data, American Geophysical Union 2016 Fall Meeting Abstract.

Blakely, R.J., & Sherrod, B.L., 2020, High-resolution aeromagnetic survey of the Centralia Area, southwestern Washington, U.S. Geological Survey data release, https://doi.org/10.5066/P9T4UC6W.

Bloch, W., Bostock, M.G., and Audet, P., 2023, A Cascadia slab model from receiver functions, Geochemistry, Geophysics, Geosystems, v. 24, e2023GC011088, https://doi.org/10.1029/2023GC011088.

Bockheim, J.G., Kelsey, H.M. and Marshall, J.G., 1992, Soil development, relative dating and correlation of Late Quaternary marine terraces in southwestern Oregon; Quaternary Research, v. 37, p.60-74.

Bockheim, J. G., Marshall, J. G., and Kelsey, H. M., 1996, Soil-forming processes and rates on uplifted marine terraces in southwestern Oregon, USA; Geoderma, 73, 39-62.

Bodmer, M., Toomey, D.R., Roering, J.J., and Karlstrom, L., 2020, Asthenospheric buoyancy and the origin of high-relief topography along the Cascadia forearc, Earth and Planetary Science Letters, v., 531, 10 p.

Booth, D.B., 1987, Timing and processes of deglaciation along the southern margin of the Cordilleran ice sheet, *in* Ruddiman, W.F., and Wright, H.E., Jr., eds., North America and adjacent oceans during the last deglaciation, Geological Society of America, The Geology of North America, v. K-3, p. 71-90.

Booth, D.B., Troost. K.G., Clague, J.J., and Waitt, R.B., 2003, The Cordilleran ice sheet, Developments in Quaternary Science, v.1, p. 17-41.

Bradley, W.C., and Griggs, G.B., 1976, Form, genesis, and deformation of central California wave-cut platforms, Geological Society of America Bulletin, v. 87, p. 433-449.

Brandon, M.T., and Vance, J.A., 1992, New statistical methods of analysis of fission-track grain-age distributions with applications to detrital zircon ages from the Olympic subduction complex, Western Washington State, American Journal of Science, v. 292, p.565-636.

Brandon, M.T., Roden-Tice, M.K., and Garver, J.I., 1998, Late Cenozoic exhumation of the Cascadia accretionary wedge in the Olympic Mountains, northwest Washington State, Geological Society of America Bulletin, v.110, p.985-1009.

Brocher, T.M., Wells, R.E., Lamb, A.P. & Weaver, C.S., 2017, Evidence for distributed clockwise rotation of the crust in the northwestern United States from fault geometries and focal mechanisms, Tectonics, v. 36, p. 78-818, doi: 10.1002/2016TC004223.

Bufe, C.G., Harsh, P.W., and Burford, R.O., 1977, Steady-state seismic slip – a precise recurrence model, Geophysical Research Letters, v. 4, n.2, p. 91-94.

Buylaert, J-P., Jain, M., Murray, A.S., Thomsen, K.J., Theil, C., and Sohbati, R., 2012, A robust feldspar luminescence dating method for Middle to Late Pleistocene sediments, Boreas, v. 41, p. 435-451.

Campbell, K.A., and Nesbitt, E.A., 2000, High-resolution architecture and paleoecology of an active margin, storm-flood influenced estuary, Quinault Formation (Pliocene), Washington, Palaios, v.15, p.553-579.

Cashman, S.M., Kelsey, H.M., Erdman, C.F., Cutten, H.N.C, & Berryman, K.R., 1992, Strain partitioning between structural domains in the forearc of the Hikurangi subduction zone, New Zealand, Tectonics, v. 11., p. 242-257.

Chappell, J. and Shackleton, N.J., 1986, Oxygen isotopes and sea level, Nature, v. 324, p. 137-140.

Cheloni, D., D'Agostino, N., and Selvaggi, G., 2014, Interseismic coupling, seismic potential and earthquake recurrence on the southern front of the Eastern Alps (NE Italy), Journal of Geophysical Research, Solid Earth, v. 119, p. 4448-4468.

Clague, J. J., 1997, Evidence for large earthquakes at the Cascadia Subduction Zone, Review of Geophysics, v. 35, n. 4, p. 439-460.

Clark, K., Berryman, K., Litchfield, N., Cochran, N., and Little, T., 2010, Evaluating the coastal deformation mechanisms of the Raukumara Peninsula, northern Hikurangi subduction margin, New Zealand and insights into forearc uplift processes, New Zealand Journal of Geology and Geophysics, v. 53, n.4, p.341-358.

Clark, M.K., Royden, L. H., Whipple, K.X., Burchfiel, B.C., Zhang, X., and Tang, W., 2006, Use of a regional, relict landscape to measure vertical deformation of the eastern Tibetan Plateau, Journal of Geophysical Research, v. 111, FO3002, doi:10.1029/2005JF000294.

Clifton, H.E., and Phillips, R.L., 1980, Lateral trends and vertical sequences in estuarine sediments, Willapa Bay, Washington, Conference papers for Society for Sedimentary Geology, 17p.

Clifton, H. E., 1983, Discrimination between subtidal and intertidal facies in Pleistocene deposits, Willapa Bay, Washington: Journal of Sedimentary Petrology, v. 53, no. 2, p. 353-369.

Creveling, J.R., Mitrovica, J.X., Hay, C.C., Austermann, J., and Kopp, R.E., 2015, Revisiting tectonics corrections applied to Pleistocene sea-level highstands, Quaternary Science Reviews, v. 111, p. 72-80.

Creveling, J.R., Mitrovica, J.X., Clark, P.U., Waelbroeck, C., and Pico, T., 2017, Predicted bounds on peak global mean sea level during marine isotope stages 5a and 5c, Quaternary Science Reviews, v. 163, p. 193-208.

Dalrymple, R.W., and Choi, K., 2007, Morphologic and facies trends through the fluvial-marine transition in tide-dominated depositional systems: A schematic framework for environmental and sequence-stratigraphic interpretation, Earth-Science Reviews, v. 81, p 135-174.

Delano, J.E., Amos, C.B., Loveless, J.P., Rittenour, T.M., Sherrod, B.L., and Lynch, E.M., 2017, Influence of the megathrust earthquake cycle on upper-plate deformation in the Cascadia forearc of Washington State, USA, Geology, v.47, p. 155-158.

Delph, J.R., Thomas, A.M., Levander, A., 2021, Subcretionary tectonics: linking variability in the expression of subduction along the Cascadia forearc, Earth and Planetary Science Letters, v. 556, 116724.

DiBiase, R.A., Whipple, K.X., Heimsath, A.M., and Ouimet, W.B., 2010, Landscape form and millennial erosion rates in the San Gabriel Mountains, CA, Earth and Planetary Science Letters, 289, p. 134-144.

Doubrovine, P.V & Tarduno, J.A., 2008, A revised kinematic model for the relative motion between Pacific oceanic plates and North America since the Late Cretaceous, Journal of Geophysical Research, v. 113, B12101, pp. 20, doi:10.1029/2008JB005585.

Duvall, A., Kirby, E., and Burbank, D., 2004, Tectonic and lithologic controls on bedrock channel profiles and processes in coastal California, Journal of Geophysical Research, 109, F03002. http://dx.doi.org/10.1029/2003JF000086.

Eddy, M.P., Clark, K.P., & Polenz, M., 2017, Age and volcanic stratigraphy of the Eocene Siletzia oceanic plateau in Washington and on Vancouver Island, Lithosphere, v. 9, p.652-664.

Emmett, R. Llanso, R., Newton, J., Thom, R., Hornberger, M., Morgan, C., Levings, C., Copping A., and Fishman, P., 2000, Geographic signatures of North American west coast estuaries, Estuaries, v., 23, n.6, p. 765-792.

Fialko, Y., 2006, Interseismic strain accumulation and the earthquake potential on the southern San Andreas fault system, Nature, v. 441, p. 968-971.

Finn, C., 1990, Geophysical Constraints on Washington Convergent Margin Structure, Journal of Geophysical Research, v.95, no. B12, p.19533-19546, doi:10.1029/JB095iB12p19533.

Finn, C., Phillips, W.M., & Williams, D.L., 1991, Gravity anomaly and terrain maps of Washington, scale 1:500,000 and 1:1,000,000, U.S. Geological Survey Geophysical Investigations Map GP-988.

Flint, J.J., 1974, Stream gradient as a function of order, magnitude, and discharge, Water Resources Research 10, p.969-973.

Flueh, E.R., Fisher, M.A., Bialas, J., Childs, J.R., Klaeschen, D., Kukowski, N., Parsons, T., Scholl D.W., ten Brink, U., Trehu, A.M., and Vidal, N., 1998, New seismic images of the Cascadia Subduction Zone from Cruise S0108-ORWELL, Tectonophysics, v. 293, p. 69-84.

Forte, A.M., and Whipple, K.X., 2019, Short communication: the Topographic Analysis Kit (TAK) for TopoToolbox, Earth Surface Dynamics, v. 7, p. 87-95. https://doi.org/10.5194/esurf-7-87-2019.

Foster, M.A., and Kelsey, H.M., 2012, Knickpoint and knickzone formation and propagation, South Fork Eel River, northern California, Geosphere, v. 8, no. 2, p. 403-416.

Freisleben, R., Jara-Muñoz, J., Melnick, D., Martínez, J.M., and Strecker, M.R., 2021, Marine terraces of the last interglacial period along the Pacific coast of South America (1°N-40°S), Earth System Science Data, v. 13, p. 2487-2513. https:doi.org/10.5194/essd-13-2487-2021.

Galbraith, R. F., and Roberts, R. G., 2012, Statistical aspects of equivalent dose and error calculation and display in OSL dating: an overview and some recommendations, Quaternary Geochronology, v. 11, p.1-27.

Garrett, E., Shennan, I., Woodroffe, S.A., Cisternas, M., Hocking, E.P., and Gullier, P., 2015, Reconstructing paleoseismic deformation, 2: 1000 years of great earthquakes at Chucalen, south central Chile, Quaternary Science Reviews, v. 113, p. 112-122.

Geosoft Oasis montaj, 2021, Educational software edition, version 2021.2, Seequent, The Bentley Subsurface Company.

Gibbs, G., 1854, Report of George Gibbs on a reconnaissance of the county lying upon Shoalwater bay and Puget's south, *in* Stevens, I.I., Report of exploration of a route for the Pacific railroad near the forty-seventh and forty-ninth parallels, from St. Paul to Puget Sound *in* Report of the secretary of war communicating the several Pacific railroad explorations, volume 1, Executive documents printed by order of the House of Representatives during the first session of the thirty-third congress, no. 129, p. 483-494.

Globerman, B.R., Beck, M.E. Jr., & Duncan, R.A., 1982, Paleomagnetism and tectonic significance of Eocene basalts from the Black Hills, Washington Coast Range, Geological Society of America Bulletin, v. 93, p. 1151-1159.

Goldfinger, C. Klum, L.D., Yeats, R.S., Mitchell, C., Weldon, R., II, Peterson, C., Darienzo, M., Grant, W., and Priest, G.R., 1992, Neotectonic map of the Oregon continental margin and adjacent abyssal plain, State of Oregon, Department of Geology and Mineral Industries Open-File Report 0-92-4, 17 p., 2 pls.

Goldfinger, C., Kulm, L.D., Yeats, R.S., McNeill, L., & Hummon, C., 1997, Oblique strike-slip faulting of the central Cascadia submarine forearc, Journal of Geophysical Research, v. 102, p. 8217-8243.

Gower, H.D., & Pease, M.H., 1965, Geologic map of the Montesano Quadrangle, Washington, Map GQ-274, scale 1:62,500, U.S. Geological Survey.

Guérin, G., Mercier, N., and Adamiec, G., 2011, Dose-rate conversion factors: update, Ancient TL, v.29, p.5-8.

Hack, J.T., 1973, Stream-profile analysis and stream-gradient index, Journal of Research of the U.S. Geological Survey, v.1, p. 421-429.

Hanson, K.L., Wesling, J.R., Lettis, W.R., Kelson, K.I., and Mezger, L., 1994, Correlation, ages and uplift rates of Quaternary marine terraces: south-central coastal California, in Alterman, I.B., McMullen, R.B., Cluff, L.S., and Slemmons, D.B., eds., Seismotectonics of the Central California Coast Ranges, Geological Society of America Special Paper 292, p. 45-72.

Harel, M.-A., Mudd, S.M., and Attal, M., 2016, Global analysis of the stream power law parameters based on worldwide 10Be denundation rates, Geomorphology, v. 268, p. 148-196.

Hawkes, A.D., Horton, B.P., Nelson, A.R., Vane, C.H., and Sawai, Y., 2011, Coastal subsidence in Oregon, USA, during the giant Cascadia earthquake of AD 1700, Quaternary Science Reviews, v. 30, p. 364-376.

Heaton, T.H., and Hartzell, S.H., 1987, Earthquake hazards on the Cascadia subduction zone, Science, v. 236, pp. 162-168.

Hearty, P.J., and Kindler, P., 1995, Sea-level highstand chronology from stable carbonate platforms (Bermuda and The Bahamas), Journal of Coastal Research, v. 11, p. 675-689.

Holbrook, J., and Schumm, S.A., 1999, Geomorphic and sedimentary response of rivers to tectonic deformation: a brief review and critique of a tool for recognizing subtle epeiorogenic deformation in modern and ancient settings, Tectonophysics, v. 305, p. 287-306.

Hong, I., Cahill, N., Engelhart, S.E., Hawkes, A.D., Padgett, J.S., and Horton, B.P., 2021, Land-level changes during six megathrust earthquakes over the last 35000 years at the Cascadia subduction zone using a diatom-based Bayesian transfer function, Geological Society of America Abstracts, v. 53, doi: 10.1130/abs/2021AM-368007.

Huntley, D.J., Godfrey-Smith, D.I., and Thewalt, M.L.W., 1985, Optical dating of sediments, Nature, v. 313, p.105-107.

Huntley, D.J., and Lamothe, M., 2001, Ubiquity of anomalous fading in K-feldspars, and measurement and correction for it in optical dating. Canadian Journal of Earth Sciences, v. 38, p.1093-1106.

Hyndman, R.D., and Wang, K., 1993, Thermal constraints on the zone of major thrust earthquake failure: the Cascadia subduction zone, Journal of Geophysical Research, v. 98, p. 2039-2060.

Hyndman, R.D., and Wang, K., 1995, The rupture zone of Cascadia great earthquakes from current deformation and the thermal regime, Journal of Geophysical Research, v. 100, p. 22,133-22,154.

Jain, M. and Ankjaergaard, C., 2011, Towards a non-fading signal in feldspar: insight into charge transport and tunneling from time-resolved optically stimulated luminescence, Radiation Measurements, v. 46, p.292-309.

Jobe, J.T., Briggs, R., Gold, R., Bauer, L., and Collett, C., 2024, Limited evidence of late Quaternary tectonic surface deformation in the eastern Tennessee seismic zone, United States, Bulletin of the Seismological Society of America, https://doi.org/10.1785/0120230094.

Keller, E.A., and Pinter, N., 2002, Active Tectonics: Earthquakes, Uplift, and Landscape, 2nd Ed., Prentice Hall, pp.362.

Kelsey, H., 1990, Late Quaternary deformation of marine terraces on the Cascadia subduction zone near Cape Blanco, Oregon, Tectonics, v. 9, no. 5, p. 983-1014.

Kelsey, H.M, and Bockheim, J.G., 1994, Coastal landscape evolution as a function of eustasy and surface uplift rate, Cascadia margin, southern Oregon, Geological Society of America Bulletin, v. 10, p. 840-854.

Kelsey, H.M., Engebretson, D.C., Mitchell, C.E., and Ticknor, R.L., 1994, Topographic form of the Coast Ranges of the Cascadia Margin in relation to coastal uplift rates and plate subduction: Journal of Geophysical Research, v. 99, p. 12,245-12,255.

Kelsey, H., Ticknor, R., Bockheim, J., and Mitchell, C., 1996, Quaternary upper plate deformation in coastal Oregon, GSA Bulletin, v. 108, n. 7, p. 843-860.

Kelsey, H.M., Witter, R.C., and Hemphill-Haley, E., 2002, Plate-boundary earthquakes and tsunamis of the past 5500 yr, Sixes River estuary, southern Oregon, Geological Society of America Bulletin, v. 114, p. 298-314.

Kelsey, H., Satake, K., Sawai, Y., Sherrod, B., Shimokawa, K., and Shishikura, M., 2006, Recurrence of postseismic coastal uplift, Kuril subduction zone, Japan, Geophysical Research Letters, v. 33, L13315, doi: 10.1029/2006GL026052, pp. 5.

Kemp, A.C., Cahill, N., Engelhard, S.E., Hawkes, A.D., and Wang, K., 2018, Revising estimates of spatially variable subsidence during the A.D. 1700 Cascadia earthquake using a Bayesian foraminiferal transfer function, Bulletin of the Seismological Society of America, v. 108, p. 654-673.

Kennedy, G.F., 1978, Pleistocene paleoecology, zoogeography and geochronology of marine invertebrate faunas of the Pacific Northwest Coast (San Francisco to Puget Sound), Doctoral Thesis, University of California, Davis, 824 pp.

Kennedy, G. L., Lajoie, K.R., and Wehmiller, J.F., 1982, Aminostratigraphy and faunal correlations of late Quaternary marine terraces, Pacific Coast, USA, Nature, v. 299, p. 545-547.

Kirby, E., and Whipple, K., 2001, Quantifying differential rock-uplift rates via stream profile analysis, Geology, 29, p. 415-418.

Kirby, E., Whipple, K., Tang, W., and Chen, Z., 2003, Distribution of active rock uplift along the eastern margin of the Tibetan Plateau: inferences from bedrock channel longitudinal profiles, Journal of Geophysical Research, 108, 2217. http://dx.doi.org/10.1029/2001JB000861.

Kirby, E., and Whipple, K.X., 2012, Expression of active tectonics in erosional landscapes, Journal of Structural Geology, v., 44, pp. 54-75.

Kvenvolden, K. A., Blunt, D. J., and Clifton, H. E., 1979, Amino-acid racemization in Quaternary shell deposits at Willapa Bay, Washington: Geochimica et Cosmochimica Acta, v. 43, p. 1505-1520.

Lajoie, K.R., 1986, Coastal tectonics, *in* Wallace, R.E., chairman, Active Tectonics, Studies in Geophysics, National Academy Press, Washington, D.C., p. 95-124.

Lajoie, K.R., Ponti, D.J., Powell, C.L.II, Mathieson, S.A., and Sarna-Wojcicki, A.M., 1991, Emergent marine strandlines and associated sediments, coastal California: A record of Quaternary sea-level fluctuations, vertical tectonic movement, climatic changes, and coastal processes, *in* Morrison, R.B., ed., Quaternary nonglacial geology: Coterminous U.S., G.S.A., p. 190-203.

Lamothe, M., Brisson, L.F., and Hardy, F., 2020, Circumvention of anomalous fading in feldspar luminescence dating using Post-isothermal IRSL, Quaternary Geochronology, v. 57, 101062.

Leopold, L.B., and Maddock, T., 1953, Hydraulic geometry of stream channels and some physiographic implications, U.S. Geological Survey Professional Paper 252, pp. 57.

Li, B., Jacobs, Z., Roberts, R.G., Li, S., 2014, Review and assessment of the potential of post-IR IRSL dating methods to circumvent the problem of anomalous fading in feldspar luminescence, Geochronometria, v.41, n. 3, p. 178-201.

Li, S., Wang, K., Wang, Y., Jiang, Y., and Dosso, S. E., 2018, Geodetically inferred locking state of the Cascadia megathrust based on a viscoelastic Earth model, Journal of Geophysical Research: Solid Earth, 123, 8056–8072.

Lisiecki, L.E., and Raymo, M.E., 2005, A Pliocene-Pleistocene stack of 57 globally distributed benthic d18O records, Paleooceanography, 20, PA1003, doi:10.1029/2004PA001071.

Mackin, J.H., 1948, Concept of a graded river, Geological Society of America Bulletin, v. 59, p. 463-512.

Marple, R. and Hurd, J., 2020, Interpretation of lineaments and faults near Summerville, South Carolina, USA, using LiDAR data: implications for the cause of the 1886 Charleston, South Carolina, earthquake, Atlantic Geology, v. 56, p. 73-95, https://doi.org/10.4138/atlgeol.2020.003.

Martin, K.M., Gulick, S.P.S., Bangs, L.B., Moore, G.F., Ashi, J., Park, J., Kuramoto, S., & Taira, A., 2010, Possible strain partitioning structure between the Kumano fore-arc basin and the slope of the Nankai Trough accretionary prism, Geochemistry, Geophysics, Geosystems, v. 11, Q0AD02, doi:10.1029/2009GC002668.

Matsu'ura, T., Kimura, H., Komatsubara, J., Goto, N., Yanagida, M., Ichikawa, K., and Furusawa, A., 2015, Late Quaternary uplift rate inferred from marine terraces, Shimokita Peninsula, northeastern Japan: a preliminary investigation of the buried shoreline, Geomorphology, v. 209, p. 1-17.

Matsu'ura, T, Komatsubara, J., and Changjiang, W., 2019, Accurate determination of the Pleistocene uplift rate of the NE Japan forearc form the buried MIS 5e marine terrace shoreline angle, Quaternary Science Reviews, v. 212, p. 45-68.

McCaffery, R., Qamar, A.I., King, R.W., Wells, R., Khazaradze, G., Williams, C.A., Stevens, C.W., Vollick, J.J., & Zwick, P.C., 2007, Fault locking, block rotation, and crustal deformation in the Pacific Northwest: Geophysical Journal International, v. 169, p. 1315-1340.

McCaffery, R., King, R.W., Payne, S.J., & Lancaster, M., 2013, Active tectonics of northwestern U.S. inferred from GPS-derived surface velocities, Journal of Geophysical Research: Solid Earth, v. 118, p. 709-723.

McCrory, P.A., 1996, Tectonic model explaining divergent contraction directions along the Cascadia subduction margin, Washington, Geology, v. 24, no. 10, p. 929-932.

McCrory, P.A., 1997, Evidence for Quaternary tectonism along the Washington coast, Washington Geology, v. 25, n. 4, p.14-20.

McCrory, P.A., Foster, D.A., Danforth, W.W., and Hamer, M.R., 2002, Crustal deformation at the leading edge of the Oregon Coast Range block, offshore Washington (Columbia River to Hoh River): U. S. Geological Survey, Professional paper 1661-A, 53 pp.

McCrory, P.A., and Wilson, D.A., 2019, A kinematic model for Late Cenozoic fault motion within the greater Cascadia Subduction Zone, Seismological Research Letters, v. 90, n. 2b, p. 891.

McInelly, G.W., and Kelsey, H.M., 1990, Late Quaternary tectonic deformation in the Cape Arago-Bandon region of coastal Oregon as deduced from wave-cut platforms, Journal of Geophysical Research, v. 95, p. 6699-6713.

Melnick, D., Bookhagen, B., Echtler, H.P., and Strecker, M.R., 2006, Coastal deformation and great subduction earthquakes, Isla Santa Maria, Chile (37° S), GSA Bulletin, v. 118, p. 1463-1480.

Merritts, D.J., and Bull, W.B., 1989, Interpreting Quaternary uplift rates at the Mendocino Triple Junction, northern California, from uplifted marine terraces, Geology, v.17, p. 1020-1024.

Merritts, D., and Vincent, K.R., 1989, Geomorphic response of coastal streams to low, intermediate, and high rates of uplift, Mendocino triple junction region, northern California, Geological Society of America Bulletin, v. 101, p. 1373-1388.

Merritts, D.J., Vincent, K.R., and Wohl, E.E., 1994, Long river profiles, tectonism, and eustasy: a guide to interpreting fluvial terraces, Journal of Geophysical Research, v. 99, p. 14,031-14,050.

Meyer, C.E., Sarna-Wojcicki, A.M., Hillhouse, J.W., Woodward, M.J., Slate, J.L., and Sorg, D.H., 1991, Fission-track age (400,000 yr) of the Rockland tephra, based on inclusion of zircon grains lacking fossil fission tracks, Quaternary Research, vol. 35, p. 367-382.

Michalsen, D.R., Babcock, S.T., and Lin, L., 2010, Barrier island restoration for storm damage reduction, Willapa Bay, Washington, USA, Proceedings of the International Conference on Coastal Engineering, No. 32, 14 p.

Miller, K.G., Kominz, M.A., Browning, J.V., Wright, J.D., Mountain, G.S., Katz, M.E., Sugarman, P.J., Cramer, B.S., Christie-Blick, N., and Pekar, S.F., 2005, The Phanerozoic record of global sea-level change, Science, v. 310, p. 1293-1298.

Moothart, S.R., 1992, Geology of the Middle and Upper Eocene McIntosh Formation and adjacent volcanic and sedimentary rock units, Willapa Hills, Pacific County, southwest Washington, Master's Thesis, Oregon State University, 280 pp.

Muhs, D.R., Kelsey, H.M., Miller, G.H., Kennedy, G.L., Whelan, J.F., and McInelly, G.W., 1990, Age estimates and uplift rates for late Pleistocene marine terraces: southern Oregon portion of the Cascadia forearc, Journal of Geophysical Research, v. 95, p. 6685-6698.

Murray, A.S., and Wintle, A.G., 2000, Luminescence dating of quartz using an improved single-aliquot regenerative-dose protocol, Radiation Measurements, v. 32, p. 57-73.

Nelson, A.R., DuRoss, C.B., Witter, R.C., Kelsey, H.M., Engelhart, S.E., Mahan, S.A., Gray, H.J., Hawkes, A.D., Horton, B.P., and Padgett, J.S., 2021, A maximum rupture model for the central and southern Cascadia subduction zone — reassessing ages for coastal evidence of megathrust earthquakes and tsunamis, Quaternary Science Reviews, v. 261, 106922.

Newton, T.J., Weldon, R., Miller, I.M., Schmidt, D., Mauger, G., Morgan, H., and Grossman, E., 2021, Assessment of vertical land movement to support coastal hazards planning in Washington State, Water, v. 13, n. 281, 18 pp.

Nishimura, T., 2014, Pre-, co-, and post-seismic deformation of the 2011 Tohoku-Oki earthquake and its implication to a paradox in short-term and long-term deformation, Journal of Disaster Research, v. 9, p. 294-302.

O'Leary, D.W., Friedman, J.D., and Pohn, H.A., 1976, Lineament, linear, lineation: some proposed new standards for old terms, Geological Society of America Bulletin, v. 87, p. 1463-1469.

Ouchi, S., 1985, Response of alluvial rivers to slow active tectonic movement, Geological Society of America Bulletin, v. 96, p. 504-515.

Padgett, J. S., Kelsey, H. M., and Lamphear, D., 2019, Upper-plate deformation of Late Pleistocene marine terraces in the Trinidad, California, coastal area, southern Cascadia subduction zone, Geosphere, v. 15, n.4, p. 1323-1341.

Palmer, L.A., 1967, Marine terraces of California, Oregon, and Washington, Ph.D. Dissertation, University of California, Los Angeles, 376 pp.

Parsons, T., Wells, R.E., Fisher, M.A., Flueh, E., & ten Brink, U.S., 1999, Three-dimensional velocity structure of Siletzia and other accreted terranes in the Cascadia forearc of Washington, Journal of Geophysical Research, v. 104, n. B8, p. 18015-18039.

Pazzaglia, F.J., and Brandon, M.T., 2001, A fluvial record of long-term steady-state uplift and erosion across the Cascadia forearc high, western Washington State, American Journal of Science, v. 301, p. 385-431.

Pazzaglia, F.J., Thackray, G.D., Brandon, M.T., Wegmann, K.W., Gosse, J., McDonald, E., Garcia, A.F., and Prothero, D., 2003, Tectonic geomorphology and the record of Quaternary plate boundary deformation in the Olympic Mountains, in Swanson, T.W., ed, Western Cordillera and adjacent areas, Geological Society of America Field Guide 4, p. 37-67.

Pease, M. H., Jr. and Hoover, L., 1957, Geology of the Doty-Minot Peak area, Washington, U.S. Geological Survey, Oil and Gas Investigations Map OM 188, scale 1:62,500.

Personius, S.F., 1995, Late Quaternary stream incision and uplift in the forearc of the Cascadia subduction zone, western Oregon, Journal of Geophysical Research, v. 100, p. 20,193-20,210.

Plafker, G., and Rubin, M., 1978, Uplift history and earthquake recurrence as deducted from marine terraces on Middleton Island, Alaska, *in*, Proceedings of Conference VI, Methodology for identifying seismic gaps and soon-to-be gaps, U.S. Geological Survey Open-File Report 78-943, p. 687-721.

Polenz, M., and Kelsey, H.M., 1999, Development of a late Quaternary marine terraced landscape during on-going tectonic contraction, Crescent City coastal plain, California, Quaternary Research, v. 52, p. 217-228.

Polenz, M., Allen, M.D., Paulin, G.L., Eungard, D.W., Cakir, R., Scott, S.P., & Mahan, S.A., 2016, Geologic map of the Shelton valley 7.5-minute quadrangle, Mason County, Washington, 1:24,000 scale, Map Series 2016-02, Washington Division of Geology and Earth Resources, 1 sheet, 46 p. text.

Polenz, M., Vermeer, J.L., Legoretta Paulin, G., Tepper, J.H., Mahan, S.A., & Cakir, R., 2017, Geologic map of the Littlerock 7.5-minute quadrangle, Thurston County, Washington, 1:24,000 scale, Map series 2017-01, Washington Geological Survey, 1 sheet, 36 p., text.

Polenz, M., Toth, C.H., Samson, C., Sadowski, A.J., Becerra, R.I., Lau, T.R., Anderson, M.L., Nesbitt, E.A., Tepper, J.H., DuFrane, S.A., & Legorreta Paulin, G., 2019, Geologic map of the Rochester 7.5-minute quadrangle, Thurston County, Washington, 1:24,000 scale, Map series 2019-02, Washington Geological Survey, 1 sheet.

Prescott, J. R., and Hutton, J. T., 1988, Cosmic ray and gamma ray dose dosimetry for TL and ESR, Nuclear Tracks and Radiation Measurements, v. 14, p. 223-235.

Preusser, F., Degering, D., Fuchs, M., Hilgers, A., Kadereit, A., Klasen, N., Krbetschek, M., Richter, D., and Spencer, J.Q.G., 2008, Luminescence dating: basics, methods and applications, Eiszeitalter und Gegenwart Quaternary Science Journal, v. 57, p. 95-149.

Rabineau, M., Berne, S., Olivet, J., Aslanian, D., Guillocheau, F., and Joseph, P., 2006, Paleo sea levels reconsidered from direct observation of paleoshoreline position during Glacial Maxima (for the last 500,000 yr), Earth and Planetary Science Letters, v. 252, p. 119-137.

Raming, L.W., and Whipple, K.X., 2022, When knickzones limit upstream transmission of base-level fall: an example from Kaua'i, Hawai'i, Geology, v. 50, p. 1382-1386.

Reid, H.F., 1910, The California earthquake of April 18, 1906 *in* California Earthquake Investigation Commission Report, v. 2, 190 pp.

Sadowski, A.J., Keller, W.E., Polenz, M., Lau, T.R., Cakir, R., Nesbitt, E., Tepper, J.H., DuFrane, S.A., & Legoretta Paulin, G., 2018, Geologic map of the Centralia 1.5-minute quadrangle, Lewis County, Washington, 1:24,000 scale, Map series 2018-05, Washington Geological Survey, 1 sheet, 43 p. text.

Sadowski, A.J., Becerra, R.I., Toth, C.H., Polenz, M., Anderson, M.L., Lau, T.R., Nesbitt, E.A., Tepper, J.H., & DuFrane, S.A., 2019, Geologic map of the Adna 7.5-minute quadrangle, Lewis County, Washington, 1:24,000 scale, Map Series, 2019-01, Washington Geological Survey, 1 sheet.

Saillard, M., Hall, S.R., Audin, L., Farber, D.L., Herail, G., Martinod, J., Regard, V., Finkel R.C., and Bondoux, R., 2009, Non-steady long-term uplift rates and Pleistocene marine terrace development along the Andean margin of Chile (31° S) inferred from $^{10}$Be dating, Earth and Planetary Science Letter, v. 277, p. 50-63.

Saillard, M., Hall, S.R., Audin, L., Farber, D.L., Regard, V., and Herail, G., 2011, Andean coastal uplift and active tectonics in southern Peru: $^{10}$Be surface exposure dating of differentially uplifted marine terrace sequences (San Juan de Marcona, ~15.4° S), Geomorphology, v. 128, p. 178-190.

Saillard, M., Audin, L., Rousset, B., Avouac, J.-P., Chlieh, M., Hall, S.R., Husson, L., and Farber, D.L., 2017, From the seismic cycle to long-term deformation: linking seismic coupling and Quaternary coastal geomorphology along the Andean megathrust, Tectonics, v. 36, p. 241-256.

Saltus, R.W., & Blakely, R.J., 2011, Unique geologic insights form “non-unique” gravity and magnetic interpretation, GSA Today, v., 21, p. 4 – 11.

Sawai, Y., Satake, K., Kamataki, T. and Nasu, H., Shishikura, M., Atwater, B.F., Horton, B.P., Kelsey, H.M., Nagumo, T., and Yamaguchi, M., 2004, Transient uplift after a 17th-Centruy earthquake along the Kuril subduction zone, Science, v. 306, p1918-1920.

Schmalzle, G.M., McCaffrey, R., & Creager, K.C., 2014, Central Cascadia subduction zone creep, Geochemistry, Geophysics, Geosystems, v. 15, doi:10.1002/2013GC005172.

Schwanghart, W., and Scherler, D., 2014, TopoToolbox 2 – MATLAB-based software for topographic analysis and modeling in Earth surface sciences, Earth Surface Dynamics, v. 2, p. 1-7, http://dx.doi.org/10.5194/esurf-2-1-2014.

Seybold, H., Berghuijs, W.R., Prancevic, J.P., and Kirchner, J.W., 2021, Global dominance of tectonics over climate in shaping river longitudinal profiles, 2021, Nature Geoscience, v. 14, p. 503-507.

Shimazaki, K., and Nakata, T., 1980, Time-predictable recurrence model for large earthquakes, Geophysical Research Letters, v. 7, n. 4, p. 279-282.

Simms. A.R., Rouby, H., and Lambeck, K., 2015, Marine terraces and rates of vertical tectonic motion: the importance of glaci-isostatic adjustments along the Pacific coast of central North America, Geological Society of America Bulletin, v. 128, p. 81-93.

Smedley, R. K., Duller, G. A. T., Pearce, J. G., and Roberts, H. M., 2012, Determining the K-content of single-grains of feldspar for luminescence dating, Radiation Measurements, v. 47, p. 790-796.

Snavely, P.D. Jr., Rau, W.W., Hoover, L. Jr., & Roberts, A.E., 1951, McIntosh Formation, Centralia-Chehalis Coal District, Washington, Bulletin of the American Association of Petroleum Geologists, v. 35, p. 1052-1061.

Snavely, P.D. Jr., Brown, R.D. Jr, Roberts, Roberts, A.E., & Rau, W.W., 1958, Geology and coal resources of the Centralia-Chehalis district, Washington, U.S. Geological Survey Bulletin 1053, pp. 159.

Snavely, P. D., Jr., Macleod, N. S., Wagner, H. C., 1973, Miocene tholeiitic basalts of coastal Oregon and Washington and their relations to coeval basalts of the Columbia Plateau, Geological Society of America Bulletin, v. 84, p. 387-424

Snavely, P.D., Jr. and MacLeod, N.S., 1974, Yachats Basalt – An upper Eocene differentiated volcanic sequence in the Oregon Coast Range: U.S. Geological Survey Journal of Research, v. 2, p. 395-403.

Snavely, P.D., Jr. and Wagner, H.C., 1982, Geologic cross section across the continental margin of southwestern Washington, U.S. Geological Survey Open File Report 82-459.

Solomon, S., and Ghebreab, W., 2006, Lineament characterization and their tectonic significance using Landsat TM data and field studies in the central highlands of Eritrea, Journal of African Earth Science, v. 46, p. 371-378.

Staisch, L., Kelsey, H., Sherrod, B., Moller, A., Paces, J., Blakely, R., and Styron, R., 2017, Miocene-Pleistocene deformation of the Saddle Mountains: Implications for seismic hazard in central Washington, USA, Geological Society of America Bulletin, 27 p., https://doi.org/10.1130/B31783.1

Stanton, K.M., 2021, Geologic map of Quaternary deposits south of Grays Harbor and near Willapa Bay, southwestern Washington coast, Research Products by Graduate Students in Earth and Space Science, University of Washington Research Works Archive, https://doi.org/10.6069/4MX8-3C96.

Stanton, Kelsay M., Crider, Juliet G., Kelsey, Harvey M., and Feathers, James K., 2023, The signature of accumulated permanent uplift, northern Cascadia subduction zone, Quaternary Research, 1-21, https://doi.org/10.1017/qua.2023.59.

Stanton, K.M., Crider, J.G., Anderson, M., Lau, T., Staisch, L., and Kelsey, H. M., in preparation, Gravity and magnetic evidence for potentially active crustal faulting, central Cascadia forearc.

Steely, A., Anderson, M., von Dassow, W., Reedy, T., Lau, T., Horst, A., Amaral, C., Cakir, R., West, T., Stanton, K., Linneman, C., Lockett, A., Duckworth, C., Woodring, D., Tepper, J., and Staisch, L., 2021, Geologic and geophysical assessment of the tectonic uplift and fault activity in the Doty and Willapa Hills, southwest Washington: final report, Washington Geological Survey, Washington State Department of Natural Resources.

Sykes, L.R. and Quittmeyer, R.C., 1981, Repeat times of great earthquakes along simple plate boundaries *in* Earthquake Prediction: An International Review, Volume 4, *eds* Simpson, D.W., and Richards, P.G., American Geophysical Union, p.217-247.

Szeliga, W., Bilham, R., Kakar, D.M., and Lodi, S.H., 2012, Interseismic strain accumulation along the western boundary of the Indian subcontinent, Journal of Geophysical Research, v. 117, B08404.

Tabor, R.W., & Cady, W.M., 1978, The structure of the Olympic Mountains, Washington: Analysis of a subduction zone: U.S. Geological Survey Professional Paper 1033, pp. 38.

Taylor, J.R., 1997, An introduction to error analysis: The study of uncertainties in physical measurements, University Science Books, Sausalito, CA, 327 pp.

Thackray, G.D., 1996, Glaciation and neotectonics deformation on the western Olympic Peninsula, Washington, University of Washington, PhD Dissertation, 139 pp., 2 plates.

Thackray, G.D., 1998, Convergent-margin deformation of Pleistocene strata on the Olympic coast of Washington, USA, in, Stewart, I.S., and Vita-Finzi, C. (eds.), Coastal Tectonics, Geological Society of London Special Publications, 146, p. 199-211.

Thatcher, W., 1984, The earthquake deformation cycle, recurrence, and time-predictable model, Journal of Geophysical Research, v. 89, p. 5674-5680.

Thomsen, K. J., Murray, A. S., Jain, M. & Bøtter-Jensen, L., 2008, Laboratory fading rates of various luminescence signals from feldspar-rich sediment extracts, Radiation Measurements, v. 43, p. 1474-1486.

Thorson, R.M., 1980, Ice sheet glaciation of the Puget Lowland, Washington during the Vashon Stade, Quaternary Research v. 13, p.303-321.

Ticknor, R.L., 1993, Late Quaternary crustal deformation on the central Oregon coast as deduced from uplifted wave-cut platforms, M.S. thesis, Bellingham, Western Washington University, pp.70.

Tideland Oil & Gas Corporation, 1959, No. 1 Weyerhaeuser 7-11 well log, Pacific County, Washington State, obtained from Wash. State Dept. of Natural Resources, Geologic Information Portal, https://www.dnr.wa.gov/geologyportal in July 2023.

Tsuji, T., Ashi, J., & Ikeda, Y., 2014, Strike-slip motion of a mega-splay fault system in the Nankai oblique subduction zone, Earth, Planets, and Space, v. 66, 14 p.

U.S. Geological Survey National Map Viewer, https://apps.nationalmap.gov/viewer/ , accessed 2019.

U.S. Geological Survey, Quaternary fault and fold database for the United States, accessed December 5, 2023, at: https://www.usgs.gov/natural-hazards/earthquake-hazards/faults.

Vacher, H.L, and Hearty, P., 1989, History of Stage 5 sea level in Bermuda: review with new evidence of a brief rise to present sea level during substage 5a, Quaternary Science Review, v. 8, p. 159-168.

Wagner, H.C., 1967a, Preliminary geologic map of the Raymond Quadrangle, Pacific County, Washington, U.S. Geological Survey, Open-file report, scale 1:62,500.

Wagner, H.C., 1967b, Preliminary geologic map of the South Bend Quadrangle, Pacific County, Washington, U.S. Geological Survey, Open-file report, scale 1:62,500.

Walsh, T.J., compiler, 1987, Geologic map of the Astoria and Ilwaco quadrangles, Washington and Oregon, Open File Report 87-2, Washington Division of Geology and Earth Resources, 1 plate, 28 pp.

Walsh, T.J., Korosec, M.A., Phillips, W.M., Logan, R.L., and Schasse, H.W., 1987, Geologic Map of Washington – Southwest Quadrant, Washington Division of Geology and Earth Resources, Geologic Map GM-34.

Walter, G.W., & MacLeod, N.S., 1991, Geologic map of Oregon, U.S. Geological Survey, scale 1:500,000.

Wang, K., Wells, R., Mazzotti, S., Hyndman, R.D., and Sagiya, T., 2003, A revised dislocation model of interseismic deformation of the Cascadia subduction zone, Journal of Geophysical Research, v. 108, B1, 2026.

Wang, P., Engelhard, S.E., Wang, K., Hawkes, A.D., Horton, B.P., Nelson, A.R., and Witter, R.C., 2013, Heterogeneous rupture in the great Cascadia earthquake of 1700 inferred from coastal subsidence estimates, Journal of Geophysical Research: Solid Earth, v. 118, p. 2460-2473.

Washington State Department of Natural Resources, Geologic Information Portal [Dataset and maps], last accessed Dec. 5, 2023, at https://www.dnr.wa.gov/geologyportal.

Washington Department of Natural Resources Lidar portal, https://lidarportal.dnr.wa.gov/ , accessed 2019.

Washington Division of Geology and Earth Resources, 2016, Surface geology, 1:100,000 – GIS data, November 2016. Washington Division of Geology and Earth Resources Digital Data Series DS-18, version 3.1, previously released June 2010.
http://www.dnr.wa.gov/publications/ger_portal_surface_geology_100k.zip

Washington State Department of Transportation Geotechnical Services Branch, 1997, SR-105: Geological Study of the North Channel of Willapa Bay – Vicinity of North Cove, Washington, Willapa Bay Channel Restoration Project C.S. 2532, OL-2431, 124 p.

Watt, J.T., and Brothers, D.S., 2020, Systematic characterization of morphotectonic variability along the Cascadia convergent margin: implications for shallow megathrust behavior and tsunami hazards, Geosphere, v. 12, https://dooi.org/10.1130/GER02178.1

Wells, R.E., 1979, Geologic map of Cape Disappointment-Naselle River area, Pacific County, Washington, U.S. Geological Survey Open File Report 79-389.

Wells, R.E., 1981, Geologic map of the Eastern Willapa Hills, Cowlitz, Lewis, Pacific, and Wahkiakum counties, Washington, U.S. Geological Survey Open File Report 81-674.

Wells, R.E., 1989a, Geologic map of Cape Disappointment-Naselle River area, Pacific County, Washington, U.S. Geological Survey Open File Report 79-389.

Wells, R.E., 1989b, Mechanisms of Cenozoic tectonic rotation, Pacific Northwest convergent margin, U.S.A. *in* Kissel, C. and Laj, C. (eds), Paleomagnetic Rotations and Continental Deformation, Kluwer Academic Publishers, p. 313-325.

Wells, R.E., & Coe, R.S., 1985, Paleomagnetism and geology of Eocene volcanic rocks of southwest Washington, implications for mechanisms of tectonic rotation, Journal of Geophysical Research, v. 90, p. 1925-1947.

Wells, R.E., Weaver, C.S., & Blakely, R.J., 1998, Fore-arc migration in Cascadia and its neotectonic significance: Geology, v. 26, p.759-762.

Wells, R.E., Bukry, D., Friedman, R., Pyle, D., Duncan, R., Haeussler, P., and Wooden, J., 2014, Geologic history of Siletzia, a large igneous province in the Oregon and Washington Coast Range: Correlation to the geomagnetic polarity time scale and implications for a long-lived Yellowstone hotspot, Geosphere, v. 10, 29 p.

Whipple, F.J.W., 1936, On the theory of the strains in an elastic solid bounded by a plane when there is a nucleus of strain at an interval point, and on the relation of the theory to seismology, Geophysical Supplements to the Monthly Notices of the Royal Astronomical Society, v. 3, p. 380-388.

Whipple, K.X., and Tucker, G.E., 1999, Dynamics of the stream-power river incision model: implications for height limits of mountain ranges, landscape response timescales, and research needs, Journal of Geophysical Research, v. 104., p. 17,661-17,674.

Whipple, K.H., and Tucker, G.E., 2002, Implications of sediment-flux-dependent river incision models for landscape evolution, Journal of Geophysical Research, v. 107, 2039, 10.1029/2000JB000044, pp. 20.

Whipple, K.X., DiBiase, R.A., and Crosby, B.T., 2013, Bedrock rivers, in Shroder, J. (ed. in chief) and Wohl, E. (ed.), Treatise on geomorphology, Academic Press, San Diego, CA, vol. 9, Fluvial Geomorphology, pp. 550-573.

Wilson, D.S., and McCrory, P.A., 2022, A late Cenozoic kinematic model for fault motion within greater Cascadia, Geochemistry, Geophysics, Geosystems, v. 23, e2022GC010442, https://doi.org/10.1029/2022GC010442.

Witter, R.C., Kelsey, H.M., and Hemphill-Haley, E., 2003, Great Cascadia earthquakes and tsunamis of the past 6700 years, Coquille River estuary, southern coastal Oregon, GSA Bulletin, v. 115, p. 1289-1306.

Wobus, C., Whipple, K.X, Kirby, E., Snyder, N., Johnson, J., Spyropolou, K., Crosby, B., and Sheehan, D., 2006, Tectonics from topography: Procedures, promise, and pitfalls, in Willett, S.D., Hovius, N., Brandon, M.T., and Fisher, D.M., eds., Tectonics, Climate, and Landscape Evolution, Geological Society of America Special Paper 398, p. 55-74.

Wolfe, E.W., & McKee, E.H., 1968, Geology of the Grays River Quadrangle, Wahkiakum and Pacific counties, Washington, Geologic Map GM-4, Washington Division of Mines and Geology.

Wolfe, E.W., & McKee, E.H., 1972, Sedimentary and igneous rocks of the Grays River quadrangle, Washington, U.S. Geological Survey Bulletin 1335, 70p.

Yonkee, W.A. & Weil, A.B., 2015, Tectonic evolution of the Sevier and Laramide belts within the North American Cordillera orogenic system, Earth-Science Reviews, v. 150, p. 531-593.

# Appendix 1. ~1:24,000-scale Quaternary geologic map

## Pamphlet to accompany 1:24,000-scale geology mapping, coastal region south of Grays Harbor and east of Willapa Bay

### Overview

Southwestern Washington geology encompasses a broad range of Cenozoic lithologies and a complex structural and tectonic history. Modern estuarine systems are found in Grays Harbor and Willapa Bay, with highlands south of Grays Harbor and east of Willapa Bay. The coastal region adjacent to these modern estuaries was previously mapped as a single unit, with Quaternary sediments at elevations up to 160m a.s.l. Wagner (1967a, b) defined the sediments as undifferentiated terraces deposits (Qt) consisting of "relatively unconsolidated" clay to gravel, and with "ancient bay-fill deposits" at elevations over 100m. Although later mapping differentiated some deposits in the southern part of Willapa Bay (Wells, 1979; Wells, 1981), maps continued to show the region directly south of Grays Harbor and around Willapa Bay as a single unit (Walsh et al., 1987). The region does not have 1:24,000 scale geologic mapping. The 1:250,000-scale map describes the unit as "Silt, sand, and gravel of diverse composition and origins, such as … uplifted marine and estuarine deposits" (Walsh et al., 1987).

Clifton (1983) provided detailed description of the Quaternary coastal sediments that are well exposed along the modern shoreline on the east side of Willapa Bay between Goose Point and Pickernell Creek. Both subtidal and intertidal sediments comprise the exposures, which suggest a varying depositional environment, much like today's modern estuary. The deposits show laterally alternating environments, such as estuarine deposits cut by tidal channel deposits (Clifton and Phillips, 1980), and are dated to the Pleistocene based on amino acid racemization

ages from bivalve shells (Kvenvolden et al., 1979). Clifton (1983) describes the exposed sediments as marine estuarine deposits that have been uplifted since deposition during past sea-level high stands and notes that higher elevation deposits are likely older terraces, implying a similar depositional setting to the lowest elevation deposits. The Pleistocene estuarine deposits are preserved only at this location on the coast, suggesting the region has long been estuarine. Higher elevation deposits were not described in any detail, mostly due to poor access. The potential for unmapped faults or a record of subduction-related long-term permanent uplift incited this investigation, aided by recent lidar data for the region. This pamphlet describes the geologic and geomorphic characteristics of newly differentiated units as well as field observations portrayed in the accompanying maps and stratigraphic sections. I also describe interpretations of unit origin and relative geologic relationships as based on my field observations and the vast work that precedes me. Field notes and photographs, as well as all figures referred to in this pamphlet, can be found at http://hdl.handle.net/1773/46938.

**Methodology**

I used digital elevation models (DEMs) to conduct GIS-based geomorphic analyses as well as base maps for mapping. Both 1m and 10m DEMs are available for the field area. I compared a GIS-based topographic smoothness analysis for a small section of the field area using both 1m and 10m DEM. The results were comparable so for efficiency, I used the 10m DEM for the remainder of the geomorphic analyses including analyses to determine slope angle, topographic smoothness, and to construct topographic profiles (see Appendix 1). The 1m DEM was obtained from lidar collected and processed by Quantum Spatial in 2019, contracted by the U.S. Geological Survey and the Washington Geological Survey. I used the 1m DEM as a base

map for ~1:24,000 geologic mapping (Maps 1-3). The 1:100,000 geologic mapping is shown on the maps outside of the field area (Washington Division of Geology and Earth Resources, 2016)

Observations made at outcrops or in hand-dug pits in the field area support my unit descriptions, geologic maps, and stratigraphic sections. Geologic mapping was conducted during field seasons 2019 and 2020. I described hand samples of sediments in the field, including descriptions of soil profiles where exposures were near ground surface. In most of the gravel deposits the clasts are weathered through or have thick oxidation rinds, rendering lithologic identification difficult. Where gravels were less weathered I conducted point counts of lithology in random locations at an outcrop within a set measured area ranging from 18-48cm wide by 12-36cm high, of all clasts between 4mm-8cm. (e.g. granitic, metamorphic, sedimentary, volcanic, not identifiable). I measured dip and dip-direction of cross-beds where present. For the two units exposed as sea-cliffs I measured stratigraphic relationships with a transit to create simplified stratigraphic sections (Plates 1 and 2). Stratigraphic observations along topographic profiles are schematic, with approximate measurements made at outcrops using measuring tapes (Plates 3-5). Portions of the field area were not accessible due to locked gates or private property. Where these regions were geomorphically and spatially conformable with nearby field observations they were included within a given unit. Where inaccessible areas lack nearby observation or nearby observations include conflicting unit interpretation they are mapped as “not accessed”. In some instances, terrace 1 (Qt1) is mapped by geomorphic characteristics and direct observations by previous workers.

All field data is organized according to field station name (Table 1). Field notes and field photographs are organized by date and field station number and deposited in the UW ResearchWorks archive at http://hdl.handle.net/1773/46938 .

**Unit descriptions in mapped areas**

Please note that these unit descriptions are not in age order. For a discussion of age relationships and an interpretation of geologic history of the area, please see Stanton et al. (2023)(Chapter 2). I have noted the probable age (where known) in terms of marine isotope stage (MIS) based on interpretations in Stanton et al. (2023) (Chapter 2).

*Marine terrace deposits, MIS 5a (Qt1)*

Geomorphically smooth surfaces, between 13-22 m a.s.l. Thinly bedded silts and fine sands with minor clay and massive-to-cross-bedded, fine to medium sands with silt rip-up clasts (Plate 1). Sands are generally quartzo-feldspathic with trace to abundant mica. At many locations between 0.8-2 m above modern beach level is a 0.5-1 m-thick bed of broken shells, underlying a bioturbated massive silt-to-sand layer with trace wood fragments and branches (Figure A1-1). According to Clifton (1982), all beds are cut by channel deposits. Where observed, the channel deposits consist of cross-bedded, medium-to-coarse sand to cobbles, with rip-up clasts of silt and clay. Cross beds are less than 0.25 m high. Channel deposits are between several meters to tens of meters wide. Depth to Cox horizon in soils is between 0.5 m-0.75 m.

*Marine terrace deposits, MIS 5c 2 (Qt2)*

Geomorphically smooth surface between 35-48 m a.s.l. mantled by thinly bedded blue-grey to brown silts and fine sands and massive-to-cross bedded, fine to medium sands (Figure A1-2). Where terrace is exposed, these deposits are underlain by older estuarine deposits (TQss), although the sands and silts of terrace 2 (Qt2) are also present in stream channels and minor embayments cut into the TQss deposits (see below). Soils are orange to brown, with depth to Cox horizon between 1-2 m.

*Late Pliocene to early Pleistocene shallow marine and near-shore deposits (TQss)*

Indurated, stiff, thinly bedded silts and fine sands, and massive-to-cross bedded, fine to medium sands cut by oxidized, cross-bedded medium-to-fine sand to cobbles with silt rip-up clasts (Plate 2; Figure A1-3). The thinly bedded silts and fine sands show soft sediment deformation (Figure A1-4) and are occasionally gently tilted, with other layers at angles to the dipping sediment (Figure A1-5). Geotechnical investigations by the Washington Department of Transportation (1997) near northwestern Willapa Bay at the main Willapa Bay tidal channel include both borings and seismic surveys. These show dense to very dense silts and sands extending several hundred feet offshore to depths up to ~27 m below sea-level. These dense sediments form a bench, with the upper bench surface at ~9 m below sea-level. Slightly less dense sands and silts sit stratigraphically above the denser material in some locations. Very loose Holocene sands and gravels form a wedge atop the dense sands and silts, which are interpreted to be Pleistocene “terrace” deposits and correlated to the cliff-forming “terrace” deposits along the northern side of Willapa Bay (DOT, 1997). Addicott (1966, 1974) notes that the compact silts and very fine sands in the cliff-forming deposits contain fossilized, extinct, bivalves, providing a

Pliocene to early-Pleistocene age for the deposits, although later work suggests sediments bearing these bivalves may be as young as mid-Pleistocene (Meyer et al., 1991). Clifton (1982) refers to these as the "older estuarine deposits," and I suggest they are the very dense silts and sands forming offshore benches at northwestern Willapa Bay. Above sea-level these older deposits appear to have been wave cut in some locations, creating the flat and smooth surface between 35-48m a.s.l., while in other locations there are sea-cliff exposures of the indurated estuarine deposits but without a geomorphically distinct surface. While these older deposits do not always form a distinct geomorphic surface, they are not found at elevations over about 60m a.s.l.. Additionally, there appear to be less indurated sands and silts on the higher surface and deposited in valleys incised into that surface that I map as terrace 2 (Qt2). It is possible this unit also underlies unit terrace 1 (Qt1) deposits. Figure A1-6 shows a possible stratigraphic relationship between units Qt1, Qt2, and TQss.

*Sands near South Bend, MIS5c (Qss)*

Thinly bedded, blue-grey to tan silts and clays to bedded to massive, slightly oxidized fine sands with silt lag deposits (Figure A1-7). Silts and clays occasionally with hard, iron-rich interbeds approximately 1-1.5 cm thick. Sands are quartz- and lithic-rich and infrequently with faint cross-bedding. Often sand has manganese oxide (?) coating. Soil has depth to Cox between 1-1.5 m. The relationship of these deposits to Qt2 and TQss are not obvious in the field.

*Chehalis River deposits near Cosmopolis (Qfch)*

Indurated, cross-bedded, medium sand to cobble underlying interbedded blue-grey sandy clay to silt. Sandier portions contain minor pumice layers and are cut by coarser sands and

gravels. Cobbles are oxidized but not weathered through and with minor or no weathering rind (Figure A1-8). Includes clasts of granitic and metamorphic lithology. Depth to Cox horizon in soil less than 1 m.

*Sands between Westport and Tokeland (Qsg)*

Cross-bedded fine-medium sand interfingered with coarse sand and gravel and silts at elevations from near sea-level to over 60 m a.s.l. forming an abrupt western escarpment north of North Cove between Willapa Bay and Grays Harbor (Figure A1-9). Cross-bedding height often up to 1-2 m, with dip direction west to northwest. These are commonly capped with loose, fine-to-medium, massive to cross-bedded quartz rich sands (Figure A1-10). Soils have depth to Cox horizon between 0.75 and 1.5 m. The cross-bedded deposits resemble descriptions by Clifton and Phillips (1980) of tidal deposits in the Willapa Bay main tidal channel, called North Channel, which is south of these sediments. Side scanning sonar and oriented cores indicate the main tidal channel has irregular- and straight-crested bedforms up to 4 m high comprised of sands, gravels, shells, and wood fragments. North Channel experiences intense tidal currents, between 1-1.5 m/s, and is known to move laterally through time; present-day shoreline erosion is occurring on the northeast side of the channel, encroaching on Cape Shoalwater and Hwy 105 near North Cove (Washington Department of Transportation, 1997). I suggest the sands and gravels are tidal channel deposits and/or offshore current deposits. The cross-bed height suggests large currents and the capping of clean sand suggests the depositional environment changed from high currents to a beach. The relationship of this unit to other units is not obvious in the field, although along the western side of this unit there are no other units stratigraphically below that can be observed in the field.

*Gravels and sands south of Grays Harbor, MIS6 (Qgs)*

Oxidized, cemented, cross-bedded to massive, medium-to-coarse sands to gravels in regionally extensive beds at elevations over 60 m a.s.l (Figure A1-11). Sands are quartz- and lithic-rich with trace to no mica. Cross-bedding ranges from several centimeters high up to approximately 0.75m high, with dip direction generally to the west and southwest. Infrequently, sand and gravel associated with silt and clay beds up to 4 m thick. In these cases, there may be rip-up clasts of silt and clay within the cross-bedded coarser sediment. Manganese-and-iron rich weathering rinds of 1 mm thick and greater are common on gravels. Sediments are highly weathered with some gravels weathered entirely through. Where not weathered through, gravel lithology includes sedimentary rocks (~17% of clasts) as well as granitic rocks (~14% of clasts), metamorphic rocks (11% of clasts) and volcanic rocks (11% of clasts). Most gravels were too weathered for definite identification (47% of clasts). Soils are orange-red, commonly showing platy to blocky ped structure, mature, with depth to Cox horizon greater than 2 m. The relationship of these deposits to other units is not obvious in the field.

*River terraces (Qrt)*

River terraces geomorphically identified as low-lying platforms above the modern platform (Qal). Field observations show silts, fine-to-medium sands, and occasional gravel.

*Quaternary alluvium (Qal)*

Modern river deposits, identified in lidar as lowest geomorphic platforms surrounding streams.

*Quartzite bearing deposits in southern Willapa Bay (Qfcr)*

Silty sands to cobbles, commonly faintly cross-bedded and with clay to silt rip-up clasts. In general, modal percentage of sands consist of 40% feldspar, 10-15% quartz, 10% dark minerals, possibly amphiboles, 2-4% mica, and 31-38% lithic fragments and/or unidentifiable minerals. Where present, cobbles are well rounded, and consist of abundant quartzite and minor granitics. Sands and silts weather to orange-brown. Soils forming on the deposits are generally orange-red and silt rich with minor clay component. Rip-up clasts consist of light tan clay to silt, commonly elongate with orientation parallel to cross-bedding. Geomorphically similar to other terraces in region, so identification hinges on presence of quartzite cobbles.

*Bedrock*

Oil and gas exploratory well logs from 1940s and 1950s indicate thick deposits of sand and gravel in the higher elevations south of Grays Harbor, with the depth to bedrock ranging from approximately 50 m to nearly 450 m. The regional sedimentary bedrock consists of siltstone, sandstone, and conglomerate, which are frequently loosely indurated where fresh and weather to very loosely indurated. It is difficult to determine the exact depth to bedrock from descriptions of drill cuttings because notes describing “sand and siltstone” may be referring to loosely indurated bedrock or to compact sediments. Generally, the bedrock surface beneath the Quaternary sediments appears to undulate, possibly representing regional folding. Additionally, the well logs suggest that Quaternary sediments thin to the east.

My field observations indicate some exposures of bedrock in road cuts near the eastern contact in what was previously mapped as Quaternary. These exposures may be more recent than

available for previous studies. I map these as “likely bedrock.” When obvious, I have suggested probable regional units for field stations at bedrock exposures in Table 1 and within my field notes.

*Landslides (Qls)*

Landslides are abundant in southwestern Washington and there are numerous landslides ranging from several square meters to several square kilometers in area. In some instances, I make note of these landslides in my field notes and photographs, particularly when they involve portions of roads. Only a single landslide appears on my geologic map. This slide appears on the 1:100,000 geologic map and I have included it in roughly the same location. Field observations indicate it includes blocks of sediment that resemble Qgs.

## Tables

Table A1-1. Field station numbers with general unit description.

| Station | Unit | Comments |
|---|---|---|
| 19GW715.1 | mica rich sand with silt ripups and ocs silt beds | mica-rich sands, silt rip-ups, photos 19GW715.1a,b |
| 19GW715.2 | basalt, jointed, weathered | n/a |
| 19GW715.3 | basalt, jointed, weathered | fabric with attitudes, photo 19GW715.3a |
| 19GW715.4 | silty soil with qtzt and granitic cobbles | quartzite cobbles, minor granitics |
| 19GW715.5 | silts with quartzite cobbles | quartzite cobbles |
| 19GW715.6 | deeply weathered soils | mature soils |
| 19GW715.8 | Crescent Basalt, jointed, weathered | n/a |
| 19GW715.9 | McIntosh Formation, silts | weathered, jointed |
| 19GW716.1 | McIntosh Formation, silts | n/a |
| 19GW716.2 | McIntosh Formation, silts | n/a |
| 19GW716.3 | contact McIntosh Fm & CRB, Saddle Mountain (?) | contact, photos 19GW716.3a,b,c |
| 19GW716.4 | silty clay with thick weathering | n/a |
| 19GW716.5 | McIntosh Formation, silts | attitude on possible bedding, photo 19GW716.5a |
| 19GW716.6 | Columbia River Basalt, Saddle Mountain (?) | landscape photos showing terraces 19GW716.6a,b,c |
| 19GW716.8 | contact McIntosh Fm & Crescent Basalt | n/a |
| 19GW87.1 | Chehalis river terrace, younger, near estuarine | see notes for photos, samples |
| 19GW87.1 | sands, gravels, soils | thicker soil |
| 19GW88.1 | soil | see notes for photos, samples |
| 19GW88.1c | modern beach | sample |
| 19GW88.1d | cross bedded sands with massive sands on top | samples and notes |
| 19GW88.2 | crescent basalt | n/a |
| 19GW89.1 | sands and silts | n/a |
| 19GW89.2 | soil | description |
| 19GW813.1 | sands and silts | n/a |
| 19GW813.2 | Crescent basalt | n/a |
| 19GW813.3 | silt & clay | sample, photo, attitudes |
| 19GW813.4 | sand & silt, | n/a |
| 19GW813.5 | sand & silt, | n/a |
| 19GW813.6 | Crescent basalt | n/a |
| 19GW813.7 | sand & silt, | n/a |
| 19GW813.8 | siltstone, McIntosh ? | n/a |
| 19GW813.9 | Crescent basalt | n/a |
| 19GW813.10 | Crecent basalt | n/a |
| 19GW814.1 | thinnly bedded silts and sands | n/a |
| 19GW814.2 | sands with shells | n/a |
| 19GW814.3 | sands with shells | n/a |
| 19GW814.4 | siltstone,Lincoln Creek | n/a |
| 19GW814.5 | sands and gravels | n/a |
| 19GW814.6 | sands and gravels | n/a |
| 19GW814.7 | cross bedded sands | photos |
| 19GW814.8 | thinnly bedded silts | n/a |
| 19GW814.9 | thinnly bedded silts | n/a |
| 19GW814.10 | cross bedded sands and gravels, oxidized | sample IRSL, sample provenance, attitude 20GW0922 |
| 19GW814.11 | thinnly bedded silts | n/a |
| 19GW814.12 | siltstone, Lincoln Creek | n/a |
| 19GW827.2 | siltstone, Astoria | incorrect GPS reading, this is approx spot |
| 19GW827.3 | sandstone, Astoria | attitudes |
| 19GW827.4 | weathered gravels | attitudes, also visited on 20GW0921.2 |
| 19GW827.5 | location of 2018 cosmo pit, soil w/thick Bt | n/a |
| 19GW827.6 | weathered gravels | also visited on 20GW0921.3, photos, attitudes |
| 20GW0629.1 | Quinault Fm (?), outwash (Qapo?) | photos and descriptions |
| 20GW0629.2 | sand, unknown unit | photo |
| 20GW0629.3 | silt and sand with some gravels, possibly fluvial | n/a |
| 20GW0630.1 | silt with clay | descrip, soil, photos, drawings |

| | | |
|---|---|---|
| 20GW0630.2 | gravels, well dev soil, older deposits now in ls | descriptions, photos, soil descript |
| 20GW0630.3 | gravels, fluvial, older deposits now in ls | photos, descript |
| 20GW0630.4 | gravels, sandy silts, fluvial, older depos? | photos and brief descrip |
| 20GW0630.5 | v.f. sand and silt, capped by weathered gravels | photos, drawings |
| 20GW0630.6 | silt and sand | n/a |
| 20GW0701.1 | sand | descrip, photos, depth of bt |
| 20GW0701.2 | sand | soil descrip |
| 20GW0701.3 | sand and silt | n/a |
| 20GW0701.4 | landslide | n/a |
| 20GW0701.5 | sand | descrip, soil, depth of bt |
| 20GW0701.6 | bedrock, sandstone, highly fractured | n/a |
| 20GW0701.7 | bedrock, siltstone | n/a |
| 20GW0701.8 | none, landscape photos | photos |
| 20GW0701.9 | fluvial seds with quartzite, Columbia River | decription |
| 20GW0701.10 | fluvial seds, mica rich sand, Col River | descrip, soil, depth of bt |
| 20GW0702.1 | Montesano Fm in alluvial terrace (strath) | descrip, samples |
| 20GW0706.2 | v.f. mica-rich sand and silt | descrip, samples |
| 20GW0706.3 | clayey silt, possible mica | n/a |
| 20GW0704.4 | clayey silt | soil descrip |
| 20GW0707.1 | silt, sand - lowest terrace | strat sec, descrip, photos |
| 20GW0707.2 | silt, sand - lowest terrace | strat sec, descrip, photos |
| 20GW0707.3 | Hologcene beach sand | sample for provenance |
| 20GW0707.4 | Holocene beach sand | sample for provenance |
| 20GW0707.5 | bedrock, Lnc Ck or Astoria | n/a |
| 20GW0707.6 | alluvium, Naselle | n/a |
| 20GW0707.7 | bedrock, Lnc Ck or Astoria | n/a |
| 20GW0707.8 | bedrock, Lnc Ck or Astoria | n/a |
| 20GW0707.9 | silts, fine sands, marine terrace or Nemah unknown | n/a |
| 20GW0708.1 | silts, sands, weathered gravels - higher terrace | strat, photos |
| 20GW0708.2 | silty sand | soil |
| 20GW0708.3 | silt | n/a |
| 20GW0708.4 | sandy silt | n/a |
| 20GW0708.5 | weathered gravels | n/a |
| 20GW0713.1 | outcrop poor but with rounded pebbles | n/a |
| 20GW0713.2 | fine to v. fine sand | soil profile |
| 20GW0713.3 | fluvial sands and gravel | decription, sample |
| 20GW0713.4 | silt | n/a |
| 20GW0713.5 | beach sand | samples, descrip |
| 20GW0714.1 | cobbles, fine mica sand, bdrck, fluv? see 0706.2 | descrip, soil, samples |
| 20GW0714.2 | upper soil for previous | n/a |
| 20GW0714.3 | sands and gravels, bedrock? fluvial? | descrip, dz samples |
| 20GW0714.5 | cross bedded sands, fluvial or tidal channel | n/a |
| 20GW0714.6 | cross bedded sands, fluvial or tidal channel? | n/a |
| 20GW0715.1 | Montesano FM | n/a |
| 20GW0715.2 | Lincoln Ck | n/a |
| 20GW0715.3 | silts and fine sands in a ls | n/a |
| 20GW0715.4 | silt with minor clay and fine sand | soil, photos |
| 20GW0715.5 | weathered gravels, silts to sand, bdrck? | descrip, photos |
| 20GW0715.6 | silt to v. fine sand, estuarine | descrip |
| 20GW0715.7 | clayey silt, dark grey | descript, photos, st/d |
| 20GW0715.8 | clayey silt, dark grey | n/a |
| 20GW0715.9 | fluvial sands and gravels, Lincoln Ck | n/a |
| 18GW0718.1 | silt, sands, weathered gravels | descrip, photos |
| 18GW0718.2 | weathered silts, clays, gravels over basalt | descrip, photos |
| 18GW0719.1 | sand with gravel over v.f. sand and silt, Astoria | descrip, photos |

| | | |
|---|---|---|
| 18GW0719.2 | silt and sand, Astoria Fm | descrip |
| 18GW0719.3 | sand, possibly Astoria Fm | descrip |
| 18GW0904.1 | sand | soil descrip, sample for Be-10 dating |
| 18GW0905.1 | basalt underlying gravels and sands | n/a |
| 18GW0905.2 | sands, gravels, silts, Chehalis River deposits | soil descrip |
| 18GW0905.3 | cross bedded sands and gravels | n/a |
| 18GW0905.4 | soil | soil profile |
| 20GW0921.4 | view photos | n/a |
| 20GW0921.5 | gravels | photos, descrip, attitudes |
| 20GW0921.6 | gravels | clast point counts |
| 20GW0922.1 | gravels | photos, samples |
| 20GW0922.2 | gravels cutting into Lincoln Ck | photos, sample for biostratigraphy |
| 20GW0922.3 | Lincoln Creek silstone, highly fractures | photo |
| 20GW0922.4 | gravels | photo |
| 20GW0922.5 | gravels | n/a |
| 20GW0922.6 | oxidized gravels | n/a |
| 20GW0922.7 | oxidized gravels | n/a |
| 20GW0922.8 | silts in soil | n/a |
| 20GW0922.9 | gravels | point counts, photos |
| 21GW0819.1 | fine sand, older glacial drift? | descrip, pt count sample |
| 21GW0819.2 | silt, fine sand, gravel, older glacial drift? | descrip |
| 21GW0819.3 | silt and sand, possibly Montesano Fm | descrip, photo |
| 21GW0819.4 | sand, gravel, older glacial drift | descrip, luminescense sample |
| 21GW0819.6 | silts and clays, compact | descrip, photos |
| 21GW0819.7 | photos of lineament break in slope | photos only |
| 21GW0819.8 | weathered gravels and sand, v. compact | descrip, ,photos |

**Figures**

Figure A1-1. Outcrop located at field station 19GW814.3 near Bay Center, Washington. Scraping tool is approximately 0.25 m long and is sitting on a sandy layer with abundant broken shells. Massive sands are stratigraphically above the shell layer, with silts and very fine sands located stratigraphically below. These are part of unit Qt1. View to the east.

Figure A1-2. Blue-grey thinly bedded silts and fine sands at field station 20GW0714.7. These are part of unit Qt2. View to the south-southwest.

Figure A1-2. Thinly bedded, indurated silts and fine sand (bottom) with indurated, weathered and oxidized gravels above (darker layer with some vegetation), capped by sands and silt. Two-meter stick for scale in center bottom of photo. Field station 20GW0708.1, near Bridgeport. I interpret this as unit TQss with unit Qt2 on the geomorphically flat surface. This outcrop is represented in Plate 2. View to the southeast.

Figure A1-3. Silts and fine sands at field station 19GW815.1 showing soft sediment deformation. Unit TQss. View to the southeast.

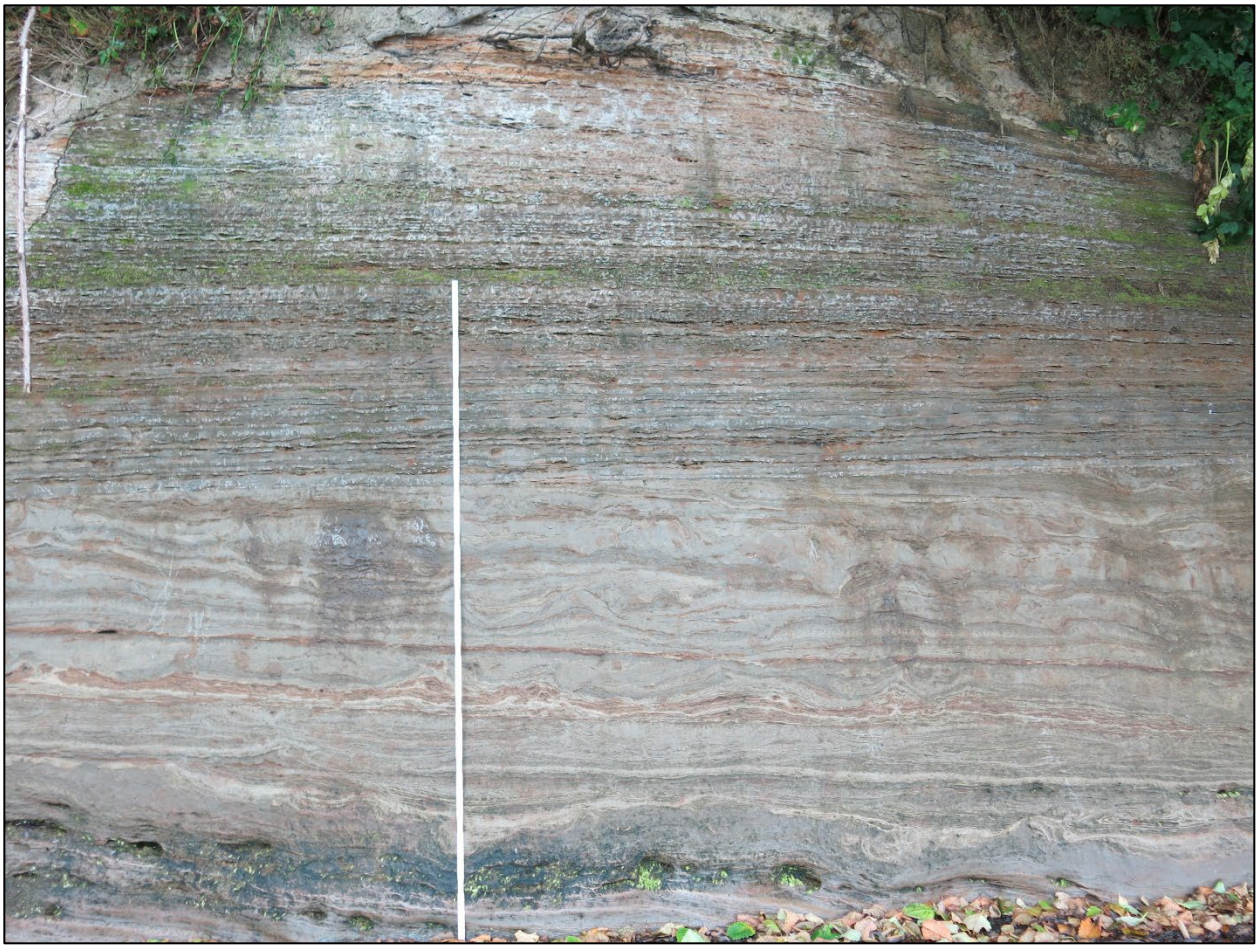

Figure A1-4. Indurated, thinly bedded silts and fine sands at field station 19GW815.1 showing soft sediment deformation and change in dip angle of beds. Two-meter stick for scale. Unit TQss. View to the southeast.

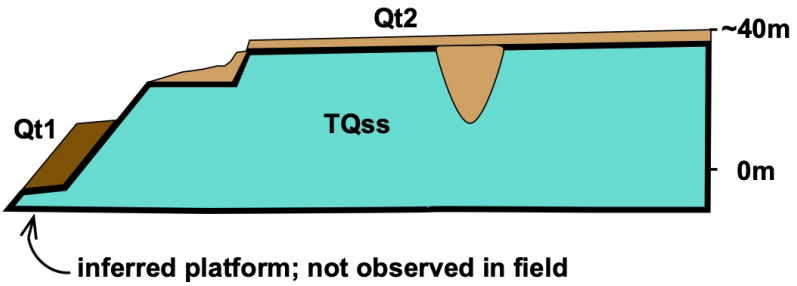


Figure A1-5. Schematic cross section showing possible relationship between units TQss, Qt1 and Qt2. Sands and silts of Qt2 are found in embayments and mantling geomorphically smooth portions of TQss, which is not terraced at all locations in the field area but not found at elevations above 60m a.s.l. The platform of TQss under Qt1 is not observed in the field but inferred from geotechnical studies near North Cove.

Figure A1-6. Subangular to subrounded, fine quartz-rich sand with minor lithics, thinly bedded with minor cross bedding. Oxidized and with minor interbeds of silts. These are field station 19GW89.1 and 20GW0701.1. Unit Qss. View to the east-northeast.

Figure A1-7. Light grey to tan sand with minor pumice layers (left) cut by oxidized sand to cobble deposit (right) at field station 19GW87.1. Scraper is approximately 25 cm long. Unit Qfch, probable fluvial and tidal deposits related to Chehalis River. View to north.

Figure A1-8. Cross-bedded fine-medium sand interfingered with coarse sand and gravel and silts at elevations from near sea-level to over 60 m a.s.l. Field station 20GW0714.6. Portion of wall from top of central talus cone to top surface is approximately 10-12 m high, with cross beds up to 1.5 m high, dipping generally to the southwest here. Unit Qsg. View to the northeast.

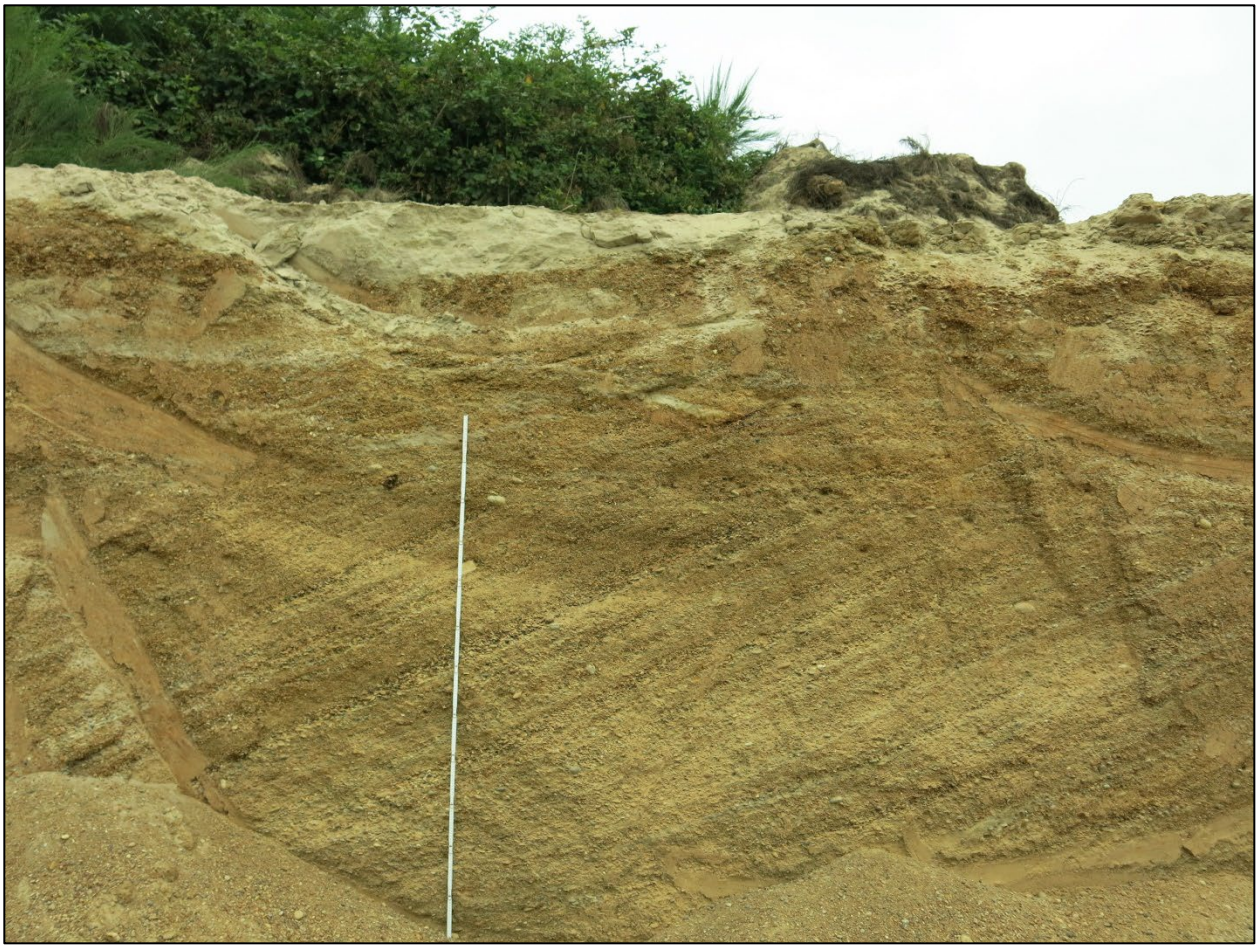

Figure A1-9. Medium to coarse sands and gravels with crossbedding dipping to the west at field station 19GW88.1. Two-meter stick for scale. Loose, gently cross bedded quartz rich sand capping the coarser deposits. Unit Qsg. View to the north.

Figure A1-10. Coarse sand to gravel, with cross bedding less than 0.75 m high, dipping to west at station 20GW0922.9. Highly indurated and oxidized, with many clasts weathered through. Where identifiable, a portion of clasts are granitic and metamorphic. Unit Qgs. Scraper approximately 25 cm long. View to the southwest.

## Maps and Plates

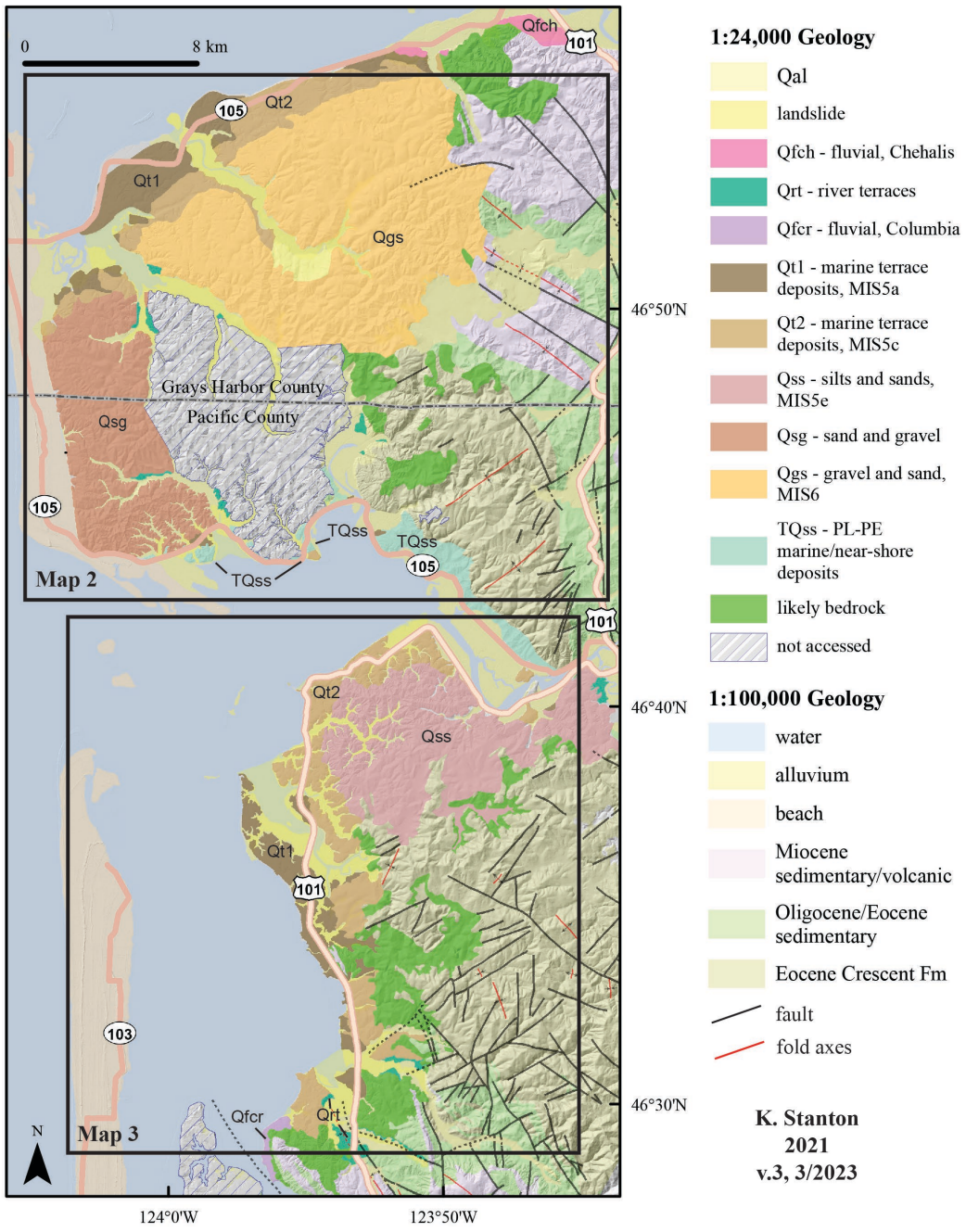


Map 1. Quaternary geology, southwestern Washington coast, south of Grays Harbor and near Willapa Bay. ~1:24,000 mapping over 1m and 10m DEM, with nearby 1:100k geology.

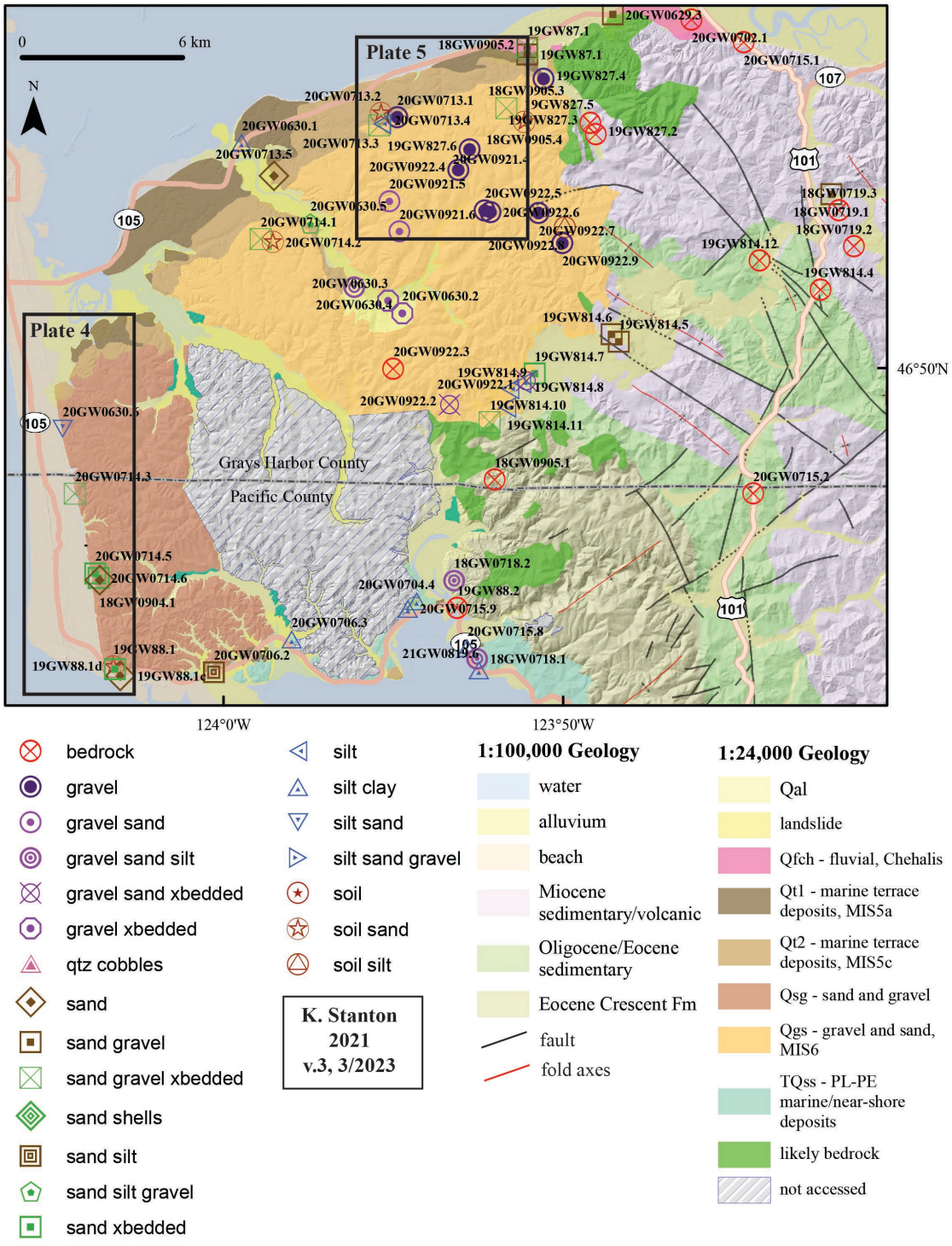


Map 2. Quaternary geology with labeled field station locations showing primary lithology, region south of Grays Harbor. ~1:24,000 mapping over 1m DEM, with nearby 1:100k geology.

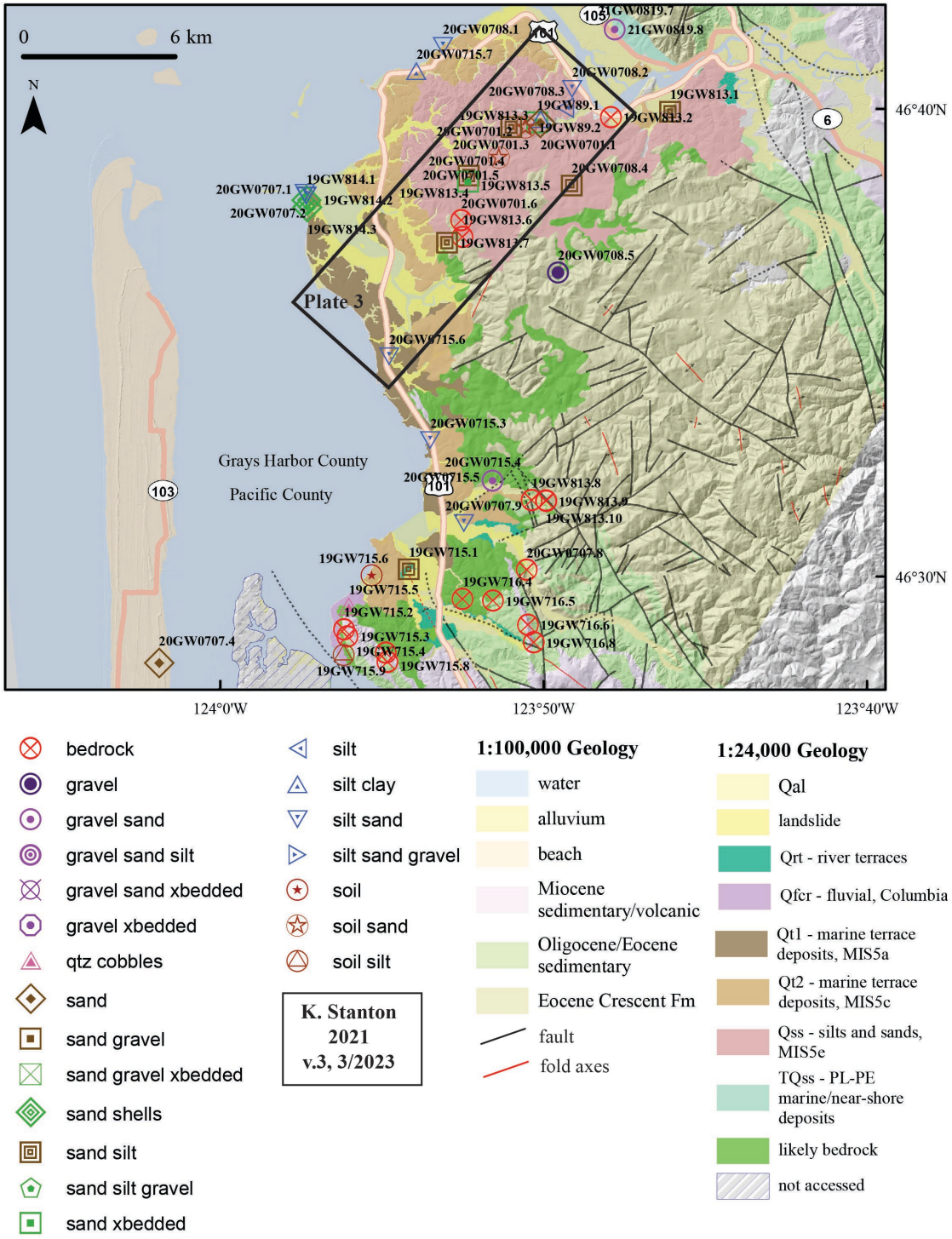


Map 3. Quaternary geology with labeled field station locations showing primary lithology, Willapa Bay. ~1:24,000 mapping over 1m DEM, with nearby 1:100k geology.

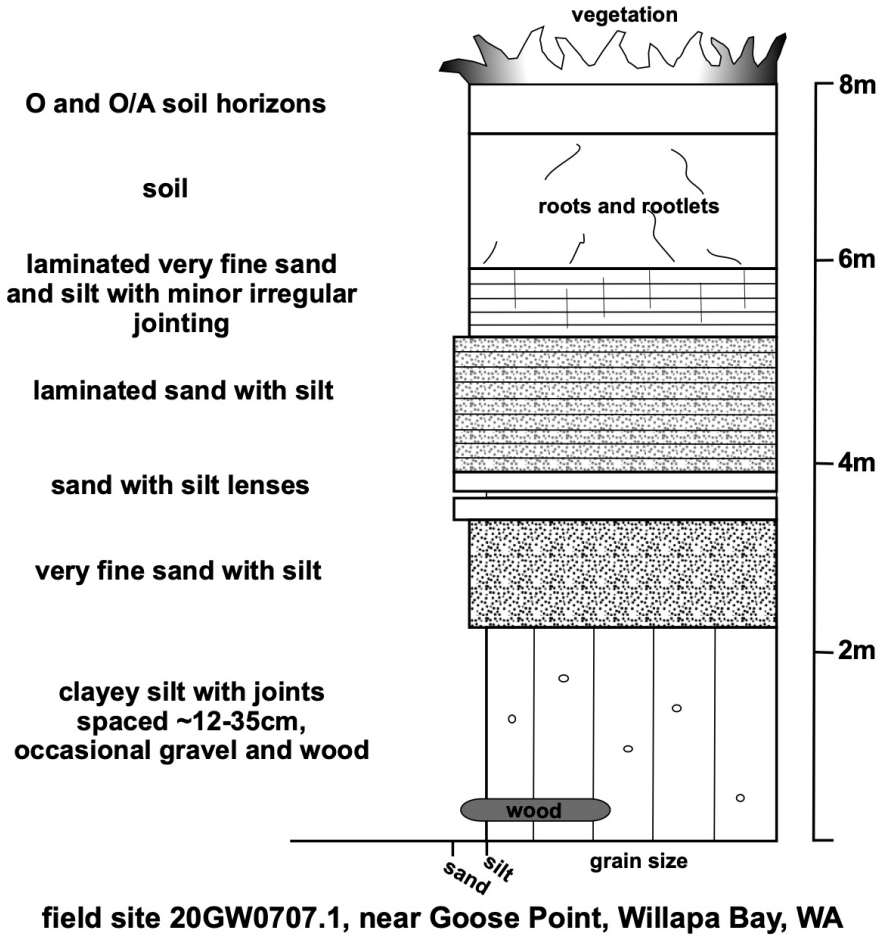


Plate 1. Measured stratigraphic section for unit Qt1.

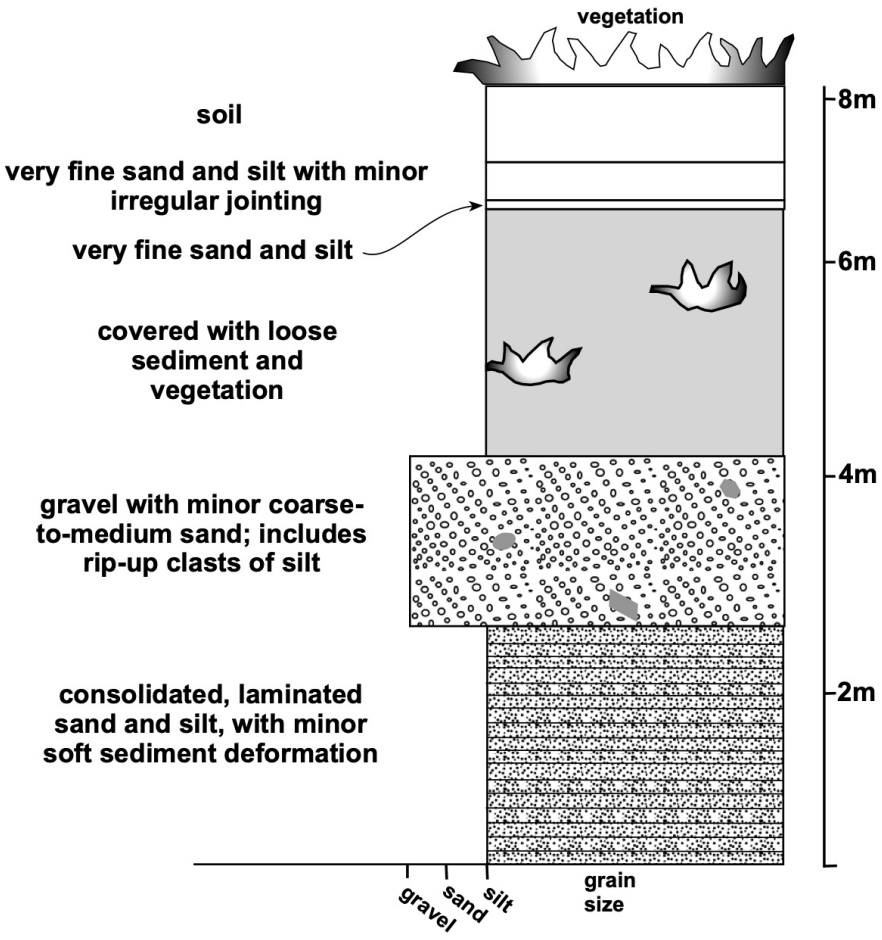


Plate 2. Measured stratigraphic section for unit TQss, Qt2.

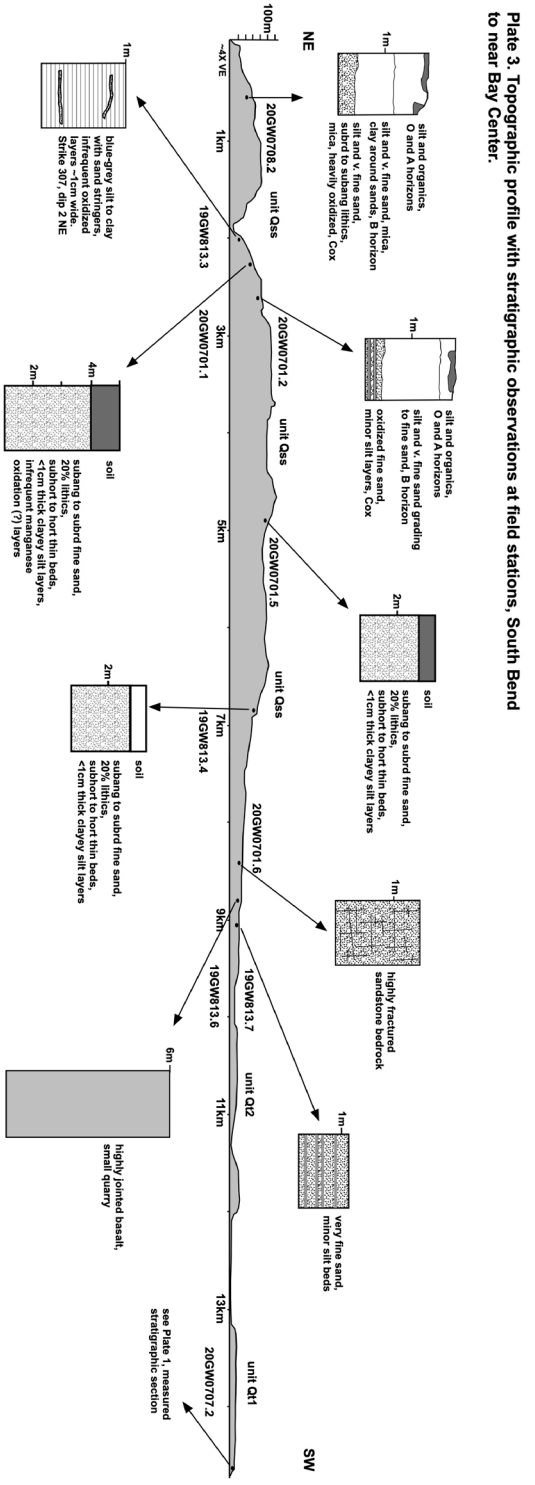


Plate 3. Topographic profile with schematic stratigraphic observations at field stations, South Bend area.

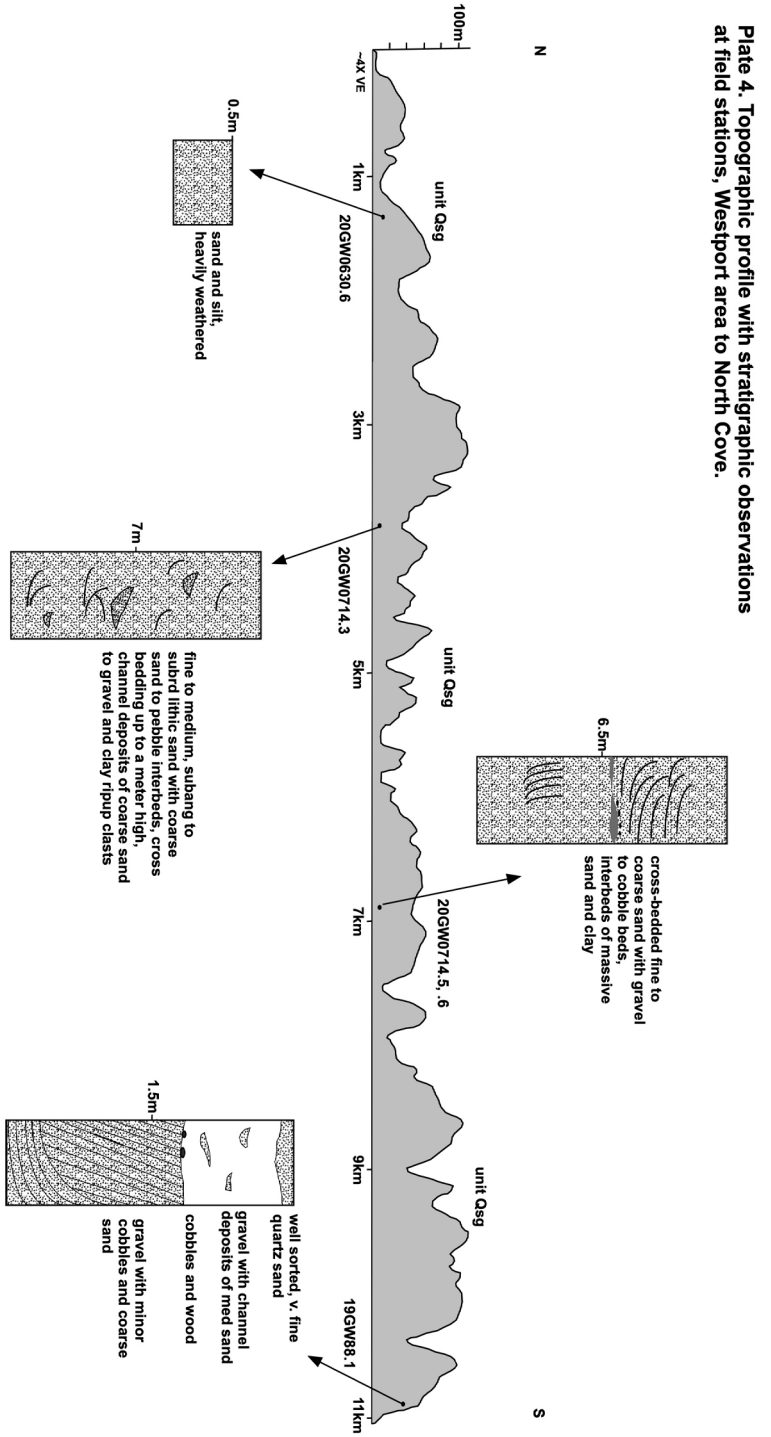


Plate 4. Topographic profile with schematic stratigraphic observations at field stations, Westport area to North Cove.

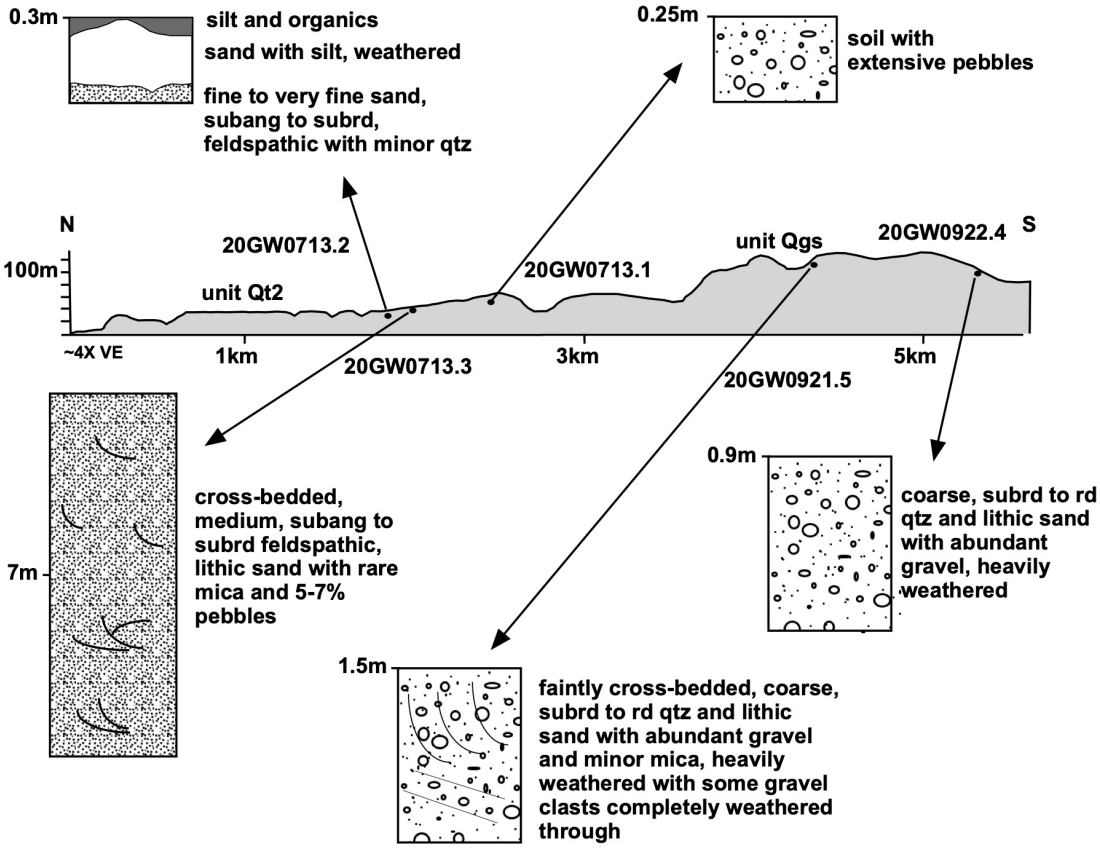


Plate 5. Topographic profile with schematic stratigraphic observations at field stations, south of Grays Harbor.

## Map Pamphlet Appendix: Geomorphic analyses for terrace identification.

### Overview

Sediments south of Grays Harbor and east of Willapa Bay were originally mapped collectively as "Quaternary terrace" deposits (Wagner 1967a, b; Walsh et al., 1987) although multiple terraces sets were acknowledged (Clifton, 1983). Marine terraces can form by erosion from wave action or from the buildup of sediments or reef material (Palmer, 1967; Lajoie, 1986). Regardless of their origin, marine terraces generally are low relief (smooth), with low slope angle (flat), originally dipping seaward between 1-5 degrees, although later tectonic deformation can warp the surfaces. Marine terraces are also laterally continuous along a shoreline (Bradley and Griggs, 1976; Lajoie, 1986; Keller and Pinter, 2002). Tectonic uplift or sea-level change can create multiple sets, or flights, of terraces along a coast (Lajoie, 1986; Bradley and Griggs, 1976).

Digital elevation models at 10m and 1m allow for an automated identification of geomorphic features using GIS analyses. To identify terraces, whether the origin is erosional or depositional, we use multiple criteria, including low angle, laterally continuous slopes, common elevation ranges, low relief and field observations showing related and continuous deposits (Table A1a-1).

### Methodology and Results

*Swath profiles*

I used a swath profile plugin tool for ArcGIS which takes topographic profiles for 500 m on either side of a profile line to calculate the maximum elevation (red line) and minimum

elevation (yellow line) topographic profile (Figure A1a-1). In the figure, the grey lines represent individual profiles. The figure shows swath profiles at two locations south of Grays Harbor where DEMs suggest possible terrace flights (Figure A1a-1a, b), as well as a location from South Bend to near Bay Center on the eastern side of Willapa Bay (Figure A1a-1c).

Swath profiles indicate dissection by streams of all surfaces at all locations in the field area. The maximum elevation likely represents a pre-erosion surface. Swath profiles show distinct elevation breaks at lower elevations, with common elevations having low slope angles between approximately 13-22 m and 28-40 m a.s.l. There are two possible continuous surfaces with low slope angle at around 45m and 60-75 m a.s.l. but only in swaths A and B. Regions above 75 m a.sl. are more highly dissected.

In addition to these examples, I used the swath profile tool at numerous locations in the field area. There are gently sloping, low relief surfaces with average elevations between 13-22 m a.s.l. and between 35-48 m a.s.l. along the southern side of Grays Harbor, and all along the eastern side of Willapa Bay. Except for the locations a and b in Figure A1a-1, all regions above 60 m a.s.l. in the field area are highly dissected when seen in profile.

*Standard deviation of elevation*

The standard deviation of elevation characterizes relative relief. Low standard deviation of elevation represents low relative relief, or in other words, flat and smooth regions. I used the Focal Statistics tool in ArcGIS to determine the standard deviation of elevation for a region south of Grays Harbor that appears to have terrace flights. I used both a 10 m DEM and the 1m DEM, using a 10X10 rectangular moving cell and a 3X3 rectangular moving cell to calculate standard

deviation of elevation. Both cell sizes and both DEMs identify similar regions of low standard deviation of elevation (Figure A1a-2), with the 1m DEM providing more detail. This analysis is intended to locate regions likely to be flat and smooth (terraces) and the detailed analysis provided by the 1m DEM is not necessary for this study. Because the study region is approximately 2000 $km^2$, for computational efficiency I used a 10X10 rectangular moving cell on the 10 m DEM to determine standard deviation of elevation for the entire field area.

The areas with the lowest standard deviation (flat and smooth) correspond with the low slope and low relief elevations ranges from the swath profiles (Figure A1a-3). South of Grays Harbor, the elevation range between approximately 60-75 m a.s.l. also has a relatively low standard deviation of elevation, although this elevation range in other parts of the study area does not show continuous low standard deviation of elevation. Northern Willapa Bay is mostly devoid of broad, continuous regions of low standard deviation of elevation. For most of the study region, elevations higher than 60 m a.s.l. have low standard deviation of elevation only along ridgelines.

*Slope and Aspect*

The study region has slopes between 0 and 80 degrees, as determined for the 10m DEM (Figure A1a-4). Approximately three quarters of the region have slopes less than 18 degrees, with a quarter of the region with slopes below 3 degrees. Areas appearing the most flat and smooth from standard deviation of elevation have slopes between 0 and 3 degrees. These slope seaward as indicated by swath profiles. Slopes in the field area do not show distinct alignment in terms of slope aspect, although coastal features tend to have seaward slope aspects (Figure A1a-5).

**Discussion**

Along the south side of Grays Harbor and the east side of Willapa Bay are two geomorphic flat and smooth features, that also have low slope angle. Generally, these correspond to elevations between 13-22 m a.s.l. and 35-48 m a.s.l. These features do not have distinct back edges, and both are dissected by streams. I infer these flat, smooth, low angle, continuous surfaces to be terraces. These features are absent along the northern side of Willapa Bay, and between Westport and North Cove.

Although there are regions that are geomorphically flat and smooth at elevations above 60 m a.s.l., these are not as continuous, as flat or smooth, nor with as shallow angle slopes as the two lower elevation terraces. The flat and smooth regions tend to be along ridge lines. It is possible these represent a relict surface and are erosional remnants.

## Tables

Table A1a-1. Criteria of geomorphic features to identify as marine terrace.

| CRITERIA | MEASURE |
|---|---|
| Topography | Continuous slope, common elevation ranges |
| Relief | Low relief (low standard deviation of elevation) |
| Slope | Low slope (<1-3 degrees) |
| Field observations | Related and continuous deposits or facies |

Table A1a-2. Elevation ranges and slope of geomorphic features.

| FEATURE | ELEVATION RANGE (M) | SLOPE (DEGREES) |
|---|---|---|
| 1 | 13-22 | 0-3 |
| 2 | 35-48 | 0-3 |
| 3 | 50-75 (?) near Grays Harbor only | 0-12 |
| 4 | >60 | 3-80 |

**Figures**

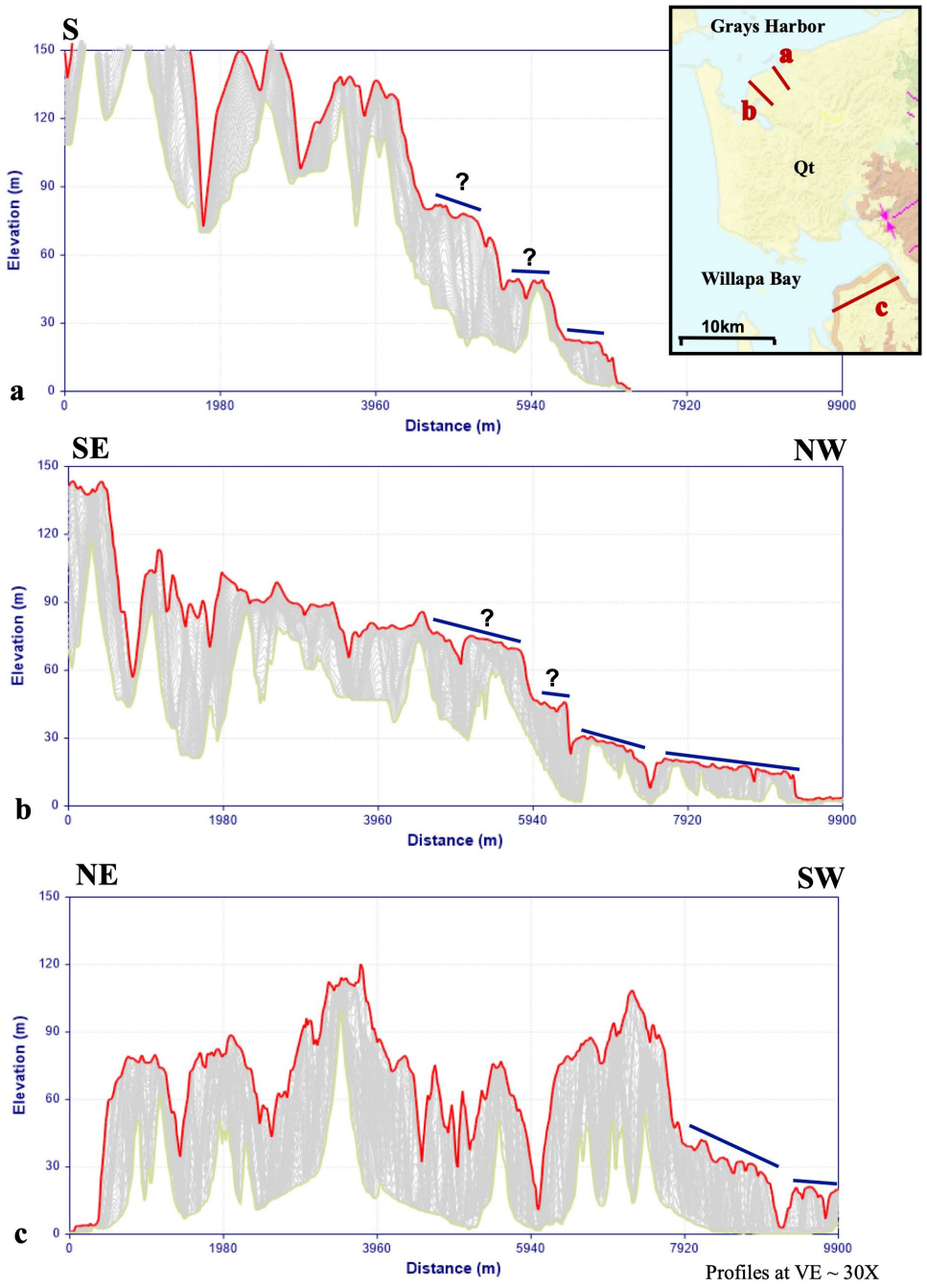


Figure A1a-1. Swath profiles showing maximum elevation in red and minimum elevation in yellow. Blue lines indicate flat and smooth surfaces.

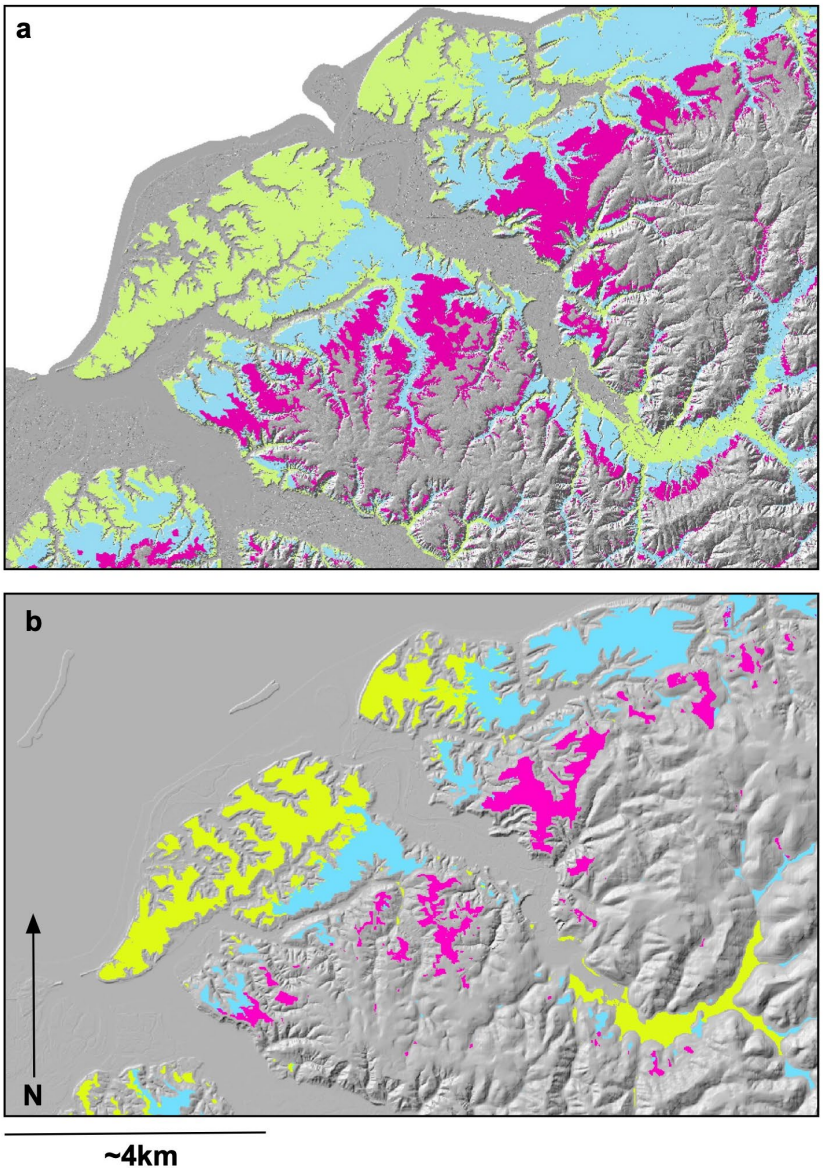


Figure A1a-2. Standard deviation of elevation colored by elevation using a) lidar and b) 10 m DEM. Yellow-green are elevations between 10-25 m a.s.l., blue are elevations between 25-50 m a.s.l., and pink are elevations between 50-68 m a.s.l.

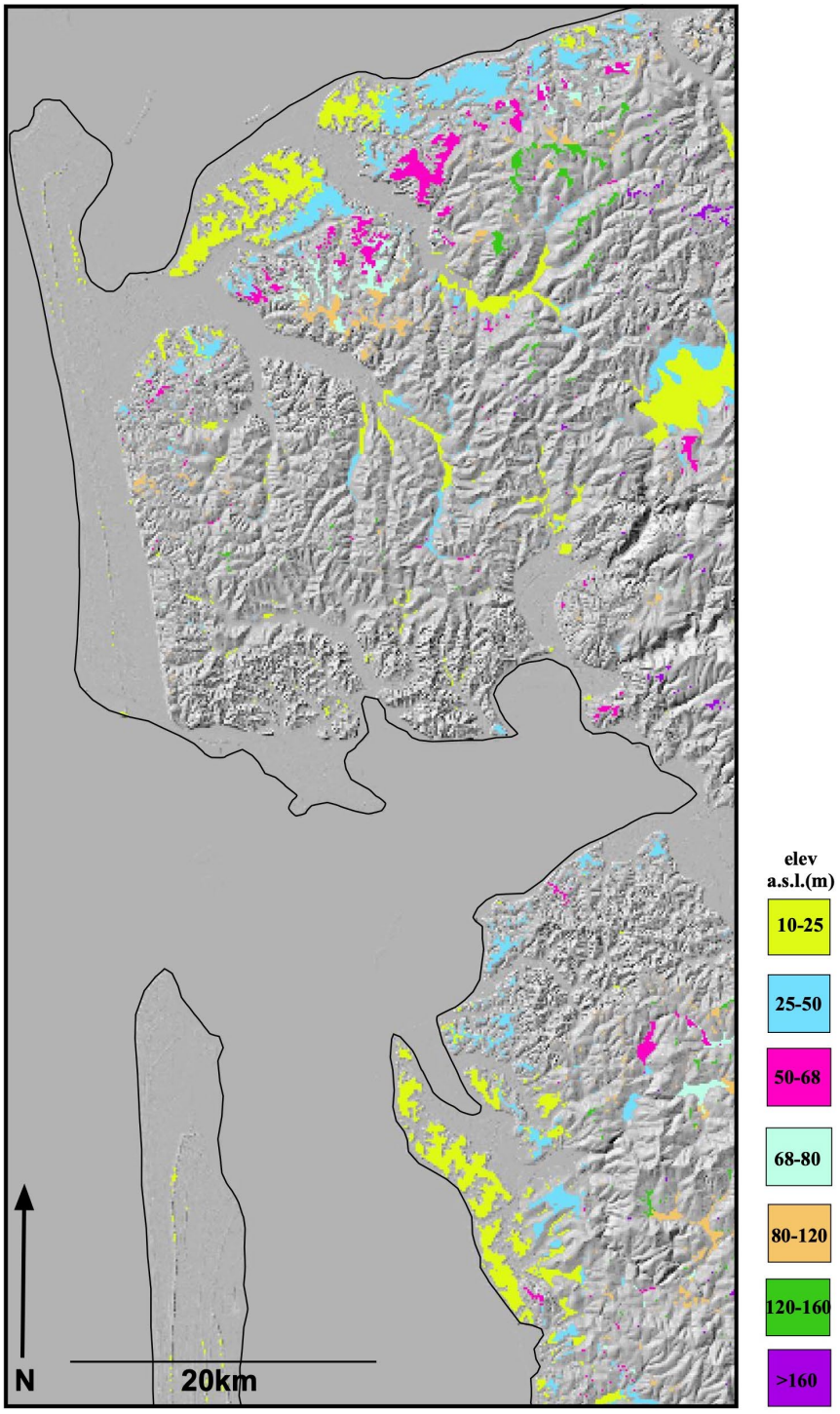


Figure A1a-3. Standard deviation of elevation below 2 from 10 m DEM colored by elevation.

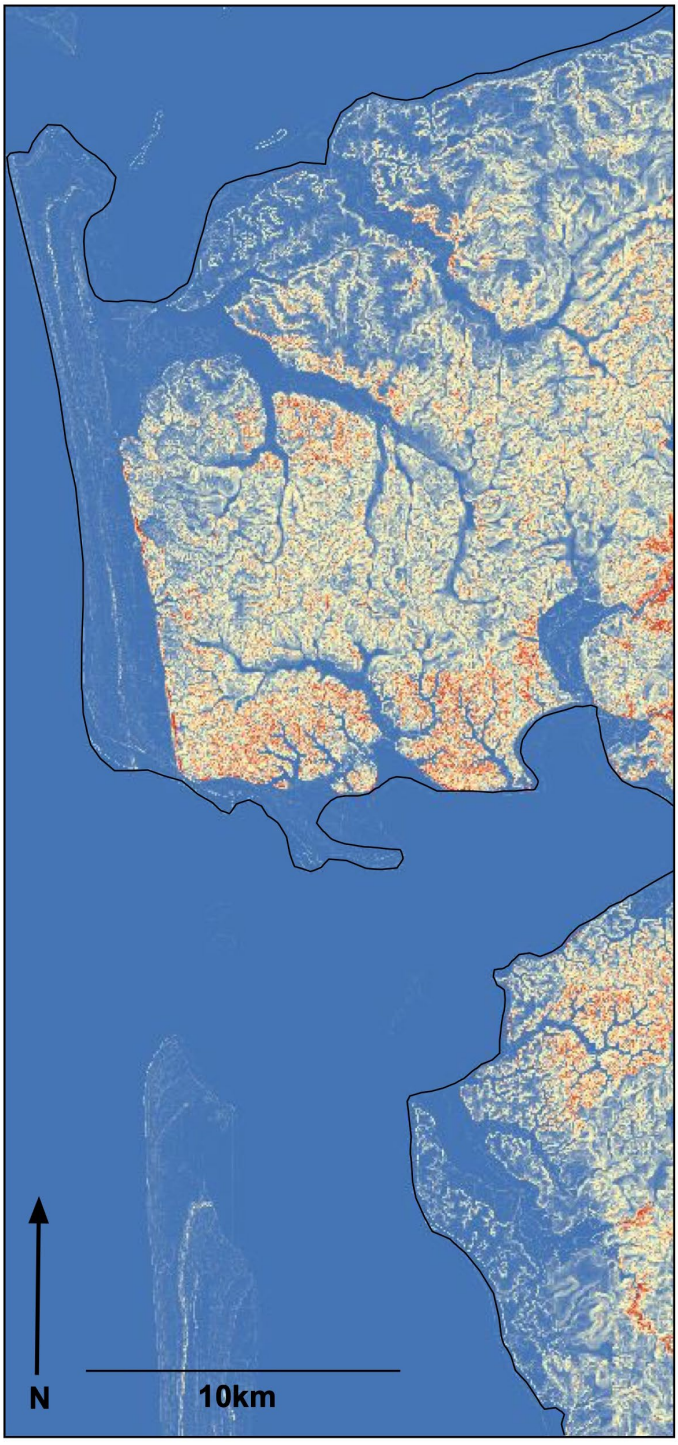


Figure A1a-4. Slope from 10m DEM. Cooler colors are lower slopes with slope range between 0-80 degrees.

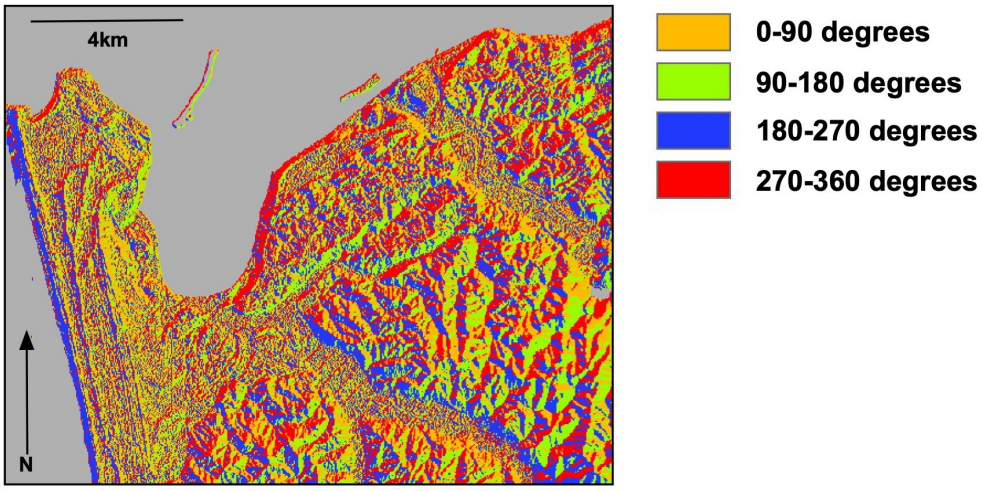


Figure A1a-5. Slope aspect of region south of Grays Harbor colored by aspect direction.

# Appendix 2. Supplementary text to Stanton et al., The signature of accumulated permanent uplift, northern Cascadia subduction zone

## Discussion of ages for luminescence dating for non-estuarine deposits

In addition to dates on estuarine sediments in the main manuscript (Tables 2-2 through 2-6), we also report feldspar luminescence ages from sediments collected in fluvial sands and gravels (sample 19GW827.1 in unit Qgs; Stanton, 2021), for sands related to the Nemah River (sample 19GW826.2 in unit Qrt; Stanton, 2021) and for sands and gravels near Elma, WA mapped as undifferentiated, pre-Fraser-glaciation continental glacial drift (Qgp) from the 1:250,000 regional geologic map (sample 21GW0819.4; Walsh et al., 1987). The ages are not discussed in the main manuscript because these samples are not from estuarine or marine sediments and are not relevant to the uplift history of the region. However, the ages of these samples contributed to the Quaternary mapping (Stanton, 2021) and may be of interest to regional studies. The sample ages are discussed in turn. Reference can be made to the radial graphs of Fig. A2-1 which show the distribution of single-grain ages from the uncorrected pIRIR measurements.

Sample 19GW826.2 is from sands in a terrace related to the Nemah River on the southeastern side of Willapa Bay at Lynn Point. An age from pIT-IRSL could not be obtained because the natural signal did not intersect the growth curve, an indication of a very old, probably over-estimated age, which could indicate partial bleaching. The FMM (uncorrected; Table 2-4 in the main text) shows a small percentage of young grains which are likely contamination. The minimum age is best represented by the second component, which gives an age of 76.7 ± 6.11 ka. The third component, representing 68% of the grains, gives a much older age of 180 ± 9.13 ka. Because sample 19GW826.2 is from deposits mapped as Nemah River terraces, it is equally

possible that the terraces are very old or are younger with partially bleached, reworked sediments.

Sample 19GW827.1 is from fluvial gravels and sands at high elevation within unit Qgs. It contains some young grains, but more than 60% of the grains are more than about 200 ka. This is consistent with the high degree of weathering and oxidation of the sediments. We interpret these as outwash related to the Double Bluff glaciation (MIS6).

Sample 21GW0819.4 is from sands and gravels in a high terrace above the Chehalis River between Montesano and Elma. It has been mapped as pre-Fraser-glaciation, undifferentiated glacial drift (Qgp; Walsh et al., 1987). It has a few young grains, but almost 90% of the grains are older than about 160 ka, consistent with pre-Fraser-glaciation deposits.

## Tables

**Table A2-1. Measured depth to Cox horizon at field stations.**

| Field Station* | Unit | Depth to Cox (cm) |
|---|---|---|
| 18GW0905.2 | Qfch | 52 |
| 19GW814.6 | bedrock | 54 |
| 19GW813.1 | Qt1 | 72 |
| 20GW0701.10 | out of field area, Qfcr? | 80 |
| 18GW0904.1 | Qsg | 80 |
| 20GW0715.6 | Qt1 | 90 |
| 19GW87.1 | Qt1 | 100 |
| 19GW88.1 | Qsg | 110 |
| 20GW0715.4 | Qt2 | 110 |
| 20GW0713.5 | Qt2 | 125 |
| 20GW0704.4 | Qt2 | 140 |
| 19GW89.2 | Qss | 150 |
| 20GW0630.2 | Qls/Qt2 | 150 |
| 20GW0701.2 | Qss | 150 |
| 20GW0701.5 | Qss | 175 |
| 20GW0708.2 | Qss | 180 |
| 19GW715.6 | Qt2 | 200 |
| 19GW716.4 | bedrock | 200 |
| 19GW89.1 | Qss | 200 |
| 20GW0630.1 | Qt1/2 | 200 |
| 20GW0708.5 | Qgs | 200 |
| 18GW0905.4 | Qgs | 200 |
| 20GW0714.1 | Qgs | 300 |

*See Stanton, 2021 for field station locations.

**Table A2-2. Range of uplift rates for terraced estuarine sediments near South Bend, WA.**

| Unit | MIS | Back edge elevation (m) [1] | Cover sediment thickness (m) [2] | Inner edge elevation (m) | Sea-level fluctuation (m) [3] | Paleo sea-level compared to modern (m) [4] | Uplift (m) [5] | Age (ka) [6] | Uplift rate (mm/y) [7] |
|---|---|---|---|---|---|---|---|---|---|
| **Qt1** | 5a | 21 | 4 | 17 | 2 | -12 | 31 | 82 | 0.4 |
| | | | | | | -26 | 45 | 82 | 0.5 |
| | | | | | -2 | -12 | 27 | 82 | 0.3 |
| | | | | | | -26 | 41 | 82 | 0.5 |
| | | | 14 | 7 | 2 | -12 | 21 | 82 | 0.3 |
| | | | | | | -26 | 35 | 82 | 0.4 |
| | | | | | -2 | -12 | 17 | 82 | 0.2 |
| | | | | | | -26 | 31 | 82 | 0.4 |
| **Qt2** | 5c | 42 | 4 | 38 | 2 | -3 | 43 | 96 | 0.4 |
| | | | | | | -17 | 57 | 96 | 0.6 |
| | | | | | -2 | -3 | 39 | 96 | 0.4 |
| | | | | | | -17 | 53 | 96 | 0.6 |
| | | | 14 | 28 | 2 | -3 | 33 | 96 | 0.3 |
| | | | | | | -17 | 47 | 96 | 0.5 |
| | | | | | -2 | -3 | 29 | 96 | 0.3 |
| | | | | | | -17 | 43 | 96 | 0.4 |

**[1] Terrace back edge elevation estimated from eroded traces on DEM.**

**[2] Minimum sediment thickness from Qt2 exposures at modern sea-cliffs near Bay Center. Qt1 sediment thickness is at least 14 m, greater than the lowest terrace surface elevation of ~13 m.**

**[3] Wave cut benches mark mean sea-level, which varies with tides and storms. We use the tidal fluctuation for Willapa Bay of ±2 m (Michalsen et al., 2010).**

**[4] Paleo-sea-level elevation has not been modeled for the field area so we used the range of rates at Coquille, OR from geodynamic models (Creveling et al., 2017).**

**[5] Uplift is the difference between the paleo sea-level elevation and the current elevation of the inner edge (back edge minus sediment thickness) plus/minus the sea-level fluctuation.**

**[6] MIS peak age (Lisiecki and Raymo, 2005).**

**[7] Uplift rate is the total uplift divided by the age of the terrace surface.**

**Table A2-3. Range of uplift rates for estuarine sediments near South Bend, WA using eustatic paleo-sea-level estimates.**

| Unit | MIS | Back edge elevation (m) | Cover sediment thickness (m) | Inner edge elevation (m) | Sea-level fluctuation (m) | Paleo sea-level compared to modern (m) * | Uplift (m) | Age (ka) | Uplift rate (mm/y) |
|---|---|---|---|---|---|---|---|---|---|
| **Qt1** | 5a | 21 | 4 | 17 | 2 | 0 | 19 | 82 | 0.2 |
| | | | | | | -24 | 43 | 82 | 0.5 |
| | | | | | -2 | 0 | 15 | 82 | 0.2 |
| | | | | | | -24 | 39 | 82 | 0.5 |
| | | | 14 | 7 | 2 | 0 | 9 | 82 | 0.1 |
| | | | | | | -24 | 33 | 82 | 0.4 |
| | | | | | -2 | 0 | 5 | 82 | 0.1 |
| | | | | | | -24 | 29 | 82 | 0.4 |
| **Qt2** | 5c | 42 | 4 | 38 | 2 | -6 | 46 | 96 | 0.5 |
| | | | | | | -12 | 52 | 96 | 0.5 |
| | | | | | -2 | -6 | 42 | 96 | 0.4 |
| | | | | | | -12 | 48 | 96 | 0.5 |
| | | | 14 | 28 | 2 | -6 | 36 | 96 | 0.4 |
| | | | | | | -12 | 42 | 96 | 0.4 |
| | | | | | -2 | -6 | 32 | 96 | 0.3 |
| | | | | | | -12 | 38 | 96 | 0.4 |

***MIS 5c and 5e eustatic sea-level from Chappell and Shackleton (1986). All other values as for Table S2.**

**Table A2-4. Range of uplift rates for estuarine sediments near South Bend, WA using geodynamic model estimates of paleo-sea-level elevation near 46° N latitude from Simms et al. (2016).***

| Unit | MIS | Back edge elevation (m) | Cover sediment thickness (m) | Inner edge elevation (m) | Sea-level fluctuation (m) | Paleo sea-level compared to modern (m) | Uplift (m) | Age (ka) | Uplift rate (mm/yr |
|---|---|---|---|---|---|---|---|---|---|
| **Qt1** | 5a | 21 | 4 | 17 | 2 | -15 | 34 | 82 | 0.4 |
| | | | | | | -33 | 52 | 82 | 0.6 |
| | | | | | -2 | -15 | 30 | 82 | 0.4 |
| | | | | | | -33 | 48 | 82 | 0.6 |
| | | | 14 | 7 | 2 | -15 | 24 | 82 | 0.3 |
| | | | | | | -33 | 42 | 82 | 0.5 |
| | | | | | -2 | -15 | 20 | 82 | 0.2 |
| | | | | | | -33 | 38 | 82 | 0.5 |
| **Qt2** | 5c | 42 | 4 | 38 | 2 | -10 | 50 | 96 | 0.5 |
| | | | | | | -25 | 65 | 96 | 0.7 |
| | | | | | -2 | -10 | 46 | 96 | 0.5 |
| | | | | | | -25 | 61 | 96 | 0.6 |
| | | | 14 | 28 | 2 | -10 | 40 | 96 | 0.4 |
| | | | | | | -25 | 55 | 96 | 0.6 |
| | | | | | -2 | -10 | 36 | 96 | 0.4 |
| | | | | | | -25 | 51 | 96 | 0.5 |

*** All other values as for Table S2.**

**Table A2-5. Uplift rates for sites along Cascadia as numbered in Figure 2-6.**

| ID | Latitude | Longitude | Location * | Max long-term uplift or incision (mm/yr) |
|---|---|---|---|---|
| **1** | 47.608372 | -124.37574 | Kalaloch | -0.03-0.4 |
| **2** | 47.542588 | -124.349716 | Clearwater | <0.1-0.9 |
| **3** | 46.98736 | -123.650423 | Wynoochee | 0.4±0.3-1.8±0.3 |
| **4** | | | near South Bend, average of 2 sites | 0.4±0.1 |
| **5** | 45.804667 | -123.814833 | Cougar Creek, NF Nehalem River | 0.9±0.1 |
| **6** | 45.2785 | -123.778833 | Tony Creek, Nestucca River | 0.5±0.1 |
| **7** | 44.786167 | -123.795833 | Lower Gorge, Siletz River | 0.7±0.2 |
| **8** | 44.714833 | -123.932 | Camp Twelve, Siletz River | <1.3±0.3 |
| **9** | 44.511 | -123.833167 | Drift Creek Meadows | 0.1±0.3 |
| **10** | 43.940833 | -123.897833 | Sweet Creek, Siuslaw River | <0.1±0.2 |
| **11** | 43.759667 | -123.506667 | Hudson Slough, Smith River | <0.2±0.2 |
| **12** | 43.802333 | -123.807333 | Bear Creek, Smith River | <0.3±0.3 |
| **13** | 43.683333 | -124.096833 | Crestview, Umpqua River | <0.4±0.3 |
| **14** | 44.777126 | -124.073402 | north of Cape Foulweather, OR | 0.1-0.3 |
| **15** | 44.677275 | -124.078634 | Yaquina Head, OR | 0.5-0.8 |
| **16** | 44.316177 | -124.107496 | Yachats, OR | 0-0.4 |
| **17** | 43.30847 | -124.39416 | Cape Arago, OR | 0.5-0.8 |
| **18** | 42.8422 | -124.54838 | Cape Blanco, OR | 0.5-1.4 |
| **19** | 42.10351 | -124.35116 | Cape Ferrelo, OR | 0.7-0.9 |
| **20** | 42.04285 | -124.25645 | Harbor Bench, OR | 0.1-0.2 |
| **21** | 41.761769 | -124.224339 | Crescent City, CA | 0-0.3 |
| **22** | 41.005109 | -124.151146 | Trinidad, CA | 0.6-1.1 |

*** See accompanying Table S6 for sources and additional information at each site by location.**

**Table A2-6. Compilation of uplift or incision rates from Cascadia coastal deformation studies.**

| Source | Location | Latitude | Longitude | Deformation type | How deformation determined | Max long-term uplift or incision (mm/yr) | Holocene or geodetic uplift (mm/yr) | Surface expression of crustal fault | Evidence of folding | Notes | Sea level used (m relative to modern) | MIS |
|---|---|---|---|---|---|---|---|---|---|---|---|---|
| Kelsey, 1990; Muhs et al., 1990,1992; Kelsey et al., 1994 | Cape Blanco, OR | 42.84220000 | -124.54838000 | uplift along fold axis | marine terraces | 0.5-1.4 | 6.0-10.0 | Y | Y | Uplift along E-W trending anticlinal axis, uplift req. due to reoccupation of terraces, Holocene rate based on storm berm. Fold possibly onshore extension of mapped offshore fold belt. Used two sea-level models for uplift; New Guinea model from Chappel and Shackleton, 1986 and C-J model from Machida, 1975 and Muhs et al., 1988. Imroves on ages from previous studies of same terraces, such as West and McCrumb, 1988. | 80k:-19±5 and -5±2; 105k:-9±3 and -2; 125k:+6 | 5a, 5c, 5e; probable 7; highest terrace possibly early Pleistocene based on fossils, soil development, dissection. |
| McInelly and Kelsey, 1990; Muhs et al., 1990, 1992; Kelsey et al., 1994 | Cape Arago, OR | 43.30847000 | -124.39416000 | uplift and folding | marine terraces | 0.5-0.8 | n/a | Y | Y | Holocene deformation identified by folding and faulting of lowest terrace with drowned Sitka spruce age control; other terraces warped in broad, N-S trending fold; Used two sea-level models for uplift; New Guinea model from Chappel and Shackleton, 1986 and C-J model from Machida, 1975 and Muhs et al., 1988. Also considered tilt and strain rates, not reported in this table. | 80k:-19±5 and -5±2; 105k:-9±3 and -2; 125k:+6; 200k: +2 | 5a,5c,5e; probable 7; highest terrace age not discussed |
| Kelsey and Bockheim, 1994 | Harbor Bench, OR | 42.04285000 | -124.25645000 | uplift | marine terraces | 0.05-0.2 | n/a | Y | N | Soil chronosequence to match terraces in the region, then correlated to terraces near Capes Blanco, Arago for ages. Used Muhs et al 1992 CA sea level model. Location of terraces indicate Whaleshead fault zone active in Quaternary with vertical uplift rate of about 0.5 m/ky, and | 80k: -5±2; 105k: -2 | 5e |

| | | | | | | | | | | | | |
|---|---|---|---|---|---|---|---|---|---|---|---|---|
| | | | | | | | | | | sinistral slip since 200ka of about 2.5 m/ky. | | |
| Kelsey and Bockheim, 1994; Kelsey et al., 1994 | Cape Ferrelo, OR | 42.10351000 | -124.35116000 | uplift | marine terraces | 0.7-0.9 | n/a | Y | N | Soil chronosequence to match terraces in the region, then correlated to terraces near Capes Blanco, Arago for ages. Used Muhs et al 1992 CA sea level model. Location of terraces indicate Whaleshead fault zone active in Quaternary with vertical uplift rate of about 0.5 m/ky, and sinistral slip since 200ka of about 2.5 m/ky. | 80k: -5±2; 105k: -3 | 5a, 5c, 5e, 7; three additional terraces older than 7. |
| Kelsey et al., 1996; Ticknor, 1993 | north of Cape Foulweather, OR | 44.77712600 | -124.07340200 | uplift | marine terraces | 0.07-0.27 | n/a | Y | N | North of the Cape Foulweather fault. Soil chronosequence to match terraces with ages correlated from Kennedy, 1978 and Kennedy et al., 1982. | 80k:-3, -7; 125k:6 | 5a, 5e |
| | Yaquina Head, OR | 44.67727500 | -124.07863400 | uplift | marine terraces | 0.48-0.82 | N/a | Y | N | between Cape Foulweather fault and Yaquina Bay fault. Soil chronosequence to match terraces with ages correlated from Kennedy, 1978 and Kennedy et al., 1982. | 80k: -3, -7; 105k:-2; 125k: 6 | 5a, 5c, 5e |
| | Yachats, OR | 44.31617700 | -124.10749600 | uplift | marine terraces | 0-0.35 | n/a | Y | N | South of Yaquina Bay fault. Soil chronosequence to match terraces with ages correlated from Kennedy, 1978 and Kennedy et al., 1982. | 105k: -2; 125k: 6 | 5c, 5e |
| Personius, 1995 | Henderer Rd, Umpqua River | 43 38.39 | -12336.30000000 | incision | stream terraces | 0.3 ± 0.2 | n/a | N | N | bedrock sandstone and siltsone with rock strength rating of 66; TL age 125,000 ±20,000 | n/a | 5e possibly |
| | Crestview, Umpqua River | 43.68333300 | -124.09683300 | incision | stream terraces | <0.4±0.3 | n/a | N | N | bedrock sandstone with rock strength rating of 77; TL age of greater than 200,000 ±50,000 | n/a | could be 5e or 6 |

| | | | | | | | | | | | | |
|---|---|---|---|---|---|---|---|---|---|---|---|---|
| | Bear Creek, Smith River | 43.80233300 | -123.80733300 | incision | stream terraces | <0.3±0.3 | n/a | N | N | bedrock sandstone and siltstone with rock strength rating of 68; radiocarbon age of >43,600 ±5,000 B.P | n/a | MIS 3 |
| | Hudson Slough, Smith River | 43.75966700 | -123.50666700 | incision | stream terraces | <0.2±0.2 | n/a | N | N | bedrock sandstone and siltstone with rock strength rating of 68; radiocarbon age of >39,600 ±5,000 B.P | n/a | MIS 3 |
| | Sweet Creek, Siuslaw River | 43.94083300 | -123.89783300 | incision | stream terraces | <0.1±0.2 | n/a | N | N | bedrock sandstone with rock strength rating of 72; radiocarbon age of >42,000 ±5,000 B.P. | n/a | MIS 3 |
| | Drift Creek Meadows | 44.51100000 | -123.83316700 | incision | stream terraces | 0.1±0.3 | n/a | N | N | bedrock sandstone with rock strength rating of 65; calibrated radiocarbon age 12,010 ±1500 | n/a | MIS1 |
| | Camp Twelve, Siletz River | 44.71483300 | -123.93200000 | incision | stream terraces | <1.3±0.3 | n/a | N | N | bedrock sandstone and shale with rock strength rating of 58; noted that prob min age and max incision rate; calibrated radiocarbon age of 14,300 ±1,000 | n/a | MIS 1 |
| | Lower Gorge, Siletz River | 44.78616700 | -123.79583300 | incision | stream terraces | 0.7±0.2 | n/a | N | N | bedrock basalt with rock strength rating 77; radiocarbon age of 41,600 ±5,000 B.P.; noted additiona age of >36,000 B.P. may indicate max incision rate | n/a | MIS3 |
| | Tony Creek, Nestucca River | 45.27850000 | -123.77883300 | incision | stream terraces | 0.5±0.1 | n/a | N | N | bedrock slate and shale with rock strength rating of 60; calibrated radiocarbon age 15,400 ±1,000 | n/a | MIS 1 |
| | Cougar Creek, NF Nehalem River | 45.80466700 | -123.81483300 | incision | stream terraces | 0.9±0.1 | n/a | N | N | bedrock slate and shale with rock strength rating of 60; calibrated radiocarbon age 12,030 ±1,000 | n/a | MIS 1 |
| Thackray, 1996, 1998 | Kalaloch | 47.60837200 | -124.37574000 | uplift, folding | wave-cut surface and outwash sediments | 0.1-0.5 if 5c; -0.03-0.35 if 5e | 0.08-3.2 | N | Y | uplift rates based on best estimate for age of platform (MIS5e or 5c), if older (MIS7), could represent up to 0.7 mm/yr uplift; refers to these as geologic uplift rate as different from geodetic; notes interseismic strain rate less here than on OR coast, and less on Olympic coast than inland | 5a: -5; 5c: -2; 5e: +6; 7:-7 | 5c or 5e; possibly 5a or 7 but unlikely |

| | | | | | | | | | | | | |
|---|---|---|---|---|---|---|---|---|---|---|---|---|
| Pazzaglia and Brandon, 2001; Pazzaglia et al., 2003 | Clearwater | 47.54258800 | -124.34971600 | incision | incision of streams | <0.1-0.9 | n/a | N | N | incision on Clearwater River with increased incision toward head; suggest uplift due to frontal accretion based on hortizontal movement of a sea-cliff . Oldest terraces ~140k | n/a | MIS7 oldest |
| Delano et al 2017 | Wynoochee | 46.98736000 | -123.65042300 | incision | incision of streams | 0.4±0.3-1.8±0.3 | n/a | Y | N | Since ~14k, also influenced by Canyon River fault | n/a | MIS 1 |
| Padget et al 2019 | Trinidad, CA | 41.00510900 | -124.15114600 | uplift | marine terraces | 0.61-1.05 | n/a | Y | Y | accomodated by Trinidad fault and anticline so an acutal mechanism for uplift instead of accumulated uplift by unknown processes as in most cases | 5a:-8 to -14; 5c:-2 to -7;(Creveling et al 2017); 5e: 10.91 to 13.01 (Creveling et al 2015) | 5a, 5c, 5e, 7 |
| Polenz and Kelsey, 1999 | Crescent City, CA | 41.76176900 | -124.22433900 | uplift and folding | marine terraces | 0-0.3 | n/a | N | Y | accomodated by folding on Lake Earl syncline and St. George fault. | 5a: -4; 5c: -1; 5e: +6 | 5a, 5c, 5e |

**Table A2-7. Uplift rates for select Cascadia studies using propagation of error.**

| Study * | mean back edge (m) | back edge sd(m) | mean sediment thickness (m) | sediment thickness sd (m) | mean sea-level (m) | sea-level sd (m) | mean paleo sea-level (m) | paleo sea level sd (m) | uplift (m) | uncertainty (m) | age (ka) | age sd (ky) | uplift rate (mm/y) | rate uncertainty (mm/yr) |
|---|---|---|---|---|---|---|---|---|---|---|---|---|---|---|
| **Padgett et al., 1** | 40 | 3 | 8.9 | 3.3 | 0 | 2.5 | -11 | 3 | 42 | 6 | 84 | 4 | 0.5 | 0.074 |
| **Padgett et al., 2** | 85 | 3 | 12.9 | 5.4 | 0 | 2.5 | -4.5 | 2.5 | 77 | 7 | 106 | 4 | 0.7 | 0.072 |
| **Padgett et al., 3** | 140 | 3 | 7.5 | 1 | 0 | 2.5 | 11.96 | 1.05 | 121 | 4 | 120 | 4 | 1.0 | 0.048 |
| **Kelsey and Bockheim, Brookings** | 53 | 6 | 0 | 0 | 0 | 2 | -5 | 2 | 58 | 7 | 80 | 4 | 0.7 | 0.090 |
| **K&B,Cape Ferrelo** | 86 | 6 | 0 | 0 | 0 | 2 | -2 | 2 | 88 | 7 | 105 | 4 | 0.8 | 0.071 |
| **K&B, Rainbow Rock Rd** | 89 | 6 | 0 | 0 | 0 | 2 | 6 | 4 | 83 | 7 | 125 | 4 | 0.7 | 0.064 |

***Locations given in Fig. 2-6; additional information in Tables S5 and S6.**

## Figures

Figure A2-1. Radial plots of the pIRIR data. Radial graphs are x-y plots where the x-axis represents precision and the y-axis the equivalent dose. The equivalent dose is normalized by the number of standard errors the value is from a reference point. Radial graphs take into account differential precision and will give more weight to values with the smallest error terms. A radial graph also contains a second y-axis on the right to represent the measured, non-standardized value. A line drawn from the origin through any point intersects this axis at the non-standardized value. References are shown as lines drawn from the origin to the right-hand scale, intersecting it at the derived age for that reference. The references plotted are the central tendency (computed as the central age model) of the two components from the finite mixture model with the highest proportion of grains. The shaded area which the reference line bisects encompasses all points within two standard errors of the reference. The yellow shading is the oldest of these two components, the blue shading the youngest. A red line representing the age from the central age model is shown for sample 19GW826.1 (the only sample where this might be relevant).

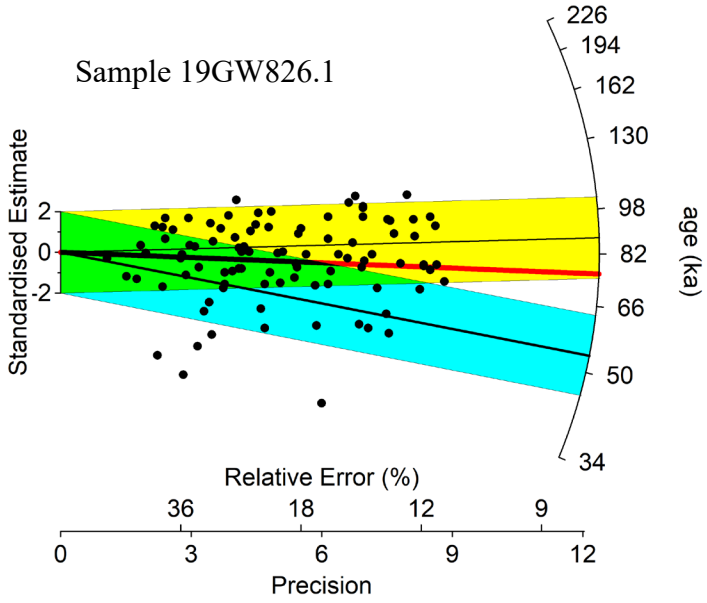

Sample 19GW826.2

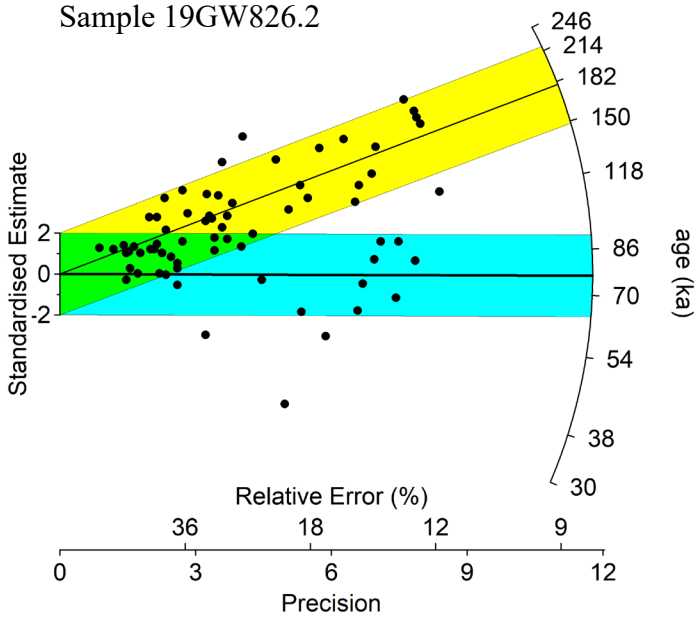


Sample 19GW827.1

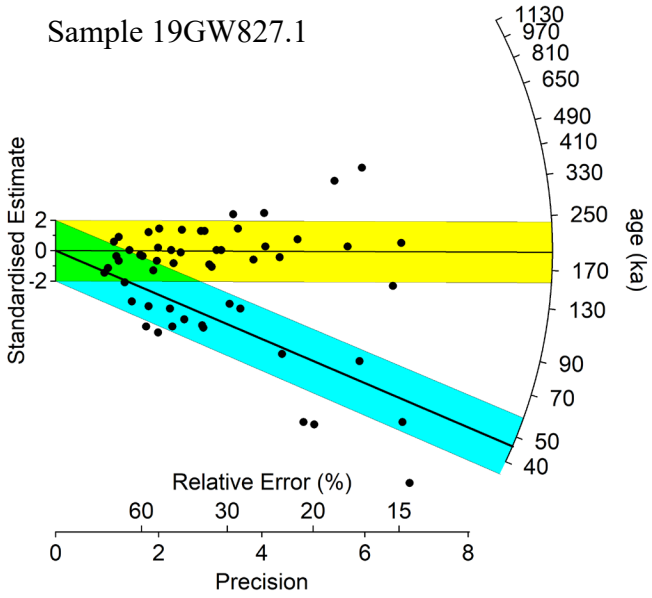

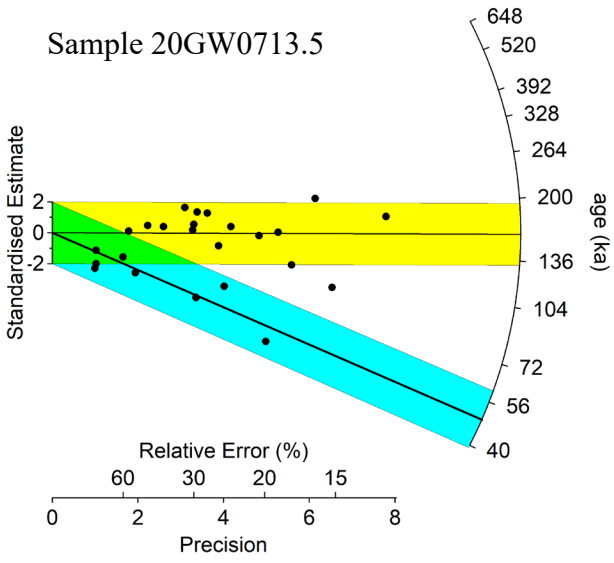
Sample 20GW0713.5
Standardised Estimate
2
0
-2
648
520
392
328
264
200
136
104
72
56
40
age (ka)
Relative Error (%)
60
30
20
15
0
2
4
6
8
Precision

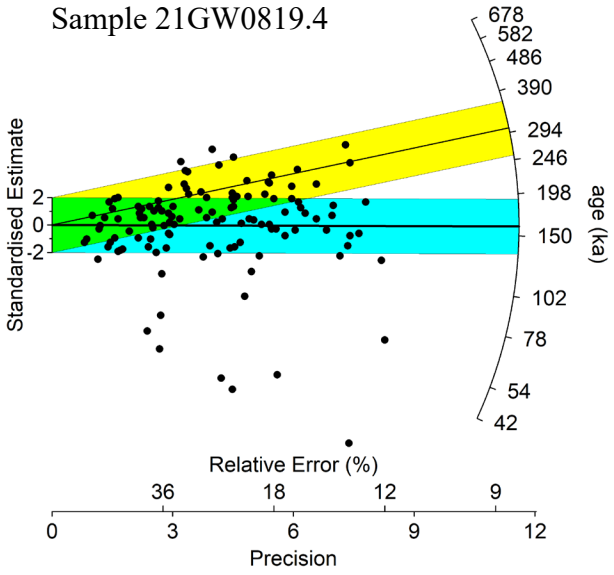
Sample 21GW0819.4
Standardised Estimate
2
0
-2
678
582
486
390
294
246
198
150
102
78
54
42
age (ka)
Relative Error (%)
36
18
12
9
0
3
6
9
12
Precision

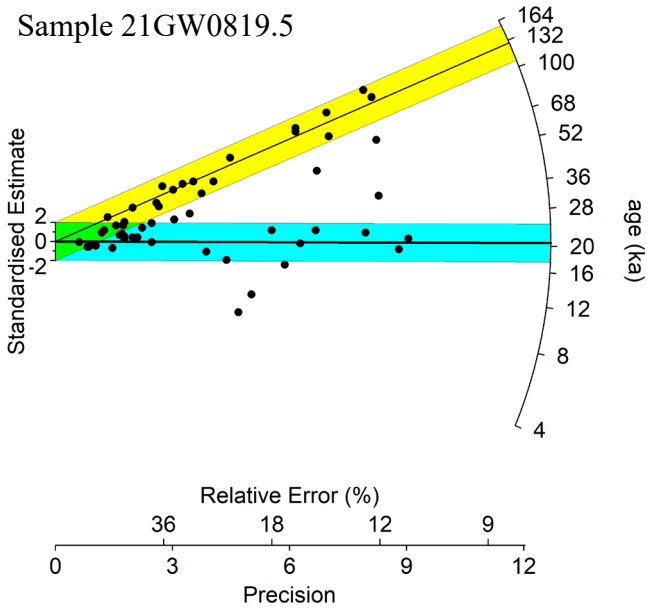
Sample 21GW0819.5
Standardised Estimate
2
0
-2
164
132
100
68
52
36
28
20
16
12
8
4
age (ka)
Relative Error (%)
36
18
12
9
0
3
6
9
12
Precision

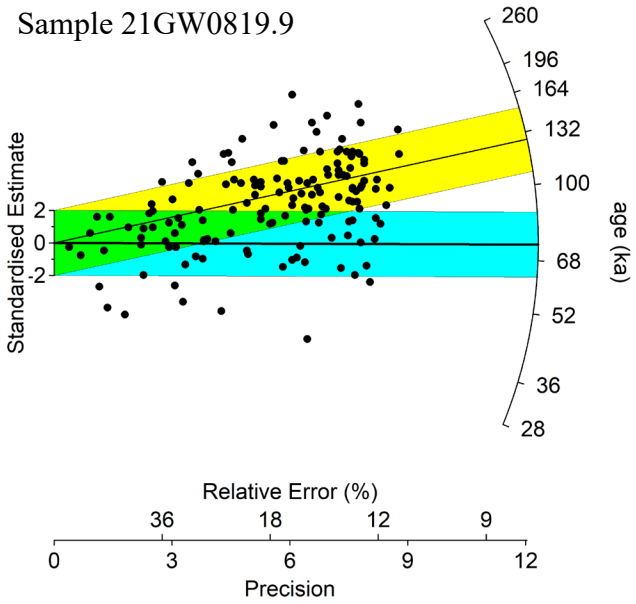
Sample 21GW0819.9
Standardised Estimate
2
0
-2
260
196
164
132
100
68
52
36
28
age (ka)
Relative Error (%)
36
18
12
9
0
3
6
9
12
Precision

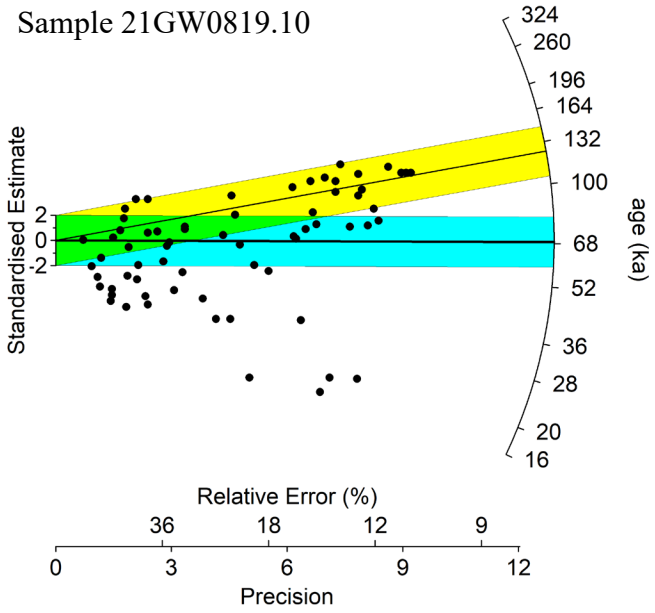
Sample 21GW0819.10
Standardised Estimate
2
0
-2
324
260
196
164
132
100
68
52
36
28
20
16
age (ka)
Relative Error (%)
36
18
12
9
0
3
6
9
12
Precision

# Appendix 3. Supporting information for Stanton et al., Gravity and magnetic evidence for potentially active crustal faulting, northern Cascadia forearc.

## Introduction

This supplement provides eleven additional figures showing individual geophysical maps as well as results from the iterative 2D geophysical modeling described in the primary text. We use the Oasis montaj software GM-SYS extension with the regional magnetic and gravity grids to produce cross-sections that display a calculated gravity and magnetic anomaly from a cross-section geometry using rock density and magnetic properties. The calculated anomalies are compared to the observed anomalies and in an iterative process, using information from geologic mapping and well logs, a final or preferred model is produced. The figures here show: magnetic and gravity maps; early stage iterations of the model that support the preferred models described in the main text; an alternative final stage model with differing geometric configuration; a wide-view final stage model showing all geologic blocks; model iterations showing fault dips that differ from preferred final model. In addition, this supplement provides a description of GUI inputs for the TAK used to produce stream profiles and projected streams segments as seen in Fig. 3-7.

### Description of GUI inputs for Topographic Analysis Kit

We used the graphical user interface (GUI) of the Topographic Analysis Kit (TAK) for TopoToolbox (Forte and Whipple, 2019) to produce longitudinal profiles of streams on the southwestern side of the Raymond Hills from 1 m DEMs (Washington State Department of Natural Resources Lidar Portal, 2019). We cropped the DEMs to the areas of interest so that run

time, particularly on the high-resolution datasets, is not overly long. Initial input for the GUI consists of GeoTiffs of DEMs in UTM format. We used standard tools in ArcMap 10.5.1 to produce the GeoTiffs. After initial upload of the DEMs into the GUI, we followed the workflow suggested by Forte and Whipple (2019) and within tutorial files from the 2020 updated TAK materials (doi:10.5281/zenodo.3608317) to produce the longitudinal stream profiles and to project stream segments along the profile. The first step in the analyses uses the input DEM to "MakeStreams" which converts the DEM into a grid usable in the rest of the analyses, as well as produces stream networks and a flow accumulation grid. The GUI requires an input for several parameters, such as threshold drainage area and reference concavity index. The GUI has an automatic process to find the threshold drainage area or the user may define the threshold area. We used the GUI auto FindThreshold method to assess the mean drainage area. Results suggest that the mean drainage area is between $10^3$-$10^5$ $m^2$. A drainage area of $10^3$ $m^2$ is very small and could represent either ephemeral streams or portions of the topography that are concave but not actually a stream. Additionally, the computational time for drainages that small is very long. We used the upper end of the range, $10^5$ $m^2$ for the minimum drainage basin area. We used the default $10^8$ $m^2$ for the minimum flat area within a stream segment, and 1 m for the no data expression. We used the default reference concavity index of 0.5. Although values between 0.45-0.5 are often used in stream analyses as a reference concavity index (e.g. Whipple and Tucker, 1999), we also used TopoToolbox functions (Schwanghart and Scherler, 2014) to find the optimal value of the concavity index from the 10 m DEM of the study area (U.S. Geological Survey National Map Viewer, 2019), resulting in a concavity index of 0.4545 for the largest drainage basin and of 0.54616 for the entire study area. For this study area, the default reference concavity index of 0.5 appears to be appropriate. We then used the TAK to select individual

streams for longitudinal profile analysis. The GUI uses the stream network dataset from the initial input in an interactive interface to allow the user to select individual streams to plot. For all stream profiles, we used streams selected from the TAK-defined stream network on 1 m DEMs. The GUI also allows the user to select segments of individual streams and to project that segment along the entire length of the stream. Output from both the stream profile process and the stream projection process are pdfs.

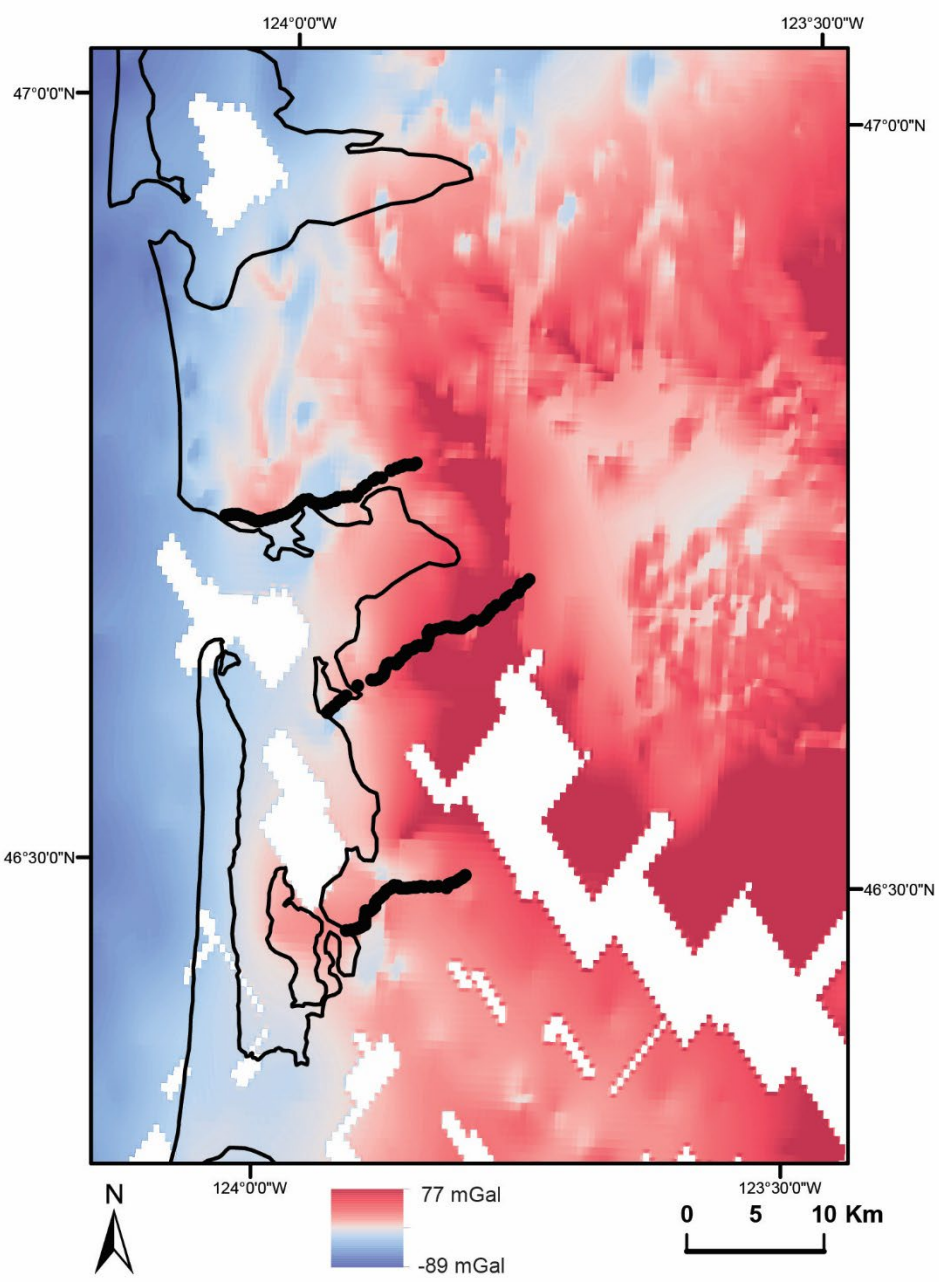


**Figure A3-1.** Map of the gravity data (mGal) in the field area shown without contours and with the locations of gravity surveys collected during this study. All gravity data used in this study can be accessed on the Washington Geological Information Portal, Department of Natural Resources.

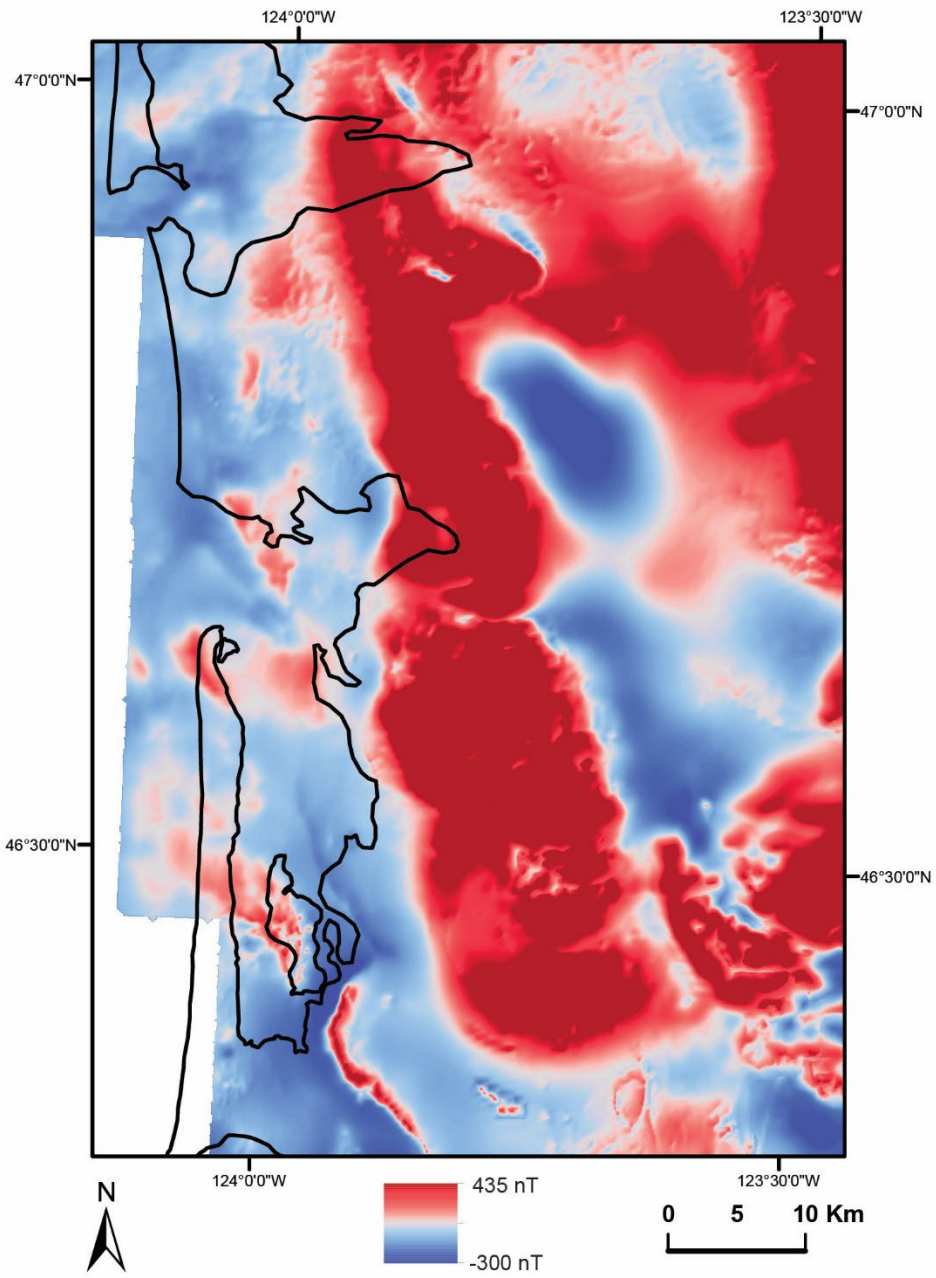


**Figure A3-2.** Map of aeromagnetic data (nT) in the field area.

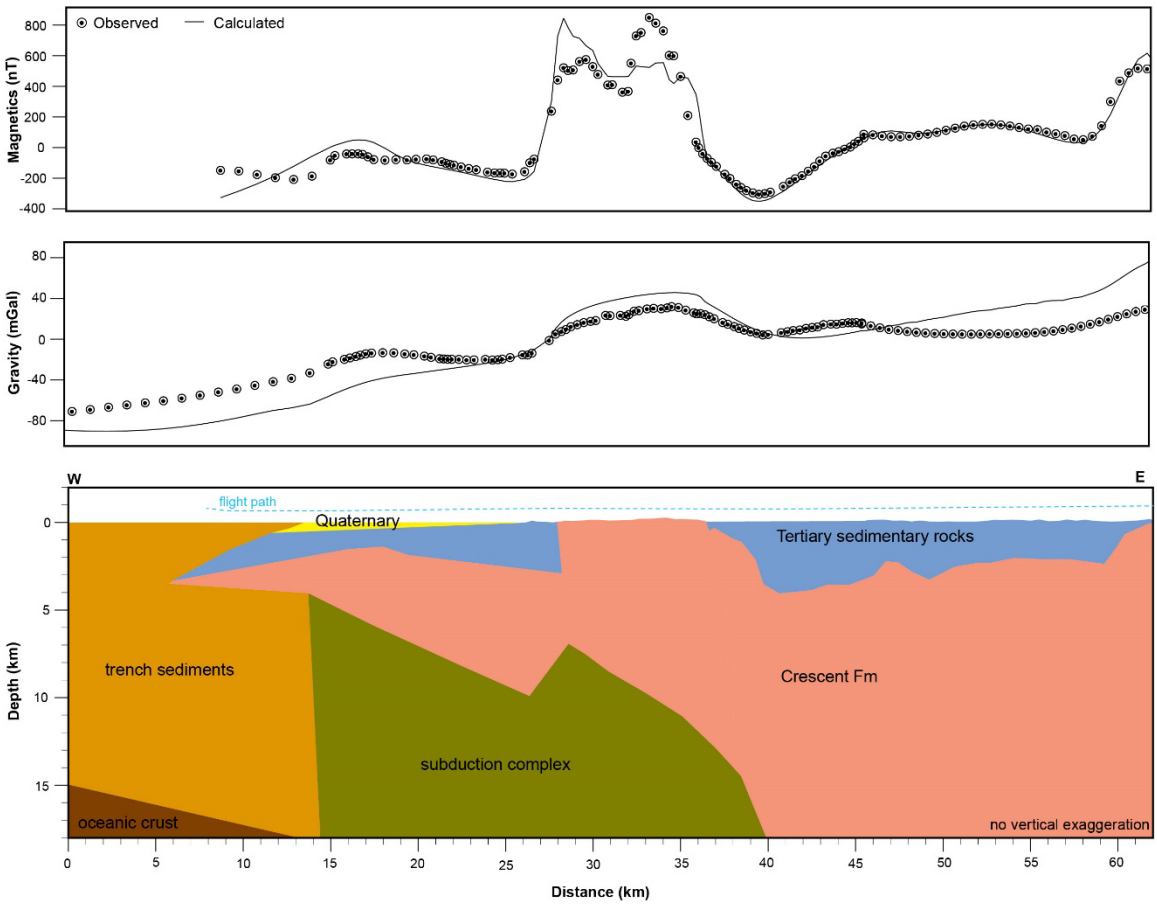


**Figure A3-3.** Early stage model for northern cross-section (see main text for methods). Error circles on gravity have radius of approximately 4 mGal; error circles on magnetics have radius of approximately 30 nT. The general layout of units approximates both the gravity and magnetic anomalies. See main text for discussion. Unit properties per Table 3-1. Raymond Hills and Blue Mountain are both characterized by gravity and magnetic highs constrained by the Crescent Formation exposed at the surface, so we model a large block of Crescent Formation from the coastline eastward. We use a geologic unit we call "subduction complex" on the western side of the model to represent the subduction-related mélange described by Snavely and Wagner (1982) as thrust under the Crescent Formation at a main thrust offshore (west of the western extent of our cross section). Although the resulting calculated gravity is low on the western side of the model and high on the eastern side of the model, the general shape is obtained, suggesting that the gravity and magnetic observations support Snavely and Wagner's (1982) interpretation.

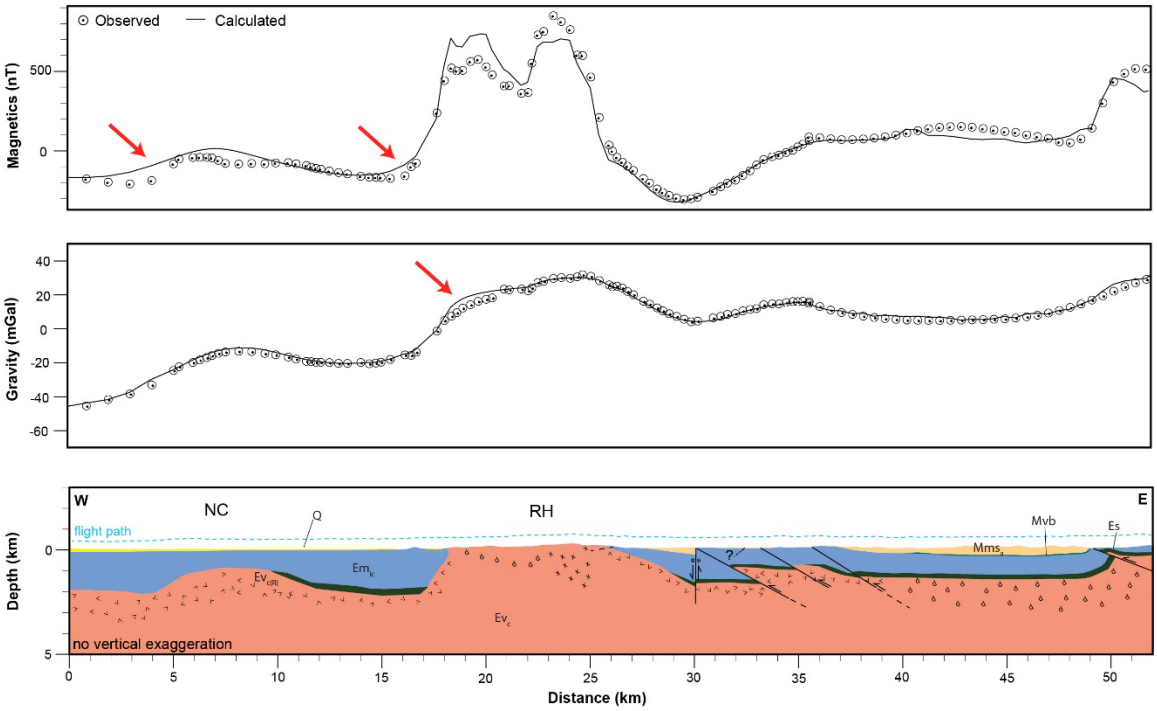


**Figure A3-4.** Final model for northern cross-section (A-A') without faults under the two western-most geophysical potential fields anomalies (see main text for methods and discussion). Error circles on gravity have radius of approximately 2mGal; error circles on magnetics have radius of approximately 25nT. Unit labels per Fig. 3-5 and unit properties per Table 3-1. Red arrows mark locations where the calculated gravity and magnetics have less fit than for preferred fault model.

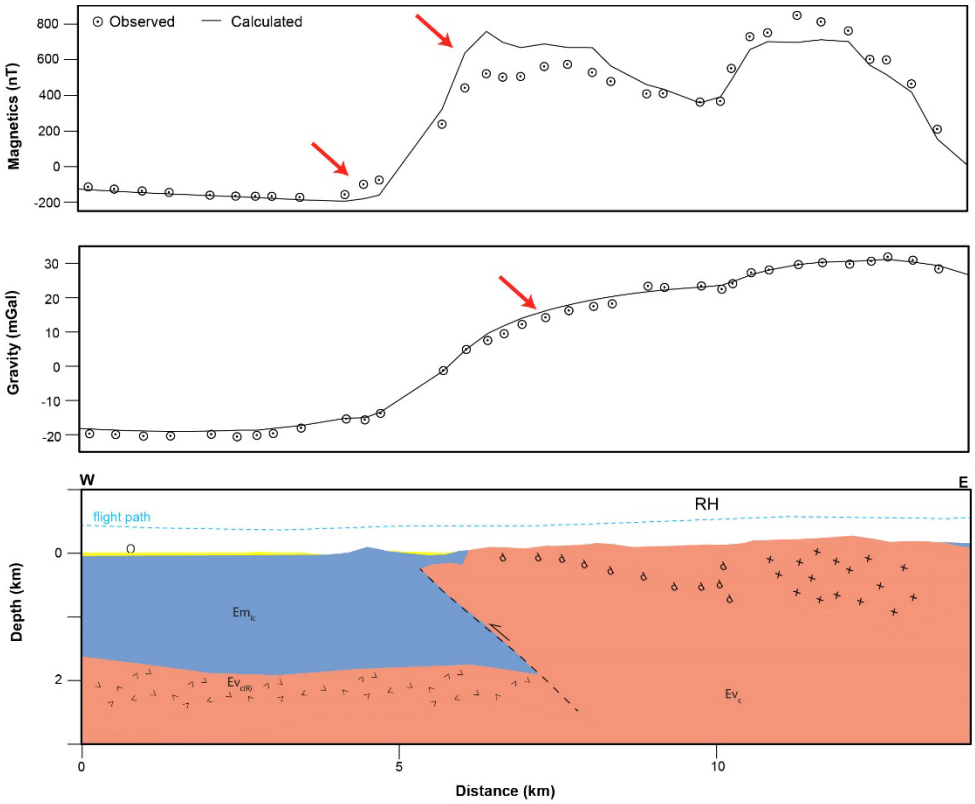


**Figure A3-5.** Model for northern cross-section (A-A') showing Raymond fault at dip of approximately 40°, steeper than in the preferred model. Error circles on gravity have radius of approximately 2 mGal; error circles on magnetics have radius of approximately 25 nT. Red arrows mark locations where the calculated gravity and magnetics have less fit than for preferred fault model. All unit colors and properties follow Fig. 3-5.

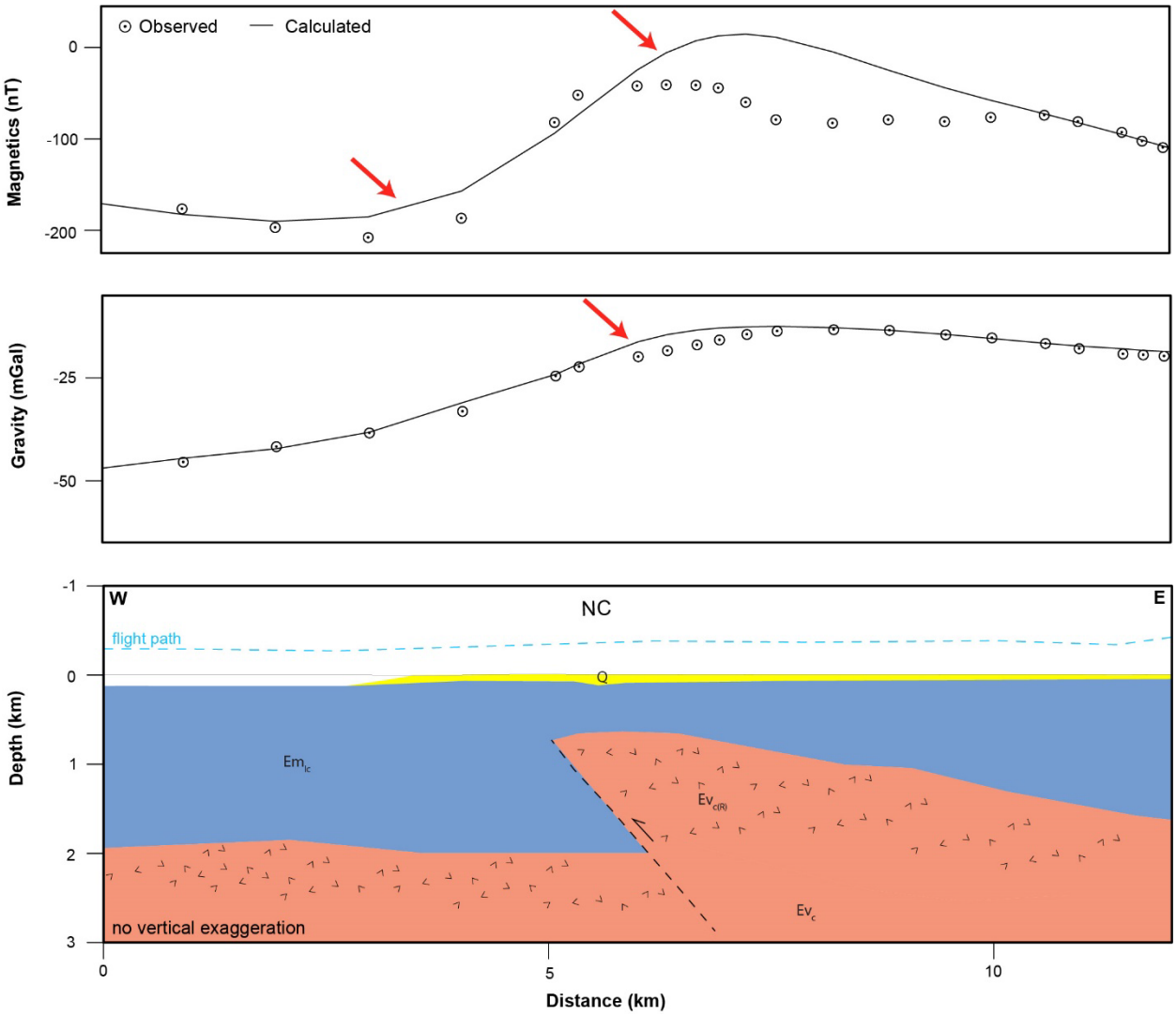


**Figure A3-6.** Model for northern cross-section (A-A') showing Willapa Bay fault at approximately 45°, steeper than in the preferred model. Error circles on gravity have radius of approximately 1.25 mGal; error circles on magnetics have radius of approximately 6 nT. Red arrows mark locations where the calculated gravity and magnetics have less fit than for preferred fault model. All unit colors and properties follow Fig. 3-5.

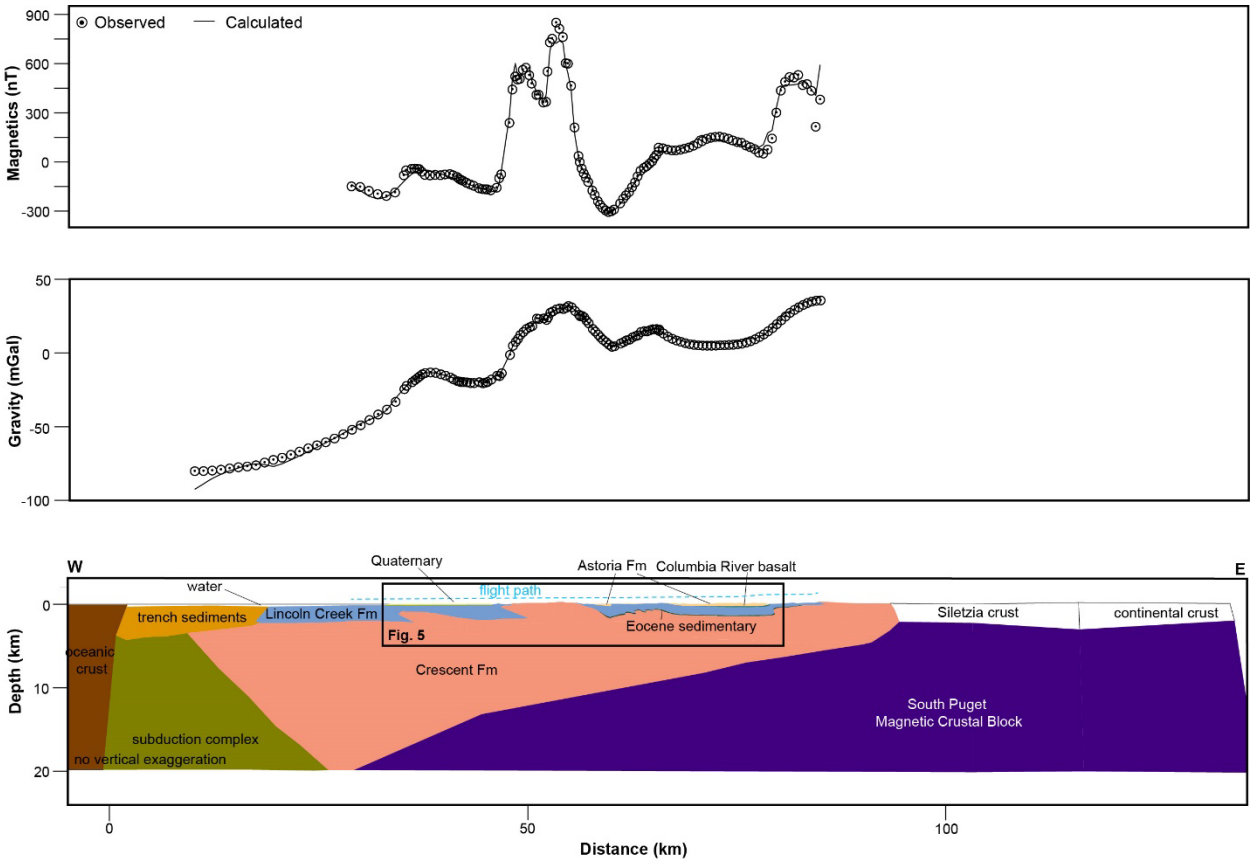


**Figure A3-7.** Final model for northern cross-section (A-A') with faults at a broad scale to show all model elements (see main text for methods). Error circles on gravity have radius of approximately 3 mGal; error circles on magnetics have radius of approximately 31 nT. Unit properties per Table 3-1.

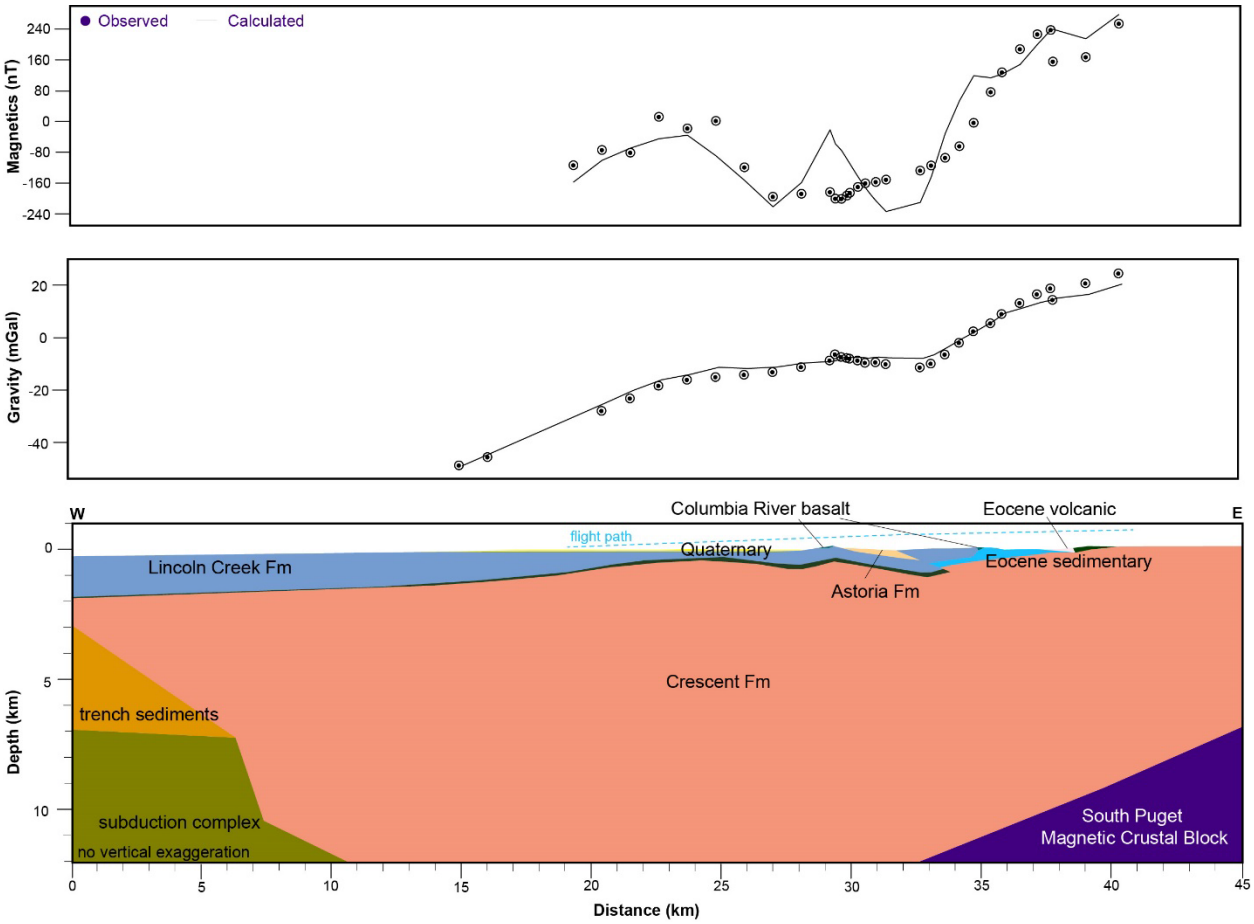


**Figure A3-8.** Early stage model for southern cross-section (B-B', see main text for methods and discussion). Error circles on gravity have radius of approximately 1 mGal; error circles on magnetics have radius of approximately 10 nT. As with Figure A3-3, the general layout of units approximates both the gravity and magnetic anomalies.

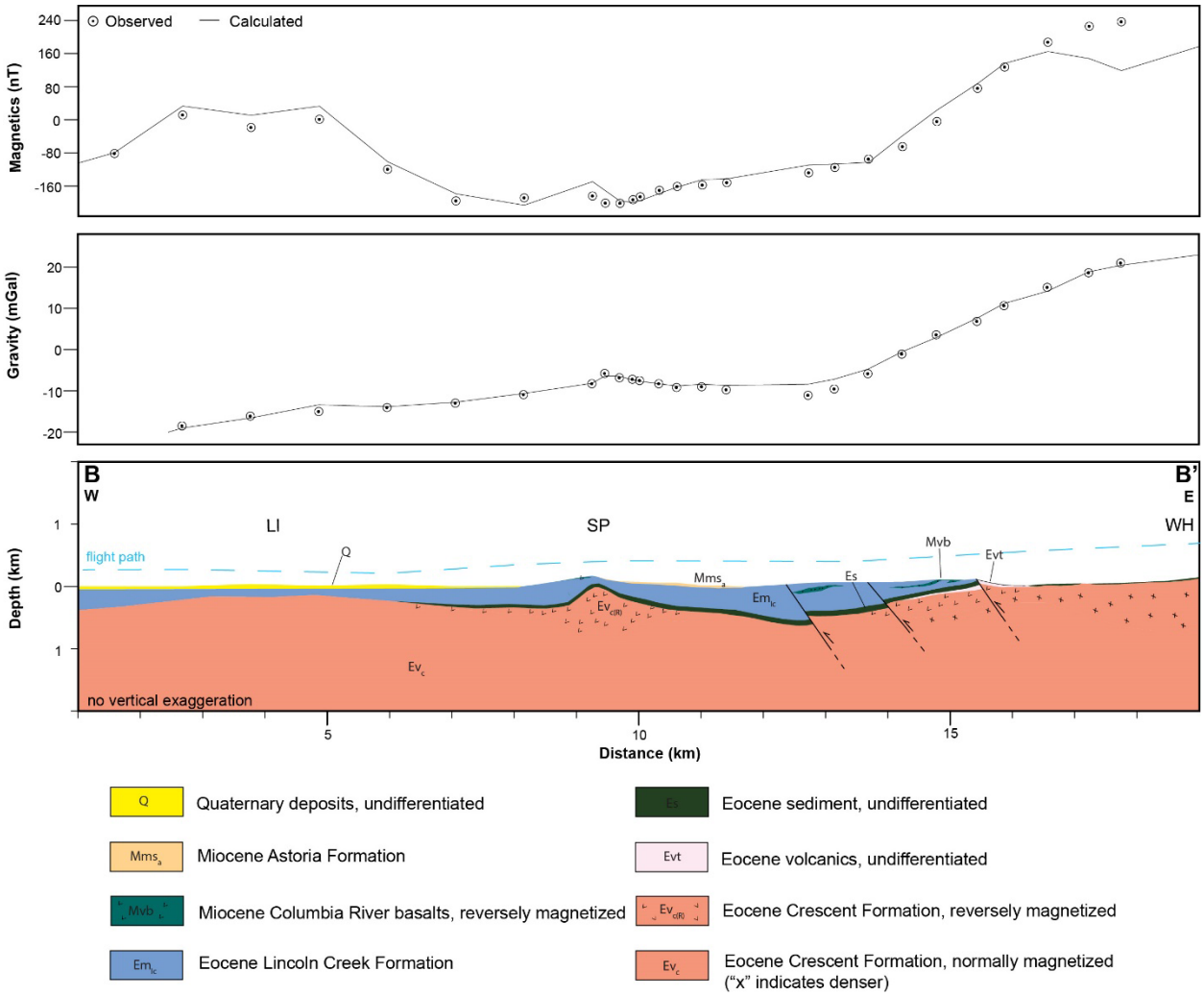


**Figure A3-9.** Final model for southern cross-section (B-B') showing folds rather than faults for western-most geophysical potential fields anomaly. Error circles on gravity have radius of approximately 1 mGal; error circles on magnetics have radius of approximately 20 nT. See main text for discussion.

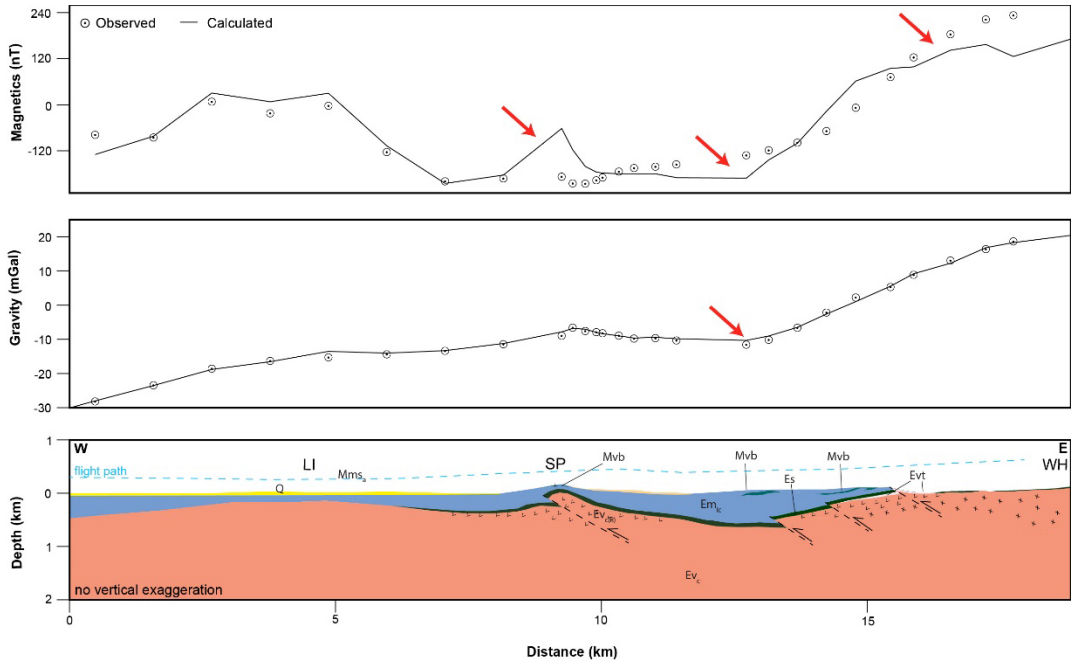


**Figure A3-10.** Model for southern cross-section (B-B') showing faults at approximately 30°, less steep than in the preferred model. Error circles on gravity have radius of approximately 2.5 mGal; error circles on magnetics have radius of approximately 10 nT. Red arrows mark locations where the calculated gravity and magnetics have less fit than for preferred fault model. All unit colors and properties follow Fig. 3-6.

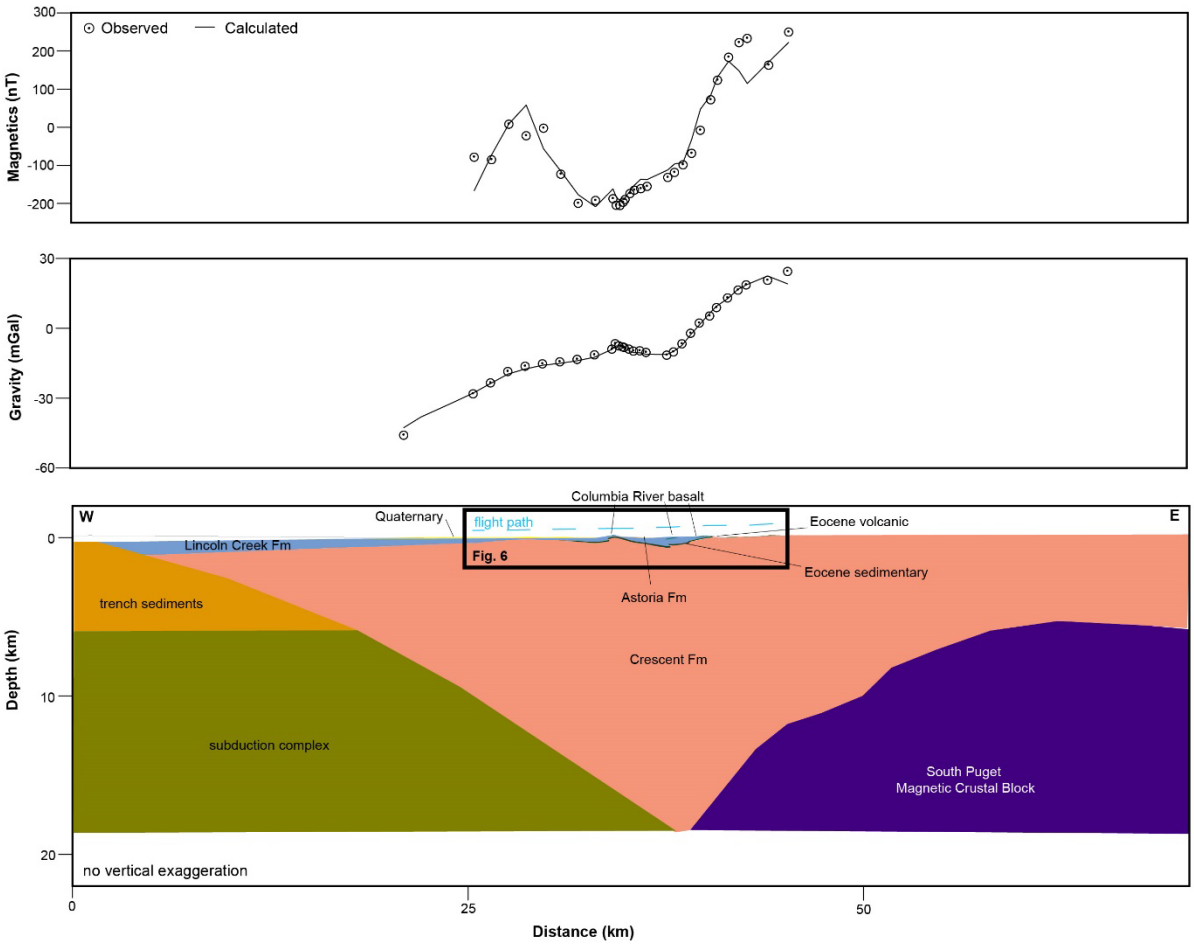


**Figure A3-11.** Final model for southern cross-section (B-B') with faults at a broad scale to show all model elements (see main text for methods). Error circles on gravity have radius of approximately 2 mGal; error circles on magnetics have radius of approximately 13 nT. Unit properties per Table 3-1.

# Appendix 4. Supporting information for Chapter 4, Tectonic geomorphic analyses of Quaternary deposits and regional bedrock, southwestern Washington

## Inputs for Topographical Analysis Kit (TAK) Graphical User Interface (GUI)

Initial input for the GUI consists of GeoTiffs of DEMs in UTM format. I used standard tools in ArcMap 10.5.1 to produce the GeoTiffs. After initial upload of the DEMs into the GUI, I followed the workflow suggested by Forte and Whipple (2019) and within tutorial files from the 2020 updated TAK materials (doi:10.5281/zenodo.3608317) to produce $k_{sn}$ analyses in map-view. For example, the first step in the analyses uses the input DEM to "MakeStreams" which converts the DEM into a grid usable in the rest of the analyses, as well as produces stream networks and a flow accumulation grid. These datasets are used in later analyses and to plot maps of $k_{sn}$.

The GUI requires an input for several parameters, such as threshold drainage area and reference concavity index. The GUI can be used to find a threshold drainage area or the threshold area may be user defined. Too large a drainage area means the MakeStreams function will create a stream network showing only the larger streams. Too small a drainage area and the stream network may include portions of the DEM that are not actually stream channels but represent locations where hillslope processes dominate rather than fluvial processes. I used the GUI auto FindThreshold method on the 10 m DEM to assess the mean drainage area. Results suggest that the mean drainage area is between $10^3$-$10^5$ $m^2$. A drainage area of $10^3$ $m^2$ is very small and could represent either ephemeral streams or portions of the topography that are concave but not actually a stream. Additionally, the computational time for drainages that small is very long. I used the

upper end of the range, $10^5$ $m^2$ for the minimum drainage basin area. I used the default $10^8$ $m^2$ for the minimum flat area within a stream segment, and 1 m for the no data expression. I used the default reference concavity index of 0.5. Although values between 0.45-0.5 are often used in stream analyses as a reference concavity index (e.g. Whipple and Tucker, 1999), I also used TopoToolbox functions (Schwanghart and Scherler, 2014) to find the optimal value of the concavity index from the 10 m DEM of the study area, resulting in a concavity index of 0.45 for the largest drainage basin and of 0.55 for the entire study area. For this study area, the default reference concavity index of 0.5 appears to be appropriate.